

DEVELOPMENT OF ADSORBENTS FOR THE CAPTURE AND STORAGE OF HYDROGEN AND CARBON DIOXIDE BY MAGNETRON SPUTTERING

Christopher Roberts

September 2013

A thesis submitted to the School of Environmental Sciences of the
University of East Anglia in partial fulfilment of the requirements for the
degree of Doctor of Philosophy.

This copy of the thesis has been supplied on the condition that anyone who consults it is understood to recognise that its copyright rests with the author and that use of any information derived there from must be in accordance with current UK Copyright Law. In addition, any quotation or extract must include full attribution.

ABSTRACT

Concerns about climate change have rejuvenated global efforts in reducing carbon dioxide (CO₂) emissions. Tactics include capture and sequestration of CO₂ from point sources and the promotion of hydrogen (H₂) as a “transport fuel”. Current H₂ vehicles use high pressure H₂ tanks which lack the convenience of their fossil fuel counterparts and present potential safety hazards. Development of adsorbent materials that reduce the energetic costs of H₂ and CO₂ capture, facilitating reversible storage under safer conditions, are hoped to increase the viability of these technologies for industrial application.

This thesis is the first to utilise magnetron sputtering, a technique allowing fine control over nano-material synthesis, for the design of novel solid adsorbents and deposition of novel dopants for H₂ storage and CO₂ capture.

Work includes an in-depth study of the influence of nitrogen as a sputter gas on the growth of carbonaceous films, and is the first to explore these films performance as H₂ and CO₂ adsorbents. Several conflicting nitrogen effects were identified, their influence on the films growth dependent upon the nitrogen fraction of the sputter gas. Performance of the deposited films as adsorbents was also dependent on the growth conditions. The H₂ storage capacity at 77 K and 20 bar of an optimised adsorbent, synthesised by magnetron sputtering, was 4.7 wt.%, comparable in performance to alternatives from the literature.

Further work provides the first evidence that cerium, deposited by magnetron sputtering, can function as an adsorbent catalyst and identified that sputtering is a worthwhile, yet slow process for adsorbent doping as it facilitates intimate binding between the adsorbent and the dopant.

The novel synthesis of graphene by magnetron sputtering was also attempted. Whilst tests failed, results collected could provide guidance for more successful attempts in the future.

ACKNOWLEDGEMENTS

This thesis is dedicated to Peter Jones, Dr Derrick Hunt and Anthony Vinters. Their passion for science inspired me to follow the path that brought me here.

I would like to take this opportunity to thank a number of people for their contributions, without which this thesis would not have been possible. First and foremost, Dr Congxiao X. Shang, my primary supervisor, words cannot express your contribution to this project. To Prof. Z. Xiao Guo and Prof. Peter Brimblecombe, I would like to express my sincerest gratitude for your specialist insights. Finally, my deepest thanks to Prof. Tim Jickells whose tremendous guidance and encouragement have helped this project in so many ways.

Many thanks to the technical staff who shared with me their analytical expertise. In particular I would like to thank Bertrand Leze, Colin Macdonald and Kevin Reeves. A massive thank you to Dr. John Brindle for fixing every leak, break, short, loose fitting and apocalyptic disaster our lab threw at him.

To Mi Tian, Dr Jennifer Weston, Yvette Eley, Jasmine Schmittmann-Davies, Jamie “Cascao” Lynch and Ashley “Felix” Smith, thank you for keeping me sane and reminding me that there was life outside the lab.

Finally, for their continuous support, patience and endless care across four difficult years I would like to express my love and gratitude for my parents, brothers, grandparents and especially my partner, Lucy Basing.

LIST OF CONTENTS

ABSTRACT	I
ACKNOWLEDGEMENTS	II
LIST OF CONTENTS	III
LIST OF FIGURE CAPTIONS	XV
LIST OF TABLE CAPTIONS	XXI
THESIS FLOWCHART	XXIII
CHAPTER 1: INTRODUCTION	1
CHAPTER 2: LITERATURE REVIEW	4
2.1 Environmentally significant gases	4
2.1.1 Carbon dioxide	6
2.1.2 Carbon dioxide capture and storage strategies	7
2.1.2.1 Oxygen-fired combustion	8
2.1.2.2 Post-combustion capture	8
2.1.2.3 Pre-combustion capture	9
2.1.3 Hydrogen	10
2.1.3.1 DOE Objectives	12
2.1.4 Syngas	14

2.2	Gas capture and storage technologies	18
2.2.1	Compressed gas/liquid storage or separation	19
2.2.1.1	Hydrogen storage	19
2.2.1.2	CO ₂ and H ₂ separation	20
2.2.2	Adsorption	22
2.2.2.1	CO ₂ materials of interest	27
2.2.2.2	Adsorption for H ₂ storage	28
2.2.2.2.1	The spillover process	29
2.2.2.2.2	H ₂ materials of interest: Carbon nanostructures	31
2.2.3	Absorption	38
2.2.3.1	Absorption for H ₂ storage	38
2.2.3.1.1	H ₂ Materials of interest: Magnesium Borohydride, Mg(BH ₄) ₂	45
2.2.3.2	Absorption for CO ₂ capture	45
2.2.3.2.1	CO ₂ Materials of interest: Layered double hydroxides	48
2.2.4	Membrane separation	49
2.2.4.1	Knudsen diffusion	51
2.2.4.2	Surface diffusion	52
2.2.4.3	Capillary condensation	52

2.2.4.4	Molecular sieving	52
2.2.4.5	Disassociative dissolution	53
2.2.4.6	CO ₂ materials of interest: Polybenzimidazole	54
2.2.4.7	H ₂ materials of interest: Palladium	55
2.3	Material synthesis	56
2.3.1	Chemical Vapour Deposition	56
2.3.2	Plasma assisted (or enhanced) CVD	59
2.3.3	Physical vapour deposition by magnetron sputtering	60
2.3.4	Ball milling	65
2.4	An introduction to the experiments performed in this study	66
2.4.1	The activation and chemical doping of activated carbon by mechanical ball milling and its influence on H ₂ and CO ₂ storage capacity	66
2.4.1.1	Proposed work	68
2.4.2	The influence of nitrogen content and the presence of a metal substrate on the growth and H ₂ storage capacity of novel carbon films deposited by magnetron sputtering	68
2.4.2.1	Proposed work	70
2.4.3	A study of magnetron sputtering as a means to chemically dope carbon nanotubes with cerium and nickel and its influence on H ₂ storage capacity	72
2.4.3.1	Proposed work	76

2.4.4	Exploring the synthesis of graphene by magnetron sputtering	77
2.4.4.1	Introduction	77
2.4.4.2	Graphene synthesis on copper	79
2.4.4.3	Graphene synthesis on nickel	80
2.4.4.4	Graphene synthesis by magnetron sputtering	83
2.4.4.5	Graphene characterisation	84
2.4.4.6	Proposed work	85
CHAPTER 3: EXPERIMENTAL		87
METHODS AND MATERIALS		
3.1	Materials	87
3.1.1	Solids and powders	87
3.1.2	Magnetron sputtering materials	87
3.1.3	Solvents	89
3.2	Experimental apparatus	89
3.2.1	Glove box	89
3.2.2	Ball mill	90
3.2.3	Magnetron sputtering device	90
3.2.3.1	Substrate stage	91
3.2.3.2	Magnetrons	92

3.2.3.3	Vacuum pumps, gas flow controllers and pressure sensors	93
3.2.3.4	Crystal monitor	93
3.2.3.5	Sample preparation	94
3.3	Material characterisation	94
3.3.1	X-ray diffraction	94
3.3.2	Raman spectroscopy	95
3.3.3	Transmission Electron Microscopy	96
3.3.4	Scanning Electron Microscopy and Energy dispersive X-ray spectroscopy	96
3.3.5	Thermovolumetric analysis of material structure	98
3.3.5.1	Calculating surface area	99
3.3.5.2	Calculating total pore volume, average pore radius and pore shape	100
3.3.6	Thermogravimetric analysis of H ₂ and CO ₂ storage capacities and material density	103
3.3.6.1	Buoyancy correction	104
3.3.6.2	Selection of an isothermal model	108
3.3.6.3	Quality of fit	110
3.3.6.4	The isosteric heat of adsorption	110
3.3.6.5	Henry's law constants	111
3.3.6.6	Calculating the selectivity of an adsorbent	112

3.4	Experimental procedures	113
3.4.1	The activation and chemical doping of activated carbon by mechanical ball milling and its influence on H ₂ and CO ₂ storage capacity	113
3.4.1.1	Material synthesis	113
3.4.1.2	Structural analysis	113
3.4.1.3	Performance as an adsorbent	114
3.4.2	The influence of nitrogen content and the presence of a metal substrate on the growth and H ₂ storage capacity of novel carbon films deposited by magnetron sputtering	114
3.4.2.1	Material synthesis	114
3.4.2.1.1	Deposition of CN _x thin films over a SiMgNi substrate	114
3.4.2.1.2	Deposition of CN _x thin films over a SiNi substrate	115
3.4.2.1.3	Deposition of CN _x thin films over a Si substrate	116
3.4.2.1.4	Thin film separation tests	116
3.4.2.1.5	Mass production of SiMgNiC50400	117
3.4.2.1.6	Thin film separation, purification and collection	118
3.4.2.2	Material characterisation	118
3.4.2.3	Performance as an adsorbent	119
3.4.3	A study of magnetron sputtering as a means to chemically dope carbon nanotubes with cerium and nickel and its influence on H ₂ storage capacity	120

3.4.3.1	Material synthesis	120
3.4.3.1.1	Purification of CNTs	120
3.4.3.1.2	Powder sputtering of lone metals	120
3.4.3.1.3	Mixed metal powder sputtering	121
3.4.3.2	Material characterisation	121
3.4.3.3	Performance as an adsorbent	122
3.4.4	Exploring the synthesis of graphene by magnetron sputtering	122
3.4.4.1	Material synthesis	122
3.4.4.1.1	Sputter deposition of the nickel catalysed graphene films.	122
3.4.4.1.2	Sputter deposition of the copper catalysed graphene films	123
3.4.4.2	Material characterisation	123

CHAPTER 4: RESULTS AND DISCUSSION 124

4.1	The activation and chemical doping of activated carbon by mechanical ball milling and its influence on H₂ and CO₂ storage capacity	124
4.1.1	Material characterisation	124
4.1.1.1	TEM analysis	124
4.1.1.2	Micropore analysis	126

4.1.2	Hydrogen storage capacities of ball milled AC	133
4.1.2.1	Calculation of adsorption energy	140
4.1.2.2	Calculation of the heat of adsorption	1142
4.1.2.3	Theoretical maximum storage capacities	144
4.1.3	Carbon Dioxide Storage Capacities of ball milled AC	145
4.1.3.1	Calculation of adsorption energy	150
4.1.3.2	Calculation of the heat of adsorption	151
4.1.4	Discussion	153
4.1.5	Conclusions	155
4.2	The influence of nitrogen content and the presence of a metal substrate on the growth and H₂ storage capacity of novel carbon films deposited by magnetron sputtering	156
4.2.1	Material Characterisation	156
4.2.1.1	Analysis of CN _x films deposited at 600 °C in varying nitrogen atmospheres on SiMgNi substrates	156
4.2.1.1.1	SEM and EDX analysis	156
4.2.1.1.2	Raman analysis	164
4.2.1.1.3	TEM analysis	167
4.2.1.1.4	Surface morphology of deposited MgNi layers post annealing	171

4.2.1.2	Analysis of CN _x films deposited at different annealing temperatures on a SiNi substrate in a 50 vol.% nitrogen atmosphere	174
4.2.1.2.1	SEM and EDX analysis	174
4.2.1.2.2	Raman analysis	179
4.2.1.2.3	TEM Analysis	179
4.2.1.3	Analysis of CN _x films deposited at 600 °C in varying nitrogen atmospheres on SiNi substrates	181
4.2.1.3.1	SEM and EDX analysis	181
4.2.1.3.2	Raman analysis	187
4.2.1.3.3	TEM analysis	188
4.2.1.4	Analysis of CN _x films deposited at 600 °C onto silicon substrates under varying nitrogen atmospheres	191
4.2.1.4.1	SEM and EDX analysis	191
4.2.1.4.2	Raman analysis	194
4.2.1.4.3	TEM analysis	195
4.2.2	Thermogravimetric analysis of hydrogen storage	198
4.2.2.1	Density correction and anomalous results	199
4.2.2.2	Hydrogen storage capacities of films deposited on SiMgNi substrates at 600 °C in varying nitrogen atmospheres	201
4.2.2.3	Hydrogen storage capacities of films deposited at varying temperatures on SiMgNi substrates within a 50 vol.% nitrogen atmosphere	203
4.2.2.4	Hydrogen storage capacities of films deposited on SiMgNi, SiNi or Si substrates at 600 °C in 50 or 100 vol.% nitrogen atmospheres	204

4.2.3	Adsorbent performance of cleaved CN _x films	206
4.2.3.1	Separation of the CN _x films from the substrate	207
4.2.3.2	Volumetric analysis of the separated foils	209
4.2.3.3	Gravimetric H ₂ storage capacity of the MgNiC50400 foil	211
4.2.3.4	Gravimetric CO ₂ storage capacity of the MgNiC50400 foil	214
4.2.4	Conclusions	216
4.3	A study of magnetron sputtering as a means to compositionally dope carbon nanotubes with cerium and nickel and its influence on H₂ storage capacity	218
4.3.1	Preparation	218
4.3.1.1	Tuning sputter deposition conditions	218
4.3.1.2	Target melting during co-deposition	221
4.3.2	Material characterisation	222
4.3.2.1	Purification of CNTs	222
4.3.2.2	Powder sputtering of lone metals	232
4.3.2.3	Mixed metal powder sputtering	242
4.3.3	Gravimetric hydrogen storage capacity	245
4.3.3.1	Density calculation	245
4.3.3.2	Raw and pure CNTs	246

4.3.3.3	Powder sputtering of lone metals	250
4.3.3.4	Mixed metal powder sputtering	259
4.3.3.5	Summary of all hydrogen storage results	260
4.3.4	Conclusion	261
4.4	Exploring the synthesis of graphene by magnetron sputtering	263
4.4.1	Results and discussion	263
4.4.1.1	Visual inspection of the films	263
4.4.1.2	Raman analysis	264
4.4.1.3	SEM analysis	271
4.4.2	Conclusions	278
	CHAPTER 5: JOINT DISCUSSION	279
5.1	Comparison to the literature	279
5.1.1	Hydrogen storage	279
5.1.2	Carbon dioxide storage	282
5.2	The catalytic performance of nickel	285
5.3	The role of sputtering for adsorbent design	286
	CHAPTER 6: CONCLUSIONS	288

CHAPTER 7: FUTURE WORK	290
REFERENCES	292
APPENDIX A: TOTH MODEL SYNTAX SCRIPT	312
APPENDIX B: SAMPLES, SYMBOLS AND ABBREVIATIONS	314
APPENDIX C: ADDITIONAL RAMAN DATA (SECTION 4.2)	327

LIST OF FIGURE CAPTIONS

2.1	A summary of the energy input and output of US electrical generators in 2011 in Quadrillion British thermal units	5
2.2	Illustrative diagram of how the spillover process improves the performance of a physisorbent	31
2.3	An illustration and TEM image of activated carbons structure	32
2.4	Structure of GNFs	33
2.5	Structure of the different SWCNTs	35
2.6	Structure of MWCNTs	36
2.7	Theoretical sites for hydrogen adsorption	37
2.8	Comparison of the binding energies of different hydrogen storage materials	39
2.9	Potential energy curve for the absorption of hydrogen onto a metal surface	41
2.10	Variation in the nucleation path from α to β phase for large and small particles during H_2 adsorption and desorption	43
2.11	Transport mechanisms in porous membranes	50
2.12	Mechanism for disassociative dissolution	53
2.13	The sequence of gas transport and reaction processes fundamental to CVD film growth	57
2.14	Diagram of the magnetron sputtering gun set-up	61
2.15	Illustrative diagram of the different interactions that occur when a target surface is bombarded with energetic ions	62
2.16	Structure of a graphene sheet	77
2.17	Mechanisms for copper or nickel catalysed graphene synthesis	79
2.18	Interface boundaries for graphene layers	81

2.19	Typical Raman spectra for copper catalysed graphene films synthesised at 850 and 1000 °C	85
3.1	SPEX 8000 ball mill	90
3.2	Inside the Magnetron sputter chamber	91
3.3	Sputter gun cross-section	92
4.1.1	TEM images showing the influence of ball milling upon AC particle size and the effect of milling time on the particle size of ACs based upon TEM analysis	125
4.1.2	Isothermal plot of argon adsorption at 77 K for three ball milled AC samples and unmilled AC and comparison of ideal isothermal shapes	126
4.1.3	Effects of milling time upon the pore volume and surface area of Acs	128
4.1.4	Effect of milling time on the half pore width of ACs in terms of pore volume calculated using the DFT equation	130
4.1.5	Variation in pore diameter and particle width with milling time of pure AC samples	132
4.1.6	Isothermal H ₂ storage capacities of pure and doped ACs milled for varying lengths of time from 0 to 10 bar at 77 and 298 K	133
4.1.7	Composite graphs for the comparison of H ₂ storage capacity with pressure of different milled samples at either 77 or 298 K	135
4.1.8	Effect of milling time upon the pore volume and H ₂ storage capacity at 10 bar of Acs	137
4.1.9	Variation in the adsorption potential of milled AC samples with changes in H ₂ storage capacity at 77 or 298 K	141
4.1.10	Variation in adsorption enthalpy with H ₂ storage capacity	143

4.1.11	Isothermal CO ₂ storage capacities of pure and doped ACs milled for varying lengths of times from 0 to 10 bar at 273 and 298 K	146
4.1.12	Composite graphs for the comparison of CO ₂ storage capacity with pressure of different milled samples at either 273 or 298 K	147
4.1.13	Effect of milling time upon the CO ₂ storage capacity and pore volume of ACs	149
4.1.14	Variation in the adsorption potential of milled AC samples with changes in CO ₂ storage capacity at 273 or 298 K	151
4.1.15	Variation in adsorption enthalpy with CO ₂ storage capacity	152
4.2.1	Surface topography and cross-sectional structures of SiMgNiCN _x films deposited at 600 °C in varying nitrogen atmospheres	157
4.2.2	Variation in the film thickness and average cluster size, or cross sectional area, with variation in the nitrogen content of the sputter gas of CN _x films deposited on SiMgNi substrates at 600 °C	159
4.2.3	Variation in the sputter rate of carbon in different nitrogen sputter gas contents, measured by the crystal rate monitor	160
4.2.4	Raman spectra for SiMgNiC ₅₀ N ₆₀ including assignment of the key peaks identified	165
4.2.5	TEM images of carbonaceous species grown at 600 °C on SiMgNi substrates at different magnifications	168
4.2.6	SEM images of the MgNi layers deposited on silicon annealed at different temperatures	172
4.2.7	Surface topography and cross sectional structure of SiMgNiCN _x films deposited at varying temperatures in a 50/50 N ₂ :Ar atmosphere	175

4.2.8	Variation in the film thickness and average cluster size with variation in temperature of the annealing and carbon deposition processes	176
4.2.9	TEM images of carbonaceous species grown at 400 and 700 °C on SiMgNi substrates	180
4.2.10	Surface topography and cross-sectional structures of SiNiCN _x deposited at 600 °C in varying nitrogen atmospheres	182
4.2.11	Variation in the film thickness and average cluster size with variation in the nitrogen content of the sputter gas of CN _x films deposited on SiNi substrates at 600 °C	183
4.2.12	Appearance of Ni film annealed on the surface of a silicon substrate for 30 minutes at 600 °C	185
4.2.13	TEM images of carbonaceous species grown at 600 °C on a SiNi substrates	189
4.2.14	Topography of SiCN _x deposited at 600 °C in varying nitrogen atmospheres	192
4.2.15	Examples of the structures identified in TEM analysis of SiC films	195
4.2.16	Variation in the film thickness with variation in the nitrogen content of the sputter gas of CN _x films deposited on silicon substrates at 600 °C	197
4.2.17	Variation in the recorded sample densities with the nitrogen sputter gas fraction of the deposition process	200
4.2.18	Isothermal H ₂ storage capacities of SiMgNiC600 films with an increase in pressure at 77 and 298 K	201
4.2.19	Isothermal H ₂ storage capacities of SiMgNiC50 films with an increase in pressure at 77 and 298 K	203
4.2.20	Isothermal H ₂ storage capacities against pressure of CN _x films grown on different substrates in either a 50 or 100 vol.% nitrogen atmospheres at 77 K or 298 K	204
4.2.21	Foil separation tests	208

4.2.22	Volumetric characterisation of MgNiC50400 foil structure	210
4.2.23	Isothermal H ₂ storage capacities of MgNiC50400 foil against pressure at 77 and 298 K	212
4.2.24	Isosteric heats of adsorption and its variation with storage capacity for MgNiC50400 foil	213
4.2.25	Isothermal CO ₂ storage capacities of MgNiC50400 foil against pressure at 273 and 298 K	214
4.2.26	Isosteric heats of CO ₂ adsorption and its variation with storage capacity for MgNiC50400 foil	215
4.3.1	<i>In situ</i> sputter rate determination based upon sputter power	219
4.3.2	<i>Ex situ</i> deposition rate determination from the deposition time	220
4.3.3	X-ray diffraction patterns for raw and purified CNTs	222
4.3.4	Raman spectra for the raw and purified CNTs	223
4.3.5	TEM images indicative of the raw and purified CNTs	225
4.3.6	Isothermal N ₂ adsorption for the raw and purified CNTs with pressure	226
4.3.7	Comparison of approaches for surface area calculation	229
4.3.8	Change in the pore size distribution and cumulative pore volume with half pore width of RCNT and PCNTs, calculated from DFT analysis	230
4.3.9	Comparison of x-ray Diffraction patterns for PCNT and cerium doped CNTs and PCNT and nickel doped CNTs	232
4.3.10	Raman spectra for CNTCe0.1	233
4.3.11	TEM images representative of the cerium coated CNTs	235
4.3.12	DFT pore size distribution of cerium doped CNTs	241
4.3.13	Comparison of PCNT and CeNi doped CNT diffraction patterns	243
4.3.14	TEM images of textured CeNi doped CNTs	244

4.3.15	Isothermal H ₂ storage capacities for RCNT and PCNT with pressure	247
4.3.16	Isosteric heat of adsorption for RCNT and PCNT, and its variation with storage capacity	249
4.3.17	Hydrogen storage capacities for nickel doped CNTs up to 20 bar at 77 and 298 K	250
4.3.18	Isosteric heats of adsorption and its variation with storage capacity for nickel doped CNTs	252
4.3.19	Hydrogen storage capacities for cerium doped CNTs up to 20 bar at 77 and 298 K	254
4.3.20	Hydrogen storage capacities for additional cerium doped CNTs up to 20 bar at 77 and 298 K	255
4.3.21	Isosteric heats of adsorption and its variation with storage capacity for cerium doped CNTs	256
4.3.22	Hydrogen storage capacities for CeNi co-doped CNTs up to 20 bar at 77 and 298 K	259
4.3.23	Isosteric heats of adsorption and its variation with storage capacity for CeNi co-doped CNTs	260
4.3.24	Comparison of the maximum hydrogen storage capacities at 77 K and 20 bar for cerium doped samples, nickel doped samples and CeNi doped samples	261
4.4.1	Changes in a films appearance with carbon deposition time	263
4.4.2	Raman spectra for carbon coated copper films	265
4.4.3	Raman spectra for carbon coated nickel films	269
4.4.4	Surface topography at different magnifications of copper and carbon films deposited at 800 °C over varying deposition times	271
4.4.5	Surface topography at different magnifications of nickel and carbon films deposited at 800 °C over varying deposition times	275





LIST OF TABLE CAPTIONS

2.1	System targets for an on-board hydrogen storage for light duty fuel cell vehicles	13
2.2	Reactions taking place within the Syngas process	16
2.3	Illustration of the experimental design for the deposition of novel carbon adsorbents by magnetron sputtering	71
3.1	List of magnetron sputter targets used in this project	88
3.2	Summary of the different solvents were used in this work	89
4.1.1	Comparison of the hydrogen storage capacities per ml of doped and pure AC samples	139
4.1.2	Comparison of the theoretical H ₂ storage capacity (assuming complete monolayer coverage) against the recorded H ₂ storage capacities at 10 bar and 77 or 298 K	144
4.1.3	Selectivity of the adsorbents for H ₂ or CO ₂	154
4.2.1	C:N ratio of the films deposited under different nitrogen atmospheres onto SiMgNi substrates, measured by EDX analysis	163
4.2.2	Summary of the results of Raman analysis of CN _x films deposited on SiMgNi substrates	166
4.2.3	SEM image analysis Results of surface topography	173
4.2.4	C:N ratio of the films deposited at different temperatures onto SiMgNi substrates, measured by EDX analysis	177
4.2.5	Summary of the results of Raman analysis of SiMgNiC ₅₀ films deposited at different temperatures	179
4.2.6	C:N ratio of the films deposited under different nitrogen atmospheres onto SiNi substrates, measured by EDX analysis	186

4.2.7	Summary of the results of Raman analysis of CN _x films deposited on SiNi substrates	187
4.2.8	C:N ratio of the films deposited under different nitrogen atmospheres onto Si substrates, measured by EDX analysis	193
4.2.9	Summary of the results of Raman analysis of CN _x films deposited on Si substrates	194
4.2.10	Physical attributes of MgNiC50400 foil	210
4.3.1	Summary of material sputter rates under different conditions	220
4.3.2	Raman data for RCNT and PCNT samples	223
4.3.3	Physical attributes of RCNTs and PCNTs	229
4.3.4	Raman results for cerium doped CNTs	234
4.3.5	Physical attributes of cerium or nickel doped CNTs	239
4.3.6	Physical attributes of cerium and nickel doped CNTs	245
4.4.1	Key Raman results from analysis of carbon coated copper films	268
4.4.2	Key Raman results from analysis of carbon coated nickel films	270
5.1	List of H ₂ storage capacities from the literature	280
5.2	List of H ₂ storage capacities from the literature	282

FLOWCHART

The flow chart below was designed to assist the reader in navigating this thesis. Coloured segments connect the introduction, experimental method and results of the four individual studies in this work. Clear segments cover topics that relate to several of the studies simultaneously. For example, the introduction for the study titled “The activation and chemical doping of activated carbon by mechanical ball milling and its influence on H₂ and CO₂ storage capacity” begins on page 82, the experimental method begins on page 139 and the results begin on page 155.

1	INTRODUCTION	1	
2	LITERATURE REVIEW	4	
2.1	Environmentally significant gases	4	
2.2	Gas capture and storage technologies	18	
2.3	Material synthesis	56	
2.4	An introduction to the experiments performed in this study	66	
2.4.1	The activation and chemical doping of activated carbon by mechanical ball milling and its influence on H ₂ and CO ₂ storage capacity	66	
2.4.2	The influence of nitrogen content and the presence of a metal substrate on the growth and H ₂ storage capacity of novel carbon films deposited by magnetron sputtering.	68	
2.4.3	A study of magnetron sputtering as a means to chemically dope carbon nanotubes with cerium and nickel and its influence on H ₂ storage capacity	72	
2.4.4	Exploring the synthesis of graphene by magnetron sputtering.	77	

3	EXPERIMENTAL METHODS AND MATERIALS	87
3.1	Materials	87
3.2	Experimental apparatus	89
3.3	Material characterisation	95
3.4	Experimental procedures	109
3.4.1	The activation and chemical doping of activated carbon by mechanical ball milling and its influence on H ₂ and CO ₂ storage capacity.	110
3.4.2	The influence of nitrogen content and the presence of a metal substrate on the growth and H ₂ storage capacity of novel carbon films deposited by magnetron sputtering.	112
3.4.3	A study of magnetron sputtering as a means to chemically dope carbon nanotubes with cerium and nickel and its influence on H ₂ storage capacity	117
3.4.4	Exploring the synthesis of graphene by magnetron sputtering	120
4	RESULTS AND DISCUSSION	122
4.1	The activation and chemical doping of activated carbon by mechanical ball milling and its influence on H ₂ and CO ₂ storage capacity.	122
4.2	The influence of nitrogen content and the presence of a metal substrate on the growth and H ₂ storage capacity of novel carbon films deposited by magnetron sputtering.	151
4.3	A study of magnetron sputtering as a means to chemically dope carbon nanotubes with cerium and nickel and its influence on H ₂ storage capacity	213
4.4	Exploring the synthesis of graphene by magnetron sputtering	258

5	JOINT DISCUSSION	274
5.1	Comparison to the literature	274
5.2	The catalytic performance of nickel	279
5.3	The role of sputtering for adsorbent design	280
6	CONCLUSIONS	282
7	FUTURE WORK	284

CHAPTER 1: INTRODUCTION

The scope set out for this project was the design and synthesis of novel materials for the capture or reversible storage of hydrogen (H_2) and carbon dioxide (CO_2). The literature review in **Chapter 2** therefore begins with an assessment of the significance of these gases (**Section 2.1**) and is followed by a summary of the techniques for their capture and storage (**Section 2.2**).

Based upon the conclusions of **Section 2.2**, research targeted at understanding and improving the adsorptive performance of carbon based physical adsorbents was selected as the main objective of this research. The four primary reasons for selecting this approach were:

1. Carbon materials can adsorb both H_2 and CO_2 allowing investigation of their suitability as storage mediums for both gases, and allowing the contrast in the adsorptive performances of each gas to be explored mechanistically.
2. Physical adsorption seemed the most promising approach to eventually meet the DOE objectives for on board H_2 storage (**Table 2.1**) [1], as the process only suffered from one major limitation- the total storage capacity- rather than the range of problems faced by alternatives outlined in **Section 2.2**. Given the underperformance of current adsorbents compared to the DOE objectives, designing a material that achieved these targets seemed unreasonable. Recognizing the material features which increase H_2 or CO_2 adsorption and identifying how to promote their creation during synthesis was of greater importance, especially with regard to the gravimetric storage capacity.
3. Magnetron sputtering, a physical vapour deposition (PVD) process discussed in **Section 2.3.3**, was to be the primary approach for material synthesis in this project. Sputtering is already used industrially for the synthesis of carbon nanostructures [2] but no literature could be found that suggests that the adsorptive properties of materials synthesised by this method have been explored previously. As discussed in greater detail in **Section 2.3.3**, sputtering, whilst slow, offers many mechanistic advantages over alternative synthetic techniques- allowing increased control over the growth parameters of the materials synthesised. It was hoped that the increased control over the growth parameters could assist

in understanding and improving carbons adsorptive performance. Sputtering is a slow deposition process and thus seemed unlikely to become a viable method for industrial scale adsorbent synthesis, It was instead hoped that the control the process offered over material structure might assist in the understanding of the requirements of an ideal adsorbent and inform the characteristics that should be promoted in materials synthesised by processes better suited to industrial scale synthesis.

4. It seemed the field with the greatest opportunity for scientific contribution, both in terms of design of novel material structures and development of the academic understanding of “what makes an ideal adsorbent”.

Section 2.3 discusses the common processes used to synthesise nano-carbon structures highlighting the novel opportunities presented by the synthetic techniques applied in this work.

As discussed in **Section 2.2.2**, optimisation of the novel carbon structures can be achieved by a variety of different approaches. Four of these approaches were studied across three experiments. **Section 2.4** outlines the theory and principles behind the experiments performed in this study;

Section 2.4.1. The activation and chemical doping of activated carbon by mechanical ball milling and its influence on H₂ and CO₂ storage capacity. Ball milling is an established adsorbent modification process looked at in this work to evaluate its influence on both the modification of an adsorbents performance and its function for dispersing a catalytic additive. The experimental procedures are described in **Chapter 3, Section 3.4.1** and results and discussion are presented in **Chapter 4, Section 4.1**.

Section 2.4.2. The influence of nitrogen content and the presence of a metal substrate on the growth and H₂ storage capacity of novel carbon films deposited by magnetron sputtering. Optimisation of an adsorbents structure and chemical composition can drastically improve performance (**Section 2.2.2**). Magnetron sputtering

(**Section 2.3.3**) offers fine control over these factors yet has not been previously exploited for adsorbent synthesis. This section studies the influence growth conditions can have on an adsorbent and evaluates the performance of sputter deposited materials for adsorbent technologies. The experimental procedures are described in **Chapter 3, Section 3.4.2** and results and discussion are presented in **Chapter 4, Section 4.2**.

Section 2.4.3. A study of magnetron sputtering as a means to compositionally dope carbon nanotubes (CNTs) with cerium and nickel and its influence on H₂ storage capacity. Doping an adsorbent can improve its performance, but the improvement is heavily influenced by the doping process. Magnetron sputtering was explored as an approach for introducing a dopant to an adsorbent to study if the process proves advantageous. The experimental procedures are described in **Chapter 3, Section 3.4.3** and results and discussion are presented in **Chapter 4, Section 4.3**.

An additional study was performed, taking advantage of the equipment and the knowledge of sputtering carbon films gathered throughout the project, to attempt the novel synthesis of graphene by magnetron sputtering. A full assessment of the test is outlined in **Section 2.4.4. Exploring the synthesis of graphene by magnetron sputtering.** The experimental procedures for this work are described in **Chapter 3, Section 3.4.4** and results and discussion are presented in **Chapter 4, Section 4.4**.

Chapter 3 also outlines the experimental facilities, analytical processes and material characterisation techniques followed. **Chapter 5** covers a general discussion of the results presented in **Chapter 4**. **Chapter 6** concludes the key findings of this study and **Chapter 7** outlines possible avenues for future research uncovered by this investigation.

CHAPTER 2: LITERATURE REVIEW

2.1 Environmentally significant gases

Concerns about climate change have rejuvenated global efforts in reducing greenhouse gas (GHG) emissions, particularly CO₂ [3-8]. There are three objectives that must be met during the 21st century to prevent exacerbating the current environmental crisis [9]. They are:

- Increase energy efficiency by developing new energy systems which overcome the thermodynamic limitations of existing processes.
- Develop sustainable and safe energy sources including renewable resources, nuclear power and carbon neutral, sustainable organic materials from carbon-based feedstock.
- Reduce environmental pollution problems, such as stabilising GHG emissions despite increased energy utilization.

Figure 2.1 shows an energy flow chart for electricity generation in the US from 2011. 66 % of energy generation in the US was reliant upon combustion of fossil fuels with each process contributing to the release of CO₂. US fossil fuel electrical generators have an average efficiency of about 35 % contributing heavily to the 63 % of energy generated being lost in conversion to electrical power [8]. Similarly, as much as 65 to 80 % of energy input in mobile energy systems (cars) is wasted in conversion.

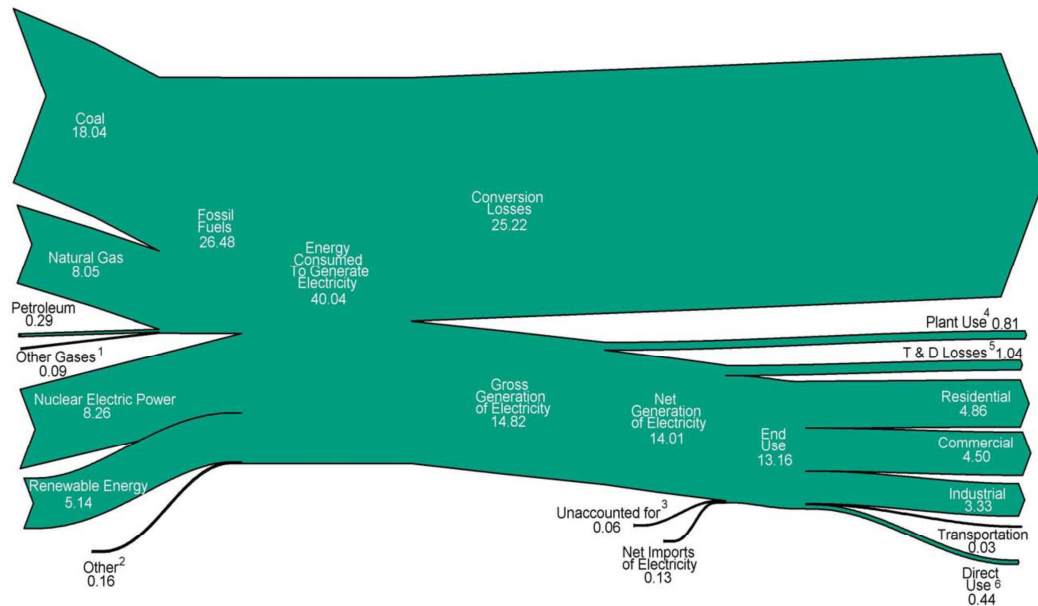


Figure 2.1. A summary of the energy input and output of US electrical generators in 2011 in Quadrillion British thermal units (BTU) [10].

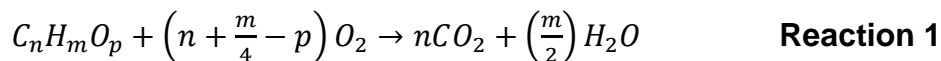
Increasing the energy efficiency of systems to limit emissions and decrease the use of dwindling supplies of non-renewable fuels is a key societal and scientific challenge. There are however two practical limitations to this approach toward mitigating climate change. Firstly, Carnot cycle efficiency states that there is a fundamental limit to energy conversion efficiencies and increasing efficiency alone will not deplete GHG emissions to a viable and safe output to avoid major climate changes [3, 11]. Secondly, measures to improve efficiency of existing power sources require complete reconstruction of the generators- a task impractical for most systems unless the goal was to harness wasted energy by retrofitting the generator with additional energy harnessing systems [9].

Massive strides have been made to increase the viability of renewable energies, such as solar, wind and hydroelectric power, to meet global demand [12, 13]. Unfortunately the technologies are not yet reliable or cost effective, forcing a continued dependence on hydrocarbon combustion for the foreseeable future [9]. The use of carbon based feedstock (biomass) for fuel generation is practically a carbon neutral

process as the carbon released as CO₂ from combustion is consumed in the growth of the next season's crop [14]. The proportionally slender GHG excess comes from transportation and processing of the biomass for combustion. Whilst this process is widely considered carbon neutral the viabilities of this technology's future are instead economic with concerns over the practicality of using land for growing crops for fuel, an argument referred to as the "food vs. fuel" debate [15]. Further concerns surround the impact on the stakeholders affected by the supply chain and the environment within which the supply chain operates [16].

2.1.1 Carbon Dioxide

CO₂ is a colourless and odourless gas generated by the complete oxidative combustion of carbon based organic matter (**Reaction 1**) [8, 17].



An empirical rule of thumb states that the higher the atomic hydrogen-to-carbon ratio, the lower the CO₂ release per million BTU (1 055.05585 joules) [4]. CO₂ is a linear molecule, with double bonds linking the carbon to the oxygens, that occurs in nature and is generated by a variety of different sources ranging from respiration, the process essential to life on earth, to volcano venting [18]. Removal of CO₂ from the atmosphere is also a natural process with atmospheric CO₂ serving as the major source of carbon for photosynthesis. Human activities since the industrial revolution have caused an imbalance in the natural carbon cycle. The CO₂ concentration of the atmosphere is 35 % higher now than it was at the beginning of the industrial revolution [19]. The two main contributors to the CO₂ emission imbalance are the transport and energy generation industries. The burning of liquid hydrocarbons within vehicles is responsible for up to 25 % of global CO₂ emissions and fossil fuel burning power plants comprise another 40 % [7, 20]. As of December 2004, the atmospheric volumetric concentration of CO₂ was 0.038 % (377 parts per

million by volume; ppmv) [4]. With growing rates of economic expansion and growing populations there is a constant call for more energy. However some strategies such as construction of new coal burning power stations, to address energy concerns are exacerbating the environmental crisis [18, 21]. An unfortunate curse of CO₂ is that despite being an abundant and renewable carbon source it is relatively unreactive and therefore only utilised in a handful of industrial processes as a raw material [22]. As a result, the energy consuming (endothermic) “fixing” of CO₂ is considered uneconomic and unfavourable. One potential advantage of CO₂ capture strategies beyond environmental applications is that sequestration of CO₂ from a reaction mix pushes some reactions equilibrium further toward completion, increasing the efficiency of industrial processes, unfortunately the cost and efficiency of the process currently exceeds the saving that would be made [23].

2.1.2 Carbon dioxide capture and storage (CCS) strategies

As a way to mitigate the release of CO₂ into the atmosphere carbon sequestration strategies were developed. CCS looks to capture and store CO₂ at the point of emission, generating a concentrated stream of CO₂ at high pressures that can be readily transported to storage sites for permanent or semi-permanent fixing [18, 22, 24]. Whilst CCS reduces the quantity of CO₂ emitted into the atmosphere it does not limit the production of CO₂, nor does it sever our reliance on energy generation from hydrocarbon combustion. CCS is a mid-term solution designed to mitigate the environmental impacts of continued hydrocarbon combustion until renewable energy technologies mature and are able to match energy demands [7]. Different techniques developed to capture and sequester CO₂ will be discussed in **Section 2.2**. Their suitability for use is dependent upon the technology that generates CO₂. There are three approaches to hydrocarbon fired power generation where CO₂ is emitted from large point sources, each with their own obstacles toward CO₂ capture and economic application to overcome [25, 26]:

2.1.2.1 Oxygen-fired combustion (oxy-fuel)

Complete combustion of the hydrocarbon fuel is performed within a nitrogen free, oxygen rich environment [27]. Capture and separation of CO₂ is not a concern of this process as 95 % of the flue gas stream collected after combustion is CO₂. Only minor separation, actively removing water, is required for collection of sufficiently pure CO₂ for storage [28]. The primary limitation of this process is the separation of the vast quantities of oxygen required from air to allow combustion to run to completion. Cryogenic or selective membrane separation processes to sequester the oxygen from air inflict a severe energy penalty of roughly 9 % on the energy output of the power station on top of the energetic requirements of the CO₂ purification step [29]. Furthermore, implementation of this approach requires the retrofitting of costly air separation units and gas circulation facilities.

2.1.2.2 Post-combustion capture

CO₂ is separated from the flue gas following the fuels complete combustion in air [30]. As combustion is performed in air CO₂ makes up between 10 and 15 % of the flue gas stream (70 % N₂, 14 % other gases). Some adsorption processes, such as amine stripping, can effectively separate up to 90 % of the CO₂ emitted [30]. Unfortunately this process consumes up to 35 % of the energy generated by the power station and is expensive as current CO₂ extraction materials are costly to produce, maintain and replace when their efficiency falls. The range of conditions CO₂ is expected to be captured or sequestered under by this process are greater than the other approaches but ideally pressures of approximately 1.9 to 2.1 bar have been found to perform best for optimising plant efficiency within certain set-ups [31]. Similarly temperature control is required, with amine scrubber technology working best at 313 to 323 K. Given the significant volume of gas passed through the separation column

massive energy losses are incurred heating or cooling the 85 % non CO₂ flue gas fraction to meet the adsorption requirements of the CCS process.

2.1.2.3 Pre-combustion capture

The primary fuel (coal, oil, gas) is treated with steam and oxygen (from air) to produce a mix of carbon monoxide (CO) and H₂ known as Syngas [32]. Additional processing by the water gas shift reaction (WGS), adding steam and methane to the syngas feed generates a H₂ rich feed of H₂ and CO₂ [33]. Due to its significance to both H₂ and CO₂ capture a full description of the syngas and WGS process is reported below in **Section 2.1.4** The expected energy penalty for siphoning generated power off to fuel this process is about 15 %, which is lower than the other CCS approaches [9]. Unfortunately, retrofitting power stations with this technology is difficult and utilisation of this approach seems better suited to newly constructed stations. Also, while the process has been shown to work, the reliability of the separation elements requires significant improvement [25]. To improve the efficiency of the syngas process, active removal of CO₂ or H₂ during combustion drives a shift in the reaction equilibrium increasing the efficiency of the system [23]. Selective removal of CO₂ or H₂ would therefore be required at temperatures between 298 and 1000 K, depending upon reactor set-up, for *in situ* removal [34, 35].

Cutting the cost of capturing CO₂ from the gas feed is the most important issue for increasing the viability of CCS applications and is best achieved by optimising the capture process to operate best under the conditions of the flue gas exhaust, rather than expending energy manipulating the gas stream to meet the requirements of a separation process [7]. Design of more chemically robust separation materials is also key as impurities in the primary fuel such as sulfur and nitrogen oxides irreversibly poison current adsorbent materials [30]. Similarly, incomplete combustion can lead to tar formation which can also inhibit the separation process by emulsifying adsorbents [17].

The composition of the gas stream, determined by the primary fuel source and the combustion process, will influence the suitability of a CO₂ separation process. Given the range of flue gas compositions obtainable, and the often narrow operating window of most separation techniques, it is unlikely that any one process will prove ideal for all power plant set-ups. It seems more logical that tailored processes will be designed for each method of combustion.

Once CO₂ has been captured at the point of formation by one of the above strategies it is sequestered for long term storage [18, 36]. The long term storage of CO₂ is a large field outside the remit of this research and is too broad to cover in detail. A comprehensive review of the different strategies for long term CO₂ storage are discussed by *Song* [8] and *Yang et al* [7].

Unfortunately CCS from mobile sources such as cars or planes is logistically impossible [11]. As vehicular transport makes up 25 % of CO₂ emissions an alternative approach to mitigating CO₂ release is required.

2.1.3 Hydrogen

Hydrogen energy has the potential to decouple the link between energy utilization and environmental problems. H₂, much like electricity, is an energy carrier [32]. The chemical energy per mass of hydrogen is 142 MJ.kg⁻¹, a value three times larger than that of other chemical fuels, making it a highly desirable fuel for vehicular transport applications [37]. Hydrogen is a clean, non-toxic fuel and the only by-product of its complete combustion (**Reaction 2**) is water vapour [38].



Hydrogen as a transport fuel could therefore eliminate pollutant emissions from mobile sources, effectively mitigating the 25 % of CO₂ emissions that no CCS strategy can abate. H₂ fuel technologies,

unavailable to hydrocarbon alternatives, also present advantages in terms of energy efficiency [37]. Internal combustion engines for vehicular transport can be run using either hydrocarbon fuels or H₂ combusted in air. The overall Carnot efficiency of these systems is roughly 25 %, with H₂ combustion not only running slightly more efficiently, but also reducing the concentration of GHGs such as CO₂, NO_x and SO_x, in exhaust emissions to almost trace levels. Alternatively H₂ can be “burnt” electrochemically with oxygen across a proton exchange membrane fuel cell to produce electricity and heat which in turn powers an electrical engine. Carnot efficiencies for energy conversion across fuel cells achieved 50 to 60 % as far back as 2001 [37]. The Honda Clarity was the first commercial Hydrogen powered car [39]. It ran on liquid hydrogen (LH₂) stored in a cryogenic tank at the rear of the vehicle that is fed to a hydrogen fuel cell engine. Current hydrogen vehicles lack the safety and convenience of their fossil fuel counterparts, and thus commercial demand is low [40]. Hydrogens main rivals for vehicular transport applications are electric vehicles [11, 41]. Hydrogen fuelled vehicles typically have a greater driving range and faster refuelling time. Electric vehicles don’t require the construction of a new infrastructure (as would be required for hydrogen) and are currently cheaper and safer. A synergistic future, where the fuel powering a vehicle is depicted by function (city cars are electric, cross country heavy goods vehicles are hydrogen powered), is predicted [11, 41].

Unfortunately, unlike fossil fuels, H₂ must be generated from sources of hydrogen. Hydrogen is the most abundant element on earth but less than 1 % exists as molecular H₂ gas [37]. H₂ can be generated from a number of different pathways, such as electrolysis from water, photolytic cracking of water, or gasification and pyrolysis of biomass but synthesis comes with an energetic cost equal to the combustion energy [42]. If sustainable or renewable energy sources are used to balance that cost H₂ becomes a renewable energy source [43, 44]. Whilst the need to synthesise H₂ is a disadvantage for the process, the wide range of synthetic pathways for H₂ generation does lessen the issue and

economically, would stop global reliance on fuel imports from oil rich nations that can monopolise fuel costs [11, 14, 45].

As renewable energy sources have not yet matured to a stage to cover the energy demands for renewable H₂ production alternatives approaches, such as the syngas process and steam reforming, can, and regularly are used to generate H₂ from hydrocarbon precursors [42]. Whilst CO₂ is a by-product of this process it can be sequestered directly at the point of formation to prevent environmental damage. This process will be discussed in **Section 2.1.4**.

Beyond generation costs, the greatest obstacle preventing feasible commercialisation of a hydrogen economy is effective H₂ storage [46]. Hydrogens supercritical nature (condensation temperature [T_C] = 33.19 K, condensation pressure P_C = 12.96 bar) results in a very low volumetric density of 90 g.m⁻³ under near atmospheric conditions (1 bar, 273 K) [47]. As a result storing reasonable quantities for vehicular transport within an appropriate volume is difficult. Hence the need for improved methods to store large amounts of H₂ in small volumes. To standardise and guide research and development within the H₂ storage field the *DOE hydrogen and fuel cell program* has laid down a set of objectives that hydrogen storage systems for mobile applications are expected to meet [48]. These targets are designed to make the performance of hydrogen vehicles similar to current automobiles, reducing transitional problems as fossil fuel powered vehicles are replaced. It is to these targets that most hydrogen adsorbents, including those in this study, are designed, especially in terms of gravimetric and volumetric capacities.

2.1.3.1 DOE Objectives

The overall DOE hydrogen and fuel cell program objective is the design of a system able to reliably store sufficient hydrogen to provide a 500 km driving range for a variety of different vehicle models without compromising space, performance or cost [48]. **Table 2.1** outlines the

objectives and timescales laid out by the DOE in 2012 [48] revised from their initial targets published in 2003 [49].

Table 2.1. System targets for an on-board hydrogen storage for light duty fuel cell vehicles [1].

Storage parameter	Units	2017	Ultimate
Gravimetric system capacity			
Usable H ₂ specific energy	kWh/kg	1.8	2.5
Net useful energy/max system mass	Kg H ₂ / kg system	0.055	0.075
	wt. %	5.5	7.5
Volumetric system capacity			
Usable H ₂ energy density	kWh/L	1.3	2.3
Net useful energy/max system volume	kg H ₂ / L system	0.040	0.070
Storage system cost			
Fuel cost	\$/kWh net	12	8
	\$/kg H ₂	400	266
Durability/operability			
Operating temp	°C	-40/60	-40/60
Min/Max delivery temp	°C	-40/85	-40/85
Operational cycle life	Cycles	1500	1500
Min/Max delivery pressure	bar	5/12	3/12
Onboard efficiency	%	90	90
Well to powerplant efficiency	%	60	60
Loss of usable H ₂ (Leak/vent)	(g/h)/kg H ₂	0.05	0.05
Charging/discharging rates			
Fill rate	kg H ₂ /min	1.5	2.0
Min full flow rate	(g/s)/kW	0.02	0.02
Start time to full flow (20 °C)	s	5	5
Start time to full flow (-20 °C)	s	15	15
Transient response to operating temp	s	0.75	0.75

The objectives laid out are designed to ensure that the system meets the comparative standards for packaging costs, safety, and performance of current vehicles. Other features such as controllable delivery rates, suitable lifetimes and shelf life (which should not have an effect upon the delivery rate), recharging characteristics and reasonable volumetric and weight density of the entire system, including the tank, materials, valves and regulators, mounting brackets insulation and additional cooling capacity, must also be considered before a system becomes marketable. Fuel cost evaluation must cover the cost of both the H₂ load and any additional cooling or system regeneration costs also.

2.1.4 SYNGAS

Synthetic gas (Syngas) is currently the zenith achievement for the hydrogen economy. It grants us the ability to convert hydrocarbon materials into H₂ and carbon monoxide (CO) [32]. It is utilised in the pre-combustion carbon capture approach. Following syngas formation CO and H₂ are can be separated or alternatively can be further processed in the presence of water (H₂O) and methane (CH₄) by the WGS reactions (**Table 2**) to generate a H₂ rich H₂:CO₂ stream. The H₂ is combusted with air for energy production whilst the carbon products are sequestered for storage [32]. Any carbon fuel source can be subjected to the syngas process including flue gas enriched with methane [50, 51]. Whilst alternatives which generate H₂ from water or decompose hydrocarbons to H₂ and pure carbon exist no process comes close to the efficiency and low energy cost of the syngas process [52]. Current estimates suggest that 96 % of H₂ is produced from reduced hydrocarbons [17];

- Steam methane reformation (SMR) – 48 %,
- Coal gasification – 18 %,
- Oil reformation – 30 %,
- Electrolysis – 4 %.

Such an estimate means that ensuring that clean and sustainable pathways for H₂ generation and CO₂ capture is a necessity to keep syngas production clean and effective.

The Initial step of the Syngas process is the gasification of the fuel source, which is in itself a three step process [53]. Gasification is a thermo-chemical conversion of solid fuel into a variety of different combustible gas products using a gasifying agent. Common gasifying agents include Steam, air and CO₂. Common products include H₂, CH₄, C₂H₄, C₂H₆, CO and CO₂ as well as impurities such as H₂S, Cl₂, HCl and PH₃ [17, 54]. This description does not include combustion processes which result in a product with no heating value. The three gasification steps are [55];

- Pyrolysis: at temperatures between 573 and 773 K roughly 80 % of the fuel is converted into volatile materials, tar or char.
- Cracking and reforming: At 873 K volatile matter and tar are converted into product gases.
- Pyrolysis; above 1073 K char gasification occurs converting char into product gases.

Within these steps a number of reactions are occurring which are displayed in **Table 2.2** [17, 32, 34, 56];

Table 2.2 Reactions taking place within the Syngas process.

Oxidative combustion	$C_nH_mO_p + \left(n + \frac{m}{4} - p\right) O_2$ $\rightarrow nCO_2 + \left(\frac{m}{2}\right) H_2O$	Reaction 1
Biomass reforming	$C_nH_mO_p + (2n - p)H_2O$ $\rightarrow nCO_2 + \left(\frac{m}{2} + 2n - p\right)H_2$	Reaction 3
Water Gas 1	$C + H_2O \rightarrow H_2 + CO$	Reaction 4
Water gas 2	$C + 2H_2O \rightarrow CO_2 + 2H_2$	Reaction 5
Water Gas shift	$H_2O + CO \rightarrow CO_2 + H_2$	Reaction 6
Methane reforming 1	$CH_4 + H_2O \rightarrow CO + 3H_2$	Reaction 7
Methane reforming 2	$CH_4 + 2H_2O \rightarrow CO_2 + 4H_2$	Reaction 8
Methane reforming 3	$CO_2 + CH_4 \rightarrow 2CO + 2H_2$	Reaction 9
Partial oxidation of Methane	$CH_4 + \frac{1}{2} O_2 \rightarrow CO + 2H_2$	Reaction 10
Oxidation 1	$C + O_2 \rightarrow CO_2$	Reaction 11
Oxidation 2	$C + 0.5O_2 \rightarrow CO$	Reaction 12
Boudouard	$C + CO_2 \rightarrow 2CO$	Reaction 13
Methanation	$C + 2H_2 \rightarrow CH_4$	Reaction 14

The propensity of these reactions is dependent upon the conditions within the reactor including temperature, steam to biomass ratio, the fuels used and the reaction equilibrium based upon the ratio of product to precursor [17]. Whilst unwanted reactions may occur, such as dry reforming of CH_4 by CO_2 and steam reforming of the newly formed carbon, these reactions are strongly endothermic and strict control over the reaction conditions will prevent them from occurring. Practical temperature limits for potential processes creating fuel-cell feeds are between 298.15 and 1000 K [34]. Under these conditions all oxidation reactions of carbonaceous materials will run to completion assuming sufficient oxygen, supplied by steam, content.

The best way to optimise the H_2 yield of the combined syngas and WGS reactions is the complete removal of oxygen molecules (O_2) as they result in the oxidative combustion of organic matter, generating CO_2 but not H_2 . Another common approach to improve the reaction efficiency is the removal of all nitrogen molecules (N_2). N_2 , whilst inert within the system, consumes energy in its heating and lowers the valuable species partial pressures [55]. It also adds an energy intensive separation step to separate N_2 from the syngas.

High tar concentrations (more than 3 g.Nm^{-3}) in the product gas are a perpetual problem for gasification reactors as they disrupt the reactor process [17]. If tar is not removed then limitations are placed upon the applications of the product gas as impurities can damage engines or turbines. Higher tar values mean less material has been completely converted, lowering the obtainable yield of the reaction. Tar also lowers the heat transfer rate from catalyst to gas reducing the efficiency of the system [57]. Whilst temperatures could be raised above 1073 K to assist tar pyrolysis, such a temperature increase would detrimentally affect the syngas process. Catalytic cracking is the most common method for eliminating tar. Nickel (Ni) catalysts, dolomites, or alkali metals functions as the best catalysts [58].

The generation of syngas is not purely limited to the production of H_2 [50]. The main products of the syngas process are H_2 and CO . When the $CO:H_2$ ratio is 2:1 these gases can be combined to form a multitude of other industrially useful materials such as; methanol for a multitude of polymer precursor applications, dimethyl carbonate for its use as an automotive fuel and use as a polycarbonate precursor, dimethyl ether as an aerosol propellant or hydrocarbons as long term carbon sinks [50]. If N_2 is present within the syngas feed in the ratio of $(H_2+CO):N_2$ 3:1 then further WGS reactions (**reactions 4 and 5** from **Table 2.2**) and CO_2 extraction could shift the equilibrium of $H_2:N_2$ to roughly 3:1. This syngas composition would allow for ammonia synthesis, the production of which is estimated to be responsible for 3 % of the world's energy consumption and is expected to become a growing market in the future [50].

As Syngas can be generated from treated flue gas streams it can in itself act as a carbon sequestration process when used to generate industrially valuable materials [51].

Reduction in CO_2 emissions and the promotion of a hydrogen economy are intertwined research disciplines. The industrial application of the syngas process and the development of hydrogen powered vehicles compliment both agendas. However both economies are currently dependent upon the development of efficient separation and storage processes.

2.2 Gas capture and storage technologies

Separation and storage techniques function by manipulating unique physical properties of the desired gases- such as molecular size, boiling temperature, or selective chemical reactivity- to isolate the gas or condense it within a reduced volume [59]. There are four main approaches for the separation of H_2 or CO_2 from a gas stream. They are cryogenic distillation, membrane separation, physical adsorption, or chemical absorption [60]. Similarly there are three main approaches for H_2 storage

for mobile applications [46]. They are compressed storage of pure H₂ as a liquid or a high pressure gas, physically adsorbed H₂ bound to a nanoporous materials or chemically absorbed H₂ bonded to a nanoporous structure. This section will discuss the viability of these processes for either gas separation or H₂ storage along with discussion of some of the significant materials involved in each process.

2.2.1 Compressed gas/liquid storage or separation

2.2.1.1 Hydrogen storage

Of the three approaches to H₂ storage, cryogenic or high pressure systems are currently considered the leading application as they have been implemented by the automobile industry [61]. Unfortunately, cryogenics and pressurised tanks have the least developable potential as only minor improvements are available compared to the other technologies. As a result it is expected that development of these methods will struggle to keep up with future DOE targets. Additionally, hazards associated with high pressure or cryogenic apparatus reduce the desirability of these systems for public applications [62].

Liquid hydrogen (LH₂) exists within a small range between the triple point and the critical point within a temperature range of 11 and 20 K. LH₂'s main advantage is its high H₂ density of 70.8 kg.m⁻³ at ambient pressures allowing for comparatively light and compact storage [63, 64]. The technology has matured significantly but there are still problems with gas venting. Current LH₂ storage systems lose up to 1 % of their fuel each day due to boiling while the vehicle is in use [62]. Evaporative losses within the tanks, caused by equilibrium shifts from liquid to gaseous phases, require venting and can deplete up to 64 % and the entire H₂ content of the tank [63, 65]. Not only does this result in wastage of fuel but it also means that fuel tanks can run dry if the vehicle is not topped up regularly regardless of use. Associated safety risks with hydrogen leakage mean such vehicles cannot be parked in garages or poorly ventilated car

parks due to the asphyxiation risks. By far the greatest disadvantage of LH₂ systems is the substantial energy costs involved in H₂ liquefaction and transfer (refuelling) processes [63, 65].

For pressurised cylinders to store sufficient quantities of H₂ to meet the DOE's volumetric objectives system pressures in excess of 700 bar are required. Improvement in the quality of high strength composite fibres has meant that lightweight high pressure cylinders that meet the criteria are more affordable than ever [63]. With the wealth of knowledge already available in the storage of compressed gas fuels, steady progress has been made. The primary limitations of these systems are that they maintain a high volumetric size, and refuelling incurs very high operating costs [46, 63]. The cost of pressurising H₂ during refuelling can make up approximately 10 % of hydrogens total energy output, with the fraction of energy wasted increasing non-linearly with operating pressure and temperature. Problems increasing the H₂ volumetric density at high pressures are because H₂ is not an ideal gas so increases in pressure do not lead to a proportional increase in density and overall cylinder H₂ content [63]. Furthermore, as pressure increases so too does the temperature of the system. Temperature increases decrease the hydrogen packing density, reducing the H₂ volumetric capacity of the cylinder [65]. As such, refuelling to the full system pressure at higher than ambient temperatures will not achieve the desired H₂ volumetric density and the total H₂ storage capacity will be lower than expected.

2.2.1.2 Cryogenic CO₂ and H₂ separation

Cryogenic separation approaches focus on isolating the desired gases based upon their distinct thermodynamic properties compared to the additional gases present in the flue stream. Cryogenic CO₂ sequestration involves reducing flue gas temperatures to 216 K through heat exchangers and flash compression [60]. This process pushes CO₂ toward it's triple point separating CO₂ as a liquid from the remaining

gaseous feed [66]. Strict control over the temperatures used is essential. The formation of solid CO_2 needs to be avoided to keep the system operating effectively so cryogenic separation apparatus temperature must be kept above 214 K [26]. The primary advantage of cryogenic separation is that the process generates high purity liquid CO_2 , the preferred phase for efficient transport and delivery into geo-sequestration reservoirs, saving on the additional energy demands of storage [60]. Another advantage of cryogenic separation is that it allows for fractionation of other flue gas materials with higher boiling temperatures than CO_2 such as water. This has an additional benefit because the H_2O content of the collected CO_2 feed requires strict regulation to levels below 500 parts per million (ppm) as H_2O reacts with CO_2 to form carbonic acids which cause corrosion of pipework [60]. Cryogenic separation also avoids many of the major limitations of the alternative separation processes described below. For instance, this process requires no chemical consumables that prove costly to regenerate or replace. Cryogenic CO_2 sequestration tends to be applied to pre-combustion (Syngas) rather than post-combustion capture techniques [17, 25]. This is because the cooling process, which must be applied to the entire flue gas stream, requires a large energy input. Using a refined gas stream comprised of predominantly H_2 and CO_2 (when the WGS reaction has been applied to convert CO) with some hydrocarbon and moisture impurities limits the energy wasted [55]. Despite this the primary disadvantage of this process is still the energetic cost of cooling the entire gas feed just to isolate the CO_2 . Thermal energy efficiency can be recovered using heat exchangers but a significant fraction of the power generators overall output is still required to power this process [26, 66].

Because of hydrogens low boiling temperature cryogenic separation of H_2 tends to involve hydrogen as an inactive component of the gas stream with the other gases separated based upon their boiling temperatures. Energetically the only gases that become economically viable to separate by this process based upon the boiling temperatures and fraction within a H_2 stream are CO_2 and H_2O as cooling the stream to

the boiling temperature of nitrogen, for instance, would be too energy intensive [55].

2.2.2 Adsorption

Adsorption describes physical bonding (physisorption) between a gas (adsorbate) and a solid surface (adsorbent) where no interatomic chemical bonds are formed and interaction instead relies upon van der Waals forces [37, 67]. Van der Waals interactions are of the same order of magnitude as the thermal motion energy of gas molecules on a surface making physisorption a weak and passive phenomenon characterised by weak adsorption energies [68]. Physical adsorbents (physisorbents) function best at low temperatures and high pressures [37, 64]. Advantages of physisorption include the comparatively small energy input required for either the adsorption or desorption processes to occur. Materials are often regenerated without any hysteresis making cyclic adsorption a possibility [46]. Their adsorption mechanism is very fast as all their adsorption occurs on the material surface [68]. Their performance is controlled by modification of the systems temperature, pressure and the structure of the adsorbent [69]. Limitations of the process are the low achievable storage capacities both gravimetrically and volumetrically.

Physisorption can be imagined as a monolayer of the gaseous species spread across the adsorbents surface with a packing density slightly higher than that of the surrounding gas [64]. By manipulating the pressure and temperature within a system the volumetric packing density of the adsorbed gas monolayer can be increased to equal that of a liquid under less intense conditions than would be required to liquefy the gas by conventional means. This allows high adsorbate packing densities to be achieved on an adsorbent at lower pressures than would be required for comparable packing densities to be met within pure compressed gas systems. The challenge with the design of a physisorbent is to maximise the difference in the packing density of the gas in the monolayer compared

to the packing density of the free gas, so that a liquid density can be achieved under more moderate conditions. Van der Waals interactions, or the London Dispersion forces (E_{S-D}), between the substrate (S) and the desired gas molecule (D), are given by [67]:

$$E_{S-D} \sim \frac{\alpha_D \alpha_S}{r^6} \quad \text{Equation 1}$$

Where α is the polarisability and r is the interaction distance (radius) [7]. As α_D is fixed, the only way to increase E_{S-D} is to increase the polarisability of the substrates or decrease r by increasing pressure. Approaches to increase polarisability are discussed below.

Normally only a monolayer of gas is adsorbed above an adsorbates boiling temperature. Therefore, the theoretical storage capacity of a physisorbent can be estimated as the quantity of desired gas that can be accommodated in the liquid adsorbates monolayer [64]. Optimisation is achieved by maximising the surface area proportional to the adsorbent mass [68]. This is achieved by selecting appropriate adsorbent materials with low atomic masses, improving the gravimetric H₂:adsorbent ratio, and can also form stable and highly ordered structures with large surface areas or porosities [69]. Due to the low binding affinity of hydrogen to an adsorbents surface, optimisation of the surface area alone is not sufficient to maximise performance. The polarisability of the surface must also be augmented to maximise the extent of adsorption under moderate conditions [67].

The extent of adsorption, and thus the actual storage capacity of a physisorbent, is predicted through thermodynamic equilibrium [17, 70]. Adsorption occurs spontaneously when the partial pressure of the adsorbate is greater than the adsorbates equilibrium partial pressure (P^{eq}_D) within the system, assuming there are sufficient sites for attraction. Desorption occurs when this equilibrium shifts the other way. Calculations of the equilibrium partial pressure are equivalent to calculations of the equilibrium constant (K_a);

$$K_a = P_D^{eq} = \exp\left(\frac{-\Delta G_{rxn}^o(T)}{RT}\right) \quad \text{Equation 2}$$

Where $\Delta G_{rxn}^o(T)$ is the Gibbs free energy change for the reaction calculated from thermochemical data, R is the ideal gas constant ($8.314 \text{ J.mol}^{-1}\text{K}^{-1}$) and T is temperature (K). The relationship between equilibrium pressure and adsorption temperature can be represented by the Clausius-Clapeyron equation [70];

$$P_D^{eq} = A_C \exp^{-\Delta H_{ads}/RT_{ads}} \quad \text{Equation 3}$$

Where A_C is a constant. The equilibrium between attractive and repulsive forces between the adsorbate and the adsorbent creates an energy minimum referred to as the adsorption energy or the isosteric heat of adsorption (ΔH_{ads}) which is the key characteristic for indexing the strength of physisorptive binding [67, 69]. The heat of adsorption is between 1 and 10 kJ mol^{-1} for physisorbed materials. Optimisation of the actual H_2 storage capacity of an adsorbent is achieved by increasing ΔH_{ads} . The heat of adsorption is a function of the interaction of pressure, temperature and the fractional coverage [67].

$$\left(\frac{\delta \ln p}{\delta 1/T}\right)_\theta = \frac{\Delta H_{ads}}{R} \quad \text{Equation 4}$$

A Langmuir isotherm describes the fractional coverage ratio, or the density of the monolayer, θ (the number of adsorbed molecules $[W]$ / the number of adsorption sites $[W_0]$) as a function of pressure (P), binding energy or adsorption potential (ϵ), temperature (T) and a rate constant (K_L) [68, 71]:

$$\theta = \frac{W}{W_0} = \frac{K_L P}{1 + K_L P} = \frac{1}{1 + \exp\left(\frac{\epsilon - \mu}{k_B T}\right)} \quad \text{Equation 5}$$

K_B the Boltzmann constant ($1.3806503 \times 10^{-23} \text{ m}^2.\text{kg}.\text{s}^{-2}.\text{K}^{-1}$), and μ the chemical potential of the adsorbate in the gas as a function of the

adsorbate pressure. This value is determined from tabulated values of the enthalpy and entropy.

As described in **Equation 1** optimisation of the isosteric heat of adsorption involves increasing the draw between the adsorbent and the adsorbate by increasing the polarisability of the adsorbent [67]. This can be achieved in several ways [38]. One of the most important ways to increase the storage capacity of an adsorbent is control over the micropore volume of the material [40]. Pores can be described as any cracks or crevices, regardless of shape, within a material [72]. The Chanine rule states that there should be a linear correlation between the ambient pressure H_2 storage capacity of a material and its specific surface area [73]. However, materials with a pore size distribution (PSD) below 0.7 nm outperform this rule. The improved performance is due to an increase in the hydrogen density within the sub-nanometre pores relative to that of a liquid. Within these narrow pores there is an overlap of potential fields between the attractive forces of the adsorbates pore walls producing a weak chelate effect on the hydrogen increasing the binding strength and subsequent packing density. In terms of H_2 adsorbate design, it is therefore beneficial to try and design an adsorbate with an average PSD of approximately 0.7 nm. It is also equally important to try and minimise the range of pore sizes within a sample. Pores narrower than 0.289 nm cannot fit H_2 within them so therefore are effectively dead spaces contributing to a wasted volumetric packing density [72, 74, 75]. The same is true of wide pores. Despite allowing H_2 molecules in, if the hydrogen is not interacting with at least one surface then its packing density is no greater than that of the bulk gas [73]. Pore size is also an important factor for designing selective adsorbents. Manipulation of the structure to have pores of a desired width will increase the attraction of gases with kinetic diameters half that of the pore width over larger or smaller molecules [67].

Chemical doping is another approach to increase the strength of binding between an adsorbent and the desired gas [76]. The polarisability of an adsorbent can be augmented by incorporating reactive elements into

the structure to provide a more polar draw for the desired gas [77]. The polar materials, whilst providing a strong draw for the adsorbate may be unsuitable structurally to meet gravimetric or volumetric objectives if used as an adsorbent on their own. However, when added in moderation they can supplement the capacity of other adsorbents. Electronegative elements will attract desired gases to themselves in abundance and are also known to share their electronegativity around the adsorbent structure, increasing the overall binding strength [77, 78].

Another practical approach for increasing the storage capacity of a material is Activation [71]. Activation describes textural adjustment of an adsorbent by either chemical, such as acid etching, or mechanical, such as ball milling, processes to increase the adsorbents surface area and binding affinity [67]. Activation of a physisorbent by ball milling is among the experimental approaches attempted in this study so a comprehensive analysis of activation will be reserved for the results and discussion section (**Section 4.1**).

Regeneration of a physisorbent (unloading the adsorbed phase) is very efficient. As discussed above, shifting the equilibrium partial pressure of the desired gas promotes desorption and this is best achieved by a mild increase in temperature, or a reduction in the pressure by processes known as temperature swing adsorption (TSA) and pressure swing adsorption (PSA), respectively [79]. For PSA and TSA set-up's to achieve continuous capture multiple column assemblies containing adsorbent beds are required. Whilst one column is being used in the purification stage, the other columns are in a regenerative state. During the purification stage the impure gas feed is passed through the bed, the increased pressure or reduced temperature within the column promotes selective adsorption of the adsorbent onto the adsorbate leaving an adsorbent free, pure feed to pass out of the column and down a feed gas channel. When an adsorbent bed approaches its adsorptive capacity switch valves interconnecting the columns switch the inlet valve to a fresh column and the outlet valve to an adsorbent channel. During the regenerative stage successive decreases

in pressure or increases in temperature of the column promote desorption of the adsorbent. Following regeneration of the adsorbent bed the column is returned to the conditions required for another purification stage [80].

2.2.2.1 CO₂ materials of interest

Zeolites are a porous crystalline class of aluminosilicates based upon a sporadic array of tetrahedral silicon oxides (“SiO₄”) and aluminium oxides (AlO₄) [19]. Their popularity as adsorbents is due to their large surface area and porous nature, indicating a high storage capacity. As with many other physisorbents the porosity of the zeolite has a greater effect upon the storage capacity than the surface area due to chelative binding increasing their adsorption energy [81]. Their adsorption strength stems from their aluminium content which introduces a negative charge throughout the framework. This negative charge is counterbalanced by cations on the material surface [82]. The stronger the negative charge of the field the greater the zeolites affinity for the oxygen groups of CO₂. Unfortunately, the weaker cation species tend to have larger atomic radii causing steric restrictions against adsorption. The best adsorption capacities are observed for cations with the smallest atomic radii making lithium one of the most valuable zeolite cations [83]. The physisorption strength and selectivity of the zeolite can be increased by tailoring the aluminium content of the crystal structure, varying the cations content or controlling the pore size. Most zeolites can store more than 1 mmol.g⁻¹ CO₂ below 373 K but as temperature decreases this capacity can rise to 5 mmol.g⁻¹ at 1 bar at 298 K [83, 84]. The effect of moisture on zeolite adsorption is dependent upon CO₂ pressure. At low CO₂ partial pressures, below 300 ppm, the presence of pre-adsorbed H₂O accelerates CO₂ adsorption by decreasing the activation energy for CO₂ diffusion. Preferentially adsorbed H₂O molecules block high energy CO₂ adsorption sites which, when occupied by CO₂ would slow diffusion. An alternative explanation for the improved performance is that H₂O acts as a catalyst for the formation of bicarbonate compounds on the zeolite surface [84]. At

high CO₂ pressures, above 1000 ppm, the presence of moisture begins to limit the CO₂ storage capacity because the more polar H₂O molecule is preferentially adsorbed by the zeolite surface cations.

The strong binding affinity of zeolites, even at low partial pressures, makes TSA the most effective desorption technique. If temperature can be controlled storage capacities can be maintained across numerous adsorption cycles with very little hysteresis. Excess heating however, can cause sintering of crystalline regions or promote chemisorption of CO₂ with surface oxides, reducing the zeolites porosity, surface structure and, as a result, its cyclability and total storage capacity [85].

2.2.2.2 Adsorption for H₂ storage

H₂ adsorbed on a high performance adsorbent contributes to a reduction in storage pressure. Consequently, a lower weight storage container with a better hydrogen packing density is feasible compared to high pressure or cryogenic alternatives [37]. Furthermore, as described above, volumetric packing of H₂ does not share a linear relationship with pressure at very high pressures [63]. The increased packing density provided by adsorbents would allow storage of suitable volumes of H₂ within the required pressure region with a linear relationship with packing density, reducing the energy demand required for packing the gas. The kinetics of physisorption are very fast so release and subsequent refuelling in an on-board transport system would be quicker than for adsorbent alternatives (see **section 2.2.3**). The major limitation of physisorption is achieving sufficient gravimetric H₂ storage capacities. Even at high pressure and low temperatures the monolayer coating of H₂ across the adsorbents surface still does not meet the DOE guidelines [67]. Modification of the adsorbents is required to increase the volumetric and gravimetric packing densities so that adsorbents achieve an adequate storage capacity under conditions deemed appropriate for on-board

storage [48]. As gravimetric capacity is so important heavier adsorbents such as zeolites, are unlikely to ever meet the DOE requirements [86].

The exact value for ΔH_{ads} of a flat surface depends on the adsorption stoichiometry [67]. An average value would be about 4–5 $\text{kJ}\cdot\text{mol}^{-1}$. Assuming that the structure of the hydrogen monolayer is closed-packed and face centred, the minimum surface area for the adsorption of 1 mol of hydrogen amounts to 85.917 $\text{m}^2\cdot\text{mol}^{-1}$. Therefore to store the 5 kg of H_2 required to meet DOE objectives a total surface area of at least 210,500 m^2 is required.

As low temperatures favour increased H_2 storage capacities the performance of physisorbents is significantly improved at 77 K, the temperature of liquid nitrogen (LN_2) [87]. Two significant drawbacks of this system are the additional design concerns for storing both H_2 and LN_2 in one system and minimising the significant loss in the energy efficiency of the H_2 system when the energy required generating and transporting LN_2 is deducted [61, 88]. Similar hindrances to energy efficiency are present in all storage technologies. Both physisorption and lone gas storage approaches are at a lesser disadvantage compared to absorbent in this regard, as their additional energy input is required to promote adsorption during the refuelling step and can be supplemented by an external source, such as the refuelling depot. With absorption, where additional energy is required to promote desorption for release of H_2 while the vehicle is use, this additional energy must come from within the vehicle.

For hydrogen storage there is one additional approach that can be harnessed to improve the isosteric heat of adsorption and the actual storage capacity of an adsorbent. It is called the spillover process.

2.2.2.2.1 The spillover process

The spillover process describes the behaviour of hydrogen atoms which are produced by dissociative chemisorption of hydrogen molecules

on the metal centre of a group 10 transition metal catalyst, and subsequently diffuse from the metal onto the substrate [89]. Once on the substrate, the hydrogen atoms either bind to unsaturated edge sites within the adsorbents lattice or generate a weakly bound mobile hydrogen layer across the substrate surface. The spillover process is thought to increase the active surface area for adsorption as sites that would usually be precluded from adsorption, such as narrow pores, able to fit atomic hydrogen but not molecular hydrogen, and areas that required modified energetics for reasonable binding are now accessible [90]. Spillover not only increases the storage capacity but also the adsorption kinetics [91]. Whilst the effect of the spillover process can be observed indirectly through the enhanced hydrogen storage capacities of metal doped nanoparticles, close analysis of the spillover mechanism is required to understand, control and optimise the contributing factors to enhance the extent of hydrogen spillover [92-94]. It is established that the spillover catalysts strength for hydrogen adsorption comes from the non-classical s-p-d hybridisation of the transition metal and it is thought that particle size and crystalline orientation will influence the efficiency of the spillover effect [95]. Finding the ideal crystal plane structures within storage materials may assist in lowering the spillover energy and increase the storage capacity of a material. Assuming there is a finite distance that spillover hydrogen can travel, a greater dispersion of the metal across the adsorbent would also increase the total surface of the adsorbent that can be loaded with hydrogen [92]. Tests have shown that there is an ideal catalyst dispersion which makes best use of the adsorbent surface area [96, 97]. At this dispersion the entire adsorbent surface would be within the diffusive range of one spillover catalyst particle, allowing for stronger hydrogen adsorption across the entire surface [98, 99]. Above this ideal dispersion of catalyst the addition of further catalyst brings no further benefit to the rate or quantity of hydrogen stored and, due to the additional catalysts gravimetric influence on the material density, surface area and storage capacity of the sample begin to drop off [90, 96].

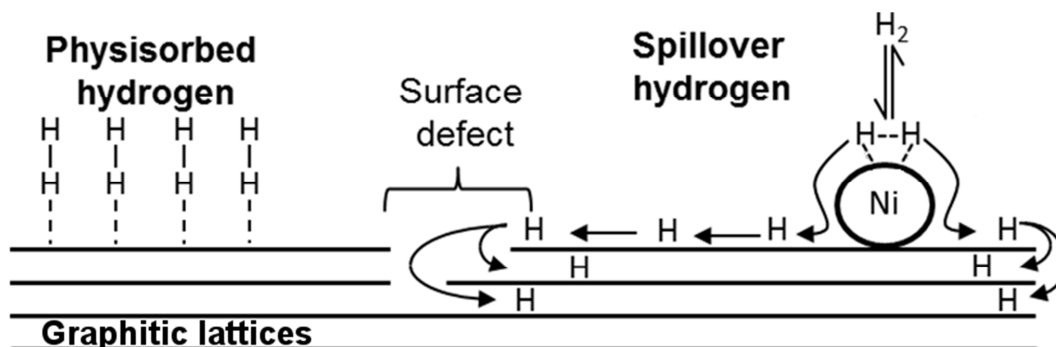


Figure 2.2. Illustrative diagram of how the spillover process improves the performance of a physisorbent [97, 100] . Spillover begins with disassociation of the H_2 molecule, surface diffusion carries the hydrogen atoms across the support. When defects exist in the adsorbent then hydrogen can diffuse between layers too thin to accommodate H_2 .

Spillover kinetics are influenced by two factors. Firstly, the extent of physical contact between the catalytic metals source and the receptor carbon structure and secondly, the rate of diffusion of atomic hydrogen on the receptor surface [90, 94]. The concentration gradient causes the spillover hydrogens to hop over the surface of the carbon material to increased diffusive distances. Intimacy of binding between the adsorbent and the spillover catalyst is required to maximise the performance [99].

Spillover does not occur at low energies. Due to the rate limiting diffusion step, spillover begins around room temperature. Hydrogen uptake experiments performed at 77 K showed no sign of spillover hydrogen, instead they were dominated by the presence of physisorbed di-hydrogen molecules [89].

2.2.2.2.2 H_2 materials of interest: Carbon nanostructures

Carbon is the most popular material for H_2 physisorption because of the huge opportunity it presents to selectively synthesise a wide selection

of chemically stable materials possessing a variety of bulk and pore structures [67]. Furthermore these materials can be easily modified with dopants or activated by a variety of different processes to improve performances. The low atomic mass of carbon helps maintain a reasonable storage capacity and the abundance of carbon precursors make synthesis affordable. The versatility of carbon makes it a popular CO₂ adsorbent also. Below is a comparison of some of the most popular carbon nanostructures and their suitability for hydrogen storage.

Activated Carbon (0.5 wt.% H₂ at 298 K; 5.5 wt.% H₂ at 77 K) [101]

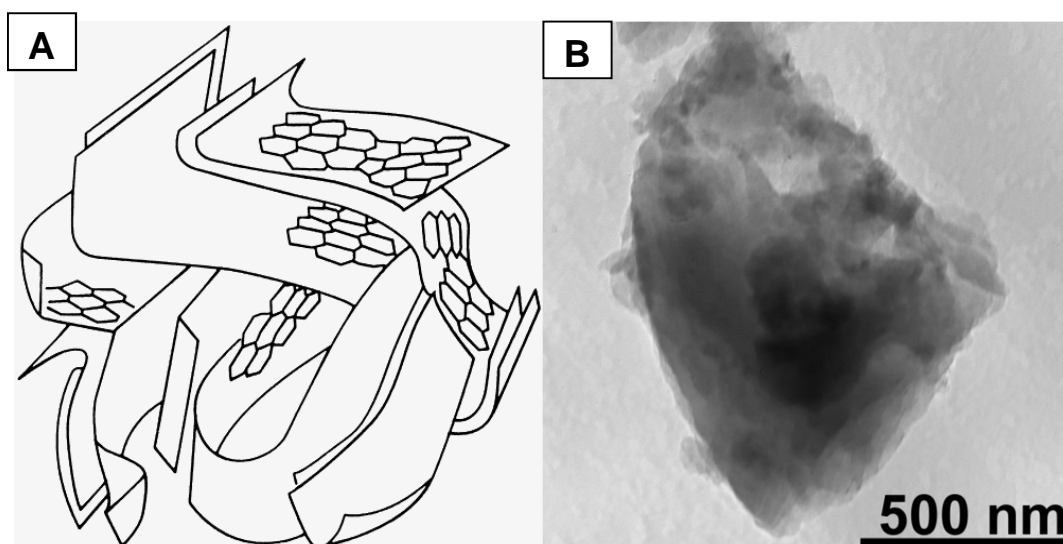


Figure 2.3. An illustration and TEM image of AC structures [102].

Activated carbons (ACs; **Figure 2.3**) are cheap and available on an industrial level [67]. They are prepared from carbon rich organic precursors by dry distillation to form carbonised organic precursors. Activation can increase pore volume as high as 3000 m².g⁻¹. The hydrogen storage capability of activated carbon depends on the microstructure, in particular the porosity of the material and the opportunity for potential field overlap. As activated carbons are heterogeneous in nature they possess a wide pore-size distribution with only a fraction exhibiting favourable overlap for hydrogen adsorption. Given this, their suitability as hydrogen adsorbents for vehicular applications seems unlikely due to the volumetric

and gravimetric penalty against efficiency incurred by dead spaces. Industrial applications, where low gravimetric densities are not primary considerations, may suit these materials better.

Graphite nanofibres (6.5 wt.% H₂ at 293 K, 12 MPa) (>1 wt.% H₂ at 298 K, 10 MPa) [67]

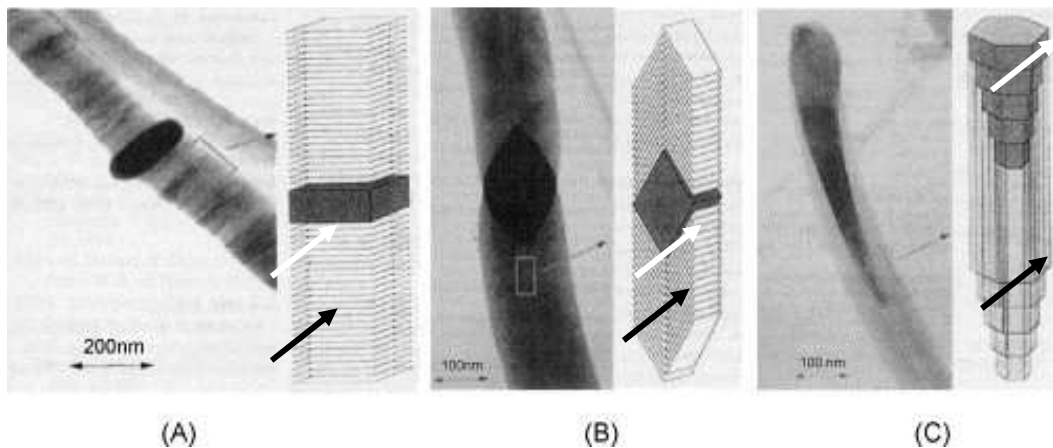


Figure 2.4. Structure of GNFs. A) Deck of cards structure; B) Herringbone structure; C) Tubular structure. White arrows indicate metal catalyst particles, black arrows indicate graphitic plates [67].

Graphite nanofibres (GNFs) are graphite platelets stacked in various orientations to the fibre axis [67]. C-C distances in plane and between sheets is the same as in pure graphite, (0.142 nm and 0.335 nm, respectively) although the distance between sheets can be augmented by post synthetic techniques [75, 103]. GNFs are formed when a hydrocarbon (or carbon containing gas and hydrogen) is adsorbed on the surface of a catalyst particle (**White arrows in Figure 2.4**), typically nickel and iron based alloys, at high temperature [104]. Carbon-carbon bonds break and carbon atoms diffuse to the interface between the catalyst particles and growing platelets (**Black arrows in Figure 2.4**). These charged carbon atoms react with the next platelet forming a carbon nanostructure. The platelets that are formed are mainly graphite, but depending on the catalyst crystal faces, less-ordered carbon may also grow. The fibres are

usually between 5 and 100 μm in length and their diameter is between 5 and 100 nm [67]. A GNFs structure and properties (such as morphology, crystallinity and shape) can be altered by varying the nature and shape of the catalyst, the ratio of the hydrocarbon/hydrogen reactant mixture, or the reaction conditions, such as temperature or pressure. “Herringbone” (so named as their structure resembles a herringbone) structures (**Figure 2.4B**) contain graphite sheets or conically shaped graphite sheets stacked at a certain angle to the fibre. The structure possesses advantageous geometry for hydrogen uptake due to the accessibility of all sheets as well as short diffusion paths into the nanostructure [75].

The specific surface areas of these ordered crystalline solids is usually in the range of 100 to 300 $\text{m}^2.\text{g}^{-1}$ but can sometimes reach values up to 700 $\text{m}^2.\text{g}^{-1}$. The total pore volume is equally variable, ranging between 0.28 and 0.52 $\text{cm}^3.\text{g}^{-1}$ but again able to extend in well prepared samples as high as 0.830 $\text{cm}^3.\text{g}^{-1}$ [105, 106] The structure of the platelets provides many edges on a nanofibre which represent a large surface with many interaction sites for adsorbates. The sites for preferential H_2 adsorption in GNFs have been identified as edge dislocations and pore spaces between separated graphitic sheets [103].

Nanotubes (5-8 wt.% H₂ at 77 K, 10 MPa; 4-5 wt.% H₂ at 298 K, 10 MPa) (9.2 wt.% H₂ at 115 K and 3MPa) (>1 wt.% H₂ at 298 K, 10 MPa) [101]

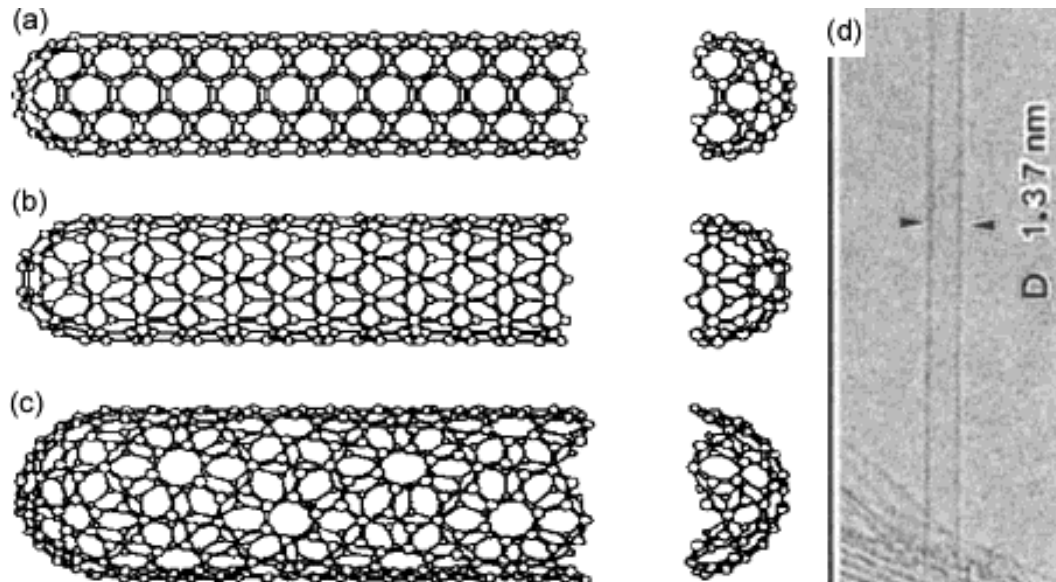


Figure 2.5. Structure of the different SWCNTs. A) Armchair; B) zig-zag; C) chiral conformations [67]. D) TEM image of a SWCNT [107].

Nanotubes are a finite graphite sheet rolled into a tube. Typically, their formation requires seeding with catalyst particles which define features such as width, diameter and thickness of the tube [46, 108]. Nanotubes one carbon layer thick are known as Single Walled Carbon Nanotubes (SWCNT or SWNTs). SWCNTs form bundles owing to the van der Waals forces between the tubes. SWCNTs form a regular triangular array with a distance of about 1.7 nm and are called nanoropes. These nanoropes typically grow in lengths of several μm with a diameter of about 1nm. The 'rolling' up of the graphene sheets is not only limited to one sheet. Several sheets can be rolled up to form multiwall carbon nanotubes (MWCNTs).

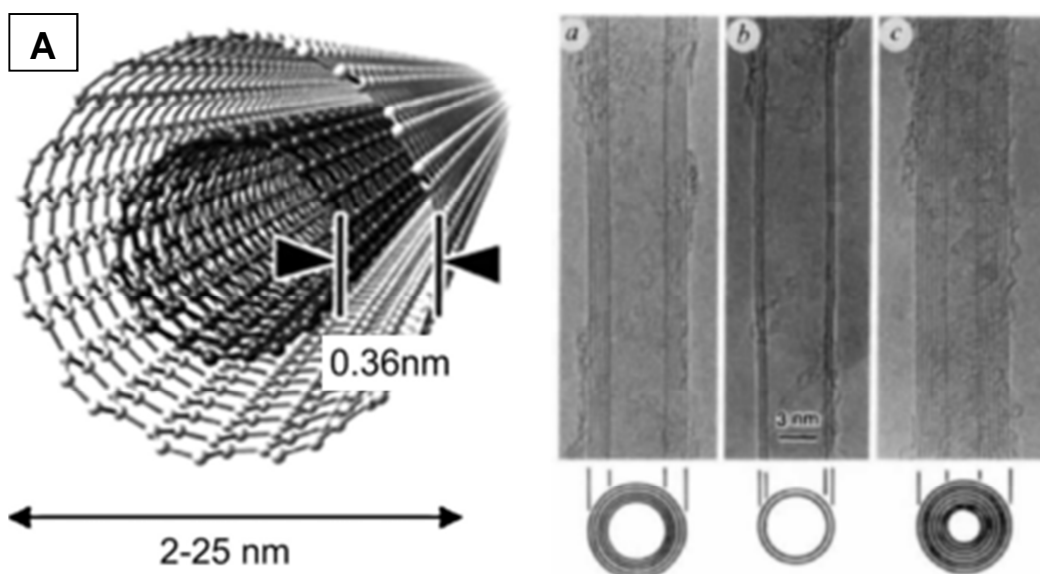


Figure 2.6. Structure of MWCNTs. A) Schematic of a 2 layer MWCNT, Figure adapted from [109]. B) TEM images of MWCNT and their correspondence to number of walls [110].

The MWCNT is an arrangement of coaxial tubes of graphene sheets forming a tube-like structure. Each MWCNT has from 2 to 50 such tubes [67]. MWCNT have inner diameters from 1.5 to 15 nm and outer diameters from 2.5 to 30 nm. The interlayer distance of the MWCNT amounts to 0.34–0.36 nm (As shown in **Figure 2.6A**). As with SWCNT's, MWCNTs can grow to several micrometers in length. MWCNTs are frequently constituted of tilted or conical tubes forming a herringbone structure.

Normally the ends of the CNTs are closed by fullerene-like hemispherical structures. The tubes could be opened via a chemical (e.g. nitric acid ;HNO₃) or ultrasound treatment. Open CNTs can be closed by thermal treatment. Due to their large bulk density, nanotubes have the best experimental volumetric storage capacity. The hydrogen storage capacities of nanotubes is hugely reliant upon sample preparation [101]. Because a graphene sheet can be formed into a tube in different ways, different types of carbon nanotubes exist, namely 'armchair', 'zigzag', and 'chiral' types (**Figures 2.5A, 2.5B and 2.5C**) [67]. The quasi-rolling direction, quantified by the "chiral vector" determines the distribution of

charge within the CNT, which is thought to influence the strength of adsorptive binding [71]. The mechanical parameters such as structural integrity are also influenced by the rolling direction. No complete agreement exists about the adsorption sites in carbon nanotubes. Theoretically the following sites exist:

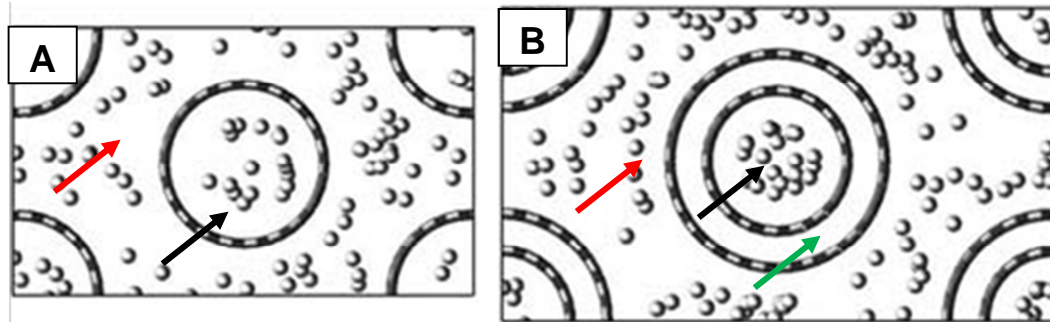


Figure 2.7. Theoretical sites for hydrogen adsorption. A) SWCNTs; B) MWCNTs. Black and grey circles represent CNTs, grey spheres are hydrogen molecules. Black arrows indicate adsorption within the tubes. Red arrows indicate adsorption between the tubes, Green arrows indicate adsorption space between walls. Image modified from [111].

Inside the tube. (Black arrows in Figures 2.7A and 2.7B). Storage capacity has been observed to increase when the hemispherical caps on the end of nanotubes are removed by oxidative opening, identifying inside the tube as an environment for H₂ adsorption [67]. For storage within the tube H₂ must either must pass through cracks in the CNT wall or diffuse down open tube ends. Diffusion down the tube is dependent upon tube width and occurs by one of the four mechanisms described in **Section 2.2.4**. To make sure that hydrogen is diffusing down the tubes sufficiently, thus reducing the dead space present, the length of the tubes should be optimised or controlled as described by the Chanine rule [75].

Between bundled tubes (Red arrows in Figures 2.7A and 2.7B). The generation of bundles (or ropes) is based on a strong cohesive interaction between the tubes. The distances between the tubes in the

bundles can be controlled for extensive intercalation of hydrogen into the ropes [75, 111]. Interstitial space can be wasted if hydrogen cannot reach it. Good diffusivity is paramount. Control of tube length will control interstitial space.

Between the walls in MWCNTs (Green arrows in Figure 2.7B).

The space between each wall in a MWCNT can only become involved in H₂ storage if there is sufficient space between walls for H₂ diffusion. As the spacing between walls is typically below the kinetic diameter of H₂ they remain inactive during adsorption and only serve to increase the carbon mass, limiting the hydrogen storage capacity.

2.2.3 Absorption

Absorption describes the process of chemical binding where the desired gas selectively reacts with another material to form a new solid compound [112]. As H₂ is an elemental gas and CO₂ is a compound their absorption mechanisms are slightly different so will be discussed independently.

2.2.3.1 Absorption for H₂ storage

Absorbents are a popular storage medium due to their characteristically high hydrogen densities and chemical stability under ambient conditions making them reliable for long term hydrogen storage applications [71]. Although the fixing of hydrogen onto solids or liquids can be achieved in a wide variety of materials, such as water or hydrocarbons, the requirements of the DOE for a pure H₂ feed and low thermodynamic demands for capture and release narrow the field almost exclusively to metal hydrides [67]. As discussed in **Section 2.2.2**, the heat of adsorption is the key unit for characterising the binding energy required for adsorption or desorption of a gas. For adsorbents, the heat of adsorption is too low,

resulting in low storage capacities. For absorbents the heats of adsorption are too high, preventing the release of H_2 under moderate conditions. **Figure 2.8** illustrates the range of binding affinities possessed by materials for either physical or chemical adsorption. As can be seen, there are very few materials available in the region believed to be ideal for reversible release of hydrogen under moderate conditions [67].

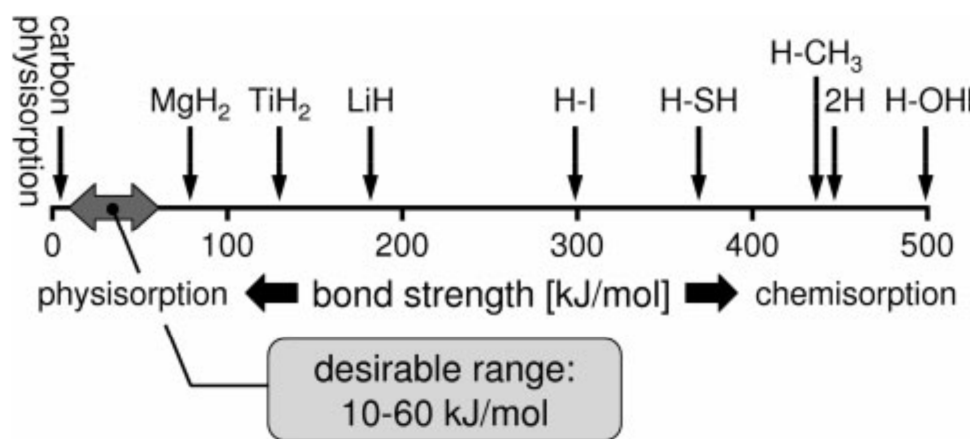


Figure 2.8. Comparison of the binding energies of different hydrogen storage materials [67, 71].

Metal hydrides, defined as single-phase compounds binding a metal host and hydrogen, can be categorised into four classes by the mode of bonding between the metal core and the hydrogen atoms [71].

1. Ionic hydrides describe alkali and alkaline earth atoms ionically bound to hydrogen. Magnesium hydride (MgH_2) is amongst the most popular ionic hydrides due to its high hydrogen storage capacity of 7.7 wt.%, putting it within the DOE 2015 gravimetric target (see **Table 1**), and its cheap and producible nature [113, 114].
2. Covalent hydrides contain non-metallic elements, such as sulfur, carbon or boron, storing hydrogen through covalent binding [71]. Methane has a hydrogen storage capacity of 25 wt.%. Unfortunately desorption of H_2 from CH_4 requires heats of adsorption in excess of $400 \text{ kJ}\cdot\text{mol}^{-1}$, which is too high for feasible application [67].
3. Metallic hydrides describe transition metal or rare-earth metal hydrides bound to hydrogen through metallic bonding [71].

4. Complex metal hydrides describe group IA, IIA and IIIA light metals from the periodic table forming anionic metal hydrides stabilised by ionic or covalent interactions with another alkali cation. Lithium alanate (LiAlH_4) has a hydrogen storage capacity of 10.55 wt.% but requires irreversible decomposition through three different reaction steps. The first two steps are able to release 7.9 wt.% H_2 at temperatures below 403 K but evolution of the final 2.65 wt.% requires heating to 993 K [115].

Storage capacity is theoretically dependent upon the molecular weight of the absorbent and its hydrogen stoichiometry but thermodynamic and kinetic restraints of the absorption/desorption process reduce the practical H_2 storage capacity of a material [116].

The primary limitations of absorbents as storage media for transport applications relate to the enthalpy of formation of these stable hydrides. Due to the strength of the ionic or covalent bonds, as well as intermolecular forces of the highly crystalline order of the hydrides, these compounds are highly stable and require a large energy input to break the bonds [115]. Additionally, due to diffusion rates of the released hydrogen through the hydride lattices the kinetics of release is slow. For most pure hydrides temperatures in excess of 473 K are required to promote desorption [71]. The energy input to promote desorption is a penalty against the efficiency of the H_2 storage process.

The adsorption process consists of several steps identified by successive minima in a potential energy curve (**Figure 2.9**) and can be described using the long-range attractive/short-range repulsive Lennard–Jones potential [71]. A full breakdown of the mechanism is described below.

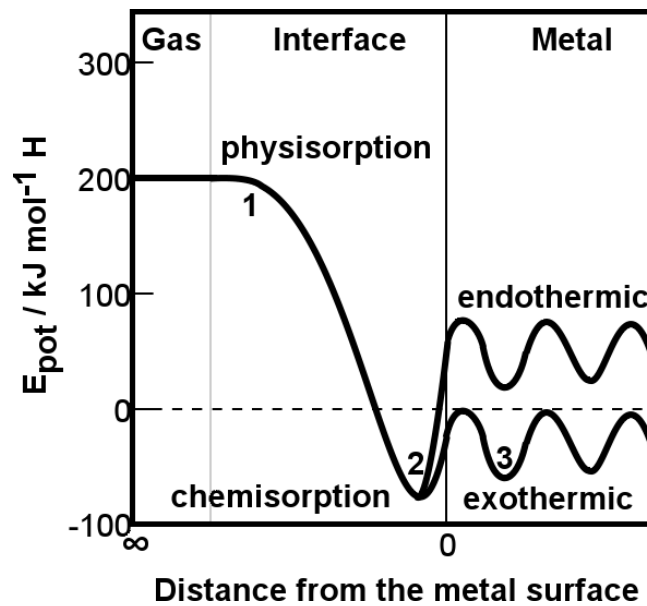


Figure 2.9. Potential energy curve for the absorption of hydrogen onto a metal surface. The steps of the process are described below. The image was modified from [64].

Step 1, Molecular adsorption: H_2 is physisorbed onto the metal surface as a monolayer. The physisorption process was described in **Section 2.2.2**.

Step 2, Atomic adsorption: Under the correct temperature and pressure conditions the hydrogen molecules dissociate at the surface and are chemically absorbed (chemisorbed) into the metal structure.

Step 3, Bulk adsorption: After surface chemisorption H atoms diffuses throughout the material. Diffused H atoms in the material are referred to as α -phase hydrogen. As this concentration increases, so to do the H-H interactions, forming a more stable β phase. The change from α to β is characterised by changes in the crystalline structure, volume expansion and a nucleation energy increase associated with the volume expansion and increased interface energy between the phases. Both exothermic and endothermic absorption processes will show potential energy maxima and minima, with exothermic reactions they will occur without further energy input.

The rate limiting step changes as the reaction progresses [117]. Initially it is the dissociation and penetration of hydrogen at the interface, at high H atom concentrations it becomes the nucleation of the β phase. Finally, Once the β phase becomes more prevalent, Hydrogen diffusion through the β layer to nucleate remaining α -phase pockets becomes the rate limiting step [117].

To overcome these limitations a number of different approaches to destabilise the hydride structure and move the thermodynamic equilibrium for adsorption and desorption closer to room temperature have been successfully demonstrated [71].

Reduction in the average adsorbent particle size, or an increase in the hydrides surface area, assists the performance of the absorbate in several ways [71]. Firstly, increasing surface area increases the surface free energy of the material. The surface free energy represents the excess energy of surface atoms with strained bond angles compared to those in the bulk. If the surface free energy of the hydride is greater than that of the metal then energy that would be released as heat during the hydriding process is sequestered to stabilise the surface free energy. The joint reduction in the fraction of the hydride that is in the bulk phase and the excess energy already possessed by surface structures reduces the thermodynamic requirements of both the adsorption and desorption processes. Secondly, reduction in the absorbate particle size reduces the distance that hydrogen would be required to diffuse through during sorption processes reducing the kinetics of the reaction and increasing H_2 uptake and release rates. **Figure 2.10** illustrates the variation in the nucleation mechanism for different sized particles.

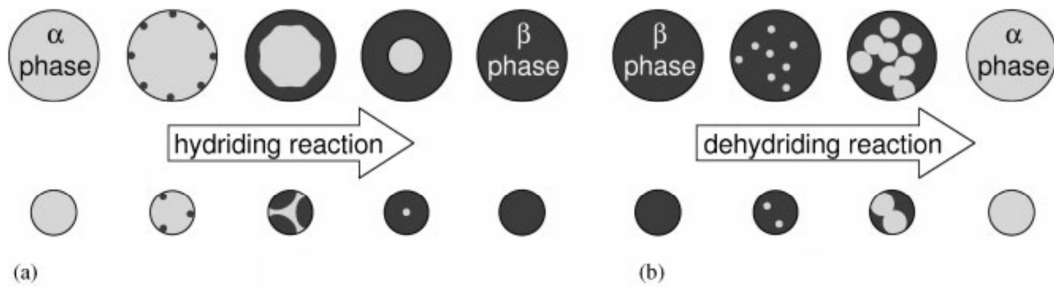


Figure 2.10. Variation in the nucleation path from α to β phase for large and small particles during H_2 and adsorption and desorption [71].

Modification of the surface area is achieved during material generation through processes such as ball milling, laser ablation, physical vapour deposition or vapour condensation [113, 115].

Increasing the number of grain boundaries within an absorbate achieves a lower energy sorption process [71]. Grain boundaries present high compressive stresses against each other or are bound together through atomic bonds with less than optimal bond angles. Each point of non-ideality stores potential energy that consumes some of the energy generated during absorption and reduces the energy input required during desorption. Grain boundary proliferation also assists the kinetics of the system as grain boundaries provide pathways for hydrogen to diffuse through the absorbates at a rate greater than that for passage through a crystalline phase. Proliferation of grain boundaries is again controlled during material synthesis either through manipulation of the reaction conditions or through addition of dopant materials, as discussed below.

Some groups have succeeded in synthesising complex metal hydrides in less stable crystalline arrangements, varying the temperatures and pressures during synthesis, to reduce the enthalpy of formation [115].

Doping the absorbent with a secondary material can improve performance in a number of ways. Some dopants provide an alternative intermediate state for the absorbent metal to return to during hydrogen desorption. The reduced enthalpy of the alloys crystalline state compared

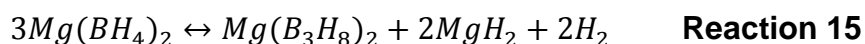
to the pure metal absorbent reduces the activation energy required for hydrogen absorption and desorption [113, 114]. Dopant addition can be used to promote grain boundary formation. Addition of incoherent second phase particles limit recrystallization of the hydride or the metal, increasing the potential energy stored in grain boundaries [115]. Dopants can also be used to mitigate the kinetics of hydriding reactions by improving the rate of the hydrogen diffusion step (step 2 in the absorption mechanism). The novel hydrogen-metal interaction properties of group 10 transition metals, known as the spillover process (discussed in **Section 2.2.2.1.2**), increase the disassociation and diffusion rate of hydrogen into the absorbates [118]. This process reduces the kinetics of absorption resulting in faster uptake and release of H₂. The addition of a dopant however compromises the gravimetric H₂ storage capacity of the material, reducing its capacity proportional to its weight fraction within the sample [114]. Use of a less stable metal hydride as the dopant can mitigate the loss of storage capacity, but their reduction in the enthalpy of formation is not as significant [71].

The methods described above to reduce the thermodynamic constraints of the absorbent storage all rely upon optimisation of the absorbates structure- whether it be the surface area, grain boundary proliferation or alloy material distribution. However, with each cycle of hydrogen capture and release these properties are degraded [64]. High temperatures generated during desorption lead to crystallisation and increased agglomeration of particles decreasing the overall kinetic efficiency of absorbates [71]. As reliable regeneration of absorbates over multiple cycles without depletion in performance is crucial for keeping absorbent materials cost and energy efficient, strategies to abate degradation in the absorbates structure are required [71]. Addition of inert structural dopants in excess increases the cyclic properties of absorbates through micro-confinement of the metal nanoparticles within the dopant matrix, preventing agglomeration [112]. The addition of the dopant material again comes at the expense of the material's gravimetric H₂

storage capacity. Other limitations to absorbent materials include high alloy costs, sensitivity to gaseous impurities and pyrophoricity [46].

2.2.3.1.1 H₂ Materials of interest: Magnesium Borohydride, Mg(BH₄)₂

Slow thermal decomposition of Mg(BH₄)₂ at 473 K *in vacuo* has been shown to selectively produce magnesium triborane, Mg(B₃H₈)₂, and H₂ (**Reaction 15**) [119].



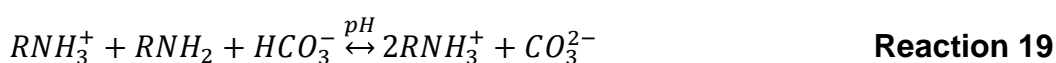
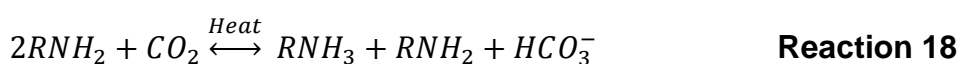
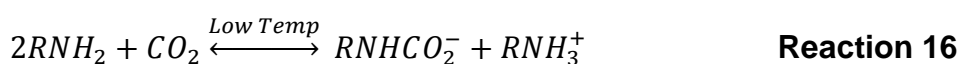
The reverse rehydriding reaction was performed within a H₂ atmosphere at 523 K and 120 bar. Following 48 hours near complete conversion back to Mg(BH₄)₂ was achieved. This result provides the first evidence of reversible solid state dehydrogenation of borohydrides occurring at temperatures below 573 K. By comparison to most hydride materials this is a real step toward the ideal kinetics and thermodynamics for vehicular transport applications. Unfortunately, whilst complete decomposition of Mg(BH₄)₂ to magnesium dodecaborane, Mg(B₁₂H₁₂), should be capable of releasing 8.0 wt.% hydrogen, the thermodynamic stability of the closo-borane system prevents rehydriding to the borohydride under reasonable conditions. The reversible reaction above has in practice a H₂ cycling capacity of only 2.5 wt.%.

2.2.3.2 Absorption for CO₂ capture

Separation of CO₂ through chemical reaction with an absorbent materials can be considered the most mature CO₂ sequestration technique as it has been applied industrially for over 60 years, predominantly by amine stripping as discussed below [7, 120]. Absorbate materials can be divided into organic absorbates relying upon the attraction between CO₂ and amine functionalities, or inorganic absorbates comprised of simple and complex metal oxides. All processes rely upon the formation of

carbonate or carbamate species to selectively sequester CO₂ [17]. In general, inorganic absorbates sequester best at high temperatures and pressures but require high energy inputs to regenerate the absorbate and release the adsorbed gases. Organic absorbates perform best at low temperatures but can require equally expensive synthesis and regeneration steps.

Organic absorbents rely upon the chemical reaction between amine groups and CO₂ to form carbamate (**Reaction 19**), bicarbonate (**Reactions 20 and 21**) or carbonate (**Reaction 22**) species depending upon the reaction conditions [8, 121, 122].

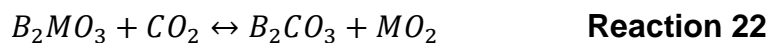


As amine groups can be tethered onto hydrophilic organic chains many of the issues with kinetics and getting CO₂ molecules to active absorbent sites can be overcome by loading the amines within an aqueous media. The process is referred to as amine scrubbing and is designed for post combustion capture or purification of syngas feeds from the flue gas [123].

Flue gas streams are passed through the amine solution until absorption of CO₂ reaches its equilibrium [123]. The CO₂ rich solution is then sent to a CO₂ stripper for regeneration by heating the solution (373 to 393 K) with steam until CO₂ is released and the amine functional groups are regenerated. The amine solution is then ready to be recycled through the absorber apparatus. The choice of amine precursor has a massive influence on the performance of the absorbates [121]. Primary and secondary amines react more efficiently than tertiary amines due to

differences in their reaction mechanisms. Similarly intra- and inter- molecular chelates also perform differently. The primary limitations of this process are the significant energetic costs in heating and maintaining conditions suitable for both adsorption and desorption [30]. Synthesis of new amine stock to replace depletion caused by poisoning or evaporation is costly and disposal of depleted amine stock is expensive both in terms of energy requirements and volumes of water required to dilute the stock to safe levels. It is estimated that the process currently consumes 20 to 30 % of the total energy generated by the combustion process. One method for improving the efficiency of the process is tethering the amines onto solid supports such as silica beads [124]. This means the same processes are occurring although this time not within an aqueous medium. Some studies have suggested that such a process could reduce the energetic cost of the process. Monoethanolamine (MEA) is the most extensively studied material and has been subjected to countless tests to maximise the operational efficiency, primarily through modification of the process or the absorbent [30]. Piperazine, however, has recently been proposed as a more efficient alternative [123].

The most popular inorganic absorbents for high temperature absorption are metal oxides, such as calcium oxides or lithium zirconates [17, 23]. Solid state absorption techniques can be applied to any CCS strategy. Absorption is exothermic and is somewhat facilitated by the attraction between the electrophilic CO₂ molecule and the basic metal oxide [19].

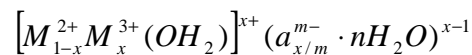


The mechanism of CO₂ absorption is slightly different to H₂ absorption. Physisorption of the gas to the absorbent surface is still the first and the initial rate limiting step. There is however no disassociation and diffusion of CO₂ through the material as was seen in H₂ absorption.

The gas and absorbent surface material react and form a new compound leading to the formation of a core of unreacted absorbent coated in a shell of reacted absorbent [125]. The lack of a semi-permeable α phase, as discussed in **Figure 2.5**, makes the diffusion step even more difficult to overcome and the kinetics of complete adsorption or desorption even slower [23]. For example, lithium zirconates can take days at 979 K to reach absorption equilibrium [125]. The same approaches to overcome thermodynamic and kinetic limitations of H_2 absorption are used to improve the performance of CO_2 absorbents [23]. Dopants and material processing techniques are used to encourage increased surface area, grain boundary proliferation and formation of lower energy chemical intermediates [23, 125-127]. One major benefit of the absorbent process compared to alternative CO_2 sequestration processes is that the exothermic carbonate formation step generates heat [17, 23]. As sequestration of CO_2 within a syngas generator pushes reaction equilibria toward completion, to do so with an exothermic absorbate, releasing heat into the system, will further drive endothermic steps in the syngas process toward completion.

2.2.3.2.1 CO_2 Materials of interest: Layered double hydroxides

Layered double hydroxides (LDHs) are a class of anionic clays with the general formula;



Where M is a metal species, a is any negatively charged ligand and X is typically within the range 0.17 to 0.33 [128]. The structure is composed of cationic brucitelike layers with bivalent cations existing in the centre of octahedral hydroxides. These bivalent ions can be partially substituted for trivalent ions resulting in an excess of positive charge which is balanced by the anionic species and H_2O molecules located in the

interlayer gaps. The resulting medium is a charge balanced framework. The method of CO₂ adsorption is a two-step process [129];



Where S is an empty adsorption site and S(a+1)CO₂ is a surface complex. The general storage capacity of the LDH is lower than for the other metal chemisorbents and is usually less than 1.0 mmol.g⁻¹ [19].

The storage capacity of LDH does not have a linear relationship with temperature; rather it has peaks and troughs associated with structural evolution and decomposition of the LDH. Temperature induced structural changes, and their influence on storage capacity, can be reduced by adding steam to the CO₂ mix [130]. High vapour concentration at temperatures above 673 K maintains the hydroxyl concentration within the interlayer spaces increasing the charge ratio and promotes the formation of bicarbonates to increase the storage capacity;



The M^A species are minute impurities of alkali metals present in the material. The desirability of LDHs stems from their high cyclic stability and fast kinetics of adsorption. The kinetics are governed by a very fast mass transfer reaction by a combination of molecular, Knudsen and surface diffusion (**Sections 2.2.4.1** and **2.2.4.2**) along with the fast kinetics of the bicarbonate formation reaction.

2.2.4 Membrane separation

Membrane purification of desired gases can either actively separate the desired gas from the flue gas stream, or actively separate the

impurities to leave a pure stream of the desired material [131]. Membrane separation of desired gases is based upon one of four mechanisms: Knudsen diffusion, surface diffusion, capillary condensation and molecular disassociation each driven by a pressure gradient across the membrane [41]. **Figure 2.11** illustrates the four mechanisms with a full description of the processes beginning in **Section 2.2.4.1**. Hydrogens novel properties when interacting with group 10 transition metals and some metallic elements in group 3 to 5 of the periodic table means that H₂ membrane separation has an additional fifth option based on dissociative dissolution (**Section 2.2.4.5**) [118]. Performance of all membranes is quantified in terms of selectivity and permeability. Selectivity is measured from the permeate (filtered gas stream) purity and is influenced by factors including temperature, pressure, pore size and interaction between the gas and the membrane material [59]. Permeability is measured in terms of the rate of gas movement across the membrane [7]. Enhancement of either factor tends to come at the expense of the other.

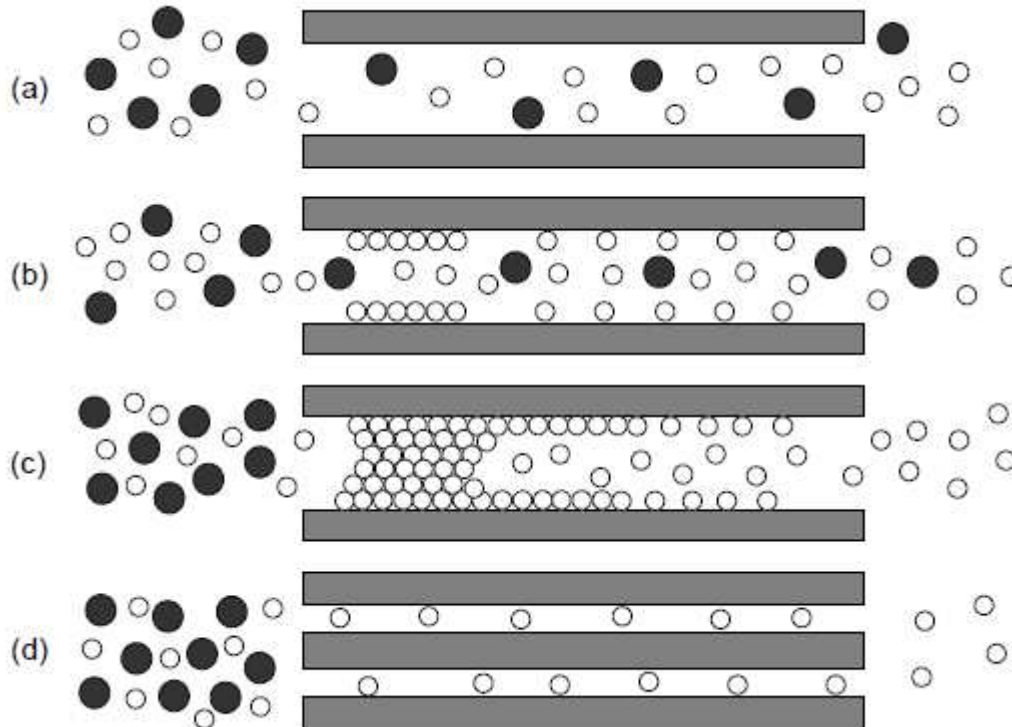


Figure 2.11. Transport mechanisms in porous membranes: A) Knudsen Diffusion, B) Surface diffusion, C) capillary condensation,

D) Molecular sieving [59]. Description of their mechanisms begins in section 2.2.4.1.

The extent of adsorption of a gas onto an adsorbent or through a membrane can be predicted through thermodynamic equilibrium as described in **section 2.2.2 (Equations 6 and 7)** [17]. Taking CO₂ separation from a syngas feed as an example, capture will be most effective in the low temperature region where the equilibrium partial pressure with the adsorbent is less than 0.1 atm [17]. Therefore, to optimise membrane performance either the reaction needs to be maintained at a constant temperature or pressure needs to increase with temperature to maintain the equilibrium. Typically the pressure can be increased by adding high pressure steam, a useful additive as the ratio of steam to hydrocarbon fuel increases the H₂ content due to the WGS and reforming reactions (**Equations 4 and 5 in Table 2**). The equilibrium partial pressure for H₂O adsorption needs to be appreciably higher than that of CO₂ at all temperatures to make sure that CO₂ adsorption remains preferential compared to H₂O adsorption [17].

2.2.4.1 Knudsen diffusion (Figure 2.11A)

Knudsen diffusion is a size exclusion process which relies upon a ratio, known as the Knudsen number, between a gaseous species mean free path and the pore radius of the membrane [59]. Larger molecules have larger mean free paths and thus are excluded from passing through the membrane [7]. Increasing the pore size increases the Knudsen number which results in a decrease in the selectivity of the membrane but also results in an increase in the permeability as the available volume for passage across the membrane increases.

2.2.4.2 Surface diffusion (Figure 2.11B)

Surface diffusion works by the same size exclusion mechanism as Knudsen diffusion, although this time material interactions between the desired gaseous species and the membrane promote increased selectivity [59]. Selective adsorption of desired species onto pore walls increases the permeability rate and selectivity of gaseous passage through the membrane. Furthermore the adsorbed layer of desired species reduces the membranes total pore width, increasing the membranes size exclusion selectivity. Surface diffusion materials become less selective as operating pressures and temperatures increase and are of little benefit under the conditions of pre-combustion capture.

2.2.4.3 Capillary condensation (Figure 2.11C)

Capillary condensation involves reduction in the partial pressure of a gaseous species to a condensed liquid phase within the membranes pores. Only gases able to condense within the pore volume or those that are soluble within the condensed phase can pass through the membrane [59]. The process is highly selective and has reasonable permeability rates, but a membranes performance is hugely dependent upon gas composition. Costs to synthesise the membrane can be high as pore widths need to be only two or three times the diameter of the desired gaseous species and must have a narrow pore size distribution.

2.2.4.4 Molecular sieving (Figure 2.11D)

Molecular sieving relies upon membrane materials possessing regular pore sizes equivalent to the kinetic diameter of the desired gaseous species, selectively blocking any larger gases [59]. Their selectivity is high but their permeability is low. Design and synthesis of such materials are the cost and energy exhaustive steps in this process.

2.2.4.5 Disassociative dissolution

Dissassociative dissolution is a seven step process outlined in **figure 2.12**;

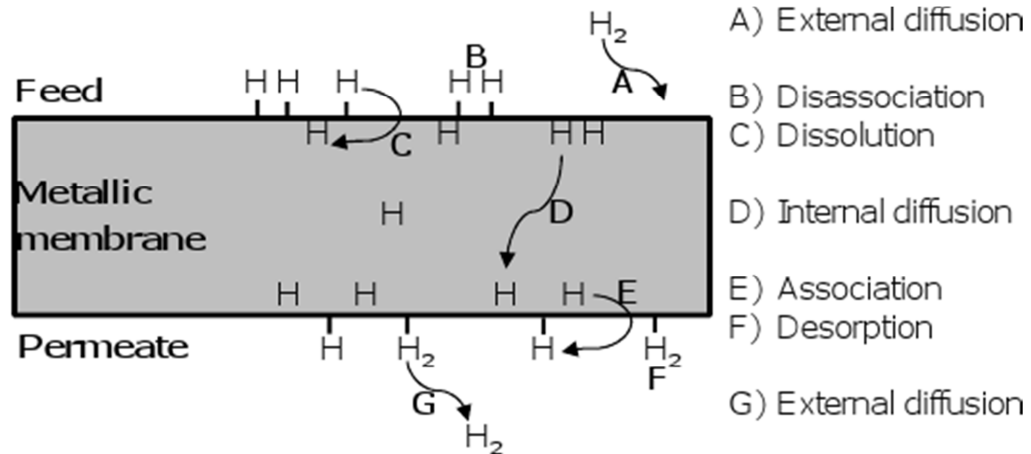


Figure 2.12. Mechanism for disassociative dissolution. The figure is modified from [118].

Membrane separation begins when H₂ molecules within the gas flue feed diffuse to a membrane surface. The molecules disassociate into atomic hydrogen (**spillover process 2.2.2.1.2**) and due to hydrogens solubility within certain metals and alloys diffuse through the membrane based upon the adsorbate concentration gradient. On the permeate side of the membrane H₂ molecules reform and desorb from the surface. Permeability is inversely proportional to the membrane thickness. Reduction in the membrane thickness to increase permeability does not, by this mechanism, compromise selectivity but it does reduce the robustness increasing the risk of membrane failure when exposed to conditions required for pre-combustion gas extraction. Reduced thicknesses loaded onto or sandwiched between other membranes have increased the robustness of the materials and have allowed for thinner, more efficient membrane formation [118]. This process however relies entirely on the quality of the thin membrane. Pin-hole breaks that allow impurities through, compromise the performance of the entire film [118]. Whilst the process is highly selective, desirability is limited by the high cost and ease of poisoning of high performance membranous materials such as palladium (Pd) [118, 132].

Membrane separation of H₂ or CO₂ is a less energy intensive process than the alternatives, as there is no phase change involved in the separation mechanism [70]. Additionally membrane separation increases the fuel combustion efficiency as removal of the product gases (H₂, CO and CO₂ if WGS is applied) *in situ* from the reactor pushes the reaction equilibrium toward completion. A disadvantage of the process compared to absorption alternatives is that because membrane separation is a diffusive process, gas separation leeches energy from the combustion process. As hot gas passes through the membrane it reduces the system pressure and temperature forcing additional energy input to drive the exothermic syngas reactions forward. The other major problem with membrane separation is that currently no membrane set-up offers sufficient selectivity and permeability whilst also being sufficiently robust to survive the high temperature and pressures of a reactor system.

2.2.4.6 CO₂ materials of interest: Polybenzimidazole

Amongst the polymer based membranes considered for pre-combustion CO₂ separation, polybenzimidazole (PBI) has three distinct advantages over its competitors [70]. Firstly its excellent chemical resistance to poisons make its longevity an economic advantage over other materials. Secondly its high glass transition temperature of 723 K give the material good mechanical properties allowing it to remain active as a membrane at temperatures between 473 and 673 K. Activity at these temperatures exceed that of most of its competitors and is consistent with the conditions of an integrated gasification combined cycle reactor. Thirdly the PBI membrane is capable of providing a concentrated CO₂ stream at elevated pressures (41 to 55 bar)- a characteristic not shared by alternative materials- reducing the energy required for re-pressurisation of CO₂ for storage. Currently the glass transition temperature is not quite up to *in situ* CO₂ capture.

2.2.4.7 H₂ materials of interest: Palladium

Hydrogen permeability is a trait shared by all group 10 elements in the periodic table [118]. palladium's increased hydrogen solubility across a wider temperature range has meant that its performance as a membrane outstrips nickel and platinum alternatives. Hydrogen permeability through these metals is proportional to the distance between adsorbent atoms and inversely proportional to the thickness of the membrane. There are however four crucial limitations with palladium as a membrane material. Firstly, hydrogen absorption leads to the formation of two different Pd crystalline phases based upon the hydrogen saturation levels within the metal. Formation of these phases causes strain and recrystallization creating defects and cracks across the bulk of the membrane allowing diffusion of impurities by alternative mechanisms. Secondly, these crystalline phases become embrittled again leading to crack formation. Thirdly, side reactions between palladium and carbonaceous materials or sulfur can consume the active Pd surface reducing permeability. Fourth, palladium is an expensive material to process. Alloying the membrane with certain metals can overcome issues with poisoning, embrittlement and phase formation. Gold alloyed palladium membranes display significantly improved performances over pure Pd membranes by reducing embrittlement and, by increasing the bond distances within the alloy, increasing the permeability. Unfortunately due to the cost of the materials large scale industrialisation is limited. To overcome financial limitations of both pure and alloyed membranes thinner films mounted onto cheap support membranes have been considered. Thinner films reduce the material cost of the membrane and increase the permeability and the cheap support compensates for lost structural integrity. Nickel powder, silica and aluminium hydroxides have all proven useful as membrane supports.

2.3 Material synthesis

It was decided that development of carbon as a physical adsorbent was the most promising approach to meet the DOE objectives for onboard storage (**Table 1**) and was a field where the specialist equipment available for this project could provide fresh insight. The synthesis of carbon nanostructures can be achieved by a number of different techniques. Below is a summary of some of the key techniques used for nano-carbon synthesis. Because of the direction of this project, this summary will be limited to vapour deposition processes, rather than including the multitude of wet chemistry approaches that can also be followed [133].

2.3.1 Chemical Vapour Deposition

Chemical Vapour Deposition (CVD) describes the process of depositing solid material films, which proliferate atomistically across a substrate, by chemically reacting a volatile gaseous species of the materials to be deposited with other gases [134]. Deposition is performed within a controlled gas environment, at a range of pressures from sub atmospheric to high pressure, and usually at elevated temperatures. **Figure 2.13** illustrates the seven fundamental steps that occur in every CVD process. Each step is described below.

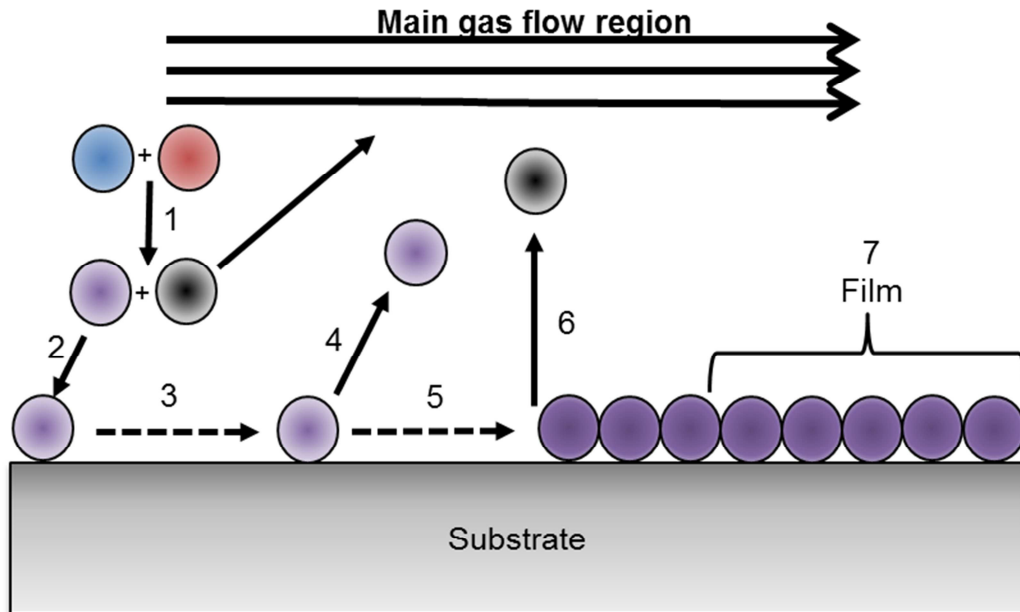


Figure 2.13. The sequence of gas transport and reaction processes fundamental to CVD film growth [135].

1. Additives undergo chemical reactions within the gas phase to form new reactive intermediates and by-products.
2. Transport of the intermediates to the substrate surface by adsorption.
3. Surface diffusion of the species across or through the substrate.
4. Whilst not an active step in the film growth process, some of the adsorbed species will desorb from the substrate surface should they not interact with other adsorbed species to perpetuate film growth through steps 5-7.
5. Heterogeneous surface reactions of the intermediates, catalysed by the substrate, lead to nucleation of thin films.
6. Desorption of volatile by-products of the film formation reactions.
7. Step growth of the propagating films.

All these steps take place within a controlled gaseous environment with conditions monitored to push the reactive equilibrium to completion. Key to film formation is the convective and diffusive transport of both fresh reactant to the substrate surface and removal of the by-product gases from the surface.

The chemical reactions employed within CVD to generate the thin films include pyrolysis, reduction, oxidation, compound formation, disproportionation and reversible transfer.

The feasibility of using CVD for thin film generation is reliant upon thermodynamic and kinetic viability of the planned reactions taking place. In terms of thermodynamic factors, care is required to select appropriate precursor materials, gas compositions and reaction conditions not only to keep the energetic costs of the synthesis process low but also to promote the desired chemical pathway and discourage side reactions. However, even viable thermodynamic pathways can be rendered impractical if the kinetics for vapour transport and vapour-solid reaction significantly retard the rate of reaction.

One of CVDs greatest advantages is the ability to selectively control the sites across a substrate where deposition is promoted. The key to harnessing this ability is substrate preparation, often involving the selective coating of the substrate with a base catalyst that will promote reaction on its surface whilst the surrounding surfaces deter deposition. Deposition of the patterned coating can be achieved with laser assisted CVD. The laser focuses the point of reaction by providing sufficient energy for reaction only on surfaces the laser is focused upon.

Limitations of the CVD process mostly relate to the requirement of an evaporated gaseous precursor. In the case of carbon, precursors, such as CH_4 , are readily available, however addition of other materials such as metals involve the formation of complex organometallic precursors making the addition of a metal to a CVD gas mixture more complex, Furthermore, as CVD relies upon a chemical reaction performed within a gaseous environment there is the opportunity for by-product gases or unreacted precursor materials to become embedded within the porous structure of the materials forcing the need for post-synthetic purification.

2.3.2 Plasma assisted (or enhanced) CVD (PACVD, PECVD)

When energetic requirements needed to force the formation of a desired thin film exceed safe or viable limits for CVD then the energy can be supplemented by exposure of the precursor gases to a plasma field [136]. Plasma can be defined as a gaseous environment containing a high density of ions and electrons that is capable of acting as an electrical conductor. Plasmas are maintained by the continuous introduction of energy to excite and eject electrons from a point source. The point source for the electrons can be secondary electrons from an ion or electron bombarded surface, electrons from a hot thermocouple-emitting source or from a cold cathode source. The electrons are excited by a number of processes including passing a low voltage-high current radio frequency (RF) or direct current (DC) arc between two electrodes within a vacuum. Alternatively excitation can be achieved with laser ablation. These excited electrons dislodge electrons from the precursor gases generating ions and radical species which promote the desired film growth pathway. Plasmas are involved in all physical vapour deposition (PVD) techniques and are used to supplement CVD. Both processes typically use weakly ionised plasmas containing more neutral gas species than ionised particles or electrons. Effective plasma performance requires a high enough fraction of the expelled electrons to be able to ionise atoms by electron-atom inelastic collisions. The energy input by the plasma process allows for a reduction in the temperature of the reaction system. The main advantage of this process over CVD is that it reduces the operating temperature of the system. This influences the variety of materials that can be produced in two ways. Firstly it makes film deposition of processes thought to be thermodynamically or kinetically stable viable at lower temperatures. Secondly, the overall reduction in the system temperature allows for the synthesis of films that are thermally unstable at the temperatures that would be required to promote chemical reaction in the precursor gases by traditional CVD. The major detriment of the process is the low energy efficiency of the plasma and, as with CVD, selection of gaseous precursors of some materials can be expensive and volatile.

2.3.3 Physical vapour deposition by Magnetron sputtering

Sputtering of a material involves the physical vaporisation of target atoms by bombarding a target (cathode) surface with highly energised ions generated within a plasma [137]. The energy required for surface atoms to break free of their solid state structure and travel to the substrate is provided by the transfer of momentum from the impacting ionised particles. Addition of a magnetron below the cathode, with one magnetic pole positioned below the centre of the target and the second pole forming a ring around the outer target edge, creates a magnetic field running parallel to the target surface [138]. The magnetron serves to contain the electrons within its magnetic field, creating a dense plasma directly above the target. Confinement of the electrons increases the chance of electron impingement with any gas species within the field, producing the ionised particles which then impact on the target surface [139]. The negative pole of the magnetron then further serves to increase ion bombardment of the target by attracting the positively charged ions directly toward the target centre, increasing the sputter rate. The magnetrons influence upon the efficiency of ionisation allows sputtering to be performed at lower pressures and operating voltages than either CVD or alternative plasma set-ups. Whilst the magnetic field has no direct influence on the trajectory of the sputtered atoms it does control the trajectory of the ions, which in turn guide the sputtered atoms. The angle of sputter emission is related to the angle of ion impingement. As the magnetic field assures that ions travel in the direction of their field, and this is set horizontally to the target, impinged particles are predominantly sputtered along the same axis as the magnetic field. Intelligent positioning of the substrate in the path of the impinged ions increases the deposition rate. To explore the deposition process in more detail **Figure 2.14** displays the set-up of a magnetron sputtering device.

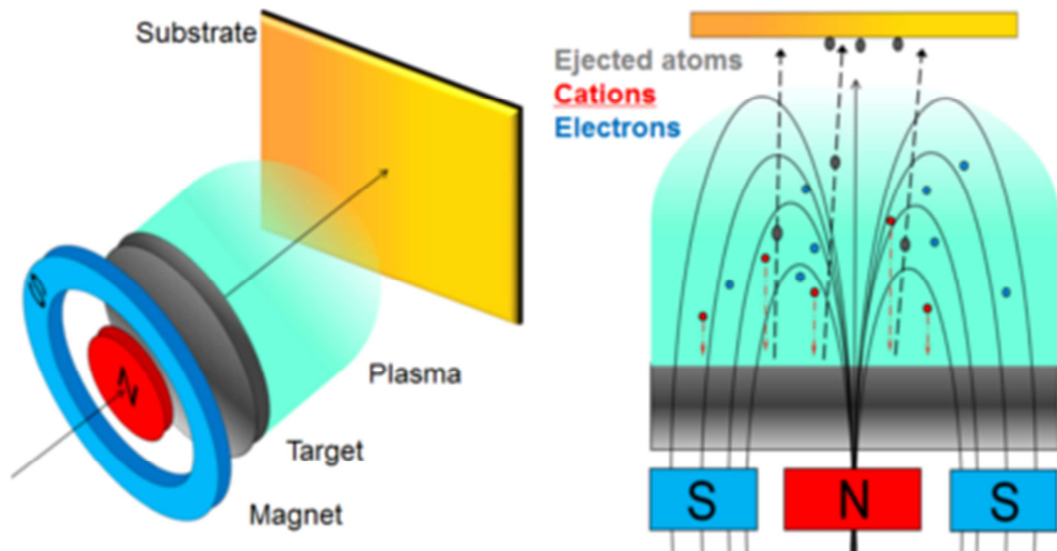


Figure 2.14. Diagram of the magnetron sputtering gun set-up.

In the first instance an electrical current is run through the magnetron system. The electrons are ejected from the cathode into the magnetic field of the magnetron which steers their movement. Within the magnetic field these electrons collide with gaseous species and the energy of impingement knocks electrons out of their orbitals generating positively charged ionic species. In low pressure systems the energy potential of the ion is equal to the energy drop between the target surface and the point within the electric field that the ion is formed (essentially the distance between the ion and the target). The greater the distance, assuming no collisions with sputtered particles or other gaseous species occur, the greater the momentum the ion can achieve and the greater the force of impact and quantity of energy transferred. Upon collision between the ionised species and the substrate surface a number of events can occur. They are summarised in **Figure 2.15**.

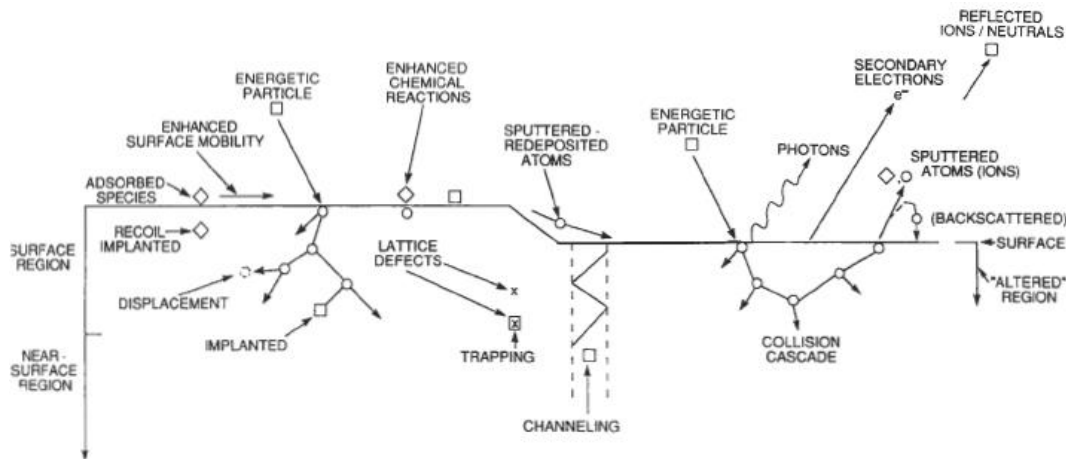


Figure 2.15. Illustrative diagram of the different interactions that occur when a target surface is bombarded with energetic ions [140].

Whilst up to 95 % of energy transferred during sputtering is changed into heat in the surface and near-surface regions, some transfers of momentum lead to surface particle ejection. These ejected particles traverse the space between the target and the substrate. The greater the distance and the higher the relative pressure in the system the smaller the energy of the sputtered particle becomes during its journey as energy is lost in collisions with other species. This process is known as thermalisation. Furthermore, as the distance between target and substrate widens or the system pressure increases deflection of the sputtered materials increases and the overall quantity of particles that reach the substrate decreases, reducing the overall sputter rate. Once impacted on the substrate surface the sputtered particles condense to form a film. Substrate heating occurs from energy provided from both the transfer of kinetic energy of the deposited particles and the exothermic release of energy from the condensation reaction. This heat effect will influence both the crystalline nature of the structures grown and also promote the evaporation of any volatile species that have been formed on the surface. Should crystalline materials with energies of formation that exceed the energy provided by the sputter process be desired then the energy can be supplemented by heating the substrate.

Magnetron sputtering, unlike CVD, can be employed for the deposition of any elemental solid as the material precursor is a target of the pure material. Alloy deposition can be achieved by a number of different techniques such as the use of alloy targets, mixed targets (containing discrete regions of both materials) or simultaneous sputtering from multiple magnetrons. The stoichiometry of the deposited film can be tailored by controlling the quantities of the materials present in the targets or, if using multiple magnetrons, by varying the electrical current passed through the magnetron. As the sputter rate of each material is unique, fine control of co-deposition rates by using multiple magnetrons is the most effective technique for alloy sputtering. An additional approach for alloying materials is to incorporate some of the features of CVD and use a gaseous precursor that is activated when passing through a magnetron plasma. This is the most effective way to generate oxides, nitrides or carbonates by magnetron sputtering.

Magnetron sputtering is a very similar process for thin film deposition to CVD but CVD is often considered slightly more complicated. The four significant differences that separate these approaches are [141]:

1. Where CVD relies upon gaseous precursors, PVD instead utilises solid or molten sources.
2. Building upon this, the process by which the precursor material enters the gas phase is also different. CVD materials are evaporated, PVD relies upon collisional impacts to excite material expulsion.
3. CVD is performed at atmospheric pressure, PVD is performed under vacuum.
4. CVD relies upon chemical reactions on the substrate surface for film propagation. PVD, excluding reactive PVD processes, is performed in the absence of chemical reactions.

Advantages of the sputter process include the ability to deposit any element, alloy or compound with control over stoichiometry [142]. The process is easily reproducible and scalable from a well described experimental method. The small amount of radiant heating generated

during film condensation, compared to the heating required within the entire CVD chamber allow for the deposition of low temperature material conformations. One of the greatest advantages of sputtering is the simplicity of the process. Assuming a reasonable apparatus set-up containing multiple magnetrons then one-pot synthesis of complex materials can be performed. Targets and substrates can be cleaned by sputter etching to remove surface impurities. Samples made up of several materials can be deposited in any stoichiometry from one material coated on top of the other to a 50:50 alloy or any stoichiometry in between. Also, as the process does not involve any chemical reactions no by-products are formed and no purification steps are required. With due attention paid to the selection of the metal cathodes and by controlling the current and sample exposure, features such as the thickness, composition, interface energy and crystallinity of a film can be controlled.

Limitations of the sputter process include the low energy efficiency of the process as up to 95 % of energy transferred to the substrate during sputter contacts is converted into heat rather than particle emission. Additionally, compared to CVD, sputtering has a greatly reduced deposition rate due to the reduced vapourisation rate, higher running costs, and given that sputtering is a “line-of-sight” process deposited films are not equally distributed on surfaces obscured from the sputter gun.

Whilst carbon films have been grown and studied by magnetron sputtering no evidence can be found for the process being explored for the synthesis of nanocarbon materials for hydrogen storage or carbon dioxide separation. This work aims to be the first to analyse the performance of the sputter deposited materials for gas sorption technologies and also assess the strengths and weaknesses of using magnetron sputtering for the synthesis of these materials. **Section 2.4** outlines the experimental approaches designed to meet these criteria

2.3.4 Ball milling

Ball milling is not a materials synthesis process, it is rather a material activation process capable of improving an adsorbents performance [67]. The milling process involves the pulverisation and dispersion of an adsorbent through high energy impacts with milling balls within sealed milling vials [143]. Milling vials are shaken at high speeds in a complex figure 8 motion that transfers significant centrifugal forces to the milling balls and sample. The milling balls are made of a material with a high hardness, such as stainless steel, to prevent contamination of the milled sample. The figure 8 motion alternates the centrifugal direction within the vial, churning the material to assist in even pulverisation of the sample. When the vials are shaken at high rates (1200 RPM) the energy of impact between the sample particles, the vials, and the milling balls can equal 40 times what is achievable by gravitational acceleration alone. Materials being milled undergo four microstructural phase changes. Transition through all the phases is dependent upon the materials and the milling time.

Phase 1. Powdered particles are flattened under compressive impacts with the milling balls and vial walls changing the particle shape by micro-forging.

Phase 2. As milling proceeds cold-welding and fracturing of particles proliferates. If the vial contains two samples then the dispersion of the materials increases reducing the distance between constituents to the micrometre range.

Phase 3. Samples milled for longer times see an increase in the fracturing rate, decreasing the average particle sizes. The dispersion of the materials increases and a more homogeneous sample mix is achieved (note that homogeneity of the mixture is different to homogeneity of the nanostructure).

Phase 4. This phase represents the best dispersion achievable by the ball milling process. By this point the samples are typically deformed

metastable structures. Continued milling would have only a fractional influence on the dispersion and average particle sizes of a sample.

The effects of mechanical milling that benefit the adsorption capacities of a material include increase in a materials heterogeneity, caused by fracturing of microstructures, and generating fresh, higher energy adsorption sites [67, 144]. Practically, a popular use of milling is to fracture closed-tip CNTs to allow diffusion of H₂ down their tube for increased adsorption. Pulverisation reduces particle size and increases surface area, increasing the potential surfaces available for adsorption. The ability of milling to generate a fine, uniform dispersion of two materials makes it a popular process for addition of dopants.

2.4 An introduction to the experiments performed in this study

So far this review has addressed the motives behind and the challenges facing sequestration of H₂ and CO₂. Capture and sequestration techniques have been outlined, including discussion about how to best improve each processes performance. Based upon the outcomes of that review it was decided that adsorption was the most promising approach for providing a novel contribution. This was followed by a discussion of the methods by which controlled synthesis of adsorbents can be achieved. The following section is an introduction to the actual studies performed in this work, outlining the theory, novelty and purpose of the research.

2.4.1 The activation and chemical doping of activated carbon by mechanical ball milling and its influence on H₂ and CO₂ storage capacity

Activated carbons as physical adsorbents are listed amongst the most promising contenders for the efficient storage of H₂ and CO₂ (**Section 2.2.2.2.2**) [17, 19, 67]. ACs alone do not meet the DOE

requirements. They require activation to improve their physical characteristics and chemical doping to further augment their storage capacities. Chemical doping of ACs with transition metals, acting as either a complementary adsorbent or as spillover catalysts, is a popular technique for improving adsorption performance [46, 103, 145-147]. The dispersion of the dopant throughout the material is a consequential factor. Improved homogeneity within the mix of adsorbent and dopant enhances the adsorbents performance.

Ball milling has long been used to activate materials by exposing fresh surfaces to reactive environments and increasing the surface area [144]. It is also a common technique for generating a homogenised mixture of two materials. High energy milling in particular is capable of pulverising materials down to nanoparticle sizes [143].

Nickel was selected as the dopant of choice for this work for several reasons. Firstly, although nickel is not a particularly potent spillover catalyst it is cheap, compared to alternatives such as platinum and palladium [97, 148]. Secondly nickel is already used industrially as a catalyst for the oxidation of carbon materials into carbon monoxide or dioxide [51, 149]. Whilst nickels oxidative properties are of no consequence for this experiment, in industrial fossil fuel combustion reactors adsorption hysteresis induced by carbon char poisoning is a common problem [17]. The addition of nickel oxidation catalysts to adsorbent materials is already common practice to stem the rate of hysteresis [150]. Identifying a combined functionality for the nickel, as an oxidation and adsorption catalyst would increase adsorbent efficiency, and reduce adsorbent mass and production costs by reducing the number of material additives required and, as a result, increase the desirability of such an adsorbent. Also, ACs are known to adsorb both H₂ and CO₂, and nickel is known to improve hydrogen adsorption but its influence on CO₂ adsorption is unclear. Were nickel able to enhance the adsorption of one gas but not the other, then it could be used to improve an adsorbent selectivity.

2.4.1.1 Proposed work

This study looks to characterise the effects of ball milling upon AC and to identify how such textural adjustments influence the material's H₂ and CO₂ storage capacities. The milling times that the samples were subjected to was varied because, as described in **Section 2.3.4**, the textural properties of the milled samples change with continued milling. A near identical study was performed, this time doping the activated carbons with nickel, to establish nickel's influence on the H₂ and CO₂ storage capacities or adsorbent selectivity. Milling time was again of consequence because not only does it result in modification of both the adsorbent and dopants particle size, it also improves dispersion.

Microstructure of the ACs and dopant particles were characterised by Transmission Electron Microscopy (TEM). Volumetric analysis equipment was employed to characterise the effect of milling on the open porosity of the samples. H₂ and CO₂ storage capacities were tested by gravimetric analysis.

2.4.2. The influence of nitrogen content and the presence of a metal substrate on the growth and H₂ storage capacity of novel carbon films deposited by magnetron sputtering

Carbon is a popular adsorbent for H₂ storage due to the array of different lightweight, porous nanostructures it can generate [40]. Optimisation of the structure of these materials, by the processes described in **Section 2.2.2**, are paramount to the design of an ideal adsorbent capable of meeting the DOE objectives for on-board storage [1, 38, 72]. The most promising carbon materials are CNTs. The characteristics of CNTs are described in **Sections 2.2.2.2.2**. Control over the structure of a CNT, its tube length, tube width, number of walls and the packing density of ropes, bundles or forests is dependent upon the growth conditions.

Alongside structural optimisation of an adsorbent, doping with transition metals has been shown to improve hydrogen storage capacities of carbon materials [77, 145, 151]. Nickel is a popular transition metal catalyst capable of increasing an adsorbent's hydrogen storage capacity via the spillover process [97]. Spillover describes the dissociative chemisorption of hydrogen molecules on a metallic centre followed by their diffusion from the metal centre onto an adsorbent [89]. Atomic hydrogen's reduced size compared to a H₂ molecule increases the active surface area of an adsorbent and facilitates an adsorption state with an increased binding energy unobtainable without the metal centres. Nickel is also an effective catalyst for the optimisation of nanostructure synthesis [148]; The diameter of nickel nanoparticles, when used as the catalyst to promote nanotube growth, directly influence nanotube diameter. Reactive carbon atoms diffuse through or across a nickel nanoparticle and form a curved graphitic ring around its circumference. This graphitic ring is the nano-seed from which tube growth propagates. Hence, the larger the nickel particle, the wider the nanotube [152]. These combined functions make nickel an important dopant for modifying the properties of hydrogen storage materials.

Nitrogen is a popular *p*-block dopant which, when chemically bound to an adsorbent, is able to donate lone pairs of electrons across the structure. Spreading of electron density increases an adsorbent's partial charge, strengthening the adsorbate-adsorbent interaction and improving hydrogen storage capacity [145]. Nitrogen is also a useful element for the generation of nano-carbonaceous materials. Nitrogen substitution into the growth front of a graphitic sheet causes curvature in the plane. If successive nitrogen incorporations promote enough curvature, two growth fronts can meet, fuse and form a nano-seed for nanotube growth. Furthermore, as nanotube growth is slowed by energetic restrictions against formation of curved graphitic structures, incorporation of nitrogen, and the curvature it encourages, greatly reduces the energetic growth barrier and increases nanotube proliferation [153, 154]. The resulting CN_x materials possess a high nitrogen content controlled by the synthesis

parameters. The nitrogen content of the film is higher when incorporated during synthesis compared to post synthetic addition [77]. Liu *et al.* have suggested that by fine-tuning the structure of CN_x nanotubes, controlling their nitrogen content, tube alignment, tube diameters and wall numbers, CN_x materials can be tailored for specific applications, including applications in fuel cell technology [155].

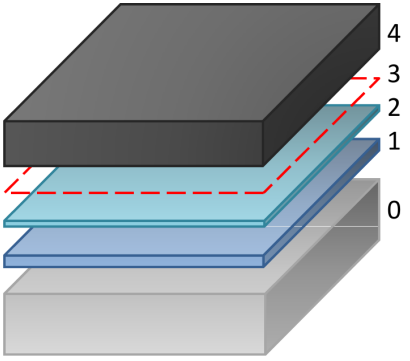
Magnetron sputtering is a versatile process allowing exceptional control over the synthesised films, however the process is slow. It is hoped with the control that the process offers then novel adsorbents better suited to hydrogen adsorption can be synthesised.

2.4.2.1 Proposed work

This study aimed to be the first to characterise the hydrogen storage capacity of carbonaceous films grown by magnetron sputtering. Results presented in this paper are an exploratory look at the influence of deposition parameters on material growth and subsequent hydrogen storage. The outcomes of this work will hopefully guide further steps in the study which will focus on the design of an ideal adsorbent. CN_x nanostructures were synthesised by magnetron sputtering.

The composition of nitrogen as a sputter gas was varied to identify the influence of nitrogen on the structure and hydrogen storage capacity of the synthesised films. The composition of the catalytic base layer used to promote carbon growth was also varied. At its most complex the base layer consisted of a magnesium (Mg) film coated with nickel, as illustrated in **Table 2.3**. An explanation for the values selected is outlined in the experimental **Section 3.4.2**.

Table 2.3. Illustration of the experimental design for the deposition of novel carbon adsorbents by magnetron sputtering.



Step	Role	Details
4	Carbon deposition	C at 13.32 W.cm^{-2} RF power in Ar:N ₂ at annealing temp
3	Annealing	673, 873 or 973 K for 30 minutes under vacuum
2	Catalyst layer	Ni at 5.92 W.cm^{-2} RF power in Ar
1	Base layer	Mg at 5.92 W.cm^{-2} DC power in Ar
0	Substrate	Si

Magnesium was sputtered to prevent nickel leaching into the silicon substrate and to increase the surface roughness, generating additional nucleation sites. Nickel was deposited and annealed into nano-islands to serve as seeding points for nanostructure formation (and to eventually act as a spillover catalyst during H₂ storage tests). The deposition was performed in a range of nitrogen environments in the absence of the magnesium layer and then the absence of both the magnesium and nickel layers to study the changes in material growth. Deposition temperature was also varied to try and identify the influence of temperature on the annealing of the base-layers and then the subsequent growth of the CN_x film.

Following preliminary H₂ storage tests of the films still bound to their silicon underlayer, the most promising material was mass produced and separated from its underlayer. Analysis of the techniques for cleaving the deposited film from the substrate was performed.

The separated CN_x foils were tested for both their H₂ and CO₂ storage capacities. Their performance as selective adsorbents was assessed and compared to those of CNTs produced by CVD.

The microstructure of the carbon materials were characterised using Scanning Electron Microscopy (SEM) and TEM. Elemental composition was analysed by Energy Dispersive X-ray (EDX), x-ray diffraction (XRD) and Raman spectroscopy. The hydrogen storage capacities were measured by thermal gravimetric analysis.

2.4.3 A study of magnetron sputtering as a means to chemically dope carbon nanotubes with cerium and nickel and its influence on H₂ storage capacity

Carbon adsorbents, in their many synthetic forms, are popular for hydrogen storage because of the diversity of their lightweight, inexpensive nanostructures [67]. Chemical doping of carbonaceous adsorbents with other materials that augment their hydrogen uptake promises to improve their performance [76]. Dopant materials such as nickel and titanium have been shown to improve hydrogen storage capacity through different catalytic pathways [95]. No approach has yet managed to augment H₂ uptake to achieve the desired system requirements.

Nickel is a popular dopant because despite not being a particularly potent spillover catalyst (**Section 2.2.2.2.1**), it is an affordable one [97, 148]. Two factors known to improve spillover efficiency are intimacy of binding between the substrate and the adsorbent and a reduction in the catalyst particle size. Control over both these factors is offered by magnetron sputtering, the dopant process explored in this work, as such the performance of nickel as a dopant was of interest. As will become evident later in this discussion, nickel was also selected because of its established influences in improving the hydriding performance of cerium (Ce).

Cerium has understandably been overlooked previously as a physical adsorbent due to its high atomic mass. However as lighter dopants seem incapable of promoting adsorption on adsorbents to meet the DOE objectives (**Table 2.1**), perhaps a less conventional material may provide a solution. Cerium was selected as a dopant for this work because of its excellent redox properties assisting oxidation of nickel in the CeNi catalysts discussed below.

Certain stoichiometries of CeNi alloys are popular dopants for enhancing the kinetics of chemisorbents [156]. Ball milling of Mg-Ce/Ni materials have been shown to reduce the desorption temperatures of MgH_2 by 20 K [156]. Nickel was shown to act as a spillover catalyst, assisting adsorption and hydrogen reformation, whilst cerium acted as a reversible adsorbent generating $\text{CeH}_{2.53}$ complexes [156]. Although the paper does not discuss it in detail, the CeNi composite has an improved kinetic performance compared to a pure nickel doped system. This is because the combination of cerium and nickel as a catalytic alloy has proven beneficial for enhancing the desirable properties of both metals, and the more intimate the dispersion the better [157]. Nickel's activity as a spillover catalyst (**Section 2.2.2.1**) improves cerium's chemical hydrogen storage capacity and adsorption/desorption kinetics [158]. Diffusion to enhance kinetics is further improved by a reduction in the crystallinity and crystalline size of the metal phases [158]. Due to mismatch between the atomic sizes of cerium and nickel atoms, crystallisation is prevented and diffusion is assisted. Cerium also increases the electrophilicity of the Ni atom increasing the alloys reactivity [159-161].

The desirable catalytic traits of Cerium and Ceria (CeO_2) for improving material kinetics are demonstrated by their performance as catalysts in methane tri-reforming and the WGS reaction, especially when they are combined with nickel or magnesium [158, 162]. This union has been exploited in catalytic hydrogen production from water/ethanol mixes [160, 163]. The nickel acts as the active catalytic species and relies upon an active redox system, generating species such as Ce^{4+} , Ce^{3+} , $\text{Ni}^{\delta+}$ and

Ni^{2+} , provided by a strong electro negative draw of close proximity cerium atoms [164]. Within the confines of the WGS reaction, cerium proves useful for attracting oxygen but also has the potential to be utilised for attracting hydrogens, as considered here.

Cerium's usefulness as a hydrogen chemisorbent has been studied and found wanting. Whilst ceria boasts the highest H_2 reactivity of all the rare earth oxides [165], cerium's stoichiometric hydrogen capacity is still limited to 2.7 wt.% (CeH_4) which drops as low as 1.85 wt.% in the oxidised and alloyed form $(\text{CeOH}_4)_{10}\text{NiO}$. The chemical absorption properties of cerium are more frequently reported when combined with nickel where they show improved kinetics but once again their capacities are poor [158, 166]. Jalowiecki-Duhamel found that the CeNi_5 oxide and CeNi_5 intermetallic compounds could store equivalent quantities of hydrogen [167, 168]. The optimised mixed oxide, $\text{H}_{6.3}\text{CeNi}_{0.7}\text{O}_{2.7}$, had a hydrogen storage capacity of 3.04 wt.% and was found to be fully rechargeable at temperatures as low as 313.5 K. Unfortunately storage capacity had to be calculated through the catalytic hydrogenation of isoprene as the thermal barrier against gaseous desorption of H_2 was too high [167]. Chemical adsorption of hydrogen on cerium is admittedly poor compared to popular metal oxide adsorbents (**Section 2.2.3**), yet the same is true of titanium or nickel, popular dopants known for increasing physisorption yields so this was not considered a valid reason to not explore cerium's catalytic performance [95, 169].

The ratio of Ni to Ce plays a large role in the kinetics and storage capacity of the material and its oxide, as does the manufacturing process [159]. Formation of the CeNi_5 alloy through electrolysis of ceria and nickel oxide follows a mechanism which sees NiO, the oxide with the lower stability, reduce to Ni and begin to agglomerate. Once Ni has been reduced ceria is reduced to cerium and begins alloying with the growing Ni aggregates [170]. This mechanism however promotes the formation of nickel in relative abundance before cerium is generated. Cerium's larger atomic radii compared to nickel, restricts diffusion of cerium through

nickel's narrower crystalline lattice resulting in nickel aggregates with a CeNi coating [170]. To achieve a thorough distribution of the metals high temperature annealing is required to promote diffusion.

PVD by magnetron sputtering (**Section 2.3.3**) is an industrial thin film synthesis process that up to now has been overlooked for use in the generation of hydrogen adsorbents. Magnetron sputtering allows for intimate binding between the sputtered material and the coated substrate with exceptional control afforded to the composition of the deposited material as well as the quantities deposited [142]. As the metals are deposited in their atomic form purification or annealing steps are not required allowing for fast one-pot deposition of multiple films or alloys. The opportunity granted by PVD to perform multiple deposition steps consecutively, all under high vacuum limits the opportunity for unexpected oxidation of a sample to occur. An issue of considerable importance for a material as easily oxidised as cerium. Simultaneous magnetron sputtering of nickel and cerium onto an adsorbent at equivalent rates should generate a better homogenised metal alloy than high temperature electrolysis because the cerium and nickel metals are being introduced to each other in atomic, not agglomerate forms allowing for better diffusion. The process should also have a lower energetic cost as it is both fast and does not require any material heating steps.

CNTs were used as the adsorbent in this study for doping with cerium or nickel due to their existing popularity as adsorbents. Cerium has previously been sputter coated onto CNT walls [171-173]. Sputtering of a material onto a powdered sample, such as the CNT's used in this study, is referred to as "powder sputtering" and is a common process used to encapsulate small particles [174]. Powder sputter devices are designed with a rotating and sonicating sample mount to ensure a homogeneous mix of sputtered particles across the entire material surface [174-177]. Within the confines of this study encapsulation of the CNTs was undesirable. As only a small fraction of the CNT surface required coating,

our apparatus' lack of a sonicating stage was decided to not be significantly detrimental to this research.

2.4.3.1 Proposed work

This work looks to be the first study of the effects of cerium as a chemical dopant of CNTs for the physical adsorption of hydrogen. Additionally, this work aims to be the first recorded instance where PVD has been applied for doping physical adsorbents with metal dopants to study their influence on hydrogen storage. The adsorbents used were CNT powder, the dopant materials explored were both cerium and nickel. The work aims to investigate the applicability of the PVD process for sample doping building upon observations reported in the literature about the desirable traits for a dopant.

Co-deposition of CeNi composite dopants were also explored to see if alloying would augment the materials performance for physisorption in much the same way as CeNi composites improve either metals individual performance in the WGS reaction [161, 178, 179]. *s*- and *d*-block metals mounted on a substrate can theoretically adsorb between 4 and 6 hydrogen atoms [180-182]. It is hoped that intimately bound *f*- and *d*-block metals known to complement each other's activity could perform similarly. Jalowiecki-Duhamel proposed an optimum CeNi ratio of 10:7 for hydrogen production from ethanol/water mixes [160]. This ratio was used for the co-deposition tests for doping CNTs.

Microstructure of the CNTs and dopant particles were characterised by SEM and TEM. Elemental analysis was performed by XRD and Raman apparatus. Volumetric analysis equipment was employed to characterise the effect of sputter doping on the porosity of the samples. Hydrogen storage capacities were tested by gravimetric analysis.

2.4.4 Exploring the synthesis of graphene by magnetron sputtering

2.4.4.1 Introduction

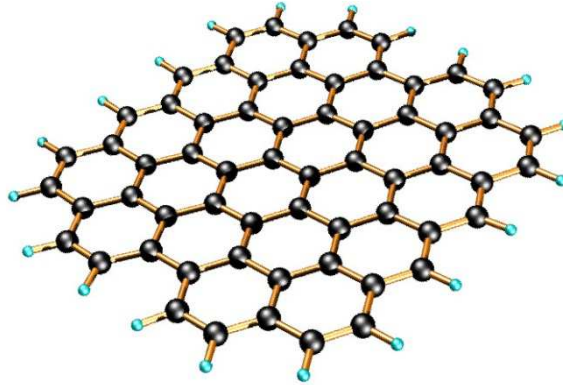


Figure 2.16. Structure of a graphene sheet [183].

Graphene is a one atom thick, sp^2 hybridised carbon layer with a tightly packed, two dimensional honeycomb lattice structure as shown in **Figure 2.16** [184, 185]. The unique electronic properties of graphene, such as the relativistic motion of its charge carriers, mark it out as an innovative platform for novel nanoelectronics [186, 187]. Industrial application of graphene is currently inhibited by the lack of a reliable large scale synthesis method that guarantees a high quality, defect free product.

There are four main approaches to graphene synthesis; Micromechanical cleavage was used for initial synthesis but cannot be scaled up for industrial applications [188, 189]. The Exfoliation technique generates high purity graphene ideal for lab scale research, but the process is only able to synthesise graphene sheets up to 1000 μm wide, too small for industrial applications [187, 190]. Graphene production through thermal decomposition of SiC requires annealing of the SiC substrate at temperatures in excess of 1723 K. Synthesis is energetically exhaustive making it impractical for industrial scale production [187]. The most reliable and scalable approach for graphene synthesis industrially is CVD over metal catalysts [186].

Developments in the CVD process have produced clearly defined mechanisms for controlled synthesis of monolayer graphene or few layer graphene (FLG) films. The mechanisms for graphene growth underpinning the CVD synthetic processes should allow for large scale production without compromising quality. Unfortunately there are still problems when trying to industrialise the process. Firstly, graphene synthesis is restricted to the surfaces of a limited number of catalytic materials [188]. Current separation and transfer processes to manipulate the graphene for industrial purposes can rip, shear or otherwise damage the graphene or FLG foil [187, 191]. Secondly the process requires temperatures in excess of 1173 K to promote decomposition of methane (the most effective hydrocarbon precursor) [192].

CVD and magnetron sputtering processes share some mechanistic similarities and the work described in this chapter aimed to evaluate if magnetron sputtering could be used as an alternative method for synthesis of graphene. Identifying sputtering as a potential synthetic method for graphene synthesis could open-up new approaches to overcome the limitations of CVD, reducing the deposition temperature and, if possible, increase the diversity of materials graphene can be grown upon. The starting point in this study for developing a sputter process for synthesising graphene was to modify the CVD methodology.

The two most popular catalysts for the synthesis of graphene through CVD are nickel and copper (Cu) because of their low cost, crystalline grain sizes and their wide use already within the relevant industrial fields [193]. Nickel is commonly used for the growth of FLG and copper for synthesis of monolayer graphene. The variation in the FLG and monolayer graphene products is due to differences in the synthetic mechanism influenced by the metal catalysts thermal expansion coefficients and their carbon solubility [194, 195].

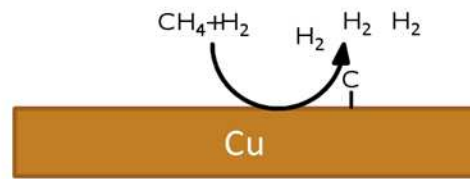
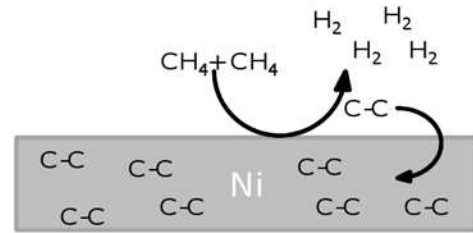
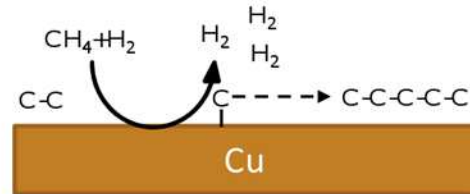
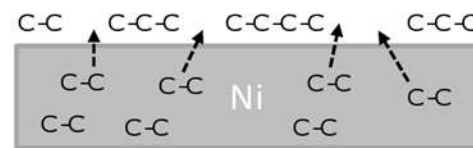
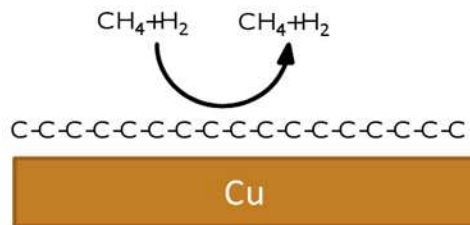
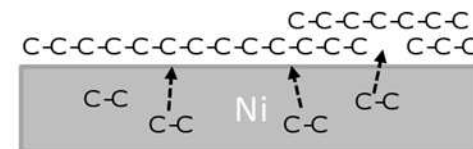
A) Cu catalysed CH₄ pyrolysis**D) High temp pyrolysis and absorption****B) Graphene propagation across Cu****E) Low temp precipitation****C) Self-limited reaction termination****F) Oversaturation generating FLGs**

Figure 2.17. Mechanisms for copper or nickel catalysed graphene synthesis. Full descriptions of the process are outlined in sections 1.1 and 1.2.

2.4.4.2 Graphene synthesis on copper (Figure 2.17A-C)

Graphene synthesis on copper by CVD is often performed at 1273 K in a mixed Ar:H₂ (25:75) atmosphere at 1 bar [186, 196]. A mixed H₂:CH₄ (80:20 standard cubic centimetres per minute [sccm] ratio) flow is introduced for three minutes in addition to the Ar:H₂ mix. Monolayer graphene synthesis on copper is a self-limiting surface adsorption process [185, 186, 190, 193, 194]. Methane decomposition is catalysed directly on the copper surface (**Figure 2.17A**). Nucleation of graphene occurs on the linear axis of the crystalline copper structure at edges or break points in the film, with growth then spreading out two dimensionally across the exposed copper surface (**Figure 2.17B**). As copper becomes buried beneath the propagating graphene the synthesis rate decreases until, at

complete graphene coverage, synthesis ends (**Figure 2.17C**; self-limiting process) [193]. Only small amounts of carbon precursors are required due to the efficiency of the process, due predominantly to the low solubility of carbon in copper (0.04 atomic.%) [187]. Despite the process being self-limiting some tests have recovered FLGs rather than monolayer films when super saturations of carbon precursors are introduced [193]. Graphene synthesis occurs readily on copper foils and on copper coated silicon oxide or silicon (SiO_2/Si) wafers, as long as the copper film is sufficiently thick (>500 nm) [191]. Thicknesses below this can disrupt formation in several ways; firstly the high reaction temperatures required for methane decomposition can cause either copper annealing or copper evaporation leaving an unsuitable surface for growth. Secondly, in some instances at temperatures of 1273 K or higher, Cu-Si interactions result in the formation of SiO surface impurities in the graphene film [191]. These impurities are the result of silicon dissolving into the copper then precipitation back out during cooling. Their mechanism of formation is unknown. Whilst they reduce the quality of the graphene film they do not inhibit its formation altogether.

2.4.4.3 Graphene synthesis on nickel (**Figure 2.17D-F**)

Typical graphene synthesis on nickel by CVD is performed with polycrystalline nickel foils at 1123 K in a H_2 atmosphere at 1 bar. Following 30 minutes annealing in H_2 , the carbon precursor (frequently CH_4) is pumped into the chamber ($\text{H}_2:\text{CH}_4$ ratio of 98:2) for 90 minutes. When the Methane flow is stopped the samples are cooled slowly in a H_2 atmosphere. Nickel grows FLG by a surface segregation followed by precipitation mechanism [186, 193-195]. The mechanism can be described in a three step process; annealing under hydrogen reduces any nickel oxides present and processes the films surface to a rough polycrystalline structure. Methane fed into the system pyrolyses on the metal surface and forms C-C dimers that are absorbed into the nickel (**Figure 2.17D**). Subsequent cooling of the film decreases nickel's carbon

solubility resulting in carbon precipitation on the surface (**Figure 2.17E**). The precipitated carbon forms graphene sheets across the nickel surface. The number of graphene sheets is dependent upon the quantity of carbon absorbed in the nickel. As nickel's carbon solubility is relatively high (2.7 atomic.%) at 1173 K, the process requires a relatively high carbon input for the mass of graphene recovered. This precipitation mechanism leads to the formation of FLGs as the quantity of carbon precipitated in the cooling process is often greater than the quantity required for monolayer formation (**Figure 2.17F**) [187, 193]. Carbon oversaturation in the nickel leads to the formation of graphite whereas carbon subsaturation leads to the formation of activated carbon [197]. The number of graphene layers can be controlled and reduced by reducing the thickness of the nickel film, reducing the mass of carbon absorbed, or by increasing the cooling time to quench adsorbed carbon in the nickel film and halt precipitation [190, 193, 198]. Nickel films thinner than 300 nm have successfully precipitated bi/monolayer graphene, however thinner films such as this are more likely to anneal at high temperature and form nano-islands which are unable to synthesise a continuous graphene film [198].

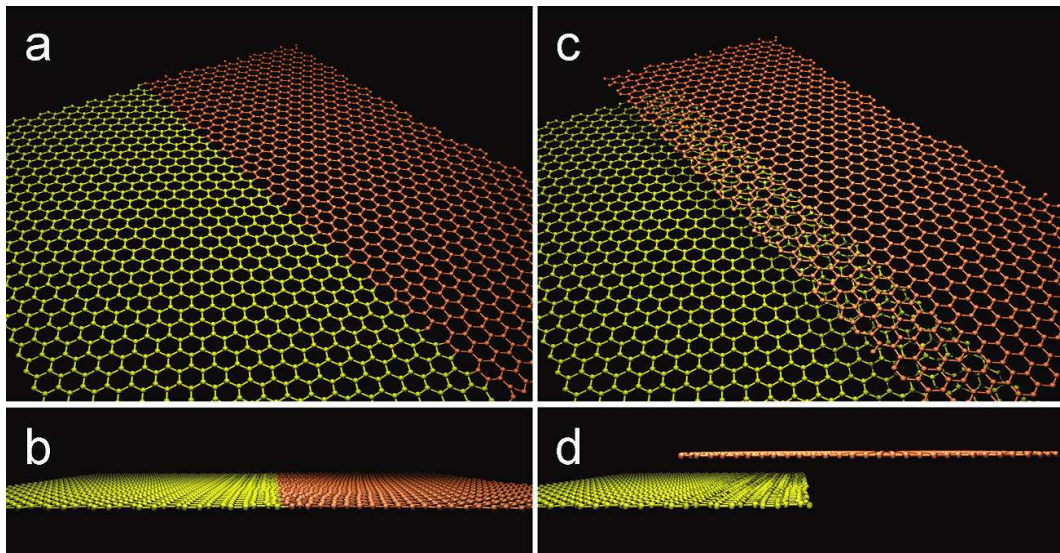


Figure 2.18: Interface boundaries for graphene layers. A + B demonstrate atomic interfacing. C+D demonstrate overlap interfacing [186].

Both nickel and copper catalysed mechanisms develop through nucleation at multiple points across the metals surface. The graphene films merge at their edges by one of two different processes. Atomic interfacing (**Figure 2.18A and 2.18B**), where direct atomic bonding occurs to form a discrete domain boundary, a process which can introduce imperfections such as pentagon or heptagon rings [186]. Overlap interfacing (**Figure 2.18C and 2.18D**), where one sheet overlaps another creating a bilayer boundary that relies upon van der Waal's forces to hold the domains together [186]. Atomic interfacing produces graphene films with better material properties than overlap interfacing. The quality of graphene's properties are inversely proportional to the fraction of imperfections in the film. The fraction of imperfections can be reduced by using single crystal metal underlayers. Single crystal films promote graphene growth in a single orientation, so when propagating graphene grain boundaries meet and bind they do so with fewer structural irregularities, such as heptagon or pentagon rings. Transition metal *fcc (111)* and *hcp (0001)* lattice orientations are the only surfaces that will promote graphene formation due to their varying degree of mismatch with the graphene lattice parameters [188, 195]. In a polycrystalline metal film some of the crystallites will possess the *fcc (111)* structure from which graphene propagates but not necessarily at the same orientation angle to each other causing grain boundary formation and, as a result, non-uniform sheets.

High temperature synthesis negatively influences graphene sheets post-synthesis. During the cooling step mismatch in the thermal coefficients of graphene and the underlayer metals lead to the propagation of wrinkles across the graphene surface. Wrinkles are due to the thermal constriction of the metal underlayer during cooling being greater than that of graphene [187, 191, 195]. Wrinkle ridge height and spacing are dependent upon the expansion coefficient of the substrate [195]. Methods to overcome wrinkle formation include performing deposition at a lower temperature to reduce the mismatch between films, or using a catalytic

material with a similar thermal coefficient to that of graphene such as hexagonal boron nitride [187].

2.4.4.4 Graphene synthesis by magnetron sputtering

Theoretically, sputtering offers three distinct advantages over CVD alternatives. Firstly, as sputtering circumvents the need for hydrocarbon pyrolysis, synthesis should be achievable at lower temperatures. Lower temperatures would mitigate thermal constriction issues and should reduce the appearance of graphene wrinkles. Secondly, some sputter apparatus allows for controlled thin film deposition of copper or nickel, and carbon consecutively for fast, one-pot synthesis. The sputter process eliminates the requirement of an annealing step in hydrogen at high temperatures to remove metal oxides as metals are sputtered as atomic particles that needn't be exposed to the reactive elements of the atmosphere, such as oxygen and moisture, before carbon deposition. Thirdly, sputtering will lower the abundance of precursor and flow gas material used, reducing the overall cost of the process and the associated risks when scaling up the production. Also, sputter deposition is potentially a quicker process.

Some incompatibilities between sputtering and the CVD mechanisms discussed in **Sections 2.4.4.2** and **2.4.4.3** graphene mechanisms could exist. The nickel mechanism is dependent upon carbon dissolution into the nickel prior to precipitation as graphene. If the temperature for carbon dissolution is similar to the temperature for methane decomposition then the sputtering process would serve no distinct advantage thermally over CVD and may be no more advantageous overall for industrial application. However, the properties of thin film surfaces tend to behave differently to a bulk material. Thin nickel films are known to sinter, anneal and absorb carbon at temperatures well below nickel's melting point and at temperatures well below those of CVD processing [199]. Copper's graphene synthesis method is self-limiting as

the copper catalyses the hydrocarbon precursors decomposition. Secondary graphene layers are not formed as contact between methane and the graphene surface does not result in methane decomposition and the propagation of a second graphene layer. Sputtering deposits pure carbon atoms or ions indiscriminately across a surface.. Should carbon be deposited in excess, formation of additional graphitic or activated carbon layers could coat the graphene film, rendering sputtering unsuitable for deposition of high purity graphene on copper. Sputtered carbon atoms are known to diffuse across a surface in search of sufficient binding sites. This free movement, with energy provided from their sputter excitation and the heat of the substrate, may negate concerns about carbon excesses if the quantity of carbon sputtered is finely regulated.

Despite the assertion that sputtering should allow for lower temperature processing, the materials in these tests were synthesised at 1073 K because no synthetic process has previously been able to decouple the methane pyrolysis step and the catalysed graphene growth. As a catalytic activation barrier for graphene formation may require satisfying it seemed prudent to run these tests under conditions as similar to the CVD mechanisms as possible. Also, the graphitic fraction of magnetron sputtered carbons has been shown to increase with deposition temperature suggesting that higher temperatures may assist promotion of graphene synthesis [200]. Graphene has previously been deposited by CVD on copper at 1073 K using ethylene but not on nickel so, were graphene synthesis achieved, then this work would evidence that lower temperature alternatives were available [191].

2.4.4.5. Graphene characterisation

Synthesised graphene can be characterised by a multitude of approaches including; ACHRTEM [186], AFM, [194], AES [195], SEM and EDX [194-196, 198], and Raman spectroscopy [201]. Brightness variation in SEM results can be used to quantify thicknesses [190]. Raman analysis

is used in this study. Raman excitation at 514 nm will generate strong spectra which can be easily compared to the literature to identify if graphene has been synthesised [202]. **Figure 2.19** demonstrates an ideal graphene Raman spectra.

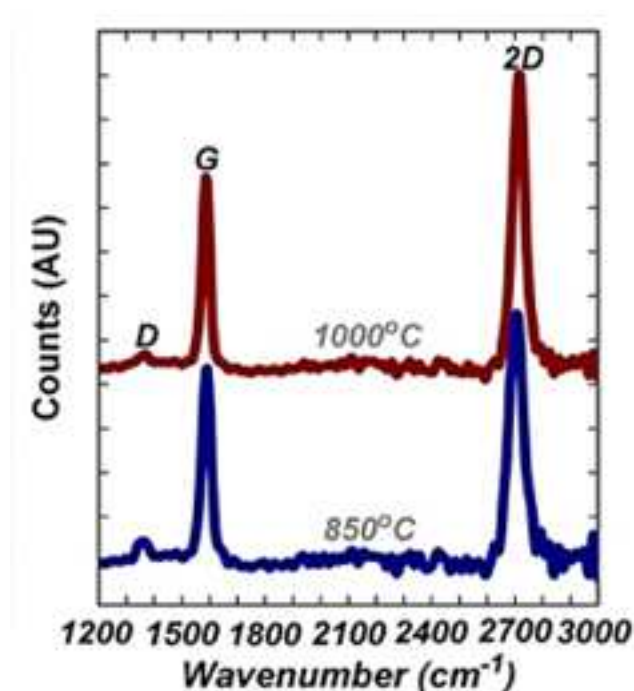


Figure 2.19. Typical Raman spectra for copper catalysed graphene films synthesised at 850 and 1000 °C [191].

Points of interest in the spectra include: no D peak at 1350 cm^{-1} , a strong G peak at 1580 cm^{-1} and a more intense but narrower 2D peak at 2680 cm^{-1} [187, 202]. The I_D/I_G ratio, comparing the intensities of the D and G peaks, can be used to estimate the defect level and the average crystallite size, while the I_{2D}/I_G ratio can identify the number of graphene layers and should ideally be between 0.4 and 0.46 [191, 192, 194].

2.4.4.6 Proposed work

This study aims to investigate the synthesis of graphene by magnetron sputtering. Thin films of copper or nickel will be deposited onto silicon (III) substrates, heated to 1073 K and coated with varying quantities

of carbon. Attempting synthesis with both nickel and copper catalysts allows for examination of whether sputtering provides a sufficient source of carbon precursors able to follow the metal catalysed CVD graphene synthesis mechanism. It is hoped that the generated films will evidence some of the conflicts between the sputter process and the graphene synthesis mechanisms as described in **Section 2.4.4.4**. Carbon will be deposited in varying quantities to determine the required carbon deposition times to form graphene and also prevent the formation of undesirable carbon deposits. The quality of the deposited films will be assessed while still attached to the metal underlayer. Raman and SEM analysis will be used to determine whether synthesis was successful.

CHAPTER 3: EXPERIMENTAL METHODS AND MATERIALS

3.1 Materials

3.1.1 Solids and powders

Activated carbon and nickel nanopowders required for the ball milling study (**Section 2.4.1**) were both purchased from Sigma-Aldrich. The AC material purity was quoted to be >99 % and possessed an approximate surface area greater than $100 \text{ m}^2\text{g}^{-1}$. The nickel nanopowder purity was >99 % and had an average particle size <100 nm.

Raw carbon nanotube (RCNT) samples for the powder sputtering study (**Section 2.4.3**) were donated to this work by *Chen et al.* from Xiamen University. The CNT's were synthesised by CVD of CH_4 or CO using a Ni-MgO catalyst and a fixed-bed continuous flow reactor. Full details of the synthesis process can be found elsewhere [203]. CNTs synthesised by this process were selected for this work due to their homogenous and narrow outer tube diameters (25 to 20 nm). The nanotubes were received in their raw form (RCNTs) and required purification to remove the Ni-MgO catalyst.

3.1.2 Magnetron sputtering materials

Sputtered materials generated in work from **Sections 2.4.2** and **2.4.4** were deposited onto 1 cm^2 silicon wafers. Preliminary work (such as sputter rate calculation) was performed on boron doped, single crystal <100> Si wafers provided by *Compart Technology Ltd* which required dicing to fit into the substrate holder. Substrates used in the structural analysis and hydrogen storage tests were provided by *PI-KEM Ltd.* and

were pre-diced, phosphorus doped, single crystal <100> Si wafer. Graphene deposition work was performed on phosphorus doped, single crystal <111> Si wafers also provided by *PI-KEM Ltd*. Sputter target specifications are summarised in the **Table 3.1**:

Table 3.1: List of magnetron sputter targets used in this project

Material	Purity	Supplier	Thickness	Radius
Nickel (Ni)	> 99.9 %	Testbourne Ltd	3.175 mm	25.4 mm
Titanium (Ti)	> 99.9 %	Testbourne Ltd	3.175 mm	25.4 mm
Magnesium (Mg)	> 99.9 %	Testbourne Ltd	3.175 mm	25.4 mm
Cerium (Ce)	> 99.9 %	Testbourne Ltd	3.175 mm	25.4 mm
Copper (Cu)	> 99.9 %	PVD Products	6.35 mm	25.4 mm
Graphite (C)	> 99.9 %	Kurt J. Lesker company	6.35 mm	25.4 mm
Graphite (C)	> 99.9 %	Kurt J. Lesker company	3.175 mm	25.4 mm

The 6.35 mm thick graphite target was used for preliminary tests and for the work performed in **Section 2.4.2**. The 3.175 mm thick graphite target was used in graphene synthesis in **Section 2.4.4**.

Oxygen free Nitrogen (OFN) and Argon (Ar) were used as sputter gases in all tests. Argon was used as the sputter gas for the deposition of all metals. OFN serviced the main sputter chamber, the glove box antechamber and was also used as a reactive sputter gas in **Section 2.4.2**. OFNs involvement as a reactive sputter gas meant it was incorporated chemically within some of the deposited materials. Both gases were purchased from *BOC industrial gases UK* and came with an assured stream purity of > 99.9 %.

3.1.3 Solvents

Table 3.2 provides a summary of the solvents used in this study.

Table 3.2. Summary of the different solvents were used in this work.

Material	Supplier	Purity
Acetone	Sigma-Aldrich	>99.5 %
Ethanol	Sigma-Aldrich	>99.8 %
Nitric acid	Fisher Scientific	AR grade
Toluene	Fisher Scientific	HPLC grade
Hydrochloric acid 10 % w/v	Fisher diluted with MQ	AR Grade
Aqueous ferric chloride	Fisher Scientific	LR Grade

3.2 Experimental apparatus

3.2.1 Glove box

To prevent oxidation, samples were prepared and run within an inert Ar atmosphere. Samples were prepared within one glove box before being transferred within sealed vials to a second glove box, which housed the mechanical ball milling apparatus, or to the sputter chamber. Gas flow recirculation systems maintained moisture and O₂ levels below 250 ppm. Samples being transferred were outgassed within the transfer chambers for 10 minutes before passage into the chambers.

3.2.2 Ball mill



Figure 3.1. SPEX 8000 ball mill.

Mechanical milling was carried out in a SPEX 8000 ball mill (**Figure 3.1**) manufactured by *SPEX CertPrep, Metuchen, NJ*. The mill possesses two mounts for loading stainless steel milling vials. The Vials are shaken in a complex figure-8 motion at a rate of 1200 rpm. Due to the high revolution rate and angular momentum of the milling process, the force of impact between the sample, the vials and the milling balls allows this process to be termed high energy milling. The 60 ml stainless steel milling vials and 5 mm radius stainless steel milling balls were abrasively cleaned with wire-wool, washed with ethanol and dried within a vacuum oven at 120 °C overnight to remove material impurities and moisture.

3.2.3 Magnetron sputtering device

Magnetron sputtering was performed with a *J00S2053 Sputter deposition system* manufactured by *PVD Products Inc, 231 Andover Street, Wilmington, MA*. The Sputter chamber is a 40.6 × 40.6 cm Stainless steel box (**figure 3.2**) with a front mounted hinged door, which seals against differentially pumped Viton O-rings, and which serves as access for system maintenance. The back of the chamber hosts a smaller hinged door sealed by Viton O-rings enclosed within a Lexan glove box which allows for sample loading and unloading within an inert atmosphere,

protecting both the sputtered samples and the low moisture environment within the main chamber from contamination. All chamber surfaces are protected against excessive sputtering by stainless steel panels coated with aluminium foil. The foil is changed periodically to preserve a clean sputter environment and maintain vacuum quality. The chamber roof houses three compression fittings for mounting three magnetron sputter sources. Other ports servicing the main chamber include rough and smooth gas inlets and pumping ports, heater feedthroughs, vacuum gauges, crystal stage motors and shutter valves.

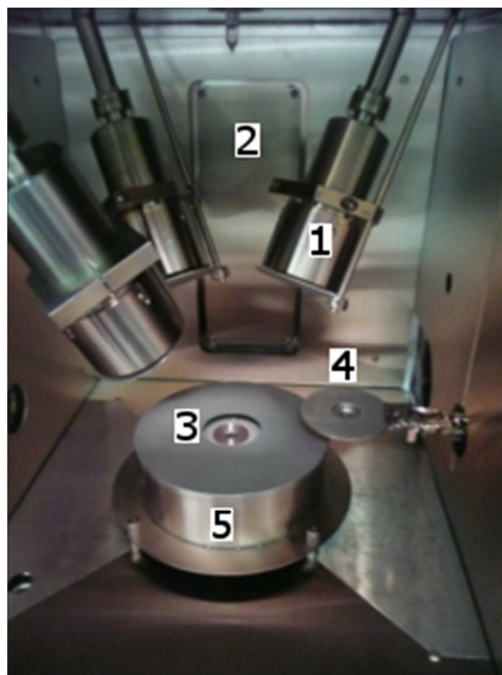


Figure 3.2: Inside the Magnetron sputter chamber. 1 (magnetron); 2 (Small door leading to glove box); 3 (Substrate Holder); 4 (Crystal rate monitor); 5 (Substrate heater and RF bias shield)

3.2.3.1 Substrate stage

The substrate stage (marked **5** in **Figure 3.2**), is mounted in the centre of the chamber upon both a heater platform and an RF substrate bias. The heater is powered by a programmable eurotherm that can achieve temperatures of 850 °C. Temperature is monitored by a type K

thermocouple mounted on the holder. Samples are loaded onto changeable substrate holders that sit in the middle of the substrate stage. For deposition work in **Sections 2.4.2** and **2.4.4** a substrate holder (marked **3** in **Figure 3.2**) designed to carry 1 cm² substrate dice was used. For powder deposition work performed in **Section 2.4.3** a spherical plate with a surface area of 5.314 cm² was used.

3.2.3.2 Magnetrons

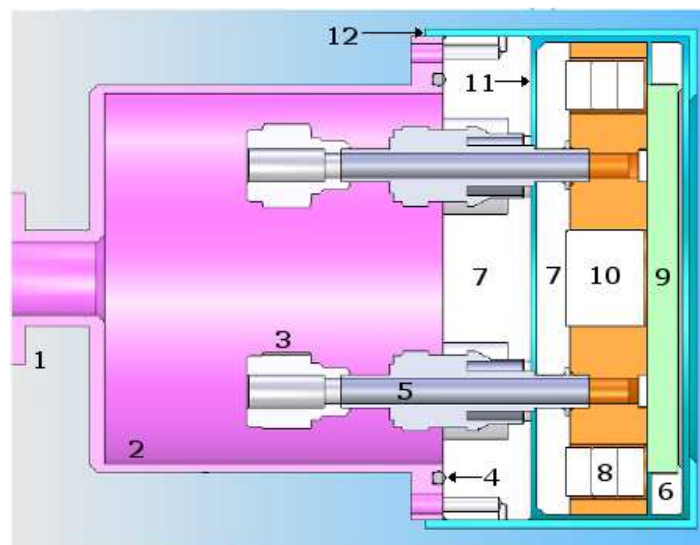


Figure 3.3. Sputter gun cross-section. Key: 1 (3.38 cm CF flange); 2 (Vacuum Housing); 3 (0.64 cm Swagelok fitting); 4 (Viton O-ring); 5 (Water/Electrical feedthrough); 6 (Target clamp); 7 (Brazed assembly); 8 (Magnets); 9 (Target); 10 (Iron Slug); 11 (Gap); 12 (Anode/ Sputter shield).

Three magnetron sources were provided with the chamber (marked **1** in **Figure 3.2**). Each source is capable of running in either DC or RF mode up to 400 W or 300 W, respectively. A cross sectional diagram of a magnetron is provided in **figure 3.3**. Target clamps are designed to hold targets with a 2.54 cm radius and a thickness of either 0.318 or 0.635 cm. The distance the target can be mounted from the substrate is theoretically variable, but a design flaw prevents the target being positioned less than 18 cm from the substrate.

3.2.3.3 Vacuum pumps, gas flow controllers and pressure sensors

Magnetron sputtering is a high vacuum process. The vacuum for this system is provided primarily by an Edwards XDS dry scroll pump. The dry pump serves to evacuate the chamber to a pressure of 0.33 mbar before transferring control to a Pfeiffer HiPAce 300 l/sec turbo pump which is capable of reducing the chamber pressure to $< 1.3 \times 10^{-10}$ bar. Chamber pressure is measured by “The Hornet”, a miniature ionisation vacuum gauge made by InstruTech Inc. The Hornets CVG101 convection gauge and IGM402 ionisation gauge measure the pressure range between 1.3 bar and 1.3×10^{-7} bar and 6.6×10^{-7} bar to 1.3×10^{-12} bar, respectively. To maintain a set pressure during sputtering the turbo pump is not closed off, rather it is restrained by a gate and throttle valve mediated by a VAT PM-5 pressure controller coupled to a 1.3 mbar full scale MSK capacitance manometer.

The system can run up to three sputter gases simultaneously. Release of the sputter gas is mediated by three digitally controlled MSK mass flow controllers allowing each gas a max flow rate of 100 sccm. Sputter gases were set as Ar, O₂ and N₂. During the sputtering process a controlled system pressure is required. The pressure and mass flow controllers allow for control of flow rate and chamber pressure in a closed loop fashion between 1.3×10^{-3} and 0.33 mbar.

3.2.3.4 Crystal monitor

Deposition rate is measured by a rack mounted Inficon SQM-160 rate monitor (marked **4** in **Figure 3.2**). Measurements of rate are taken by a quartz crystal microbalance assembly which can be extended and retracted into the sputter path of the three magnetrons for measurement of accurate deposition rates.

3.2.3.5 Sample preparation

Before loading a substrate onto the substrate holder each 1 cm square die was ultrasonically cleaned in ethanol for 15 minutes then dried in air and weighed. The sample was passed into the sputter chamber through the glove box antechamber. Using clean tweezers the old sample holder is removed from the sputter chamber and the old sample removed for storage. The new substrate is loaded onto the substrate holder and placed back inside the sputter chamber. The system is pumped down and left under vacuum for at least 12 hours to reach a suitable vacuum below 6.7×10^{-10} bar.

Calibration of material deposition rates was performed for all materials prior to the beginning of any test to assure the thicknesses of the deposited films. The metals were sputtered onto silicon targets at varying target power densities, power sources, or deposition times. The rate of sputter deposition (R_D) was measured *in situ* with the sputter apparatus crystal rate monitor and *ex situ* when extrapolated from the recorded change in sample mass, equivalent to the mass of the film (m_F), and the deposition time (T_D) using **equation 3.1**.

$$R_D = \frac{m_F}{T_D} \quad \text{Equation 3.1}$$

Tests were performed in duplicate to identify the reproducibility of results.

3.3 Material characterisation

3.3.1 X-ray diffraction

X-ray diffraction was used to identify the material composition and relative abundances of crystalline sample phases. XRD was attempted and dismissed for work where the sample is loaded on a silicon wafer as peak positions and intensities were distorted due to saturation of the spectra from silicon underlayer reflections [204].

X-ray diffraction analysis was performed using Thermo ARL Xtra equipment. The source was a copper X-ray tube exciting wavelengths of 1.54056 Å with secondary and tertiary emission at 1.54439 and 1.39222 Å, respectively. Power was set at 45 kV and 40 mA. Acquisition time was set at 3 seconds per 0.01 degrees step across a range from 3 to 80 °. A reference sample of quartz was run to calculate instrumental error. Data was analysed using MAUD [205-207].

3.3.2 Raman spectroscopy

Raman analysis was required to identify the graphitic order of the deposited carbon films in **section 2.4.2**. It was used to assess the purity of the purified nanotubes collected in **section 2.4.3** and was a powerful tool for identifying if graphene was present in the thin film work from **section 2.4.4** [202, 208].

Raman Spectroscopy was performed on a Renishaw inVia Raman Spectrometer. The equipment utilised a 514.5 nm Ar Laser with an output laser power of 1000 nW. Focusing of the laser onto the sample was performed on a microscope stage through a 50 × objective. Resolution was set to 2 cm⁻¹. Spectra were analysed using *OriginPro 8*. Background was subtracted linearly from between 10 and 15 points recognised as not belonging to peaks or troughs in the spectra. Peak positions were identified manually and then refined during the peak fitting process. Peaks were analysed by a mixture of Lorentzian and Gaussian models with a Chi-squared fit control tolerance of 0.05 [208].

To preserve material integrity Raman and XRD analysis were the last analytical techniques performed because they both involve prolonged exposure of the samples to atmosphere and some of the metals (especially cerium) studied were easily oxidised [163].

3.3.3 Transmission Electron Microscopy

TEM was employed to examine particle sizes, distributions and surface morphology. Samples were prepared by sonicating several milligrams of the sample material in acetone for 30 minutes before pipetting a single drop of the suspension onto a carbon grid and allowing the excess solvent to evaporate off [209]. Carbon coated, 3 mm, 200 mesh carbon grids were purchased from *AGAR scientific*.

TEM was performed on a *Jeol JEM-2000 EX* with a maximum magnification of 200,000 \times . The apparatus contains a hairpin W/LaB₆ filament with a DC acceleration voltage operable up to 200 kV providing a lattice resolution of 0.15 nm (line resolution). The equipment was fitted with a 4.2 megapixel bottom mounted DNC camera operated by *AMT software*. Beam saturation, wobbler alignment and focusing were performed manually.

For particle size analysis 20 images of each sample were taken and the width of each particle within each picture was measured at its widest visible point. On average 142 particles widths were measured for each sample. Despite calculation of average particle size using a two dimensional image being an inherently flawed process, as it does not account for z-axis particle measurement and false reading can be provided by particle overlap, it will serve adequately for this experiment and is a common method found within the relevant literature [210]. Due to the intricate coiling of the CNTs analysed, average tube lengths could not be calculated by this method but tube widths could be.

3.3.4 Scanning Electron Microscopy and Energy dispersive X-ray spectroscopy

SEM was used to characterise the size, distribution and morphology of the synthesised powders and films. EDX was used to identify the elemental composition of the synthesised powders and films and establish

the homogeneity of deposited materials across a material surface. Powdered samples were prepared by piling a few micrograms of a sample onto a metal loading plate coated with a sticky resin. The plate was tapped gently on its base to spread and level the sample evenly across the surface. Sputtered samples attached to a silicon substrate were mounted directly onto a thin film holder. Samples usually require coating in thin gold films but due to the predominance of carbon within the samples gold coating was not necessary.

High resolution SEM analysis was performed on a JEOL LSM-6301F spectrometer. Accelerator voltage was set to 5 keV. Topographical images were collected using the apparatus' secondary electron image signal and the SEMaFORE software and edited using ImageJ software. Low resolution SEM and EDX were performed on a JEOL JSM-5900 LV spectrometer. Acceleration voltage was set to 20 keV. Topographical images were collected using the apparatus' secondary electron image signal and the JOEL SEM control user interface V5.26 (2005). Elemental analysis was performed using the apparatus' backscattered electron image signal and INCA microanalysis suite 4.15 (2009).

Cluster size and density were calculated from analysis of top-down SEM images of the films. Cluster boundaries were outlined using *GNU image manipulation software* and the internal size of the clusters was calculated using *ImageJ* software. Cluster density results were collected by counting the number of clusters present in three images, each showing $12.6 \mu\text{m}^2$ of the materials surface, and then averaging the number of clusters present per μm^2 . Film thickness was measured using *imageJ* software and was averaged from at least 50 thickness measurements taken from three different cross-sectional images [209, 210].

3.3.5 Thermovolumetric analysis of material structure

Quantachrome's Autosorb-1 apparatus was utilised to volumetrically characterise the materials surface area, pore shape, total pore volume, and to study the pore size distribution. AS1-win software provided with the apparatus was used to analyse the isothermal data. **Sections 3.3.5.1 to 3.3.5.2** discuss the isothermal models used to characterise the materials.

Method development throughout this study resulted in two different apparatus set-ups for data collection. All samples were outgassed for three hours at 300 °C before loading onto the sample stage. Sample mass, which requires accurate calculation, was measured after analysis so that adsorbed impurities expelled during outgassing did not influence results. Work in **section 2.4.1** relied upon isothermal adsorption of argon at 77 K. For the adsorption curve, 60 data points between 1×10^{-6} and 0.09 P/P₀ were collected for micropore analysis, followed by a further 10 points between 0.1 and 0.99 P/P₀. Desorption points were collected from 10 points between 0.99 and 0.1 P/P₀. An improved set-up was designed and implemented for work in **sections 2.4.2 onwards**. This time isothermal adsorption of nitrogen at 77 K was studied. For the adsorption curve, 60 data points between 1×10^{-6} and 0.09 P/P₀ were collected for micropore analysis, 10 points between 0.1 and 0.3 P/P₀, for improved multi-point Brunauer, Emmett and Teller (BET) calculation, then 15 points to bring the isothermal run up to 0.994 P/P₀. 40 points between 0.994 and 0.1 P/P₀ were collected for the desorption curve.

The analytical precision of the data collected was calculated by repeating each test at least twice, depending upon time constraints. The % variation between experimental or modelled results of each run of each sample was averaged across the 20 samples analysed in **Section 3.4.3**. The mean and standard deviation of variance between the total adsorbed volumes recorded for each run of each sample were 8.43 ± 7.91 %. The reliability of the results expressed for each model is provided in the discussion of each modelling process.

3.3.5.1 Calculating surface area

Multi-point BET analysis was used to study a materials surface area (SA). **Equation 3.2** is the BET equation [211].

$$\frac{1}{W\left[\left(\frac{P_0}{P}\right)-1\right]} = \frac{C_B-1}{W_M C_B} \left(\frac{P}{P_0}\right) + \frac{1}{W_M C_B} \quad \text{Equation 3.2}$$

W is the weight of the adsorbed gas at a relative pressure of P/P_0 , W_M is the weight of a monolayer of the adsorbate across the adsorbent surface, and C_B is the BET constant. W_M can be extrapolated from the slope and intercept of this straight line equation. The ideal region to collect the gradient and intercept is within the pressure range of 0.05-0.35 P/P_0 . Samples surface area (S_S) is calculated from **Equation 3.3**.

$$S_S = \frac{W_M N A_{cs}}{m} \quad \text{Equation 3.3}$$

Where N is Avogadro's number (6.023×10^{23} molecules/mol), and A_{cs} and m are the cross-sectional area and the mass of the adsorbate. The specific surface area of the adsorbent, with units of $m^2 g^{-1}$, is then provided by **Equation 3.4**

$$SA = \frac{S_S}{m_A} \quad \text{Equation 3.4}$$

Where m_A is the mass of the adsorbent. The BET equation is not a measure of SA, rather a measure of adsorption capacity projected into a SA based upon theoretical principle of monolayers adsorption[212, 213]. Adsorption in micropores is believed to occur through micropore filling with multiple points of contact between the adsorbate and the adsorbent. In such a case the BET summation relates to micropore volume yet is depicted, erroneously, as SA. Despite the error, BET results were included for comparative purposes to the literature as such analysis is a widespread inaccuracy within the literature [73, 74, 214-216]. The mean and standard deviation of variance between BET results was $3.97 \pm 3.85 \%$.

3.3.5.2 Calculating total pore volume, average pore radius and pore shape

Total pore volume is derived from the amount of vapour adsorbed when pressure reaches 1 P/P₀ by assuming that all pore spaces are now filled with liquid adsorbate [211]. The volume of the adsorbate (V_{ads}) can be converted into the liquid volume of the adsorbate (V_{liq}) using **Equation 3.5**.

$$V_{liq} = \frac{P_a V_{ads} V_m}{RT} \quad \text{Equation 3.5}$$

Where V_m is the molar volume of the liquid adsorbate and P_a is the ambient pressure. The average pore size (r_{ps}) can be estimated from the pore volume and surface area using **Equation 3.6**.

$$r_{ps} = \frac{2V_{liq}}{SA} \quad \text{Equation 3.6}$$

For pore size distributions of microporous materials the Dubinin-Astakhov (DA) equation was used. The DA equation is a generalised version of the Dubinin-Radushkevich (DR) equation which quantitatively describes the adsorption of sub-critical vapours by microporous (accessible pore radii less than 0.6-0.7 nm) solids [217]. The equation is reliant upon the assumed adsorption process following a micropore filling mechanism [218]. The DR equation is most commonly expressed as;

$$A = -\Delta G = RT \ln \left(\frac{P_0}{P} \right) \quad \text{Equation 3.7}$$

Where A is the adsorption potential, ΔG is the differential free energy of adsorption, R is the ideal gas constant, T is the temperature, P is the pressure at temperature T, and P₀ is the saturated vapour pressure. The adsorption potential is a function of the degree of pore filling (θ), the characteristic energy of adsorption (E_A), and the heterogeneity factor (n) [218]. The DR equation assumes that a materials pore size distribution is Gaussian and n = 2 [219];

$$\theta = \left(\frac{W}{W_0}\right) = \exp\left[-\left(A/E_A\right)^n\right] \quad \text{Equation 3.8}$$

Where W_0 is the total volume of the micropore system, and W is the adsorbed amount. Dubinin and Astakhov realised that most distribution functions in their normalised form are best characterised by two parameters [220]. In the DA equation n is usually in the range of +1 to +3 for carbonaceous materials [221, 222]. By reiteratively calculating the values for E and n for each W value along an isothermal curve, the change in average pore radius (r) as θ increases can be solved:

$$\frac{d(\theta)}{dr} = 3n \left[\frac{K}{E_A}\right]^n r^{-(3n+1)} \exp\left[-\left(\frac{K}{E}\right)^n r^{-3n}\right] \quad \text{Equation 3.9}$$

Where K is the interaction constant (2.96 kJ.nm³mol⁻¹ for N₂; 2.34 kJ.nm³mol⁻¹ for Ar). The mean and standard deviation of variance between micropore volume and mode pore radius results, calculated by the DA method, were 4.32 ±3.85 % and 0.70 ±0.52 %, respectively.

For pore size distributions of mesoporous materials, as will be used in **Section 2.4.3**, the Barrett, Joyner and Halenda (BJH) method was used [221]. It relies upon the assumption of cylindrical pore geometries and can be expressed using a modified version of the Kelvin equation designed specifically for nitrogen adsorption using the following equations.

$$r_p = r_k + t \quad \text{Equation 3.10}$$

$$t = \left(\frac{13.99}{\log\left(\frac{P_0}{P}\right)+0.034}\right)^{1/2} \quad \text{Equation 3.11}$$

$$r_k = \left(\frac{-2\gamma V_m}{RT \ln(P/P_0)}\right) \quad \text{Equation 3.12}$$

Where r_p is the actual pore radius at any given pressure, t is the thickness of the adsorbed layer and r_k is the Kelvin radius of the pore. γ is nitrogen's surface tension at its boiling point (8.85 ergs.cm⁻² at 77 K) and V_m is the molar volume of liquid nitrogen (34.7 cm³mol⁻¹). The specific pore volume (A_p) is calculated from.

$$A_p = \frac{2V_p}{r_p} \quad \text{Equation 3.13}$$

Where V_p is the volume of the pore, extrapolated from each change in volume using:

$$V_{pn} = \left(\frac{r_{pn}}{r_{kn+\Delta t_n/2}} \right)^2 \left(\Delta V_n - \Delta t_n \sum_{j=1}^{n-1} A \left(\frac{\bar{r}_p - t_{\bar{r}}}{\bar{r}_p} \right)_j \right) \quad \text{Equation 3.14}$$

$t_{\bar{r}}$ is the thickness of the adsorbed layer at the average radius interval in the current pressure range. The mean and standard deviation of variance between surface area and pore volume, calculated by the BJH method, were 6.47 ± 4.93 % and 6.12 ± 3.78 %, respectively. Mode pore radius results generated by BJH analysis had a mean variance of 63.83 % so were not relied upon for analysis of a materials structure.

Density functionalised theory (DFT) analysis describes the behaviour of fluids in narrow pores on the molecular level and was performed to analyse the pore widths, pore size distribution and is widely regarded as the most accurate approach for pore filling calculations [211, 223]. The relation between collected isothermal data and computational simulations generated by DFT can be interpreted by the generalised adsorption isotherm equation (GAI):

$$N \left(\frac{P}{P_0} \right) = \int_{Z_{min}}^{Z_{max}} N \left(\frac{P}{P_0}, Z \right) f(Z) dZ \quad \text{Equation 3.15}$$

Where $N(P/P_0)$ is the isothermal data collected experimentally, Z is the pore width, $N((P/P_0)Z)$ is the isotherm on a single pore of width Z and $f(Z)$ is the function of the pore size distribution. GAI assumes an experimental isotherm is made up of individual isothermal events at each discrete pore size multiplied by their relative distribution, $f(Z)$, across the entire range of pore sizes. Pore size distribution is therefore solved numerically through fast non-negative least square algorithms. The mean and standard deviation of variance between pore volume and mode half pore width, calculated by the DFT method, were 8.18 ± 13.04 % and 6.27 ± 4.93 %, respectively.

3.3.6 Thermogravimetric analysis of H₂ and CO₂ storage capacities and material density.

Hydrogen storage capacities were measured gravimetrically using an Intelligent Gravimetric Analyser (IGA) manufactured by HIDEN ISOHEMA LTD. Following buoyancy correction of the raw data collected, storage capacity of the adsorbents, isosteric heat of adsorption, Henry's law constants, the selectivity of adsorbates could be calculated. The importance of these features is discussed in **sections 3.3.6.1, 3.3.6.3, 3.3.6.4 and 3.3.6.5**, respectively. Modelling of experimental data to extract the isosteric heats of adsorption and to calculate the materials selectivity was performed using PASW statistics 18 (2009). The Toth model (**Section 3.3.6.2**) was used and fitted using non-linear regression (NLR) analysis [224, 225]. Quality of fit was assessed using ANOVA R² tests (**Section 3.3.6.6**). Method development throughout this study resulted in an evolution of the data collection method. Modifications to the process improved the accuracy of data collected and the quality of fit between collected data and the isothermal models.

Samples were prepared within a glove box then transferred to the IGA sample hang-down. Time between the removal of the sample from the glove box to completed loading in the IGA with the system pressure down at approximately 5 mbar was less than 14 minutes. This was controlled to limit the potential for oxidation of samples. Following loading, samples were purged for three hours at 300 °C under vacuum before isothermal work commenced. The device switches between H₂, CO₂ and helium (He) streams. H₂ and CO₂ were used for gravimetric analysis of storage capacity. He was used for gravimetric density analysis. Between isothermal runs samples were stored under vacuum. When swapping between the adsorbate gas feeds all gas lines would be purged for five minutes to assure no cross contamination of the lines. High temperature work was performed using the intelligent cryo furnace supplied with the apparatus. Low temperature work was performed by immersing the sample holder in either liquid nitrogen or salted ice-water. To assist the

reduction of the samples temperature to -195 °C, for low temperature H₂ isotherms or helium density checks, He was pumped into the system to a pressure of 30 mbar. Thermal conductance through the He reduced the waiting time for the sample temperature to drop by approximately 30 minutes. Once temperature stability was achieved the He atmosphere was purged from the system at a rate of 180 mbar per minute for 15 minutes to achieve the highest quality vacuum prior to the beginning of experimental analysis. Pressures of 0.01 mbar could be achieved in that time. Whilst longer purging would have improved the vacuum further, after 15 minutes thermal convection from the apparatus would begin to raise the temperature of the sample above -195 °C. Error related to the temperature of the system is within 0.1 °C, Error in pressure calculation was 0.02 mbar below 100 mbar and was 4 mbar between 0.1 and 20 bar. The balance weighing resolution was 0.1 µg [226]. The precision of the data collection process was analysed by comparing 209 equivalent data points collected from repeat analyses of 21 different samples. Values compared spanned the pressure range from 0-20 bar and include both hydrogen and helium isothermal data collected at 77 and 298 K. Variance between the recorded data sets ranged between 0-3.23 % with a median value of 0.0118 %. The mean and standard deviation of the variance was 0.296 ± 0.56 %.

3.3.6.1 Buoyancy correction

The adsorbed capacity is measured gravimetrically from the weight change readings of the IGA balance's sample arm compared to its reference arm. The basic relationship between weight and mass in a vacuum is found using **Equation 3.16**:

$$w_{rec} = m_s g \quad \text{Equation 3.16}$$

Where w is the measured weight, m_s is the mass of the sample, and g is the acceleration due to gravity. As the pressure of the gas in the system increases and an adsorbed phase is formed this expression changes.

$$w_{rec} = (m_s + m_a) g \quad \text{Equation 3.17}$$

Where m_a is the mass of the adsorbed phase. However, other forces present in the system will distort this reading. The most prevalent is known as the buoyancy factor. Archimedes' principle states that there is an up-thrust on an object equivalent to the mass of fluid displaced. Ignoring contributions from the adsorbed phase for the moment, This up-thrust, described as buoyancy (C_b), is calculated from **Equation 3.18**;

$$C_b = m_s g \rho_g / \rho_s \quad \text{Equation 3.18}$$

Where ρ_g and ρ_s are the densities of the displaced gas and the sample, respectively. Buoyancy's contribution to the weight of the sample, w_s , is calculated as:

$$w_s = m_s g - C_b = m_s g - \left(1 - \frac{\rho_g}{\rho_s}\right) \quad \text{Equation 3.19}$$

Removing the buoyancy contribution from the recorded data is achieved by considering buoyancy's influence on not just the sample cell but also the reference cell. When the balance is at equilibrium (forces on either side of the balance are equal):

$$m_s g \left(1 - \frac{\rho_g}{\rho_s}\right) = m_r g \left(1 - \frac{\rho_g}{\rho_r}\right) \quad \text{Equation 3.20}$$

Where m_r and ρ_r are the mass and density of the reference material attached to the reference arm. As the earth's gravitational field can be considered to be equal across both sides of the balance, g can be removed from the expression. Rearranging this equation to calculate the sample mass gives [227]:

$$m_s = m_r \frac{\left(1 - \frac{\rho_g}{\rho_r}\right)}{\left(1 - \frac{\rho_g}{\rho_s}\right)} \quad \text{Equation 3.21}$$

A more comprehensive version of **Equation 3.21** is used by the IGA software to calculate sample mass which also considers weight, density and buoyancy contributions from the sample and reference containers, ballasts and hang-downs.

$$m_s = \frac{\left\{ \phi_D - \phi_u + \sum_{i=1,4} w_i \frac{(\rho_{gi} - \rho_{air})}{(\rho_i - \rho_{air})} - \sum_{j=1,4} w_j \frac{(\rho_{gj} - \rho_{air})}{(\rho_j - \rho_{air})} \right\}}{1 - \left(\frac{\rho_{gs}}{\rho_s} \right)} \quad \text{Equation 3.22}$$

where

$$\phi_D = \sum_{i=1,4} w_i \frac{(\rho_{gi} - \rho_{air})}{(\rho_i - \rho_{air})} - \sum_{j=1,4} w_j \frac{(\rho_{gj} - \rho_{air})}{(\rho_j - \rho_{air})} + m_s \left(1 - \frac{\rho_{gs}}{\rho_s} \right) + \phi_0 \quad \text{Equation 3.23}$$

and

$$\phi_u = \sum_{i=1,4} w_i - \sum_{j=1,4} w_j + \phi_0 \quad \text{Equation 3.24}$$

Where ϕ is the difference in weight between the sample and reference arms of the balance when perfectly balanced before loading (ϕ_0), before the sample is loaded but including the sample container and ballast (ϕ_u), and for a dry sample (ϕ_D) Objects i and j are the individual elements of the sample and counterweight arms. Information on the derivation of these equations can be found in the apparatus user manual [226]. The equation can then be adjusted to contain an expression for the contribution of adsorbed gas and be rearranged to calculate the mass of the adsorbed gas:

$$m_a = \frac{\left\{ \phi_s - \phi_u + \sum_{i=1,4} w_i \frac{(\rho_{gi'} - \rho_{air})}{(\rho_i - \rho_{air})} - \sum_{j=1,4} w_j \frac{(\rho_{gj'} - \rho_{air})}{(\rho_j - \rho_{air})} - m_s \left(1 - \frac{\rho_{gs'}}{\rho_s} \right) \right\}}{1 - \left(\frac{\rho_{gs'}}{\rho_a} \right)} \quad \text{Equation 3.25}$$

Where

$$\phi_s = \sum_{i=1,4} w_i \frac{(\rho_i - \rho_{gi'})}{(\rho_i - \rho_{air})} - \sum_{j=1,4} w_j \frac{(\rho_j - \rho_{gj'})}{(\rho_j - \rho_{air})} + m_s \left(1 - \frac{\rho_{gs'}}{\rho_s} \right) + m_a \left(1 - \frac{\rho_{gs'}}{\rho_a} \right) + \phi_0 \quad \text{Equation 3.26}$$

Where ϕ_s is a change in the weight between the sample and reference arms of the balance following adsorption of a gas on both sides of the balance. Both the uncorrected weight change with pressure and the adsorbed storage capacity, measured in %mass, are automatically provided by the apparatus software upon completion of an isothermal run.

As is apparent from the above equations, accurate buoyancy correction requires an accurate value for the sample density, ρ_s . For experiment 4.1 sample densities provided by the manufacturer were relied upon. In later tests, samples were prepared from raw materials and densities were calculated experimentally using He isotherms (described later) performed on the IGA apparatus.

When calculating density or the sample mass from either **Equation 3.22** or **3.25** there must be no adsorption interaction between the sample and the gas (m_a and $\rho_a = 0$). Sample mass is therefore best calculated under vacuum, to reduce the contribution from adsorbed impurities, and sample densities are calculated from isothermal runs in He, which does not adsorb.

He isothermal points are plotted on a graph of y vs x where

$$y = \phi_s - \phi_u + \sum_{i=1,4} \frac{w_i(\rho_{gi'} - \rho_{air})}{(\rho_i - \rho_{air})} - \sum_{j=1,4} w_j \frac{(\rho_{gj'} - \rho_{air})}{\rho_j - \rho_{air}} - m_s'$$

Equation 3.27

And

$$x = \rho_{gs'}$$

Equation 3.28

The gradient of this graph is $-V_s$, the volume of displaced gas, can be extrapolated from the least squares fitting of the rescaled straight line. This can then be added to a rearranged version of **Equation 3.22** to find a new value of m_s

$$m_s = \phi_D - \phi_u + \sum_{i=1,4} w_i \frac{(\rho_{gi} - \rho_{air})}{(\rho_i - \rho_{air})} - \sum_{j=1,4} w_j \frac{(\rho_{gj} - \rho_{air})}{\rho_j - \rho_{air}} + V_s \rho_{gs}$$

Equation 3.29

From which the sample density can be calculated from

$$\rho_s = m_s / V_s \quad \text{Equation 3.30}$$

A key assumption of this model is that the adsorbed gas phase has a consistent volume and density at a given pressure. This is a safe assumption to make for hydrogen because of its poor adsorption affinity, characterised by its low heat of adsorption. However CO₂'s quadrupole moment, making the oxygen atoms slightly negative and the carbon atom partially positive relative to each other, mean that there may be an increased adsorption affinity between the gas oppositely charged sites on the adsorbents surface. If the surface of the adsorbent was heterogeneous then the adsorbed phase density would vary depending upon the adsorption sites distribution, leading to an inaccuracy in the models assumption and an erroneous reading for m_s . From a review of the literature the extent of this error is considered small and is rarely considered when interpreting results [23, 226, 228, 229].

3.3.6.2 Selection of an isothermal model

The calculation of key features such as the isosteric heat of adsorption, or the adsorption selectivity of an adsorbent is best achieved by modelling best fit curves to experimental isotherm data. Models are beneficial for analysis of experimental data as they are capable of smoothing out inaccurate experimental data and reducing errors in the resulting enthalpy calculations [230]. The choice of model applied to the isotherms is dependent upon the quality of the models fit to the experimental data as well as the range and accuracy of the results expected to be collected from the tests. Whilst there are a number of established isothermal equations to choose from, many struggle to

accurately describe isothermal behaviour as the pressure approaches its limits [231]. Calculation of matching pressure values at equivalent storage capacities from isotherms run at different temperatures was performed by modelling best fit curves from the experimental data, then extrapolating the pressure results.

The DR and DA equations are popular models despite criticism for underestimating adsorption energies at high pressures [231], there are also the Langmuir [232] Toth [230] and Freundlich [233] equations each with their own strengths and weaknesses. Other authors have relied upon simple exponential or linear fits to match the data [234]. Following a trial of modelling isothermal results based upon the DA equation in **Section 3.4.1**, the Toth equation was selected for all future modelling work. The reasons for this selection and a description of the process are outlined below.

The Toth formula is a popular empirical equation for describing heterogeneous adsorbents. It is in essence an expansion of the Langmuir equation with an added parameter C, known as the heterogeneity factor [235]. If the heterogeneity factor reached 1 then the equation matches the Langmuir equation. Its popularity stems from its accuracy at low and high pressures as it approaches the Henry's law limits at the low adsorption levels and the saturation points at high pressures, a feature that neither the Langmuir or Freundlich equations can achieve [231]. The equations ability to predict Henry's law constants is a particular strength of the process [235]. The Toth equation takes the following form [230, 235];

$$W = W_0 \frac{bP}{(1+(bP)^C)^{\frac{1}{C}}} = \frac{mP}{(b+P^C)^{\frac{1}{C}}} \quad \text{Equation 3.31}$$

Where b is referred to as the adsorption affinity and C, as stated is the heterogeneity factor. Using the known factors of W and P, the unknown factors of W_0 , C, m and b can be solved using non-linear regression (NLR) [224, 225]. **Appendix A** contains the Syntax script for running the Toth model. Utilising the Toth equation, the Henry's law constants (K_H) can be found from [235];

$$K_H = \frac{m}{b\bar{c}} \quad \text{Equation 3.32}$$

3.3.6.3 Quality of fit

When modelling isothermal results it is important to assess the quality of the modelled data to the experimental data [235]. Selection of the correct fitting equation is as important as the fitting result. To prevent the generation of inadequate models the fitting equation and the spread of the experimental data modelled needs to be selected based upon the predictions being made. The fitting equations used in this work were the square of residuals (SOR) test (**Equation 3.33**) and the R^2 test (**Equation 3.35**) Which takes the SOR and divides it by the total sum of squares (TSS) (**Equation 3.34**) [235].

$$SOR = \frac{1}{2} \sum (W_{exp} - W_{Mod})^2 \quad \text{Equation 3.33}$$

$$TSS = \frac{1}{2} \sum (W_{exp} - W_{Mean})^2 \quad \text{Equation 3.34}$$

$$R^2 = 1 - \frac{SOR}{TSS} \quad \text{Equation 3.35}$$

Where W_{exp} and W_{mod} are the experimental and modelled storage capacities, respectively. The smaller the SOR the better the quality of fit.

3.3.6.4 The isosteric heat of adsorption

Isosteric heat of adsorption ($-\Delta H_{ads}$) describes the differential change in energy that occurs when an infinitesimally small number of adsorptive molecules are transferred from the bulk gas to an adsorbent surface and form an adsorbed phase [236]. $-\Delta H_{ads}$ can be expressed by the Clausius-Clapeyron equation [214, 231, 234];

$$-\Delta H_{ads} = \Delta H_{vap} + E \left(\ln \frac{1}{\theta} \right)^{1/2} = \left[\left(\ln \frac{P_2}{P_1} \right) \left(\frac{RT_2 T_1}{T_2 - T_1} \right) \right]_W \quad \text{Equation 3.36}$$

Where ΔH_{vap} is the isosteric heat of vaporisation (0.898 kJ mol⁻¹ for H₂, 15.326 kJ mol⁻¹ for CO₂ [237]), T_1 , P_1 , T_2 , and P_2 are the respective temperatures and pressures of isotherms 1 and 2 at equivalent adsorbed quantities (W). The isosteric heat of adsorption is equivalent to the enthalpy of adsorption (ΔH_0). There are two central assumptions to the equation. Firstly, the adsorbent surface area is constant, as is the pressure and temperature of the system. Secondly, the bulk gas phase is considered ideal and the adsorbed phase volume is neglected. These assumptions are considered viable for low pressure calculation but they can lead to overestimation at high pressures, adsorption of heavy adsorbents, and storage capacities in excess of 3 mol.kg⁻¹ [238]. H₂ and CO₂ gases considered in this work are small molecules, and as such the assumptions should not have a significant influence on the adsorption profile. Experimental results for isosteric heats of adsorption tend to be lower than theoretical predicted values due to the levels of accuracy applicable to each process. Experimental results are smaller because they tend to average $-\Delta H_{\text{ads}}$ over a pore width region (say 0.1 nm) whereas there is in effect only one specific pore size with the highest $-\Delta H_{\text{ads}}$ [239]. $-\Delta H_{\text{ads}}$ decreases as W increases suggesting that the most energetically favourable sites for adsorption are occupied first.

3.3.6.5 Henry's law constants

Henry's law describes a pressure region wherein the surface excess adsorption is proportional to the equilibrium pressure [240]. It is found in the low pressure region below 0.15 P_0/P and is characterised by its linear isothermal shape [240, 241]. Classical statistical thermodynamics have shown that Henry's law behaviour exists even at zero loading. Within this region adsorbate-adsorbate interactions are so rare, due to their low concentration that they can be ignored and only the adsorbate-adsorbent interactions are considered. Each adsorbate molecule is allowed to independently explore the entire adsorbate surface and the different

adsorption sites available [222]. The storage capacity in this region is defined by the equation;

$$W = K_H P \quad \text{Equation 3.37}$$

K_H is the Henry's law constant. Within the Henry's law region the isosteric heat of adsorption cannot be measured using the Clausius-Clapeyron equation [239]. Instead the Isosteric heat must be calculated from the Van't Hoff equation [240];

$$-\Delta H_{ads}^0 = RT^2 \left[\frac{d \ln K_H}{dT} \right]_W \quad \text{Equation 3.38}$$

Where $-\Delta H_{ads}^0$ is the isosteric heat of adsorption in the Henry's law region. K_H can be calculated from the extrapolated values from the Toth equation (**Equation 3.31**). Despite their independence, both the Henry's law constant and the isosteric heat of adsorption are quantitatively related to pore width, surface curvature and the number of adsorbate walls/layers strengthening adsorption forces [235] (as discussed in **Section 2.2.2**). Experimentation showed that the heats of adsorption expressed in the results section were calculated at pressures above the Henry's law region so could be calculated by the Clausius-Clapeyron equation.

3.3.6.6 Calculating the selectivity of an adsorbent

Selectivity of an adsorbent for one gas compared to another was calculated by the separation factor $\alpha_{N,M}$ [242, 243].

$$\alpha_{NM} \approx \frac{K_{HN}}{K_{HM}} \quad \text{Equation 3.39}$$

Where K_{HN} and K_{HM} are the Henry's constants for two adsorbates N and M, where N has a greater adsorption affinity. K_H values will be calculated from the Toth modelled data using **Equation 3.31**.

3.4 Experimental procedures

This section describes the actual experimental procedures performed for each study for this thesis.

3.4.1 The activation and chemical doping of activated carbon by mechanical ball milling and its influence on H₂ and CO₂ storage capacity

3.4.1.1 Material synthesis

2 g (1.9997 g) of AC was loaded into a milling vial along with five stainless-steel ball bearings, providing a ball to powder weight ratio of 9:1, and mechanically milled for two hours within an argon atmosphere. Samples were recovered at intervals of 15, 30, 60 and 120 minutes. This process was repeated under analogous conditions, this time doping the 2 g (2.0004 g) of AC with 0.1 g (0.08 g; 5 wt.%) nickel nanoparticles. The oxygen content and temperature within the milling system were recorded as 202 parts per million (ppm) and 294.5 K, respectively. Samples were named according to their material composition and their milling time. For example, the pure activated carbon sample milled for 30 minutes was labelled AC30. The doped sample milled for 120 minutes was labelled ACNi120.

3.4.1.2 Structural analysis

Particle size and morphology data was calculated from TEM analysis as discussed in **Section 3.3.3**. Autosorb-1 apparatus was used to characterise the material porosity and surface area. Isothermal plots of argon adsorption at 77 K were analysed by BET (**Section 3.3.5.1**) and DFT (**Section 3.3.5.2**) techniques.

3.4.1.3 Performance as an adsorbent

H₂ and CO₂ storage capacities were measured gravimetrically (**Section 3.3.6**) across a pressure range of 0 to 10 bar. An approximate sample density of 1.45 g cm⁻³, provided by the AC material data-sheet, was used for all samples. Data points were collected at 1 bar intervals for both adsorption and desorption. Storage capacity was recorded in units of wt.% and mmol.g⁻¹ (conc). Units of wt.% allow the results of this experiment to be compared to the literature, while units of mmol.g⁻¹ allowed direct comparison between the H₂ and CO₂ capacities. Both sets of units were automatically expressed by the apparatus but wt.% can be calculated from mmol.g⁻¹ for H₂ or CO₂ using **Equations 3.40** and **3.41**, respectively.

$$wt.\% = Conc \times 0.2016 + (1 \times 10^{-7}) \quad \text{Equation 3.40}$$

$$wt.\% = Conc \times 4.4009 + (2 \times 10^{-5}) \quad \text{Equation 3.41}$$

Isosteric heat of adsorption was calculated from the Toth model. As these materials were identified as microporous their adsorption potential was calculated from the DA equation (**Equation 3.7**) as their structure matched the requirements of the model.

3.4.2 The influence of nitrogen content and the presence of a metal substrate on the growth and H₂ storage capacity of novel carbon films deposited by magnetron sputtering

3.4.2.1 Material synthesis

3.4.2.1.1 Deposition of CN_x thin films over a SiMgNi substrate

Three magnetrons, loaded with nickel, magnesium and carbon targets, were aligned at a distance of 18 cm from the substrate. The initial pressure of the system was below 4×10^{-10} bar for all experiments. A

magnesium film, deposited at 5.92 W.cm^{-2} DC power, and a nickel film, deposited at 5.92 W.cm^{-2} RF power, were sputtered consecutively onto single crystal silicon <100> wafers in an argon atmosphere (15 sccm; 20 mbar) at a rate of 0.05 nm.s^{-1} for 500 seconds and 90 seconds, respectively. Following this the substrate was heated to $600 \text{ }^\circ\text{C}$ over 10 minutes and left to anneal for 30 minutes under vacuum to break down the nickel and magnesium layers into a nickel nanoparticle spread that could catalyse nanostructural carbon growth. A carbon layer was deposited at 13.32 W.cm^{-2} RF power in a mixed Ar:N₂ atmosphere (16 sccm; 13 mbar) for 4 hours at $600 \text{ }^\circ\text{C}$. The nitrogen content of the sputter gas during deposition was set at 0, 25, 50, 75 and 100 % for the five different sample runs. The carbon deposition rate varied with the nitrogen content of the sputter gas, the significance of the change in sputter rate will be discussed toward the end of **section 4.2.1.1**

Further experiments were run altering the annealing and carbon deposition temperature to 400 or $700 \text{ }^\circ\text{C}$ with a 50 % nitrogen content atmosphere. The effect of sintering temperature on the MgNi layer without carbon deposition was examined at 400 , 600 and $700 \text{ }^\circ\text{C}$. The cool down period took roughly four minutes to drop below $100 \text{ }^\circ\text{C}$.

3.4.2.1.2 Deposition of CN_x thin films over a SiNi substrate

Nickel was deposited at 5.92 W.cm^{-2} RF power onto single crystal silicon <100> wafers in an argon atmosphere (15 sccm; 20 mbar) for 90 seconds. Following this the substrate was heated to $600 \text{ }^\circ\text{C}$ over 10 minutes and left to anneal for 30 minutes under vacuum to break down the nickel layer into a nanoparticle spread to hopefully catalyse carbon nanostructural growth. A carbon layer was then deposited at 13.32 W.cm^{-2} RF power in a mixed Ar:N₂ atmosphere (16 sccm; 13 mbar) for 4 hours at $600 \text{ }^\circ\text{C}$. The nitrogen content of the sputter gas during deposition was set at 0, 25, 50, 75 and 100 % for the five different samples run.

The effect of sintering temperature on the Ni layer without carbon deposition was examined at 600 °C. The cool down period took roughly four minutes to drop below 100 °C.

3.4.2.1.3 Deposition of CN_x thin films over a Si substrate

Single crystal silicon <100> wafers were heated to 600 °C over 10 minutes and left to anneal for 30 minutes under vacuum so that the synthesis parameters were comparable to the two previous sets of tests. A carbon layer was deposited at 13.32 W.cm⁻² RF power in a mixed Ar:N₂ atmosphere (16 sccm; 13 mbar) for 4 hours at 600 °C. The nitrogen content of the sputter gas during deposition was set at 0, 25, 50, 75 and 100 %.

Samples were named after the deposited elements, then the nitrogen gas fraction and the substrate temperature of the carbon deposition step. For example, a carbon sample deposited onto magnesium and nickel layers at 600 °C in a 50 % nitrogen atmosphere was named SiMgNiC50600. Carbon films deposited onto a silicon substrate coated with a nickel layer were collectively referred to as SiNiC films.

3.4.2.1.4 Thin film separation tests

In an attempt to cleave the deposited films from their substrates, SiMgNiC, SiNiC and SiC samples were subjected to a number of different separation techniques to identify the most effective approach for isolation of the carbon foil. Note that deposited layers attached to a substrate are referred to as films but when separated they become foils. Separation approaches included:

Scratch tests; films were cleaved by scraping the surface of the substrate with a scalpel.

Micromechanical cleavage [189]: Collected sample films were coated with sellotape. Careful peeling of the tape at an angle horizontal to the substrate lifted off the foil. The foil was then separated from the tape by immersion in 25 ml pure benzene to dissolve the adhesive. The sample was washed to remove any traces of the tape adhesive by siphoning off then replacing the benzene solvent ten times. Samples were then dried under vacuum at 90 °C for 48 hours.

Acid etching of film/substrate interface [198]: Immersion of the film and substrate in dilute HCl (10 % v/v), dilute nitric acid (HNO₃) (10 % v/v) or 0.5 M acidified iron (III) chloride solution. Additional help to promote cleavage was provided by sonication of the samples for times of 30 minutes, one hour or three hours.

3.4.2.1.5 Mass production of SiMgNiC50400

Following the outcome of structural analysis, separation tests and evaluation of the materials H₂ storage capacities, SiMgNiC50600 was selected for additional testing and was therefore prepared in comparatively larger quantities. The initial pressure of the system was below 4×10^{-10} bar for all experiments. A magnesium film, deposited at 5.92 W.cm⁻² DC power, and a nickel film, deposited at 5.92 W.cm⁻² RF power, were sputtered consecutively onto three 1 cm² single crystal <100> silicon wafers in an argon atmosphere (15 sccm; 20 mbar) for 500 seconds and 90 seconds, respectively. Following this the substrate was heated to 400 °C over 10 minutes and left to anneal for 30 minutes under vacuum. A carbon layer was deposited at 13.32 W.cm⁻² RF power in a mixed Ar:N₂ atmosphere (8:8 sccm Ar:N₂ ratio; 13 mbar) for 4 hours at 400 °C. The process was repeated 16 times.

3.4.2.1.6 Thin film separation, purification and collection

CN_x films were cleaved from the substrates using a 0.5 M acidified iron (III) chloride solution [198]. Silicon wafers were floated on the surface of the solution which would consume the magnesium and nickel layers. The cleaved carbon foil would float on the surface of the solution and could be transferred to another vial for washing. The foils were washed in purified water until the pH of the system was restored to 6.6 (the pH of the water) to quench the formation of metal hydroxides on the foils. The recovered materials were dried under vacuum for 48 hours at 120 °C.

3.4.2.2 Material characterisation

The ordered carbon fraction of the deposited films was assessed by Raman analysis as discussed in **Section 3.3.2**. XRD analysis of the samples was attempted but abandoned because peak positions and intensities were being distorted by saturation of the spectra from silicon substrate reflections [204].

High Resolution SEM was used to characterise the cluster size, thickness, distribution and morphology of the synthesised films using the methods described in **Section 3.3.4**. Low resolution SEM and EDX quantified the elemental composition of the synthesised films and establish the homogeneity of deposited materials across the surface. TEM analysis examined the microstructure of the deposited layers.

Porosity and surface area analysis could not be performed for most samples as the silicon wafers would not fit within the volumetric analyser. Nitrogen isotherms at 77 K were performed as directed in **Section 3.3.5** to analyse the separated films. Characterisation was performed using BET (**Section 3.3.5.1**), DFT (**Section 3.3.5.2**) and BHJ (**Section 3.3.5.1**) analysis.

3.4.2.3 Performance as an adsorbent

H₂ storage capacity of the carbonaceous films was performed gravimetrically (**Section 3.3.6**) still mounted onto the silicon substrates. Due to the low mass of the samples and the excess weight contributed from the silicon substrate accurate calculation of sample density was required. Density calculation was performed using the apparatus software assessing the isothermal gradient of a material with no interaction with the adsorbent surface. Helium isotherms from 100 to 600 mbar were performed at 77 K to calculate the sample density. Sample density was a key consideration when correcting buoyancy error in the hydrogenation isotherms. H₂ isotherms were run from 0 to 10 bar at either 77 or 298 K with a variability of ± 1 °C and an abundance of data points collected in the low pressure range below 100 mbar. The gravimetric storage capacities of the mass produced MgNiC50400 foil was tested at 298 and 273 K for CO₂ and at 77, 298 and 273 K for H₂. The isosteric heats of adsorption for all samples tested were modelled using the Toth equation. For the mass produced foil, the Toth equation was also used as the basis for the selectivity analysis.

3.4.3 A study of magnetron sputtering as a means to chemically dope carbon nanotubes with cerium and nickel and its influence on H₂ storage capacity

3.4.3.1 Material synthesis

3.4.3.1.1 Purification of CNTs

The method for purification followed the process laid down by Zhou *et al.* [244]. RCNT powder (5 g) and HNO₃ solution (100 ml; 0.7 mol.L⁻¹) were loaded into a 200 ml three-necked bottle with a condenser and a stirrer. The suspension was heated and continuously stirred at 353 K for 6 h to dissolve the Ni-MgO catalyst [244]. Once the solution had cooled the sample was filtered using Buchner apparatus. The purified CNTs were washed with deionized water until their pH value returned to neutral. The washed sample was dried at 393 K under vacuum for 48 hours. The recovered mass of purified CNTs (PCNTs) was 4.5893g.

3.4.3.1.2 Powder sputtering of lone metals

PCNT powder (0.1 g) was loaded within an inert environment onto a circular sample holder with a surface area of 5.31 cm². The sample was levelled and evenly distributed across the area with the assistance of a cylindrical disk of equal proportions to the sample holder. The initial pressure of the system was reduced to below 4 × 10⁻¹⁰ bar for all experiments. Nickel and cerium targets were aligned at a distance of 18 cm from the substrate. Deposition was performed in an argon atmosphere (15 sccm; 20 mbar). Nickel coated CNT samples were prepared by deposition at 11.84 W.cm⁻² RF power at a rate of 7.04 × 10⁻⁰⁷ g.cm⁻²s⁻¹. Cerium coated CNT samples were prepared by deposition at 5.92 W.cm⁻² RF power at a rate of 5.3 × 10⁻⁰⁷ g.cm⁻²s⁻¹. Initially, 5 samples with varying loadings were prepared for each material.

Nickel was deposited at 1, 0.5, 0.1, 0.05 and 0.01 mol.g⁻¹ of CNT. Cerium was deposited at 0.5, 0.4, 0.3, 0.2 and 0.1 mol.g⁻¹ of CNT. Based upon the outcomes of these initial tests further cerium samples were prepared at 0.025, 0.05, 0.075, 0.125, 0.15 and 0.25 mol.g⁻¹ of CNT. Samples were named after the molar percentage of the deposited mass. For example CNTs coated with 0.1 mol.g⁻¹ of cerium were named CNTCe0.1.

3.4.3.1.3 Mixed metal powder sputtering

Final tests were performed sputtering both metals simultaneously. Limitations of the apparatus and unforeseen side-effects of the sputter process (as will be discussed in **Section 4.3.1.2**) meant that the deposition process needed to be altered for the combined tests. Nickel and cerium were deposited at 7.59 W.cm⁻² RF power at a rate of 5.45 × 10⁻⁷ g.cm⁻²s⁻¹, and 8.88 W.cm⁻² DC power at a rate of 1.86 × 10⁻⁶ g.cm⁻²s⁻¹, respectively. Deposition was performed in five minute bursts until the deposition process was complete. *i.e.* the deposited mass of dopant should have reached the target concentration. Samples were loaded with a Ce:Ni ratio of 0.1:0.07, 0.25:0.18 and 0.5:0.35 mol.g⁻¹ of CNT.

3.4.3.2 Material characterisation

The ordered carbon fraction of the raw, pure and doped CNTs was assessed by Raman analysis as discussed in **Section 3.3.2**. X-ray diffraction was used to analyse the performance of the purification step and to assess the crystallinity of the deposited cerium and nickel films as discussed in **Section 3.3.1**. CNT width, dopant thickness and the morphology of both structures was assessed by TEM analysis as discussed in **Section 3.3.3**. Volumetric analysis was used to characterise the material porosity and surface area as discussed in **Section 3.3.5**. Isothermal plots of N₂ adsorption at 77 K were analysed by BET (**Section**

3.3.5.1), DFT (**Section 3.3.5.2**), BHJ (**Section 3.3.5.3**) and DA (**Section 3.3.5.4**) techniques.

3.4.3.3 Performance as an adsorbent

H₂ storage capacity of the doped CNTs was performed gravimetrically (**Section 3.3.6**). Helium density checks were performed by running isotherms from 0-600 mbar at 77 K. H₂ isotherms were run from 0-20 bar at either 77 or 298 K with a variability of ± 1 °C and an abundance of data points collected in the low pressure range below 100 mbar. The Toth equation was used for modelling the isosteric heats of adsorption and was also used as the basis for the selectivity analysis tests performed on just the PCNT sample. Selectivity of PCNT was assessed by running an additional H₂ isotherm at 273 K as well as performing two CO₂ isotherms from 0-20 bar, one at 298 K, the other at 273 K.

3.4.4 Exploring the synthesis of graphene by magnetron sputtering

3.4.4.1 Material synthesis

3.4.4.1.1 Sputter deposition of the nickel catalysed graphene films.

Nickel and copper targets were aligned at a distance of 18 cm from the substrate. Deposition tests were not performed until a system base pressure of 1.33×10^{-9} bar was achieved to ensure a reasonable system purity. In the nickel tests, nickel layers were deposited onto single crystal Si (III) wafers at 11.84 W.cm^{-2} RF power in an Ar atmosphere (15 sccm; 20 mbar) and at 25 °C at a rate of 0.158 nm.s^{-1} for 31 minutes to generate a 300 nm thick layer. The substrates were heated to 800 °C over 15 minutes under vacuum. Carbon was then deposited at 13.32 W.cm^{-2} RF power in an Ar atmosphere (15 sccm; 13 mbar) for 30, 60, 120 and

180 seconds still at 800 °C. Cooling the substrates back to ambient temperatures took a further 15 minutes under vacuum. Cooling at the fastest rate that could be achieved, as oppose to designing a more gradual cooling profile, was designed to limit the precipitation time for FLG or graphite formation.

3.4.4.1.2 Sputter deposition of the copper catalysed graphene films

In the copper tests, Cu was deposited onto single crystal Si (III) wafers at 10.36 W.cm^{-2} DC power at a rate of 0.364 nm.s^{-1} in an Ar atmosphere (15 sccm; 20 mbar) at 25 °C for 46 minutes to generate a 500 nm thick layer. The substrates were heated to 800 °C over 15 minutes under vacuum. Carbon was then deposited onto the CuSi substrate for 10, 20, 30, 60, 120, 180 and 240 seconds still at 800 °C. Metal layers that were not coated with carbon were also studied to try and ascertain the topography of their surface. Samples were named based upon their metal layer, the letter “G” to indicate that this was a graphene tests and then the deposition time. For example, a carbon film deposited for 10 seconds on a copper layer was called CuG10.

3.4.4.2 Material characterisation

Raman and High resolution SEM analysis were used to characterise the grown carbon films still bound to their substrate and identify if graphene was present [195, 201]. If the carbon structure could not be resolved at the SEM apparatus' maximum magnification, then the presence of graphene wrinkles could be used to indirectly identify its presence (**Section 2.4.4**). XRD is commonly used for characterising crystallinity but was not attempted in this work because spectra were known to be distorted by reflections from the silicon substrate [204].

CHAPTER 4: RESULTS AND DISCUSSION

4.1 The activation and chemical doping of activated carbon by mechanical ball milling and its influence on H₂ and CO₂ storage capacity

This section discusses the influence of ball milling and compositional doping on the H₂ and CO₂ storage capacities of activated carbons. The background to this work is presented in **Section 2.4.1** and the experimental process is described in **Section 3.4.1**. Samples were named according to their composition and milling time. A list of sample names and compositions is presented in **Appendix B**.

4.1.1 Material characterisation

4.1.1.1 TEM analysis

TEM analysis was performed to identify trends in average particle size. **Figure 4.1.1D** shows that prolonged milling decreases the mean and median particle sizes.

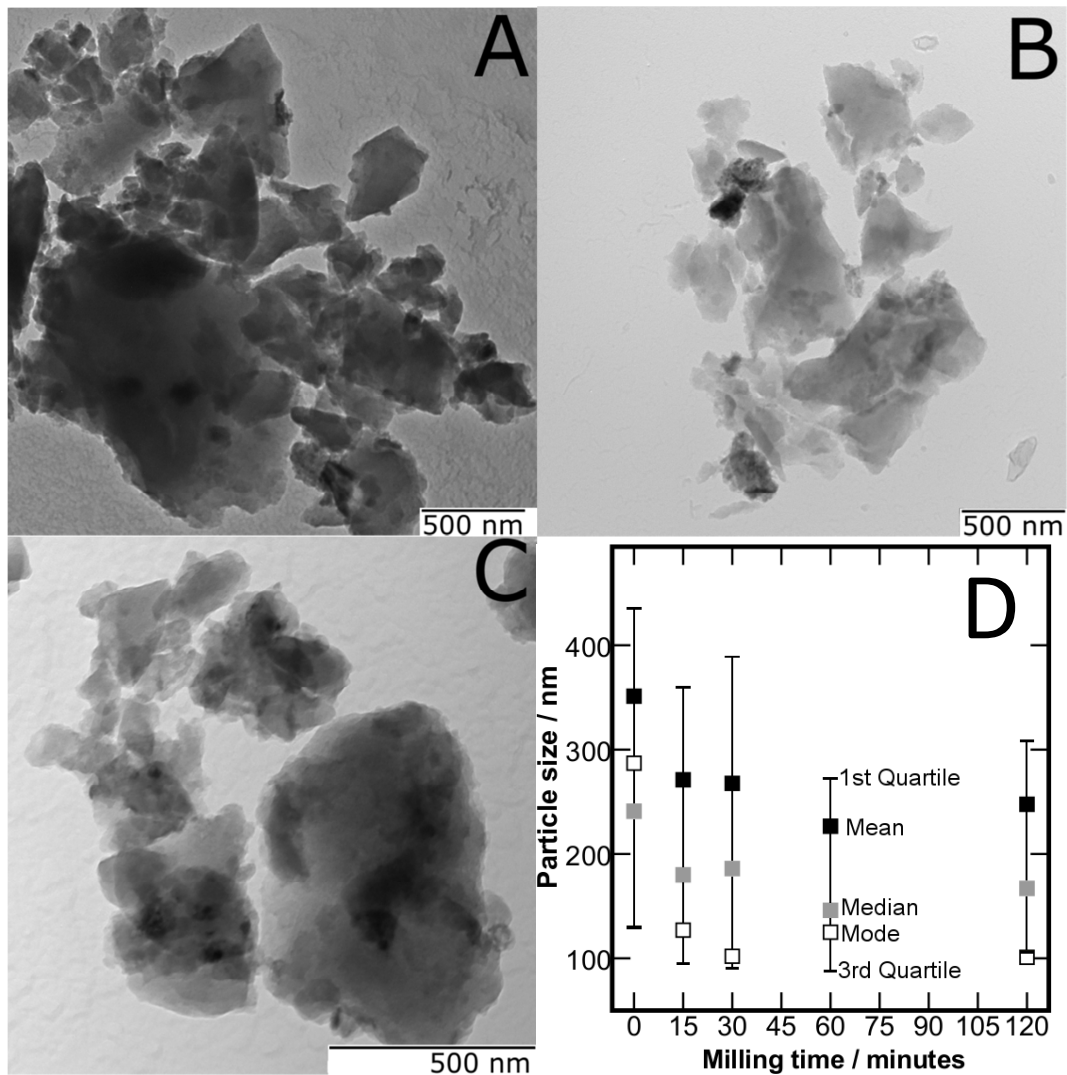


Figure 4.1.1. TEM images showing the influence of ball milling upon AC particle size: A) unmilled AC; B) AC milled for 15 minutes; C) AC milled for 30 minutes; D) Effect of milling time (minutes) on the particle size (nm) of ACs based upon TEM analysis.

The steady decrease in interquartile range shown in **Figure 4.1.1D** suggest that as the average particle size decreases the spread of particle sizes decrease with it. Milled ACNi samples had smaller particle sizes compared to the milled AC samples. This result is likely due of the addition of nickel nanoparticles which had a smaller average particle size than the AC, dropping the average due to fractional concentration. However, the nickel could be acting as an additional grinding agent, assisting the pulverisation of the activated carbon and reducing the AC particle size.

4.1.1.2 Micropore analysis

Isothermal plots collected for all samples analysed in argon at 77 K resembled the plot in **Figure 4.1.2A**. The isothermal curves most closely resemble a type IV isotherm (**Figure 4.1.2B**), characteristic of capillary condensation in mesopores [223, 245]. Different sections of the curve are understood to represent uptake over a mixed range of pore sizes: micropores are responsible for the initial rapid uptake of the molecules at relatively low pressures (below $0.1 P/P_0$), meso- and macro- pores are filled gradually as the pressure increases further. The type IV characteristics may be due to the creation of meso-/macro- pores among fine powder particles, or as discussed below may be an artefact of the experimental design. [223].

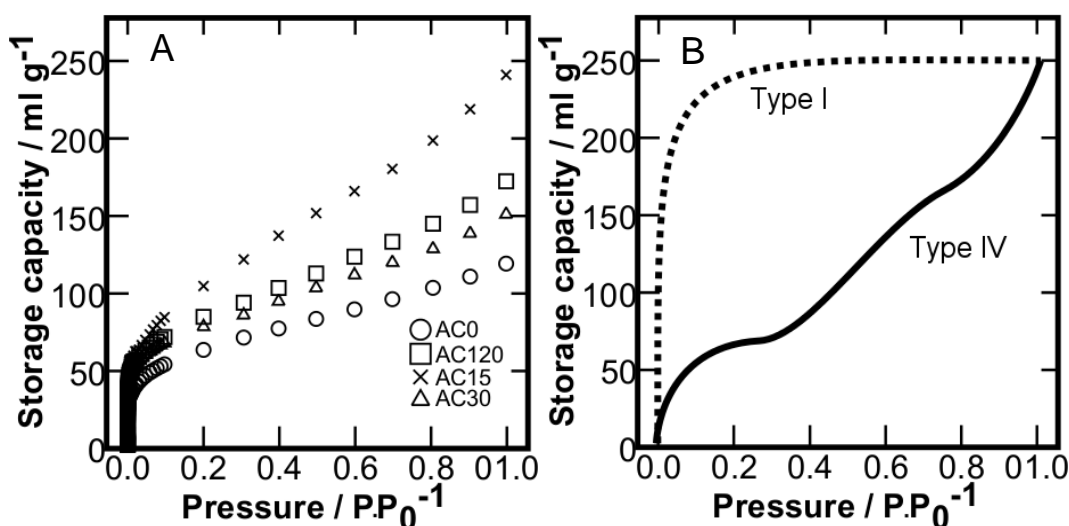


Figure 4.1.2. A) Isothermal plot of argon adsorption at 77 K for three ball milled AC samples and unmilled AC; B) Comparison of ideal isothermal shapes.

A likely cause for this discrepancy was the experimental set-up. Isotherms looking to characterise porosity tend to run at a temperature equivalent to the adsorbents boiling temperature (N_2 at 77 K, Ar at 87 K). Our set-up for this experiment used argon at 77 K as it was believed at the point of testing that this would be a valid approach for pore size analysis. According to the literature the pore size distribution data collected from this set-up remains valid for micropore and lower mesopore analysis of

carbonaceous materials (0.35 to 40 nm)[223] but is insufficient for characterisation in the meso- and macro-porous range because at 77 K argon is below its triple point (87 K) and it's bulk reference state cannot be evaluated [246]. Following discovery of the models insufficiencies we evaluated the collected data against the information we wanted to collect and decided that sufficient information for our needs could be accurately reported. The BET surface area for the as-purchased AC material agreed with the material specifications, and the data collected in the microporous adsorption region (the region we wished to explore) is considered valid within the literature.

To resolve the discrepancies regarding porosity, the collected isothermal data was analysed using BET and DFT equations. Whilst the theoretical principles of these equations apply directly to macroporous adsorption they are considered applicable for microporous applications [151, 212]. **Figure 4.1.3** compares the total surface areas, predicted by BET analysis, and the total pore volumes, predicted by DFT analysis of the samples normalised by the contribution of carbon. Normalisation was performed by calculating the dopants contribution to the total surface area and mass of the sample (**Equations 4.1 and 4.2**), then then subtracting that contribution from the samples surface area and mass (**Equation 4.3 and 4.4**) to recalculate carbons surface area (**Equation 4.5**) The specific surface area (SSA) of the nickel nanopowder was take to be $50 \text{ m}^2\text{g}^{-1}$ according to the material data sheet.

$$Dopant\ mass = \frac{Sample\ mass}{100} \times dopant\ mass\ fraction \quad \text{Equation 4.1}$$

$$Dopant\ SA = dopant\ mass \times dopant\ SSA \quad \text{Equation 4.2}$$

$$Adsorbent\ mass = total\ mass - dopant\ mass \quad \text{Equation 4.3}$$

$$Adsorbent\ SA = sample\ S\ SA \times sample\ mass - Dopant\ SA \quad \text{Equation 4.3}$$

$$Adsorbent\ SSA = \frac{Adsorbent\ SA}{Adsorbent\ mass} \quad \text{Equation 4.5}$$

The normalised SSA of the nickel doped carbon samples was approximately $7 \text{ m}^2\text{g}^{-1}$ larger than the actual recorded sample sizes. The minor change in SSA before and after normalisation can be attributed to nickel's low mass fraction within the sample. It is worth noting that no approach could be found that considers modification of the nickel powder's surface area during milling. Pore volume could not be normalised as an approximation of the nickel's porosity could not be found. Also, given the dopant's minor contribution to the SSA, it seems unlikely to have had a more significant influence on porosity. Fitting error for DFT results was less than 3.123 % for all samples, the BET model, based upon a linear equation, fitted to the experimental data between 0.05 and 0.35 P/P_0 (the usual collection range) with an R^2 value exceeding 0.99 for each sample [211].

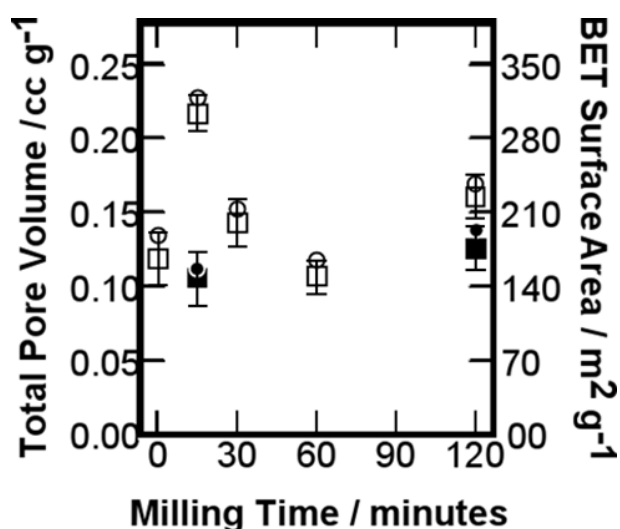


Figure 4.1.3. Effects of milling time (minutes) upon the pore volume (ml.g^{-1}) and surface area (m^2g^{-1}) of ACs. Key: (□) Pore volume of pure ACs; (○) Surface area of pure ACs; (■) Pore volume of ACNi samples; (●) Surface area of ACNi samples. Error analysis for BET data collected from four experimental runs. Pore volume error was overlooked during experimentation.

Figure 4.1.3 shows that ball milling increased the pore volumes and surface areas of the ACs. **Figure 4.1.3** also shows that Ni doped samples have lower pore volumes and surface areas after 15 and 120 minutes

milling, compared to their pure AC equivalents, because of these reduced pore volumes intermediate samples were not analysed. Decreased pore volumes for doped samples stem from dopant nanoparticles blocking newly formed pore spaces [96]. Take for example ACNi120. Before milling the material can be imagined as AC with a low pore volume and a heterogeneous mix of Ni nanoparticle aggregates. Two hours of milling will have increased the AC pore volume, as it did with AC120, however the nickel nanoparticle aggregates will have dispersed and agglomerated within or across AC pores. Nickel and the AC particles are physically compacted together so binding strength between the two materials is dependent upon the extent of physical contact between the two particles, rather than chemical bonding [143]. Strongest binding will have occurred in crooks and crevices of the AC particle that provide multiple points of contact between the two materials. Should a nickel particle be physically deposited across a pore opening then the pore volume behind the particle cannot be accessed by adsorptive gases [247]. Blockage of pore volumes in this manner will increase the amount of “dead space” adsorbent molecules cannot penetrate into and adsorb onto, subsequently reducing the pore volume of the material. DFT pore size distributions for all the samples are shown in **Figure 4.1.4**. Peak intensities (and overall pore size data) are calculated from the rate of change of adsorbed volume with increasing pressure (as shown in an isothermal plot **Figure 4.1.2A**). According to the DFT model, adsorption occurs preferentially on the strongest binding sites first (the smallest pores). Between each pair of isothermal data points an average pore size across that volume change can be calculated [248].

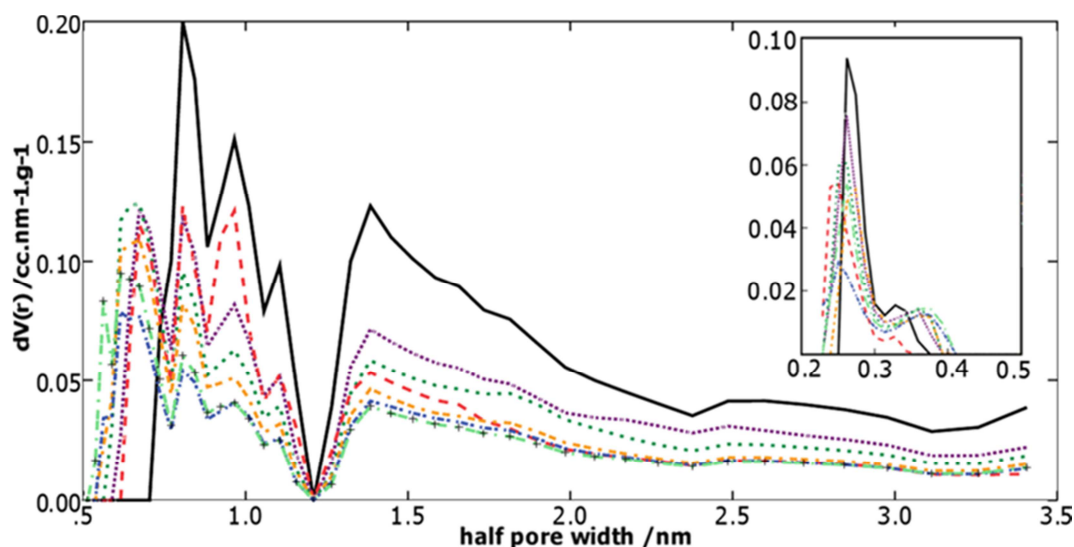


Figure 4.1.4. Effect of milling time on the half pore width (nm) of ACs in terms of pore volume ($\text{cc.nm}^{-1}\text{g}^{-1}$) calculated using the DFT equation. Key: (Red dashed line) AC0; (black solid line) AC15; (Emerald dotted line) AC30; (Lime green dash-dash-dot line) AC60; (purple dotted line) AC120; (Blue dot-dash line) ACNi15; (Orange dot-dash-dash line) ACNi120. The insert provides a magnified view of the values between 0.2 and 0.5 nm half pore width.

Results indicate the mode pore width of the samples was below 1 nm, identifying the materials as microporous [249]. These results, combined with the material specifications provided by the suppliers and further data discussed in **Section 4.1.2.4** suggest that despite the argon isotherms type IV shape, the materials do possess a large amount of micropores. Mesopores may have been created among the AC powder particles.

Figure 4.1.4 also identifies that milling for longer than 30 minutes decreases the % pore volume of pores with a half pore width between 0.88 and 1.25 nm, increases the pore volume between 0.24 and 0.6 nm, and has little effect upon the micropore volume above 1.75 nm. After milling for 15 minutes the mode half pore width had increased from 0.251 to 0.262 nm. Despite further milling altering the distribution of pore volumes (**Figure 4.1.4**) the mode half pore width remained constant (**Figure 4.1.5**).

Whilst pore volume determines the theoretical maximum storage capacity of microporous physical adsorbents, the pore diameter dictates the experimental storage capacity [73]. Ideal pore diameters allow for multiple points of contact increasing the binding energy between the adsorbent and adsorbate [72]. The centre of wide pores, where the adsorbent is within the pore but not in contact with the adsorbate, is considered to be “dead space”. Similarly, when pores get too narrow to fit an adsorbate molecule their excess volume is also referred to as “dead space. Different adsorbate molecules will occupy pores of different widths based upon their molecular diameter [67]. This leads to discrepancies between the recorded pore volumes of a material measured by two adsorbates of different molecular sizes. The radii of H₂ and CO₂ molecules, and argon atoms are 0.240, 0.330 and 0.336 nm, respectively [250, 251]. As argon is a larger molecule than H₂, the contribution to total pore volume for pores sized between 0.240 and 0.336 nm cannot be resolved and the definitive pore volume for H₂ storage cannot be reported. However change in pore diameter results can be used to characterise trends in H₂ adsorption. **Figure 4.1.5** combines and contrasts the key outcomes of both the TEM and volumetric analyses of the pure AC samples. Experimentally it has been commonly observed that there is good correlation between the N₂ BET surface areas or Ar BET surface areas and hydrogen storage capacity, However, As discussed previously, the Chanine rule (**Section 2.2.2**) states that increasing pore volumes within pore regions smaller than 0.7 nm will outperform this correlation due to increased adsorption strengths within these pores.

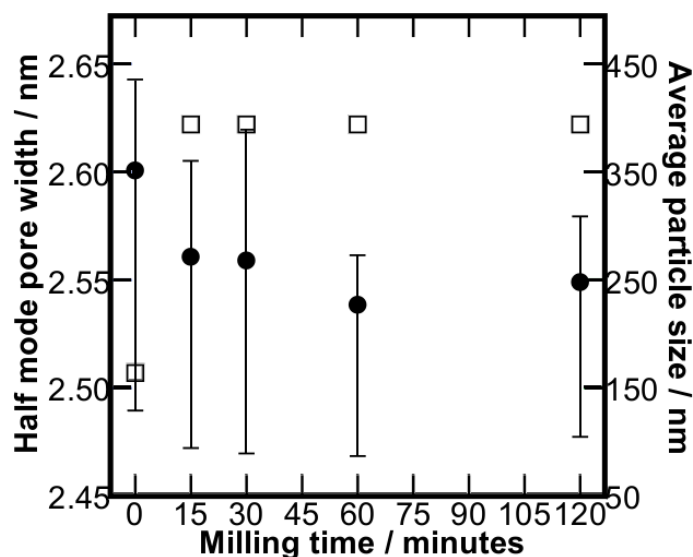


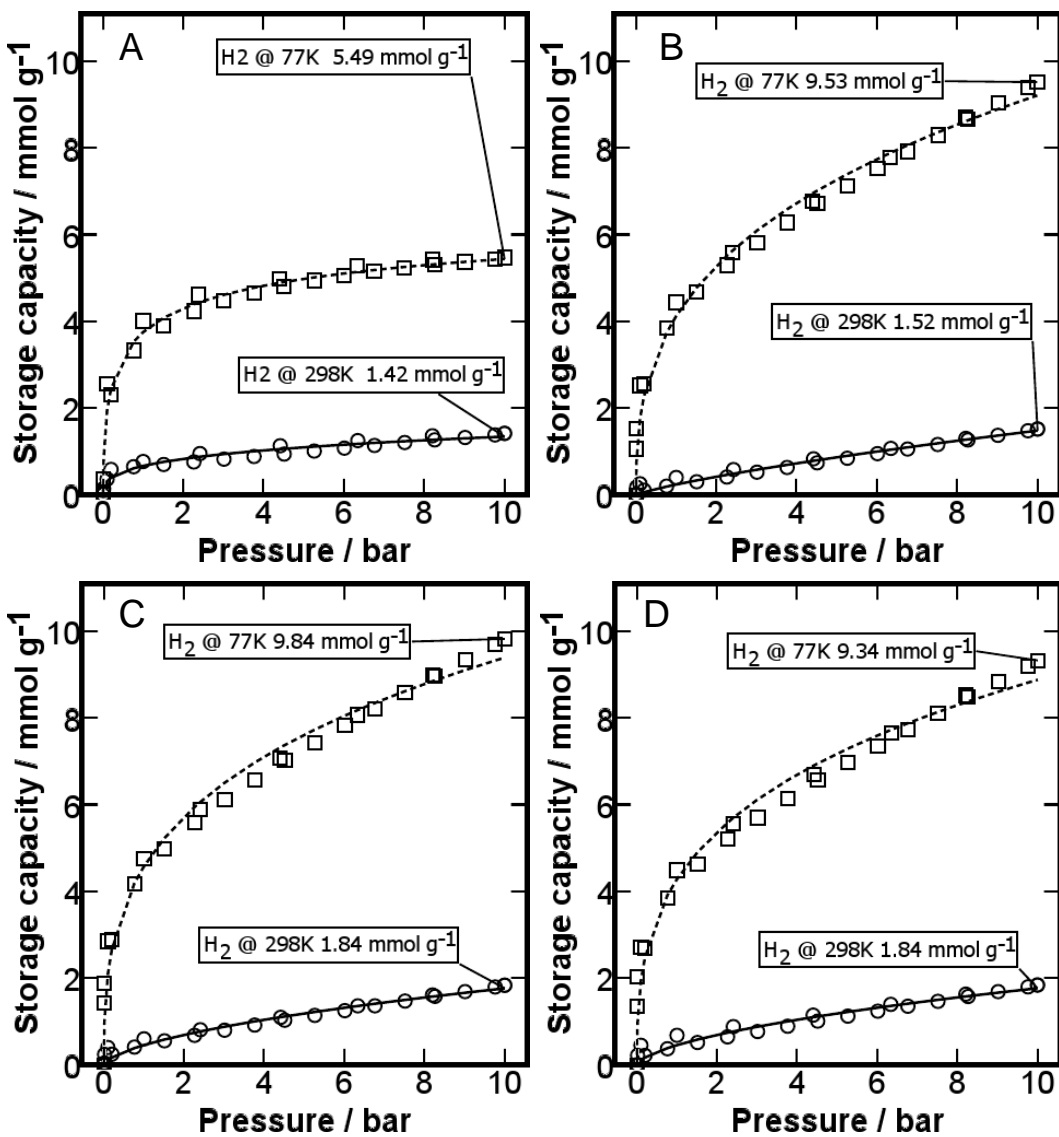
Figure 4.1.5: Variation in pore diameter (nm) and particle size (nm) with milling time (minutes) of Pure AC samples. Key: (□) mode half pore width; (●) average particle width. Error bars based upon standard deviation of particle size measurements.

Concurrent evaluation of the two trends in **Figure 4.1.5** suggest that prolonged milling increases the pore volume by breaking apart larger particles, creating new surfaces and opening up previously sealed pores. However, ball milling does not seem to change the mode half pore width at the micro-/meso- scale. There are two possible explanations for this lack of change in pore size. Firstly, the mode half pore width may be characteristic of the impact intensity of the milling process. As the ball to powder ratio and the milling speed were nearly identical in all samples their influences on the AC material will have been similar. A change in either the powder to ball ratio or milling speed may induce a greater variation in the mode half pore width. Secondly, the mode half pore width may be characteristic of the actual AC material and the milling process serves only to open or block these pore spaces, as seen by the changes in particle size (**Figure 4.1.5**) and pore size distributions (**Figure 4.1.4**). If the mode half pore width was characteristic of the AC material then increasing the milling speed or powder to ball ratio would not influence the mode half pore width results. The results and conclusions drawn about the

effects of ball milling on carbonaceous materials are supported by the literature [75, 96, 252].

4.1.2 Hydrogen storage capacities of ball milled AC

Figure 4.1.6 displays the isothermal results for H₂ uptake of the milled and doped ACs. The lines of best fit are the modelled approximation of the combined adsorption and desorption data using the Toth model (**Section 3.3.6.2**). The quality of the models fit will be discussed further in **section 4.1.2.2**.



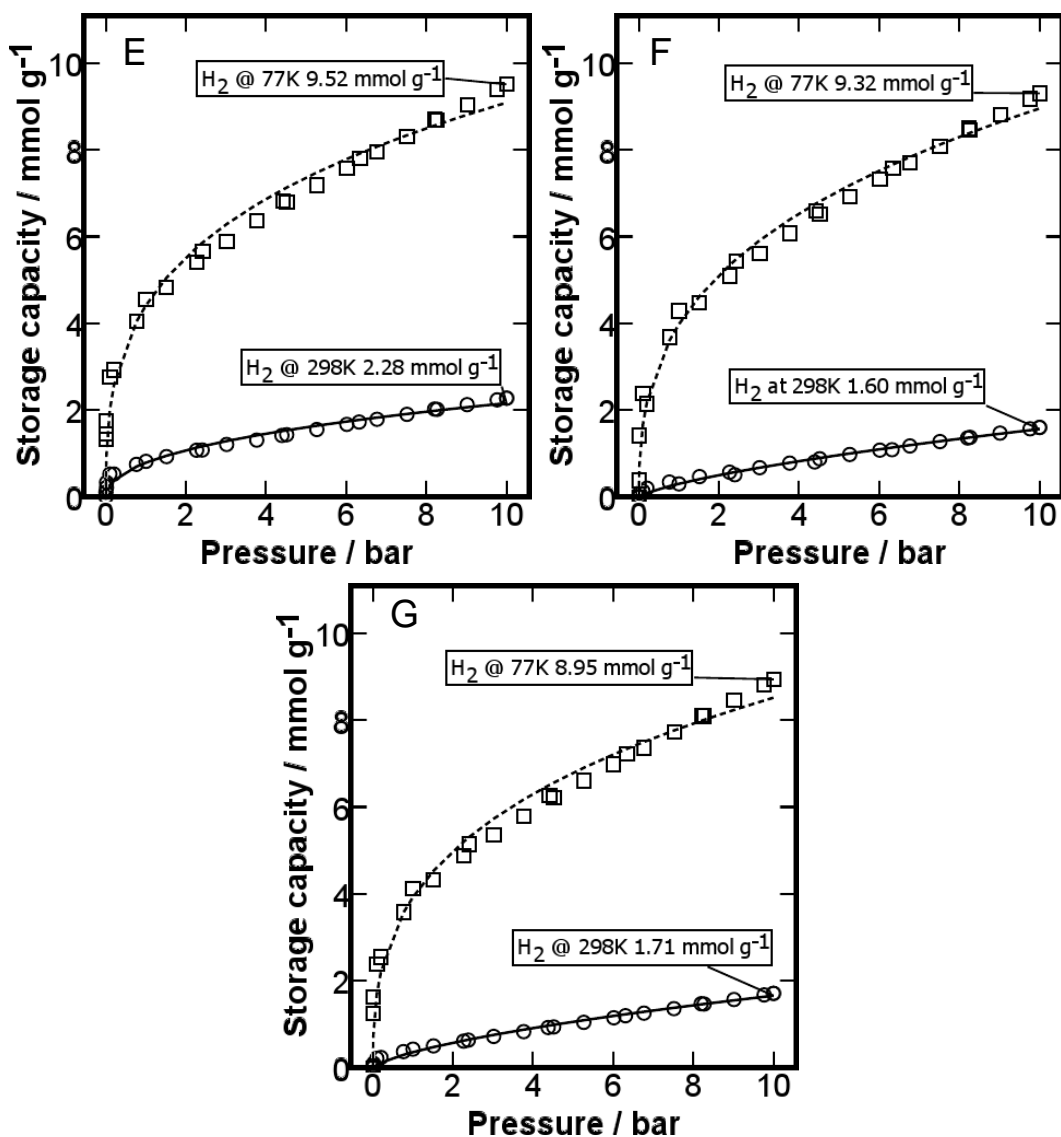


Figure 4.1.6. Isothermal H₂ storage capacities (mmol.g⁻¹) of pure and doped ACs milled for varying lengths of time from 0 to 10 bar at 77 and 298 K. A) AC0; B) A15; C) AC30; D) AC60; E) AC120; F) ACNi15; G) ACNi120. Key: (□) isotherm at 77 K; (○) isotherm at 298 K; (dashed line) Toth model at 77 K; (solid line) Toth model at 298 K.

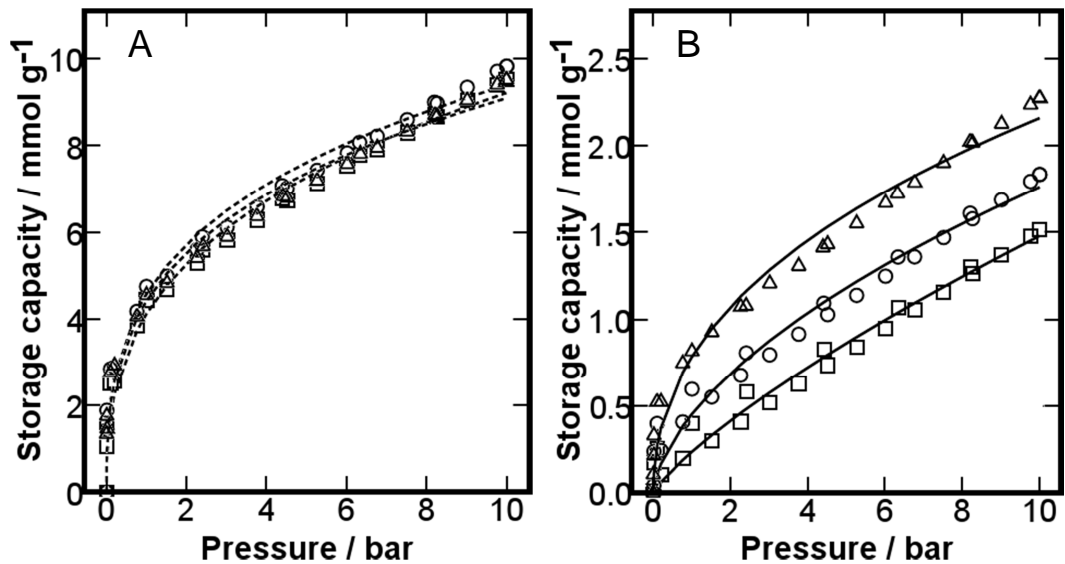


Figure 4.1.7. Composite graphs for the comparison of H₂ storage capacity (mmol.g⁻¹) with pressure (bar) of different milled samples at either 77 (A) or 298 K (B). Key; (□)AC15; (○) AC30; (Δ) AC120. (dashed line) Toth model at 77 K; (solid line) Toth model at 298 K.

At 10 bar, the highest H₂ storage capacities achieved at 77 and 298 K were 9.84 mmol.g⁻¹ (1.98 wt.%) for AC30, and 2.28 mmol.g⁻¹ (0.46 wt.%) for AC120, respectively. For all the milled samples, the gradients of the H₂ isotherms remain steep even at high pressures and do not plateau suggesting that even at 10 bar the maximum H₂ storage capacity has not been achieved. AC0, the unmilled sample, is approaching its plateau, which means that its maximum H₂ storage capacity is almost reached by 10 bar. The increase in the maximum storage capacity of the materials shows that milling has been an effective activation process for improving the total storage capacity of the AC material.

The behaviour of the isothermal results in **Figures 4.1.6** and **4.1.7** can be used to further characterise the AC materials and draw conclusions about the adsorption process. The surface sites with the strongest binding affinities adsorb gas at the lowest pressures, therefore the steeper the gradient of an isotherm, the greater the proportion of strong adsorption sites [245]. This is exemplified in (**Figure 4.1.7B**), comparing the isotherms for AC15, AC30 and AC120 at 298 K, where a longer period of

milling causes steeper isothermal gradients in the low pressure region below 1 bar. Comparing all samples from this study at 298 K and below 1 bar, AC0 and AC120 possessed the steepest gradients, and as such, the highest propensity of sites ideally suited for H₂ adsorption at 298 K. Strength of binding relates to pore width thanks to chelative adsorption from overlapping potential fields [72, 253]. Therefore samples AC0 and AC120 must contain an increased fractional volume of pores that bind strongly with H₂ compared to the other samples. From DFT pore size distribution analysis (**Figure 4.1.4**), the range of pore widths that fit this description, and likely promote hydrogen adsorption at 298 K, are between 0.60 to 0.90 nm, as AC0 and AC120 have a larger pore volume in this region than the other samples.

At 77 K (**Figure 4.1.7A**) there was little to no variation between the gradients of all samples in the low pressure region identifying that the range of pore sizes able to adsorb H₂ at low pressure increases with decreasing temperature. The near identical nature of the low pressure isothermal gradients at 77 K indicate that the influences of milling on H₂ binding strength were marginal, compared to the beneficial influence of lowering the temperature. There is a significant increase in the H₂ storage capacity between the unmilled (**Figure 4.1.6A**) and milled ACs (**Figures 4.1.6B-G**) at 77 K. This shows that whilst lowering system temperature is more effective at increasing the actual H₂ storage capacity, by reducing the energy difference between the gaseous and adsorbed H₂, milling is more effective at maximising the total adsorption capacity by modifying the structure of the adsorbent [249, 254]. All the milled samples adsorb near equivalent quantities of H₂ (**Figures 4.1.6B-G**) regardless of the disparity in their total pore volumes (**Figure 4.1.3**). DFT results for AC30 and AC60, the milled samples with the lowest pore volumes, had the largest cumulative pore volume for the pore width range between 0.37 and 0.69 nm (**Figure 4.1.4**). H₂ must adsorb favourably within this region to allow the H₂ storage capacities of these materials to remain comparative to the other samples. The literature has identified the region between 0.37 to 0.69 nm as important for H₂ adsorption [38, 87, 253, 255].

Comparison of the H₂ storage capacities at 10 bar is provided in **Figure 4.1.8**. H₂ storage capacity increased significantly at low temperatures. The unmilled AC had the lowest H₂ storage capacity at both temperatures.

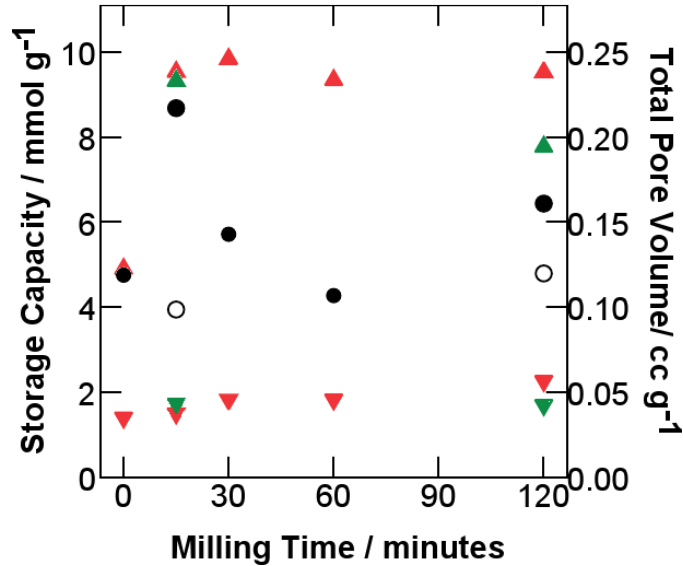


Figure 4.1.8. Effect of milling time (minutes) upon the pore volume (ml.g⁻¹) and H₂ storage capacity at 10 bar (mmol.g⁻¹) of ACs. Key: (▲) Storage Capacity of pure ACs at 77 K; (▼) Storage Capacity of pure ACs at 298 K; (▲) Storage Capacity of doped ACs at 77 K; (▼) Storage Capacity of doped ACs at 298 K; (●) Total pore volume of Pure ACs; (○) Total pore volume of doped ACs.

Milling caused significant changes in the pore volume of the materials but only a minor increase, of 0.86 mmol.g⁻¹, in the H₂ storage capacity at 298 K. The H₂ storage capacity at 10 bar was not seen to vary proportionally with the pore volume of the samples. This means that much of the additional surface generated by milling does not easily adsorb hydrogen at 298 K. This point is exemplified by sample AC30 possessing the lowest pore volume of the pure milled materials yet the highest storage capacity at 77 K and AC15 having the largest total pore volume yet its performance as an adsorbent was smaller than that of AC30 at 77 K. Using the DFT fractional pore volume data (**Figure 4.1.4**), regions where

AC30's volumes exceed AC15's volumes are pore widths likely to be better suited for H₂ adsorption.

Isotherms run at 77 K displayed a huge increase in storage capacity following 15 minutes milling which was not present in the runs at 298 K (**Figure 4.1.8**). These results mean that milling generates new surfaces with H₂ affinities too weak to adsorb H₂ at 298 K but strong enough to adsorb H₂ at 77 K. As milling time increases, 30 minutes or more, there is a continuous increase in storage capacities observed at 298 K, with a range of 0.76 mmol.g⁻¹, but an almost constant storage capacity at 77 K. These results mean that variation in pore sizes promoted by prolonged milling do not result in the generation of new pore volumes that strongly adsorb H₂, as evidenced by the similarity in H₂ storage capacity at 77 K, rather they alter the pore sizes of pores that already store H₂ at 77 K, increasing their H₂ binding affinity thus prompting the increase in H₂ storage at 298 K but not 77 K. These two observations combined agree with the above conclusion, that whilst the mode pore width remains constant, the IQR of pore sizes is narrowing.

Figure 4.1.8 shows that the storage capacities of the doped ACs were lower than for the pure ACs. As such, only the doped samples milled for 15 and 120 minutes were analysed for their H₂ storage capacities. The reduced capacity is presumed to be related to the decreased pore volumes of the samples. As the adsorption potential of H₂ is low its most likely site for adsorption is within pores where it can chelate with several adsorbate surfaces [72, 73]. A severely reduced pore volume, caused by Ni nanoparticles blocking pore entrances would limit the storage capacity of the material. Another contributing factor when the results are expressed per mass of material is the increased weight of the adsorbent thanks to the introduction of a comparatively heavy metal [74, 256]. Of the isotherms performed at 298 K, no comparative increase in the adsorption gradient at low pressures for either doped sample compared to their undoped counterparts suggests that the spillover effect either did not occur or was of less benefit than the blockage of pore volumes was detrimental.

An alternative assessment of the Ni dopants performance looks to quantify the H₂ storage capacity (mmol.g⁻¹) of the material in terms of its pore volume (ml) and is shown in **Table 4.1.1**. Some articles characterising the H₂ storage capacity of compositionally doped adsorbents have used such data to assert that doped materials, with small pore volumes outperform pure samples with larger pore volumes due to their increased storage capacity in terms of mmol.g⁻¹ per ml of total pore volume (or cm² of total surface area) [46, 101, 257].

Table 4.1.1. Comparison of the hydrogen storage capacities per ml of doped and pure AC samples.

Material	Total pore volume (ml.g ⁻¹)	H ₂ capacity per ml pore volume at 298 K (mmol.g ⁻¹ ml ⁻¹)	H ₂ capacity per ml pore volume at 77 K (mmol.g ⁻¹ ml ⁻¹)
Pure AC	0.12	21.79	75.47
AC15	0.22	6.77	42.54
AC30	0.14	22.95	122.94
AC60	0.11	18.79	95.29
AC120	0.16	16.03	67.08
ACNi15	0.10	16.67	97.05
ACNi120	0.12	18.60	84.47

Results from this study would suggest that in this case, and in the case of some of the examples in the literature, this is a misleading conclusion. The discussion in the above section identifies that the pore volumes of specific pore width were responsible for strong adsorptive binding, not the total pore volume [73]. Therefore relying upon the total pore volume to quantify nickels action as an adsorbent catalyst, as seen in **Table 4.1.1**, fails to accurately isolate and determine nickel's influence leading to false conclusions.

For example, in this test AC15 has the lowest performance of all samples (**Table 4.1.1**), doped or pure, due to its large total pore volume but limited individual pore volume in regions that effectively adsorb H₂. ACNi15's increased storage capacity compared to AC15 cannot be solely attributed to nickel's catalytic adsorption effect. It must also be attributed to factors including the reduction in pore volume caused by nickel blocking pore openings. When comparing two samples with similar pore volumes (AC60 to ACNi15 or ACNi120 in **Table 4.1.1**) the storage capacities are almost identical. These results indicate that the Ni dopant has no significant beneficial effect upon the storage capacity and that regulation of pore width is a more influential factor for maximising storage capacity.

4.1.2.1 Calculation of adsorption energy

To quantify the above conclusions, the adsorption potential (A) between the AC and H₂ was calculated from a modified version of the DR (**Equation 3.7**) [218]. The adsorption potential was plotted against the storage capacity of the adsorbent. **Figure 4.1.9** shows the adsorption potential, extrapolated from the DR equation, for all the pure milled samples at 298 and 77 K.

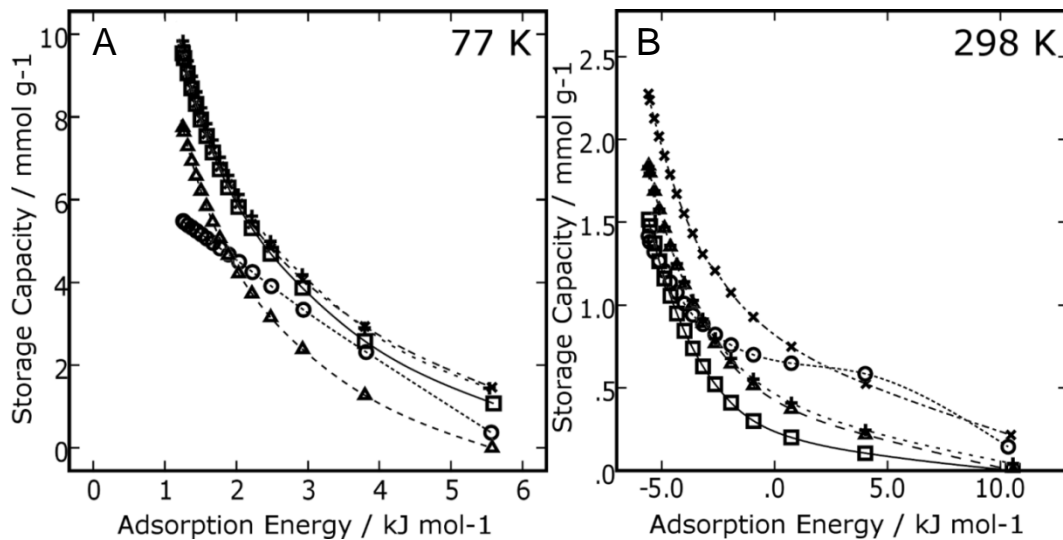


Figure 4.1.9. Variation in the adsorption potential ($\text{kJ}\cdot\text{mol}^{-1}$) of milled AC samples with changes in H_2 storage capacity ($\text{mmol}\cdot\text{g}^{-1}$) at 77 (A) or 298 K (B). Key: (\circ , dotted line) AC0; (\square , solid line) AC15; ($+$, narrow dashed line) AC30; (Δ , dashed line) AC60; (\times , dash dot line) AC120.

Results indicate that strength of binding between the adsorbate and the adsorbent are strongest at very low storage capacities. As the adsorbed volume increases the overall adsorption energy decreases because strong binding sites are filled forcing adsorbates to adsorb with weaker surfaces. In **Figure 4.1.9B**, at high storage capacities adsorption energies become negative, suggesting that adsorption has become energetically unfavourable and for the storage capacity to increase additional energy, to offset the deficit, must be added. Typically this additional energy would be supplied as either added pressure or a reduction in temperature. As the adsorption potential at 77 K (**Figure 4.1.9A**) does not become negative within the recorded storage capacity range of the test it would suggest that a significant increase in the amount of gas adsorbed could be accommodated before the adsorption process became unfavourable.

The maximum adsorption energy values recorded in the graphs are higher at 298 K ($10 \text{ kJ}\cdot\text{mol}^{-1}$) than at 77 K ($6 \text{ kJ}\cdot\text{mol}^{-1}$). This is due to the range of storage capacities collected, not the thermodynamics of the system and does not mean stronger binding at high temperatures. Storage

capacities below 1 mmol.g^{-1} were not collected at 77 K because these H_2 loadings had already been exceeded by the first pressure point recorded in the isothermal run. Comparing the adsorption energies of the materials at different temperatures but the same storage capacities, the energy of adsorption is far lower for the plots at 298 K. The adsorption potential energies for these materials are in keeping with the literature [87, 101, 214].

As previously observed in **Figure 4.1.7**, there is a difference between the isothermal trends for AC0 and AC120 compared to AC15, AC30 and AC60 at 298 K in the low pressure region. The adsorption energy results support this conclusion with the adsorption energies of AC0 and AC120 exceeding those of AC15, AC30 and AC60 at all storage capacities below 0.75 mmol.g^{-1} (**Figure 4.1.9B**). The reason for this improved binding can again be attributed to the distribution of pore volume between specific pore diameters. AC0 and AC120 have a greater fractional pore volume in pores with half pore widths of 0.70 to 0.84 nm than the other samples (**Figure 4.1.4**). Their improved adsorption energies in **Figure 4.1.9B** would suggest that this pore range is suited for adsorption at 298 K. Fractional pore volumes for pore widths between 0.37 to 0.69 nm, thought to improve adsorption capacity at 77 K (as discussed above), are highest in samples AC30 and AC60. AC30's and AC60's adsorption energies at 298 K (**Figure 4.1.9B**) are amongst the lowest suggesting that pore within this range are too wide for strong adsorptive binding at 298 K.

4.1.2.2 Calculation of the heat of adsorption

Heat of adsorption was calculated from the Clausius-Clapeyron relation (**Equation 3.36**) with data points extrapolated from Toth models (**Equation 3.31**) of the experimental results [81, 212, 234]. The correlation of the models fit to the experimental results (R^2 value) was greater than

0.963 for all samples and can be seen as the line of best fit in all isothermal plots (**Figure 4.1.6**).

The variation between the temperatures of isotherms used to calculate the heat of adsorption are usually only 10 K apart, in this case they were 221 K apart [234]. The closer the temperatures of the systems the more similar the shape of the isotherms and the better the ensuing fit. Larger temperature differences do not appear to compromise the mathematical procedure they simply require more complicated analysis to make the isothermal data comparable.

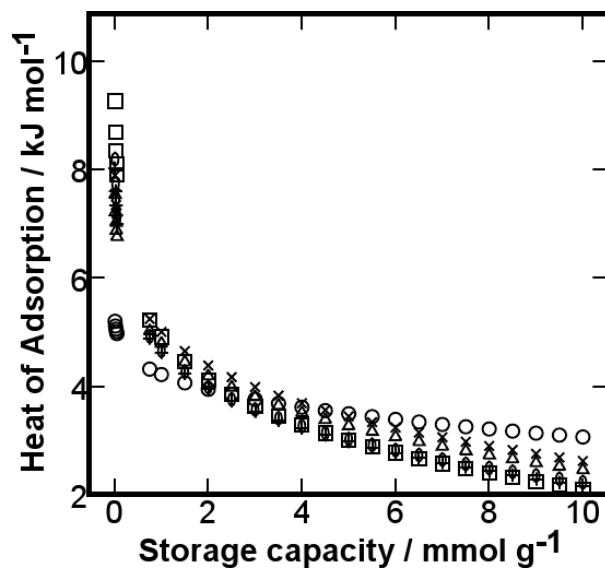


Figure 4.1.10. Variation in adsorption enthalpy (kJ mol^{-1}) with H_2 storage capacity (mmol.g^{-1}). Key: (\square) AC15; (\times) AC30; (Δ) AC60; (\circ) AC120; (\circ) ACNi15; ($+$) ACNi120.

Results for the isosteric heats of adsorption shown in **Figure 4.1.10** are in keeping with the literature and show that the heat of adsorption drops to an almost negligible value as the storage capacity increases, as would be expected for a physical adsorbent [101, 234]. The results also show that the highest heats of adsorption ($8\text{-}10 \text{ kJ.mol}^{-1}$ at low storage capacities) belong to the samples milled for only a short length of time.

4.1.2.3 Theoretical maximum storage capacities

Assuming that a H₂ molecule takes up a volume area of 4.52×10^{-20} m² and the mode of H₂ adsorption is monolayer coverage (as the kinetic energy of a hydrogen atom is such it is not expected to be able to form multi-layers) then the theoretical maximum H₂ storage capacities according to the volumetric isothermal results are provided in **Table 4.2.1**. Whilst the BET process is itself based upon a multilayer formation process, the derived BET surface area comes from a calculation of the number of surface adsorption sites multiplied by the volume area of N₂ giving the monolayer surface area of the sample. Assuming the material to be nonporous or macroporous the theoretical H₂ capacity should exceed the storage capacities recorded at 10 bar as it depicts the maximum surface area available for adsorption.

Table 4.1.2. Comparison of the theoretical H₂ storage capacity (assuming complete monolayer coverage) against the recorded H₂ storage capacities at 10 bar and 77 or 298 K

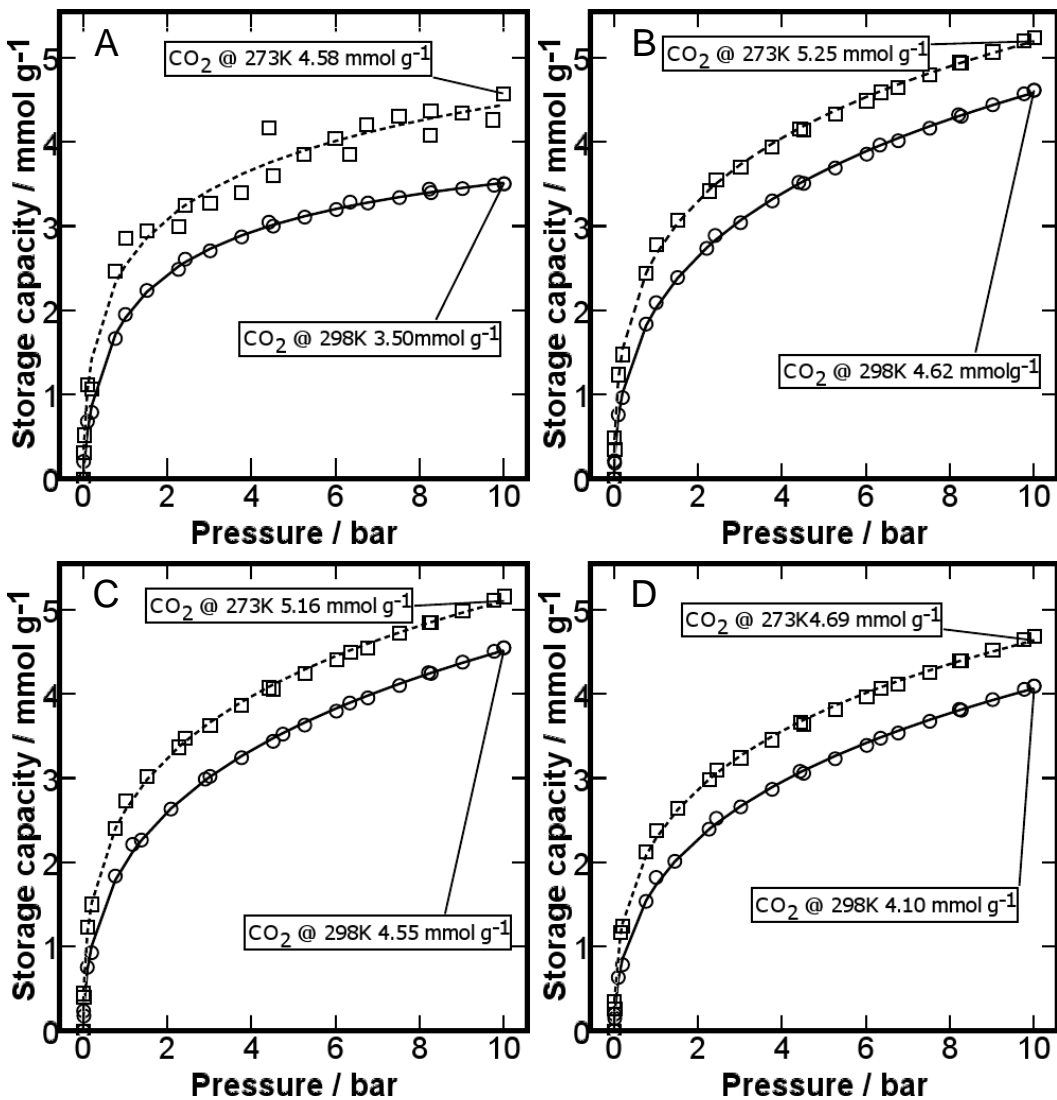
Material	BET Surface area (m ² .g ⁻¹)	Theoretical H ₂ storage capacity (mmol.g ⁻¹)	H ₂ storage capacity at 77 K (mmol.g ⁻¹)	H ₂ storage capacity at 298 K (mmol.g ⁻¹)
Pure AC	188	6.92	4.91	1.42
AC15	319	11.70	9.53	1.52
AC30	213	7.84	9.84	1.84
AC60	165	6.07	9.34	1.84
AC120	237	8.72	9.53	2.28
ACNi15	147	5.39	9.32	1.60
ACNi120	185	6.81	7.77	1.71

It is apparent that the materials actual H₂ storage capacity far exceeds the theoretical capacity for complete monolayer coverage. This finding further supports the hypothesis that adsorption is occurring through

a method other than monolayer formation, most likely micropore filling, adding further credence to the material being predominantly microporous.

4.1.3 Carbon Dioxide Storage Capacities of ball milled AC

Having considered H₂ adsorption, the CO₂ adsorption capacity of the milled samples was also considered. **Figure 4.12** shows the CO₂ storage capacities of the AC materials from 0-10 bar at 273 and 298 K.



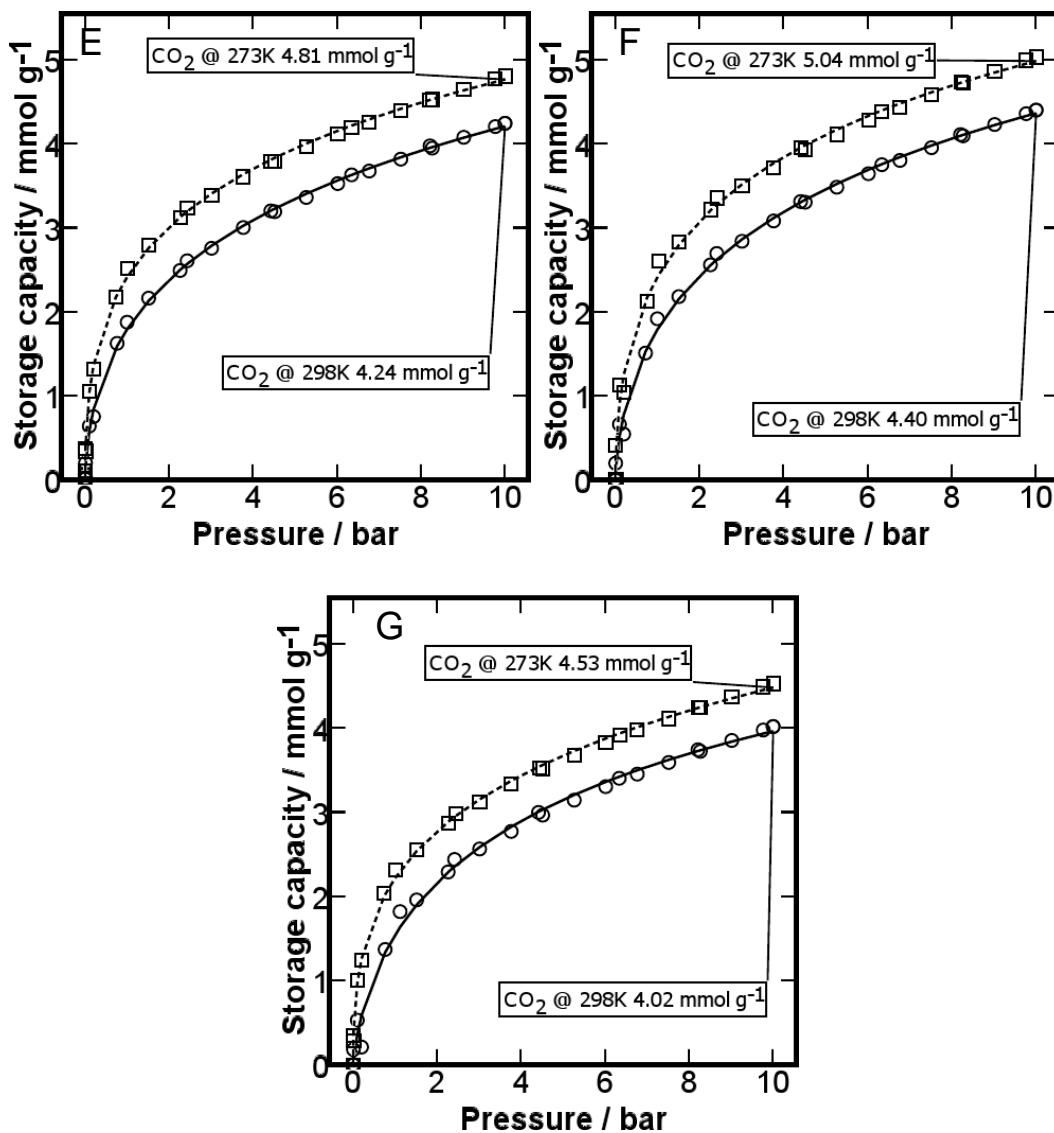


Figure 4.1.11. Isothermal CO₂ storage capacities (mmol.g⁻¹) of pure and doped ACs milled for varying lengths of times from 0 to 10 bar pressure at 273 K and 298 K. A) AC0; B) A15; C) AC30; D) AC60; E) AC120; F) ACNi15; G) ACNi120. Key: (□) isotherm at 273 K; (○) isotherm at 298 K; (dashed line) Toth model at 273 K; (solid line) Toth model at 298 K.

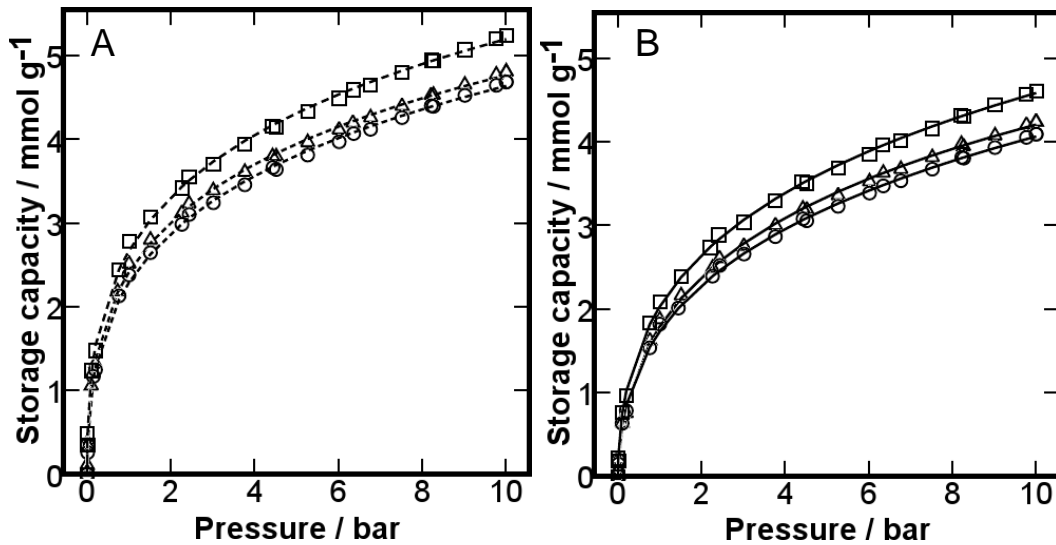


Figure 4.1.12. Composite graphs for the comparison of CO₂ storage capacity (mmol.g⁻¹) with pressure (bar) of different milled samples at either 273 (A) or 298 K (B). Key: (□) AC15; (○) AC60; (Δ) AC120; (dashed line) Toth model at 273 K; (solid line) Toth model at 298 K.

There will be a slight inaccuracy in the recorded storage capacities collected for CO₂ adsorption. The error is intrinsic to thermogravimetric analysis of CO₂, its derivation, based upon buoyancy calculation, was discussed in **Section 3.6.6.1**. AC15 recorded the highest CO₂ storage capacities at 10 bar of 5.25 mmol.g⁻¹ (23.09 wt.%) at 273 K, and 4.62 mmol.g⁻¹ (20.31 wt.%) at 298 K. The isothermal results in **Figures 4.1.11** and **4.1.12** can again be used to better quantify the adsorption process. Unlike the H₂ results, there was no clear jump in performance with milling. The isothermal gradient at low pressures were similar for all samples suggesting that the milling process did not increase the propensity of pores ideally suited for adsorbing CO₂. The variation in isothermal gradients becomes more pronounced above 1 bar suggesting that any variation in storage capacity for the samples was the result of formation of surfaces that weakly bind to CO₂.

Milling samples for 15 minutes greatly increased the storage capacity at 298 K but had only a limited effect on the storage capacity at 273 K (**Figure 4.1.11B**). Any surface that adsorbs at 298 K should also adsorb at 273 K as adsorption at 273 K is a lower energy process. This

disproportionate change in adsorption capacity at the two temperatures suggests that milling for 15 minutes generated new pore surfaces that adsorb strongly with CO₂ at both 273 and 298 K at the expense of pores that bound strongly with CO₂ only at 273 K. It is inconclusive whether the new pores that adsorb well at 298 K were generated from the modification of the pores that adsorbed well at 273 K or whether the new, strong binding surfaces were generated concurrently with the destruction of pores good for adsorption at 273 K [249].

These conclusions can be expanded upon by closer analysis of the isothermal trends of the two materials at both temperatures (**Figures 4.1.11A and 4.1.11B**). Change between the isothermal gradients of AC0 and AC15 begins at about 0.75 bar at both temperatures. As the isothermal gradient at low pressures serves as a measure of the binding strength between the adsorbent and the adsorbate this implies that 15 minutes milling has not increased the fraction of the strongest binding pore surfaces for CO₂ adsorption. Above 0.75 bar the gradient of the AC0 samples drops off compared to the AC15 samples. Isothermal variation in this mid pressure region shows that the new surfaces generated by ball milling bind with an intermediate strength to the CO₂. Above 4.5 bar the variation in gradient between the AC0 and AC15 isotherms at 273 K becomes constant whilst at 298 K the variation between gradients grows ever wider. The increased widening of gradients at this point relates to an increase in the volume of surfaces with an attraction to CO₂ at 298 K. The lack of a corresponding change in gradient at 273 K shows that these surfaces have been created at the expense of surfaces that already bound CO₂ at 273 K.

Comparison of the CO₂ storage capacities at 10 bar for both temperatures, along with the variation in total pore volume with milling time are provided in **Figure 4.1.13**.

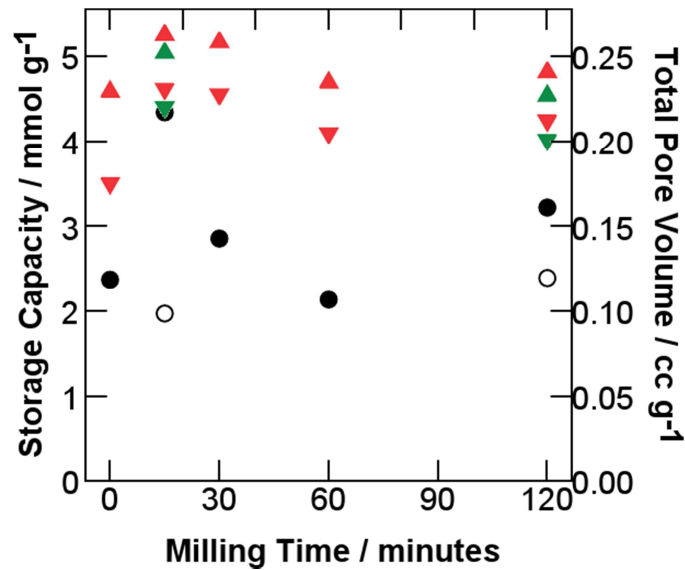


Figure 4.1.13. Effect of milling time (minutes) upon the CO₂ storage capacity (mmol.g⁻¹) and pore volume (ml.g⁻¹) of ACs. (▲) Storage Capacity of pure ACs at 273 K; (▼) Storage Capacity of pure ACs at 298 K; (▲) Storage Capacity of doped ACs at 273 K; (▼) Storage Capacity of doped ACs at 298 K; (●) Total pore volume of Pure ACs; (○) Total pore volume of doped ACs.

In all cases the milling process did increase the CO₂ storage capacity. CO₂ storage capacity was highest in the low temperature samples. Unmilled AC had the lowest capacity at both temperatures at 10 bar. Despite variation in the proportionalities, the trends in storage capacity at 10 bar for CO₂ adsorption mimic the trend for total pore volume.

The similarity in the trend of the samples storage capacities at 10 bar and 273 K and to the storage capacities at 10 bar and 298 K, after 15 minutes milling (**Figure 4.1.13**), suggests that further milling generates new surfaces for adsorption at both 298 and 273 K. Formation of pores that adsorb CO₂ exclusively at 273 K or modification of surfaces that already adsorbed CO₂ at 273 K to adsorb at 298 K would have led to variation between the trends.

AC30 and AC60 samples have practically identical pore width distributions (**Figures 4.1.4** and **4.1.5**) but vastly different total pore

volumes (**Figure 4.3**) and storage capacities (**Figure 4.1.13**). This result confirms that total pore volume was a more influential factor for CO₂ adsorption than pore size distribution. Similarly, AC120's increased storage capacity can be attributed to an increase in AC120's total pore volume.

Despite the isothermal results at 273 K consistently outperforming their 298 K counterparts, the storage capacity of AC15 at 298 K (**Figure 4.1.11B**) is greater than the storage capacity of AC0 at 273 K (**Figure 4.1.11A**). This result means that improvement of an adsorbents structure, by low energy ball milling, can be as effective for improving CO₂ adsorption as energy exhaustive cooling processes [254]. Using both simultaneously was however the most effective approach.

DFT analysis of the propensity of pore widths (**Figure 4.1.4**) can be used to identify different trends in the materials porosity. As ball milling failed to promote formation of ideal pore widths, characterised by the similarity of the low pressures isothermal gradients for all the samples, identifying the ideal pore width for CO₂ adsorption could not be done.

Nickel was not expected to act as an adsorption catalyst. It was included as a catalyst for the oxidation of char products that may compromise the adsorbate within a fossil fuel furnace [51, 149]. It was apparent that the addition of Ni reduced the storage capacity of the material (**Figure 4.1.13**). This was likely influenced by the same factors that reduced the H₂ storage capacities, namely reduction in the pore volumes [96].

4.1.3.1 Calculation of adsorption energy

Calculation of adsorption energy was once again performed using a modified version of the DR equation (**Equation 3.7**) [218]. Results for all the milled samples are presented in **Figure 4.1.14**

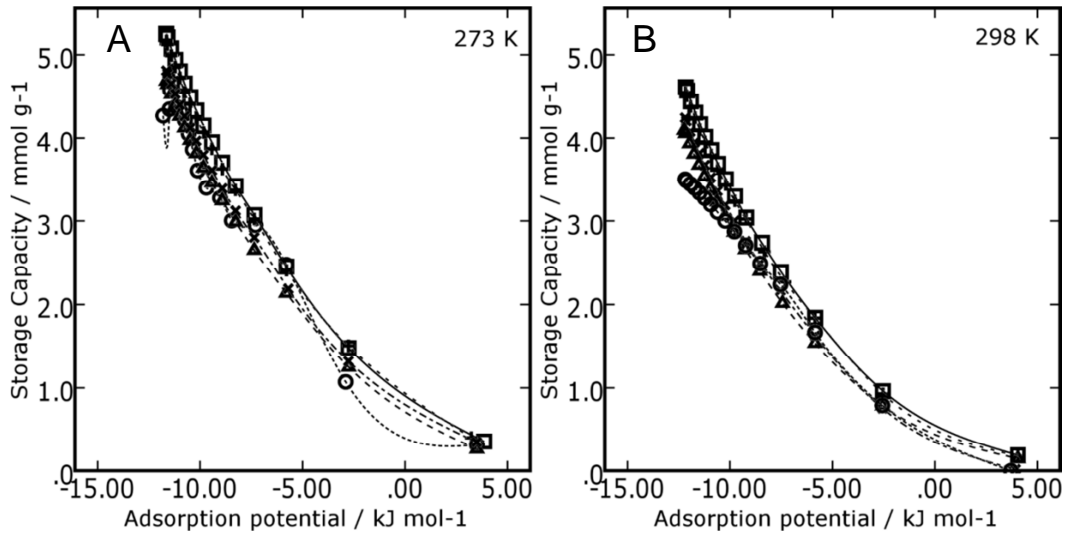


Figure 4.1.14. Variation in the adsorption potential of milled AC samples with changes in CO₂ storage capacity at 273 (A) or 298 K (B). Key: (○, dotted line) AC0; (□, solid line) AC15; (+, narrow dashed line) AC30; (Δ, dashed line) AC60; (×, dash-dot line) AC120.

Figure 4.1.14 shows that the CO₂ adsorption energies for all the samples were practically identical at both temperatures suggesting that changes in pore width induced by milling had little to no effect upon the adsorption potential of the materials.

4.1.3.2 Calculation of the heat of adsorption

Heat of adsorption was calculated from the Clausius-Clapeyron relation (**Equation 3.36**) with data points extrapolated from models of the experimental results [81, 212, 234]. Results below were extracted from a model based upon the Toth equation (**Equation 3.31**) the correlation of the models fit to the experimental results (R^2 value) was greater than 0.984 for all samples and can be seen as the line of best fit in all isothermal plots (**Figure 4.1.11**).

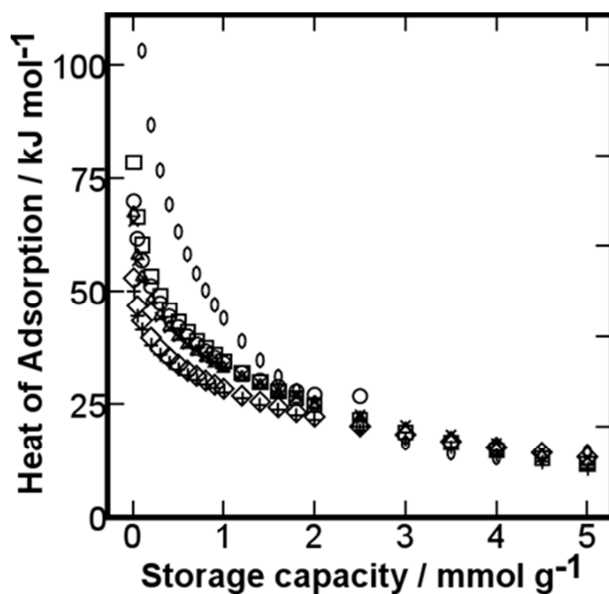


Figure 4.1.15. Variation in adsorption enthalpy (kJ mol^{-1}) with CO_2 storage capacity (mmol.g^{-1}). Key: (\circ) AC0; (\times) AC15; (Δ) AC30; (+) AC60; (\square)AC120; (\diamond)ACNi15; (\odot) ACNi120.

Isosteric heat of adsorption for AC0 could not be calculated above 2.5 mmol.g^{-1} as the Toth model curve for adsorption at 298 K (**solid line in Figure 4.1.11A**) reaches an exponential plateau at 3.5 mmol.g^{-1} . Estimation of the pressure required for storage of any CO_2 loading greater than 3.5 mmol.g^{-1} is not possible and the model becomes unsuitable for further prediction with the Clausius-Clapeyron relation (**Equation 3.36**). The enthalpy values are in keeping with those for physical adsorption of CO_2 [258, 259]. The published literature indicates the usual adsorption enthalpies are in the region of 11 to 18 kJ mol^{-1} , increasing to as high as 40 or 50 kJ mol^{-1} at lower adsorbed volumes. Results are similar here suggesting that milling would appear to have made little impact upon the heats of adsorption. This result is in agreement with the finding of the maximum adsorption capacities **Figure 4.1.13**. The gradient is a measure of the strength of binding between the adsorbate and adsorbent and a measure of the adsorbate-adsorbent interactions [234]. As the gradient of the milled samples is very similar to the results for AC0 (**Figure 4.1.11**) it further proves that the milling process does not increase the strength of binding in the samples.

4.1.4 Discussion

Calculation of the adsorption selectivity (**Section 3.3.6.4**) of the AC samples at 298 K for either H₂ or CO₂ was attempted using the Henry's law constants calculated from the extrapolated values from the Toth model (**Equation 3.31**). The selectivity equation (**Equation 3.39**) highlights that the calculation is approximate and is a measure with no units. Results are presented in **Table 4.1.3**.

Table 4.1.3 Selectivity of the adsorbents for H₂ or CO₂ at 298 K.

Sample	Selectivity direction	Selectivity ratio
Pure AC	H ₂ > CO ₂	35.1
AC15	CO ₂ > H ₂	638
AC30	H ₂ > CO ₂	2.2
AC60	CO ₂ > H ₂	1.5
AC120	H ₂ > CO ₂	5214
ACNi15	CO ₂ > H ₂	4.8
ACNi120	CO ₂ > H ₂	24.8

Given both the shift back and forth between gas selectivity's, and the range of the values collected, the validity of the results was called into question. Having explored the construction of the model it seemed the poor accuracy in the selectivity measurement was as a result of an insufficient collection of experimental data in the low pressure region of the isotherms. Selectivity, calculated by the method applied here is based upon the ratio of the Henry's law constants which describe the adsorption of a gas at extremely low pressures and are responsible for linear adsorption in the low pressure region [235, 240, 242, 243]. Selectivity measured by this approach is therefore a comparison of the adsorption gradient at very low pressures of H₂ and CO₂ based upon the strength of attraction between the adsorbate and the adsorbent. The data collection strategy used in this work was modified for all subsequent experiments to not only improve the accuracy of the selectivity model but also to increase the rate of sampling

and provide a larger data set for Toth modelling in subsequent work. Details of the changes are provided in **Section 3.4.2.3** and **Section 3.4.3.3**.

Regardless of the outcome of the selectivity study, all samples adsorbed more than twice the number of moles of CO₂ than H₂ (**Figures 4.1.8** and **4.1.13**) suggesting that these AC materials would function better as CO₂ adsorbents. However, if the materials were identified to preferentially adsorb hydrogen (as implied by three samples in **Table 4.1.3**) then the use of these materials as CO₂ adsorbents would need to be limited to hydrogen free gas streams.

The process by which ball milling increases storage capacity is often referred to as the addition of heterogeneity [38]. Increasing the heterogeneity of the material, by increasing the proliferation of defect sites across a surface, increases the fraction of sites that strongly bind to the adsorbate [74, 260]. As can be seen by the discrepancy between change in pore volume and change in storage capacity, not all defects generate sites that bind strongly with the adsorbate and contribute to an increased storage capacity. A truly heterogeneous material could never boast adsorption across more than 50 % of its surface due to the very definition of “heterogeneous”. Homogeneity is therefore the more desirable material quality, assuming that the majority of the surface has a high binding energy.

Trusting this philosophy to be correct, a critical question posed by these experiments was “can ball milling generate sufficient adsorbate materials?”. The answer to this is likely no. If ball milling were to generate truly heterogeneous materials than at least 50 % of the material would not be suitable for adsorption. Furthermore ball milling does not offer fine or repeatable control over the generation or destruction of surfaces. Even if milling were, on one occasion able to produce a material that could adsorb desirable quantities of adsorbate, the process could not be reliably reproduced. Ball milling functions best as a way to fractionally improve

storage capacities of imperfect adsorbents rather than as a means to generate an ideal adsorbent.

4.1.5 Conclusions

Ball milling was shown to increase pore volume by increasing the micro and macro porosity through a reduction in the average particle size, breaking apart larger particles and opening up previously sealed pores. In all cases this led to an increase in the storage capacity [249].

Whilst ball milling increased the hydrogen storage capacity of the ACs, for the materials to act as tolerable adsorbents the synchronous application of milling and temperature control was required. The gradient of the H₂ isotherms remain steep even at high pressures suggesting that even at 10 bar the maximum H₂ storage capacity has not been achieved. The best results for CO₂ storage were achieved with both milling and temperature control. However, due to the overlap of results, milling alone would provide a cost effective approach for CO₂ capture. Comparison of the storage capacities to the literature will be reserved until **Chapter 5** to also allow comparison to the other materials generated in this project.

In this experiment nickel showed no catalytic activity. Milling the AC materials with nickel nanoparticles increased the storage capacity of both H₂ and CO₂ compared to the unmilled AC but there was no evidence that this increase was due to the presence of the nickel. Comparing materials with similar pore sizes but with or without nickel, the presence of the metal actually appeared to impede the adsorption capacity.

4.2 The influence of nitrogen content and the presence of a metal substrate on the growth and H₂ storage capacity of novel carbon films deposited by magnetron sputtering

This section discusses how variation of synthesis conditions, namely the deposition temperature, the nitrogen fraction of the sputter gas, and the composition of the metal and silicon substrate, influences the growth and H₂ storage capacity of novel carbon adsorbents. The background to this work is presented in **Section 2.4.2** and the experimental process is described in **Section 3.4.2**. Samples were named after the deposited elements, then the nitrogen gas fraction and the substrate temperature of the carbon deposition step. For example, a carbon sample deposited onto a silicon, magnesium and nickel substrate at 600 °C in a 50 vol.% nitrogen atmosphere was named SiMgNiC50600. Carbon films deposited onto silicon and nickel substrates are collectively referred to as SiNiC films. A list of sample names and compositions is presented in **Appendix B**.

4.2.1 Material Characterisation

4.2.1.1 Analysis of CN_x films deposited at 600 °C in varying nitrogen atmospheres on SiMgNi substrates

4.2.1.1.1 SEM and EDX analysis

SEM images of the CN_x films deposited onto SiMgNi substrates in varying nitrogen atmospheres at 600 °C are displayed in **Figure 4.2.1**. Each figure displays a top-down image profiling the surface morphology and a cross-sectional image (insert) detailing the film structure and thickness. The original magnification of all the images was × 30,000 except **Figure 4.2.1E** which was at × 18,000. The variation in magnification was considered when analysing cluster size and scaling the image for the comparison to the other samples.

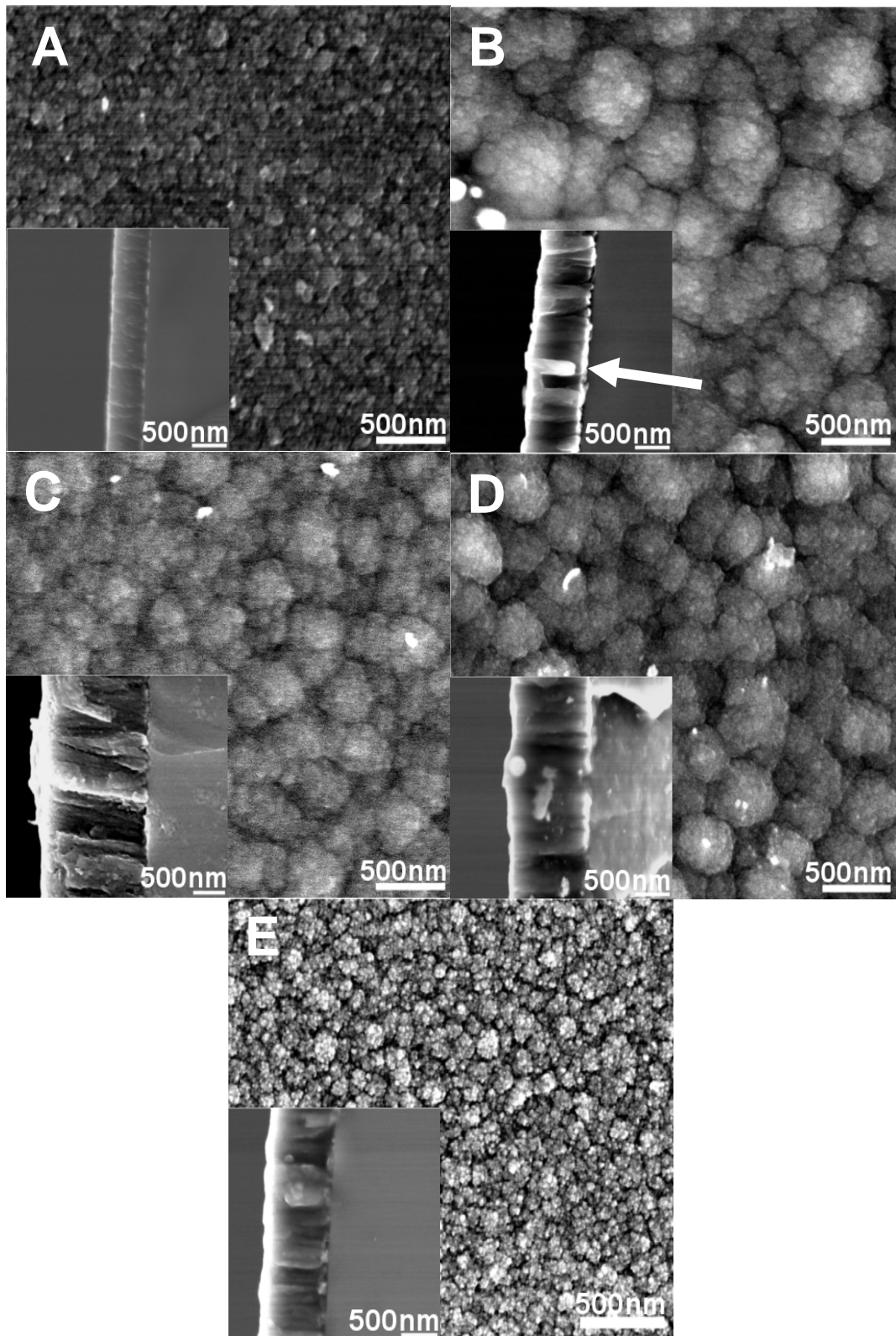


Figure 4.2.1. Surface topography and cross-sectional structures of SiMgNiCN_x films deposited at 600 °C in varying nitrogen atmospheres. A) SiMgNiC0600 ; B) SiMgNiC25600 , white arrow indicates the presence of rounded column bases where nucleation

has expanded horizontally until it conflicts with other nucleation points; C) SiMgNiC50600; D) SiMgNiC75600; E) SiMgNiC100600.

The appearance of the films suggests that nanocolumns, similar to those found by Scalese *et al.*, were formed [2]. Clusters remained denser in this work at elevated nitrogen contents than in the literature [154]. A defining difference between this work and the previous study was the presence of Mg and Ni fractions of the substrate which is likely the cause for the increased cluster density (number of clusters present per μm^2). Whilst the SiMgNi substrate was designed to promote nanotube growth, nanocolumn growth is also believed to be catalysed by the same nano-seed mechanism [154]. The films presence would be expected to reduce the energetic barrier against nano-seed formation [210, 261, 262]. The SiMgNi substrate may have also played a more passive role in the formation of nano-seeds with deposition increasing the substrate surface roughness and the propensity of low energy binding sites. Comparing the cross-sectional and top-down images, it appears that each clustered column was responsible for the appearance of one cluster on the surface.

Cross-sectional images of SiMgNiC0600 (**Figure 4.2.1A**) revealed very little in terms of ordered nanocolumn growth. It was observed that in places where ordered vertical growth did occur, the nanocolumn structure of the carbon film degraded as the distance from the substrate increased. According to the literature, ordered growth does not occur in pure argon atmospheres without a catalyst or sufficient particle energy [2, 153, 154, 263]. In the absence of nitrogen, seeding of the nanocolumns structures could only have been facilitated by the nickel nano-islands or promoted by the increased surface roughness induced by the SiMgNi substrate. The energy deficit against ordered growth in this case could have been supplemented by substrate temperature.

Films deposited within nitrogen atmospheres all contained ordered vertical columns. The structures appeared to grow in clusters from disperse seeding points and grew wider as they distanced themselves from the substrate, until they became unable to further expand horizontally

due to van der Waals repulsion from surrounding columns [264, 265]. This effect gives the columns a hemispherical appearance at their base as best exemplified in SiMgNiC25600 (**White arrow in Figure 4.2.1B**). These same van der Waals forces are not otherwise responsible for the shape of the structures.

Figure 4.2.2 profiles changes in film thickness and average cluster size, measured as the cross sectional area, with variation of the nitrogen content in the sputter gas. As the sputter gas composition was the only factor varied it is apparent that nitrogen significantly influences the materials structure.

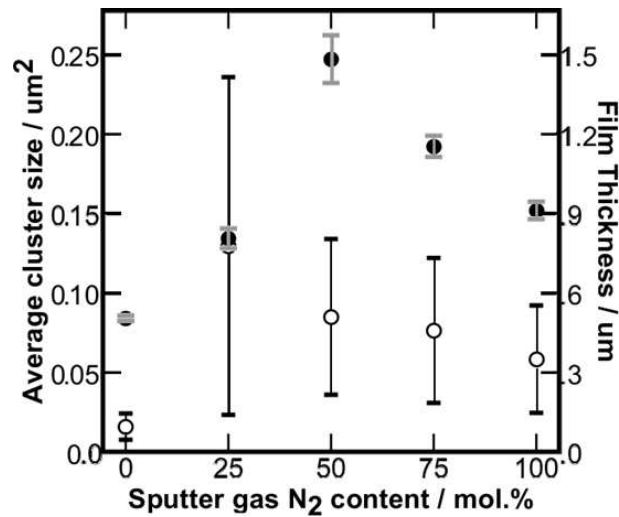


Figure 4.2.2. Variation in the film thickness (μm) and average cluster size, or cross sectional area (μm^2), with variation in the nitrogen content of the sputter gas (vol.%) of CN_x films deposited on SiMgNi substrates at 600 °C. Key: (●) film thickness; (○) cluster size. Error bars relate to ± 1 standard deviation from average.

The curved shape of the plots suggests, nitrogen influences growth in several, conflicting ways. In the absence of nitrogen the film thickness and cluster sizes were at their smallest. The introduction of nitrogen greatly increased the average film thickness and promoted the formation of large clusters. As nitrogen content rose further, beyond 50 vol.%, the average cluster size steadily decreased. Similarly the film thickness peaked before decreasing at 50 vol.%. These findings correlate with the

literature [2, 154, 266]. The discussion below outlines the different nitrogen effects on the deposition and growth of CN_x films.

The most apparent influence of nitrogen on the deposition of the materials was its effect on the rate of carbon sputtering. **Figure 4.2.3** summarises the variation in sputter rate with nitrogen content of the sputter gas, as measured by the crystal rate monitor, the collection method is described in the experimental section. Note that this is the sputter rate recorded *in situ*, not the deposition rate calculated from the deposited mass.

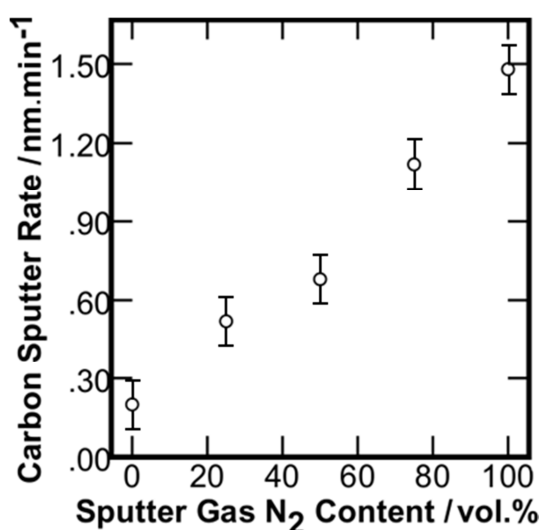


Figure 4.2.3. Variation in the sputter rate ($\text{nm}\cdot\text{min}^{-1}$) of carbon in different nitrogen sputter gas contents (vol.%), measured by the crystal rate monitor. Error bars relate to maximum deviation from sputter rate recorded by the crystal rate monitor.

As the nitrogen sputter gas content increased so too did the sputter rate. The low sputter rate within a pure argon atmosphere lead to a low growth rate in the SiMgNiC0600 film (**Figure 4.2.1A**) [267]. Low energy deposition also leads to an increase in the amorphous fraction of the film and a low level of ordering during the growth process as there is insufficient energy to allow for the diffusion or crystallisation of the sputtered atoms [265, 268]. Both the rate of growth and the structural order of the film would decrease as the amorphous fraction grew with prolonged deposition time because amorphous deposits cap the ordered

growth fronts preventing further ordered vertical growth. This would explain SiMgNiC0600's reduction in ordered growth as film thicknesses increased.

The increase in the sputter rate with the increase in the nitrogen content of the sputter gas can be attributed to the combined influence of three factors. Firstly, the disassociation of nitrogen molecules from electronic impacts would increase the ion density, potentially increasing the sputter rate [269]. Secondly, the ion density within the plasma is dependent upon the Townsend ionisation coefficient, which is inversely proportional to the ionisation potential of the plasma gas [140]. Atomic nitrogen has a lower ionisation energy than argon, 14.5341 eV (15.7 eV for N₂) and 15.7596 eV, respectively. Therefore substitution of argon with nitrogen would increase the ion density within the plasma. Thirdly, **Equation 4.6** is built from the Laws of the Conservation of Energy and the Conservation of Momentum [142]:

$$\frac{E_t}{E_i} = 4M_t M_i \cos^2 \frac{\theta^0}{(M_i + M_t)^2} \quad \text{Equation 4.6}$$

Where E is the energy and M the mass of incident particle *i* and target particle *t*. θ^0 is the angle of incidence measured from the angle of impact against the axis of the target surface. Maximum energy transfer occurs when $\cos \theta^0$ is equal to 1 or when M_i is equal to M_t [142]. Even in its dimer form nitrogen's mass is closer to carbon's than argon and transfer of kinetic energy will occur more efficiently. This will lower the minimum ion energy required to induce a carbon discharge and increase the chance of carbon sputtering.

Beside increases in sputter rate, nitrogen has three ways of positively influencing the ordered growth rate of a film. Firstly, unlike argon, nitrogen radicals also become sputtered materials, contributing to an increase in the deposited mass. Secondly, both nanotube and nanocolumn formation require seeding from a curved carbonaceous nano-seed [153, 199, 270]. For a flat graphitic sheet to fold on itself and become cylindrical it requires the formation of pentagon rings [154].

Nitrogen incorporation into the film reduces the energetic barrier against pentagon formation, stabilising curved growth and reducing the activation energy for proliferation [271]. Comparing the appearance of the films and their cross-sectional structures in **Figure 4.3.2**, it appears that as the nitrogen content of the atmosphere increased so too did the fraction of ordered column growth. This is in agreement with relevant studies [2, 154, 200, 266]. Nitrogen's final positive influence on growth rate is moderated etching. Etching describes the chemical erosion of a deposited film due to the formation and release of volatile gaseous species [2]. Nitrogen atoms cannot be nearest neighbours within a CN_x film without dissociating as N_2 or an equally volatile short chain cyanogen such as C_2N_2 [272]. Growth rate of a film decreases with deposition time as amorphous carbon deposits cover active growth sites [155]. Removal of these deposits by etching prevents capping of growth fronts and preserves ordered growth rate [155, 265, 273]. Whilst the etching process decomposes both ordered and amorphous materials, as long as the rate of ordered growth exceeds the etching rate, the process can be considered beneficial. When the etching rate exceeds the growth rate material decomposition occurs, reducing the order and thickness of deposited materials. Etching rate is mediated by the nitrogen sputter gas content [272]. Higher nitrogen gas contents increase the nitrogen fraction of sputtered ions and hence the likelihood of forming volatile species. This explains the reduced film thicknesses observed in the films deposited in sputter gases with a nitrogen content of above > 50 vol.% (**Figure 4.2.2**), as the rate of etching increases with the nitrogen fraction of the sputter gas.

EDX results, looking at the carbon to nitrogen ratio within the films, are compiled in **Table 4.2.1**. The carbon to nitrogen ratio of the CN_x films was determined from EDX data using **Equation 4.7** below [274]:

$$N_c = \left(\frac{N_f}{N_f + C_f} \right) \times 100 \quad \text{Equation 4.7}$$

Where N_c is the nitrogen content of the deposited film expressed as a percentage, N_f and C_f are the nitrogen and carbon fractions of the EDX results, respectively.

Table 4.2.1. C:N ratio of the films deposited under different nitrogen atmospheres onto SiMgNi substrates, measured by EDX analysis.

Sample	Sputter gas N ₂ content (vol.%)	Carbon composition (%)	Nitrogen composition (%)
SiMgNiC0600	0	100	0.00
SiMgNiC25600	25	79	21
SiMgNiC50600	50	81	19
SiMgNiC75600	75	82	18
SiMgNiC100600	100	84	16

Nitrogen contents of the deposited films directly contradict results in the literature [2, 266]. Following an initial increase when nitrogen was introduced to the system, the nitrogen content of the film decreased as the nitrogen content of the atmosphere increased, a trend paralleled by the decrease in the average cluster size. The decrease in nitrogen content, and film thicknesses, of samples deposited in atmospheres with nitrogen contents in excess of 50 vol.% are likely the result of nitrogen etching [266]. Assuming that N₂ was the primary material being etched from the surface, rather than any other cyanogens, the N content of the film could be reduced relative to carbon.

The presence of nitrogen promoted ordered growth within SiMgNiC25600 compared to SiMgNiC0600 (**Figures 4.2.1B** and **4.2.1A** respectively), increasing the film thickness and generating ordered structures across the full width of the film. A 21 % nitrogen content within SiMgNiC25600 is equivalent to more than one nitrogen atom per graphitic ring [154]. Given that nitrogen atoms cannot be nearest neighbours without disassociating it would suggest that the likelihood of etching was

high but the nitrogen fraction of the sputtered material was still low enough for etching to not become detrimental. For sample SiMgNiC50600 (**Figure 1C**) the film thickness increased whilst the cluster size, ordered growth fraction and the nitrogen content of the film decreased. These results indicate that deposition within a nitrogen atmosphere of 50 vol.% or lower, nitrogen's positive influences on sputter rate outweigh the negative etching effects. Once the nitrogen content in the sputter gas exceeded 75 vol.%, the detrimental rate of etching exceeded the beneficial influences of nitrogen on growth rate, resulting in a reduction in film thickness for SiMgNiC75600 and SiMgNiC100600. Similar trends were observed in comparable studies [154, 274]. Increased etching would also be responsible for the increased surface roughness apparent in the top-down image of film SiMgNiC100600 (**Figure 4.2.1E**) [266].

Several authors [2, 154, 200, 266] have discussed the benefits of nitrogen for the fast ordered growth of carbon materials compared to argon. This study presents the most comprehensive evaluation of nitrogen's influence on deposition and is the first to consider the effect of nitrogen upon the sputter rate. In light of these findings the understanding of the interplay between growth factors in a film must be reassessed as their influence may be greater than previously anticipated.

4.2.1.1.2 Raman analysis

Raman analysis of the structure was performed to identify the order of the carbonaceous films deposited [208]. **Figure 4.2.4** shows a typical Raman spectra for sample SiMgNiC50600. Additional Raman spectra for each sample run in this study can be found in **Appendix C**.

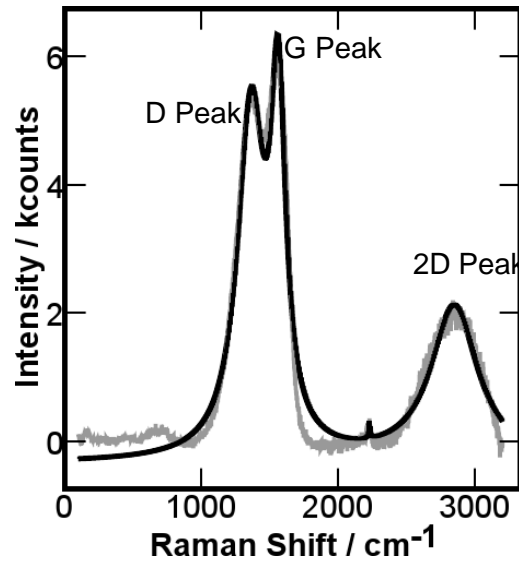


Figure 4.2.4. Raman spectra for SiMgNiC50600 including assignment of the key peaks identified. (Grey lines) background corrected experimental data. (Black lines) Lorentzian modelled peak fitting.

The key characteristics of a Raman spectra for characterising the carbonaceous films are the ratio between the full width at half maximum (FWHM) of the D peak at $\approx 1350 \text{ cm}^{-1}$ (breathing mode of sp^2 atoms in rings) and the G peak at $\approx 1580 \text{ cm}^{-1}$ (sp^2 bond stretching), referred to as the I_D/I_G ratio [208]. Position of the G peak is also important for establishing crystallinity, with the higher its Raman shift the greater the graphitic order of the system. Another important feature is the presence of the peak at approximately 2226 cm^{-1} , which correlates to a C-N stretching signal and can be used to confirm the presence of nitrogen in the structure. A summary of the results is recorded in **Table 4.2.2**.

Table 4.2.2. Summary of the results of Raman analysis of CN_x films deposited on SiMgNi substrates.

	D peak position (cm ⁻¹)	G peak position (cm ⁻¹)	I _D /I _G ratio	I _G /I _N ratio
SiMgNiC0600	1351	1593	1.94	0.00
SiMgNiC25600	1371	1574	1.88	7.61
SiMgNiC50600	1359	1560	1.45	2.38
SiMgNiC75600	1386	1576	2.14	4.45
SiMgNiC100600	1376	1578	1.93	4.27

Results for SiMgNiC0600 were as expected. No nitrogen peak was identified in the sample and the gap between the D and G peak positions was at its widest. The I_D/I_G ratio below 2 and the position of the G peak suggests a highly graphitic structure as identified by the literature [208]. For the films deposited in a nitrogen atmosphere there was no clear trend between nitrogen content of the sputter gas and the I_D/I_G or I_G/I_N ratios. The conflicting influences of nitrogen on growth and etching, as discussed in **Section 4.2.1.1.1**, are the likely causes of this outcome. The G peak position and the I_D/I_G ratio of the samples deposited in a nitrogen atmosphere were lower than for SiMgNiC0600 (except for SiMgNiC75600's I_D/I_G ratio) suggesting increased graphitisation or nano-graphitic structures compared to the sample grown in pure argon. This is consistent with the above conclusion that nitrogen's inclusion was promoting ordered growth by processes such as reducing the energy barrier against ordered formation and reactively etching amorphous deposits from the films surface.

4.2.1.1.3 TEM analysis

TEM analysis uncovered a number of different morphological features within each of the five samples deposited at 600 °C in varying nitrogen atmospheres. The propensity and dimensions of these features varied from sample to sample. **Figure 4.2.5** summarises the appearance of the different structures.

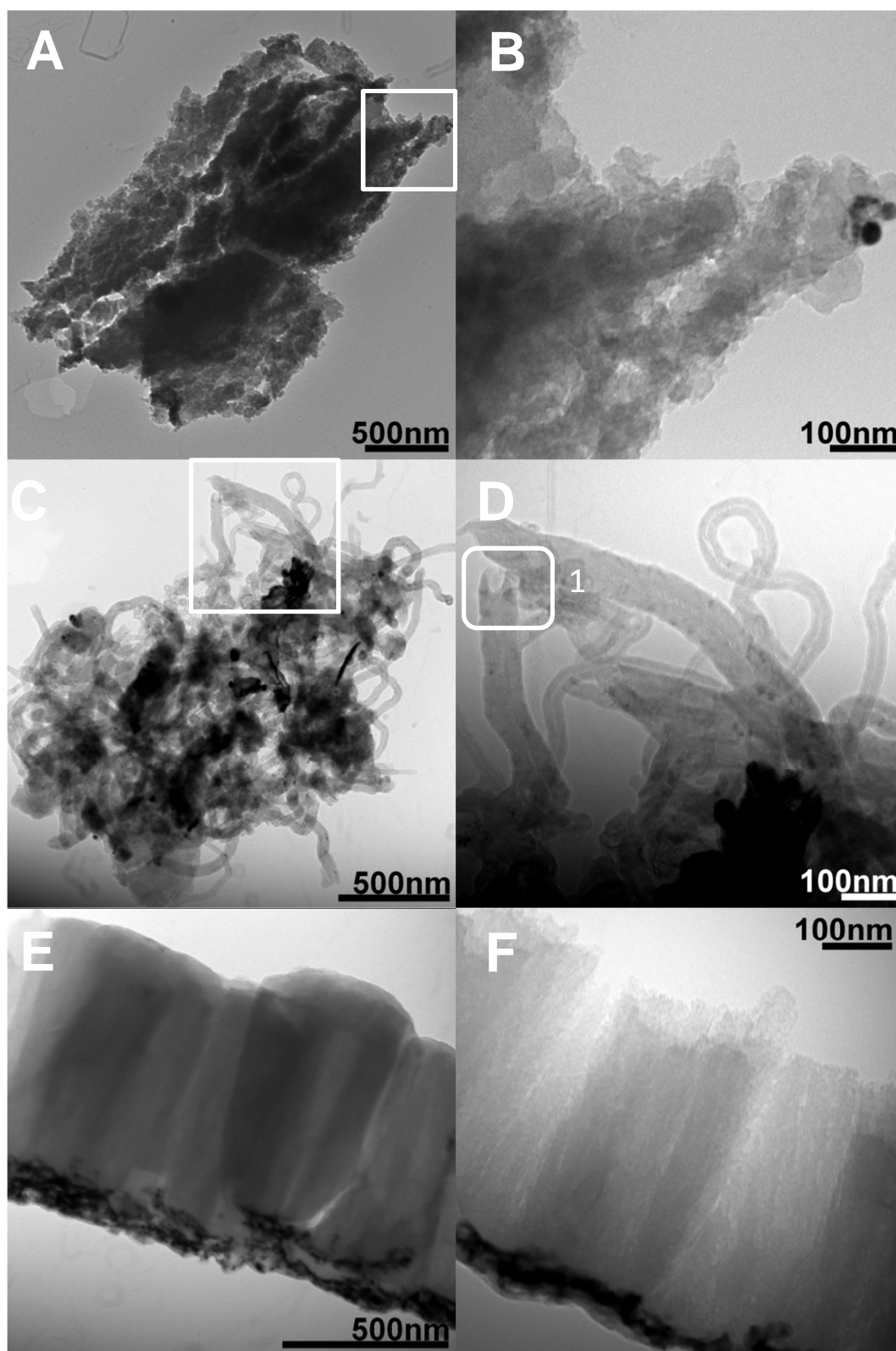


Figure 4.2.5. TEM images of carbonaceous species grown at 600 °C on SiMgNi substrates at different magnifications. A+B) Amorphous carbon structure from SiMgNiC0600; C+D) Carbon nanotubes from SiMgNiC50600; E+F) Ordered columnar carbon from SiMgNiC25600.

The sonication step in TEM sample preparation fragmented the densely packed films allowing closer scrutiny of the structures present. Amorphous carbon, as in **Figures 4.2.5A** and **4.2.5B**, was most widespread in sample SiMgNiC0600 with its prevalence decreasing sharply with increasing nitrogen content. Amorphous structures identified were often at least $0.2 \mu\text{m}^2$ in size. Nanotubes were identified in all samples deposited within a nitrogen atmosphere (**Figures 4.2.5C** and **4.2.5D**). Their propensity increased with increasing nitrogen content of the feed gas. Nanotube propensity in sample SiMgNiC25600 was limited but a small number of short nanotubes were identified beside nanocolumns sprouting from the shared MgNi base (not shown). For nitrogen atmospheres in excess of 50 vol.%, nanotubes were prolific in abundance. Whilst the growth of nanotube structures by magnetron sputtering without a catalyst has been reported at temperatures above and below those used here [153], the propensity and size of these structures were extremely limited and bore no resemblance to the results of this work. Growth of the nanotubes must therefore have been promoted by both the SiNiMg substrate and the nitrogen fraction of the sputter gas. The importance of the substrate temperature on growth will be explored further below. No literature could be found suggesting that magnesium or silicon is capable of catalysing nanotube growth, therefore the nickel fraction must have been responsible for catalysis. Nickel's catalytic influence is supported by the hollow conical structure at the ends of the nanotubes, an example is **Circled in Figure 4.2.5D** [270], which have been identified as growth fronts for metal catalysed nanotubes [199]. The example given does not contain the catalytic particle but the shape left behind is evidence of its activity. It has been repeatedly substantiated that the width of a nanotube is proportional to the width of the catalytic seed particle [270]. The lack of uniformity in nanotube widths within each sample would suggest that the nano-island dispersion of nickel generated during the annealing of the SiMgNi substrate was not uniform. Nitrogen's catalytic influence on nanotube growth is evidenced by the absence of nanotubes in sample SiMgNiC0600, grown in a nitrogen free environment. Nitrogen is unlikely

to have influenced the nickel nano-island distribution, therefore nitrogen's promotion of nanotube synthesis is the likely result of two factors; Nitrogen's influence on carbon sputter rate as a sputter gas (**Figure 4.2.3**), *and* its promotion of curved graphitic growth as a deposited material as discussed in **Section 4.2.1.1.1** [154].

Ordered nano-columnar growth, characterised by the smooth sides of the columns and their uniformity in growth direction and length (as demonstrated in **Figure 4.2.5E**), was the most abundant structure identified in all samples analysed by both TEM and SEM. Some materials identified by TEM analysis were comparable in structure and size to the SEM results. This comparison was best exemplified by SiMgNiC25600's results. **Figures 4.2.5E** and **4.2.5F** show columnar structures bound to a metal layer that are comparable in length and similar in appearance to columnar structures from the SEM results for the same material (**Figure 4.2.1B**). The lack of uniformity in the nickel particle size can be used to explain the presence of the nanocolumns. The mechanism for nanotube growth introduced by *Kuang et al.* could be modified to explain vertical nanocolumns formation [152]. The abundance of nanocolumns compared to nanotubes found in this study suggests that the annealing step designed to generate a disperse nickel nano-island distribution for nanotube growth was unsuccessful as only a small fraction of nanotubes were grown. The remaining nickel islands were too large to promote nanotube growth but may still have acted as catalysts for the formation of graphitic sheets, generating seed points that promote ordered columnar growth. This hypothesis would explain both the intimate contact between the carbon and the base layer as observed in the TEM results and the increased column density compared to similar experiments in the literature [154]. *Wang* and *Moore* propose an equally viable mechanism for nanofibre growth from a nickel catalyst too large to grow carbon nanotubes by a tip growth mechanism [275].

Other papers that have studied CN_x nanocolumns deposited by magnetron sputtering have not reported the presence of any nanotubes in

their structures [2, 154]. Similarly, papers that have reported the growth of nanotubes have not reported the growth of any nano-columnar structures [276-278]. Comparing their experimental procedures to this work, improved nanotube propagation came as a result of more refined nano-island synthesis techniques. Nanocolumn growth was devoid of nanotubes in the literature as no catalytic nano-islands were present.

4.2.1.1.4 Surface morphology of deposited MgNi layers post annealing

Figure 4.2.6 shows the SEM images of the MgNi layer deposited on silicon substrates annealed at different temperatures.

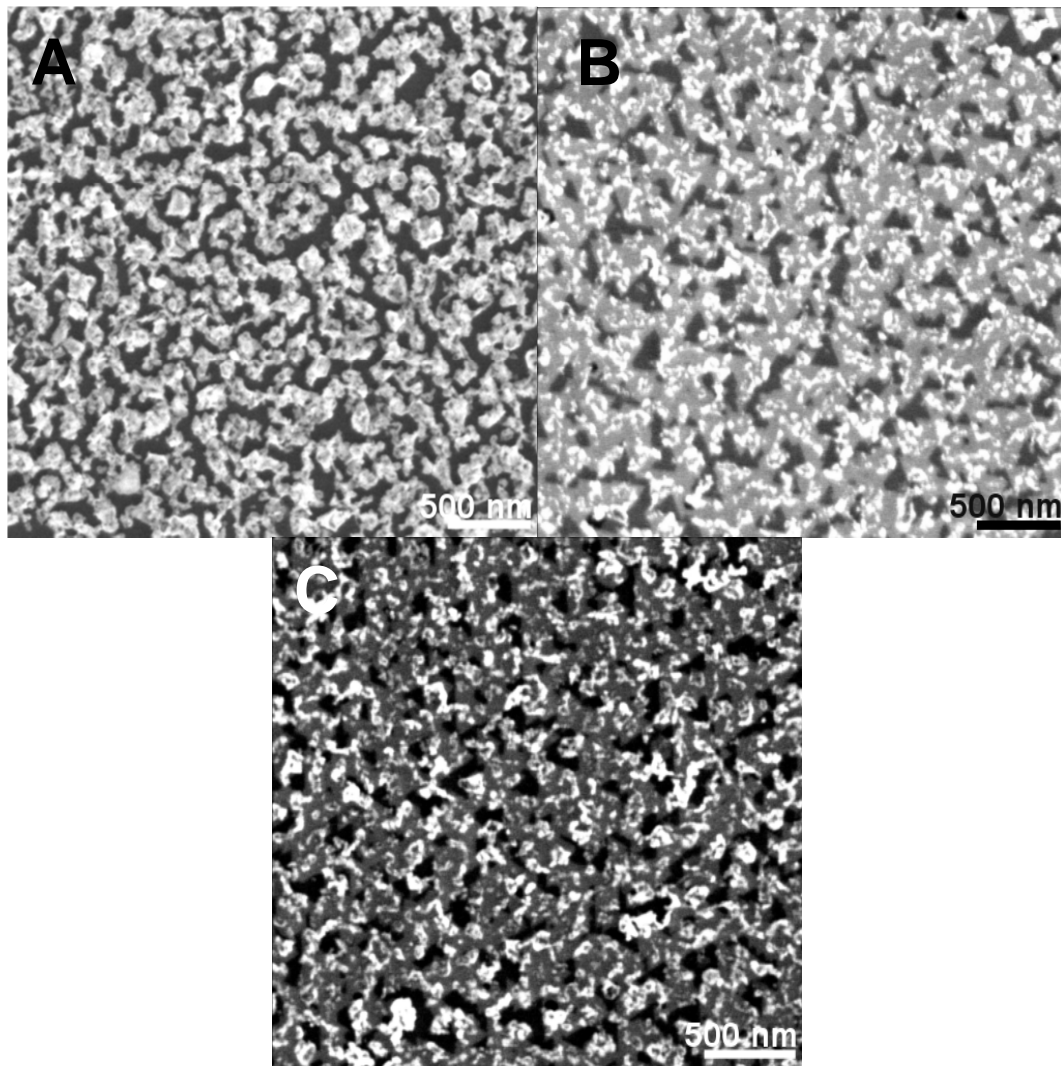


Figure 4.2.6. SEM images of the MgNi layers deposited on silicon annealed at different temperatures. A) SiMgNi400; B) SiMgNi600; C) SiMgNi700.

Annealing at 400 °C is shown in **Figure 4.2.6A** from which two distinct materials could be resolved in the SEM image. The brighter material appears to be a fractured film sat on top of a continuous film. The films are likely nickel and magnesium respectively based upon the order of deposition as magnesium was deposited first then nickel deposited on top of it. The nickel film appears to be in a transition point between continuous coverage and degeneration into a dispersion of nano-islands. Breakdown was facilitated by the energy provided from the annealing process, reducing the surface tension of the molten nickel film, and further assisted by magnesium's uneven surface beneath the film forming peaks and

troughs for pooling. This effect is exacerbated in **Figure 4.2.6B** where sintering at 600 °C has facilitated decomposition of the magnesium film revealing the silicon substrate as even darker regions. At 700 °C in **Figure 4.2.6C**, more of the silicon substrate became exposed and the clear distinction between the bright nickel and the dull magnesium layers became less apparent with an uneven alloy appearance. The brightest regions of **Figures 4.2.6B** and **4.2.6C**, thought to be nickel, were always found on top of the medium brightness regions, magnesium, but never on the darkest regions of the image, silicon. Confirmation of the elemental composition of the individual features could not be performed due to the resolution of the integrated EDX apparatus. However, **Table 4.2.3** summarises image analysis results concerning the fractional coverage of the films. Materials were identified based upon their colour from black (Si) to grey (Mg) to white (Ni). Image analysis software was used to calculate the fractional coverage of each colour on the film (**Section 3.3.4**).

Table 4.2.3. SEM image analysis Results of surface topography [279].

Film	Si fraction / %	Mg fraction / %	Ni fraction / %	Average Ni island size / nm ²	Ni island density / particle.µm ⁻¹
SiMgNi400	0 ± 4.85 %	48± 4.85 %	52± 4.85 %	33700	30 ± 1.5
SiMgNi600	19± 4.85 %	40± 4.85 %	40± 4.85 %	2880	139 ± 7
SiMgNi700	20± 4.85 %	48± 4.85 %	31± 4.85 %	2071	150 ± 7

Large average nickel island sizes for SiMgNi400 in **Figures 4.2.6A** would suggest that pre-treatment at 400 °C for 30 minutes was inadequate for sufficient deterioration in the nickel film layer leading to nano-islands formation [210]. SiMgNi700 (**Figure 4.2.6C**) achieved the smallest

average nickel particle size. SiMgNi700 also had the smallest exposed nickel fraction of the three films most likely due to the shift in physical state of the two metals as temperatures increased. Whilst the melting temperatures of magnesium and nickel are 649 °C and 1453 °C, respectively, surface properties of a material behave differently to a film and melting temperature can be reduced by up to 50 % [210, 261]. Alloying of the two materials is likely to further reduce the combined melting temperature of the two materials. Alloying can be observed at 700 °C, as the rough appearance of the film becomes smoother and more fluid with nickel dispersing throughout the magnesium layer and decreasing the apparent nickel content in the SEM image. MgNi alloying would ideally allow for improved nickel dispersion, reducing the average nickel particle size and increasing the nickel particle distribution [280, 281].

4.2.1.2 Analysis of CN_x films deposited at different annealing temperatures on a SiNi substrate in a 50 vol.% nitrogen atmosphere

This section discusses the influence of temperature on the growth of CN_x films over a SiMgNi substrate. The nitrogen fraction of the atmosphere was set to 50 vol.%. The nitrogen incorporation into the film was measured at the different temperature to isolate its dependence on reaction temperature.

4.2.1.2.1 SEM and EDX analysis

SEM images of carbonaceous growth over SiMgNi substrates at different temperatures are shown in **Figure 4.2.7**. These images correspond to the CN_x structures grown on the surface of the annealed SiMgNi substrates presented in **Figure 4.2.6B**.

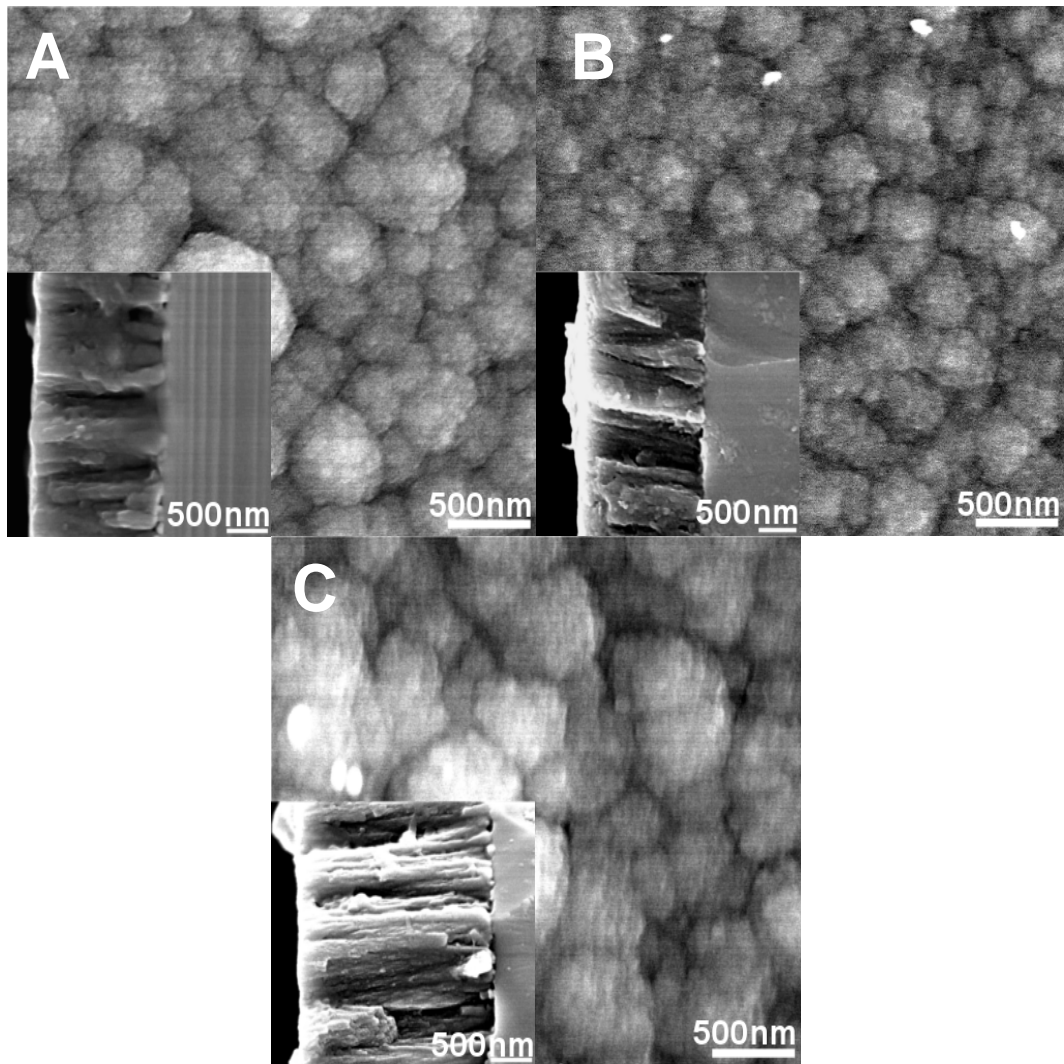


Figure 4.2.7. Surface topography and cross sectional structure of SiMgNiCN_x films deposited at varying temperatures in a 50/50 N₂:Ar atmosphere. A) SiMgNi50400; B) SiMgNi50600; C) SiMgNi50700.

The thickness and surface topography of SiMgNiC50400 and SiMgNiC50600 in **Figures 4.2.7A and 4.2.7B** were very similar. SiMgNiC50700 in **Figure 4.2.7C** was, by comparison, almost double in thickness and had significantly larger average cluster sizes. The variation in the physical features of the samples are compared in **Figure 4.2.8**.

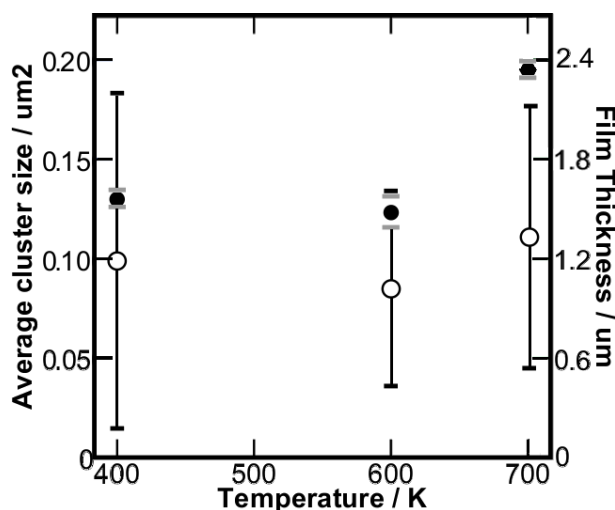


Figure 4.2.8. Variation in the film thickness (μm) and average cluster size (μm^2) with variation in temperature ($^{\circ}\text{C}$) of the annealing and carbon deposition processes. Key: (●) film thickness; (○) average cluster size. Error bars are $\pm 1\text{SD}$ from the Average cluster size or film thickness from the recorded data.

These results suggests that if temperature is having an effect upon the material growth it is doing so in tandem with other influencing factors; most notable would be the influence of nitrogen and the structure of the SiMgNi substrate. Cluster density would be expected to follow the same trend for these results as it did for nitrogen content (**Figure 4.2.2**) and increase with temperature [200]. At comparable thicknesses SiMgNiC50400 and SiMgNiC50600 obey this trend also seen in **Figures 4.2.1B, 4.2.1C, 4.2.1D** and **4.2.1E**. This trend was not adhered to by SiMgNiC50700. SiMgNiC50700 would be expected to show a smaller average cluster size and a larger cluster density because the number of nucleation sites (nickel island density) generated on the SiMgNi substrate at 700 $^{\circ}\text{C}$ was greater than on the other substrates generated at lower temperatures (**Table 4.2.3**). SiMgNiC50700's increase in average cluster size and reduced cluster density (number of clusters per μm^2) may be a by-product of an increased film growth rate, evidenced by the increased sample thickness. During growth, the lengths of clusters should remain roughly proportional to each other as the rate of deposition should be equivalent over the sample collection plate but different sized clusters will

grow at different rates [270, 282]. Any structure growing faster than the surrounding structures would continue to grow vertically for a while until its balance, previously supported by van der Waals repulsions between the different columns, became uneven and it either collapses and grows horizontally or spreads out and increase its width [265, 268]. The spreading process, known as superposition, would increase the surface area of the growing clusters and engulf any slower growing clusters around it. Superposition reduces the apparent cluster density at the surface as slower growing clusters are engulfed by the faster growing clusters. Within a system with a disperse collection of cluster sizes, the thicker the film gets the fewer number of clusters would be visible on the surface as superposition becomes more prevalent. As the thickness of the SiMgNiC50700's film was nearly double that of the other two samples more pronounced superposition was able to occur increasing the average cluster size and causing its cluster density to deviate from the expected trend. Were the SiMgNiC50700 sample an equivalent thickness to the other two samples less superposition could have occurred and the cluster density and average cluster size may have better fitted the expected trend.

EDX analysis was performed to identify the variation in the nitrogen content of the films with deposition temperature. Results are provided in **Table 4.2.4.**

Table 4.2.4. C:N ratio of the films deposited at different temperatures onto SiMgNi substrates, measured by EDX analysis.

Sample	Deposition temperature (°C)	Carbon composition (%)	Nitrogen composition (%)
SiMgNiC50400	400	79	21
SiMgNiC50600	600	81	19
SiMgNiC50700	700	79	21

Nitrogen content in the films grown at different temperatures again conflicts with the literature and shows that they stay relatively constant, where they would be expected to decrease [154]. Nitrogen content decreases with increased temperature because nitrogen absorption into the film increases equivalent to the square root of the temperature but desorption increases exponentially with temperature [283]. The increase in etching rate is because at higher temperatures the cyanogen chain size that can be removed increases, increasing the etching rate and reducing the nitrogen content of the films [266, 283]. A possible cause for the samples not following the trend could be that at higher temperatures there is a change in the structural composition of the films. Low temperatures may be forming a CN_x structure only able to incorporate a small nitrogen fraction but increasing the temperature may have promoted the growth of carbon structures able to accept larger nitrogen fractions into their structure. TEM analysis discussed below (**Section 4.2.1.2.3**) did identify that the nanocolumn fraction of the film increased with temperature. Further analysis would be needed to establish the fractional proportions of the different chemical bindings and identify if the different nanostructures present were able to store different nitrogen contents [284].

The beneficial effects of the temperature increase, such as the promotion of growth, exceed the detrimental effects, such as the promotion of further etching, within a 50 vol.% nitrogen environment. Annealing temperature clearly affected the surface structure of the SiMgNi substrate, altering the nickel island size and distribution (**Figure 4.2.6**). No corresponding change to the cluster density of the carbon structures in **Figure 4.2.7** was observed, however the effects of nitrogen and increased growth rate may be masking the true behaviour of the deposited carbon film in relation to the underlayer.

4.2.1.2.2 Raman analysis

Raman results for the CN_x films deposited on SiMgNi substrates at different temperatures are summarised in **Table 4.2.5**. Raman spectra for each sample run in this study are included in **Appendix C**.

Table 4.2.5. Summary of the results of Raman analysis of SiMgNiC50 films deposited at different temperatures.

	D peak position (cm ⁻¹)	G peak position (cm ⁻¹)	I _D /I _G ratio	I _G /I _N ratio
SiMgNiC50400	1373	1576	1.87	6.64
SiMgNiC50600	1359	1560	1.45	2.38
SiMgNiC50700	1370	1574	1.87	7.28

No trend between temperature and nitrogen content or I_D/I_G ratio can be established from these results. Similarity of the results for SiMgNiC50400 and SiMgNiC50700, especially their I_G/I_N ratios, was unexpected as it contradicted the literature, which would expect to see a fall in nitrogen content with increased temperature. This result does substantiate the similarity of the films N fractions observed in EDX analysis (**Table 4.2.4**). The results for SiMgNiC50600, in both this table and in **Table 4.2.2**, seem very different to the other samples, with drastically different G and D peak positions. Analysis was performed with fresh samples to check the validity of the results but no change was observed. Results collected were consistent across five different areas of the film suggesting homogeneity in the samples accuracy in the collected data.

4.2.1.2.3 TEM Analysis

Figure 4.2.9 summarises the morphology of the materials deposited at different temperatures.

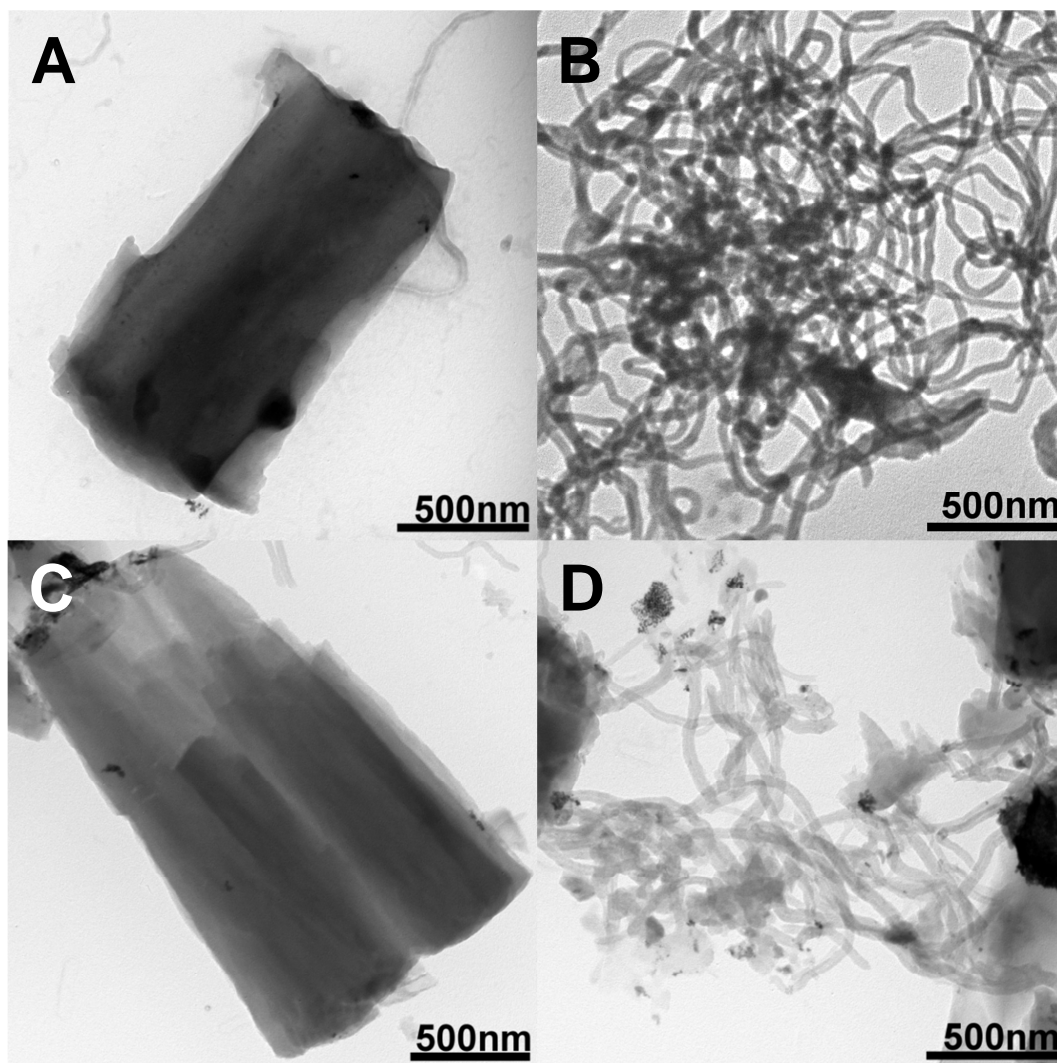


Figure 4.2.9. TEM images of carbonaceous species grown at 400 and 700 °C on SiMgNi substrates. A+B) Nanocolumns nanotubes grown at 400 °C, C+D) Nanocolumns nanotubes grown at 700 °C

Results for SiMgNiC50600 are reported in **Figure 4.2.5**. Nanocolumns and nanotubes remained the most prevalent materials identified although amorphous particles were seen (not shown). Nanocolumn thickness recorded from TEM analysis (**Figure 4.2.9**) was proportional to the film thickness results from the SEM analysis (**Figure 4.2.7**). The volume of nano-columnar structures identified within a sample increased as the deposition temperature increased. The nanotube arrangement on the TEM grid was very similar for both SiMgNiC50400 and SiMgNiC50600 with densely packed nanotube bundles made up of an assortment of different nanotube widths and lengths. The nanotube

bundles in SiMgNiC50700 were less prolific and were made up of far fewer, longer nanotubes (**Figures 4.2.9B and 4.2.9D**). The similarity of the structures present in SiMgNiC50400 and SiMgNiC50600 compared to the vastly different appearance of the structures in SiMgNiC50700 would suggest that an activation barrier limiting the rate of ordered growth is overcome as the deposition temperature increases to 700 °C. As the only factor varied in these tests was their deposition temperature, results would suggest that the increase in temperature provided additional energy to the free roaming deposited particles to bind in higher energy conformations, thus promoting ordered nanocolumn growth. This is in agreement with the finding that diffusion rate of unbound particles across a substrate surface has an exponential dependence upon temperature [270]. The mixed collection of different structures found (nanotubes, nanocolumns and amorphous film), as well as the variation in the nanotube diameters within each sample, show that the increased annealing temperature was unsuccessful in converting the nickel film into a homogeneous spread of nano-islands able to promote ordered growth of uniform CN_x nanostructures.

4.2.1.3 Analysis of CN_x films deposited at 600 °C in varying nitrogen atmospheres on SiNi substrates

Results of near identical studies performed without the magnesium deposition step are presented below to help further isolate the influences of nickel and nitrogen on the carbonaceous nanostructures.

4.2.1.3.1 SEM and EDX analysis

Figure 4.2.10 summarises the changes in film topography and thickness of CN_x films deposited onto SiNi substrates in varying nitrogen atmospheres at 600 °C. All images were collected in one analytical session on the same loading plate at a magnification of × 30,000.

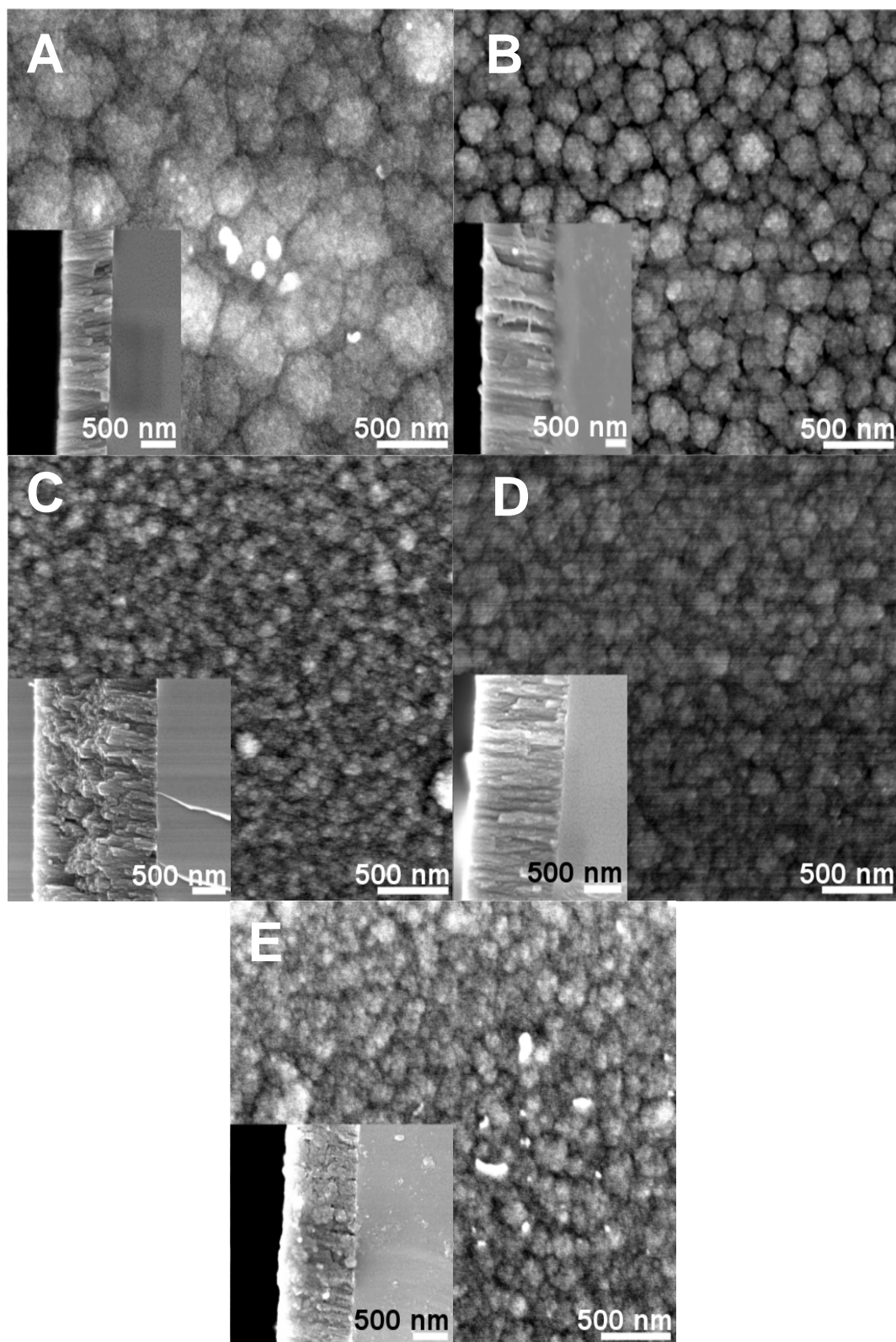


Figure 4.2.10. Surface topography and cross-sectional structures of SiNiCN_x deposited at 600 °C in varying nitrogen atmospheres. A) SiNiC0600; B) SiNiC25600; C) SiNiC50600; D) SiNiC75600; E) SiNiC100600.

The surface topography of the CN_x films deposited onto the SiNi substrates were similar to those deposited onto the SiMgNi substrates. **Figure 4.2.11** shows the variation in average film thickness and average cluster size with nitrogen content of the sputter gas.

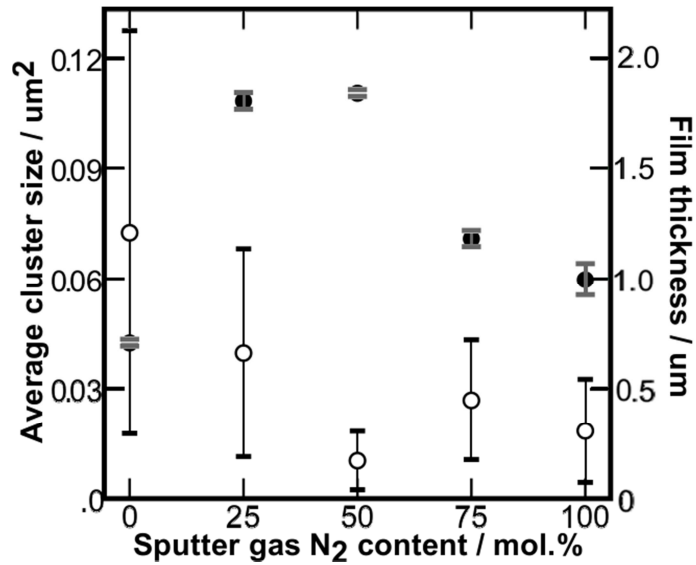


Figure 4.2.11. Variation in the film thickness (μm) and average cluster size (μm^2) with variation in the nitrogen content of the sputter gas (vol.%) of CN_x films deposited on SiNi substrates at 600 °C. Key: (●) film thickness; (○) cluster size. Error bars represent ± 1 SD from the average.

Average cluster size once again decreased with increasing nitrogen content confirming that nitrogen promotes ordered columnar growth. As discussed in **Section 4.2.1.1.1**, incorporation of nitrogen lowers the energy barrier against formation of curved graphitic planes, assisting ordered growth, whilst also increases the deposition rate and energy of the sputtered particles, further promoting growth [154]. Thickness was again shown to increase then decrease with nitrogen content, although this time SiNiC25600 was proportionally thicker, compared to the thickest film deposited, SiNiC50600 (**Figure 4.2.11**), than SiMgNiC25600 was to SiMgNiC50600 (**Figure 4.2.2**).

An explanation for this observation, along with an improved understanding of nickel's role in the promotion of ordered growth can be

found by comparing the cluster sizes and film thicknesses of the CN_x films deposited on SiMgNi substrates (**Figure 4.2.2**) to those deposited on the SiNi substrates (**Figure 4.2.11**). With the exception of films grown under pure argon, films deposited on SiMgNi substrates had larger average cluster sizes whilst films grown on SiNi substrates were thicker. The decrease in cluster size for all films grown on the SiNi substrates suggests that there were more points for nucleation of ordered growth, resulting in a closer packed system. As with the SiMgNi films, before a column could grow vertically they would first expand horizontally until van der Waals repulsions from surrounding nanocolumns forced vertical growth [265]. An increased packing density of nucleation sites limited horizontal nanocolumn widening, reducing the curved appearance of the bottoms on the nanocolumns observed in **Figure 4.2.1B**, and promoted vertical growth, increasing the film thicknesses.

The thickness of the CN_x films decreases as the nitrogen content of the sputter gas increases because of nitrogen etching as discussed in **Section 4.2.1.1.1**. The reduction in thickness also explains the downward trend in cluster sizes of CN_x films grown on SiNi substrates, because the reduced growth rate of the films prevents superposition of faster growing tubes reducing the apparent cluster density, as discussed in **Section 4.2.1.2.1**.

Both SiMgNi and SiNi substrates were shown to promote some ordered growth in carbon films deposited in a nitrogen free atmosphere. This is evidenced from the cross-sectional inserts in **Figure 4.2.1A** and **Figure 4.2.10A**, as well as TEM results in **Figure 4.2.5** and **Figure 4.2.13**. As concluded in **Section 4.2.1.1.1**, the low rate of sputtering eventually hindered ordered growth on SiMgNiC0600 and reduced the structure to an amorphous film [285]. In SiNiC0600 (**Figure 4.2.10A**) ordered growth remains apparent throughout the films thickness and is clearly observed in the film's topography, suggesting that the improved nickel dispersion, that helped promote an increased nanocolumn density, was sufficient to help the growing film retain its ordered structure. The overall thickness of the

carbon layer formed on SiNiC0600 is only fractionally thicker than that formed on SiMgNiC0600 films, showing that the growth rate remained slow despite the increase in order.

All the above conclusions point to a greater carbonaceous growth rate on top of the SiNi substrate than the SiMgNi substrate and an increased nucleation density in the SiNi films increasing their average cluster density and reducing the average cluster size (number of clusters per μm^2). These findings mean that that annealed films of pure nickel generated a finer dispersion of catalytic growth sites than nickel dispersed over magnesium. To improve the understanding of how the annealed nickel film promotes growth SEM analysis of the nickel film following 30 minutes annealing at 600 °C was performed. **Figure 4.2.12** shows a topographical view of the nickel film annealed across a silicon substrate.

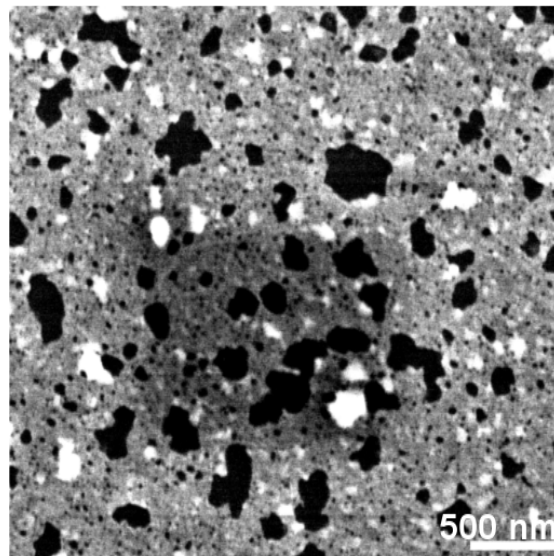


Figure 4.2.12. Appearance of Ni film annealed on the surface of a silicon substrate for 30 minutes at 600 °C.

It seems prudent to note that because this film has been subjected to a further 15 minutes cooling to room temperature, exposure to atmosphere, and other external influences during storage and transport, the structure will not be identical to the structure that carbon would have been deposited onto. Appearances would suggest that the nickel film (**grey sections in Figure 4.2.12**) had only decomposed slightly following

the annealing step and was still a patchy film as oppose to a dispersion of nano-islands with only a fraction of the silicon substrate exposed to the surface (**black sections in Figure 4.2.12**). The white sections are likely to be areas where the nickel film has either pooled during cooling or flaked during storage and has overlapped on the substrate, generating a stronger secondary electron reflection and a whiter intensity. Whilst it was expected that a nano-island dispersion as prepared by Scalese *et al.*[277] in the literature would promote increased ordered growth, this semi-decomposed film appears to have performed just as well. Possible explanations for the improved performance were informed by the results of TEM analysis and will be discussed in the results section of **Section 4.2.1.3.3**.

One factor that could influence the nickel film that could not be studied, but which will be discussed as a possible direction for future work (**Chapter 7**), is the influence of the bombarding carbon particles on the nickel film in the first few seconds of deposition. The energy they provide may have been sufficient to further modify the films appearance, perhaps generating a surface texture more commonly linked with catalysis of carbonaceous nanostructures [277].

EDX analysis was performed to identify the nitrogen fraction of the growing films. Results are presented in **Table 4.2.6**

Table 4.2.6. C:N ratio of the films deposited under different nitrogen atmospheres onto SiNi substrates, measured by EDX analysis.

Sample	Sputter gas N ₂ content (vol.%)	Carbon composition (%)	Nitrogen composition (%)
SiNiC0600	0	100	0
SiNiC25600	25	91	9
SiNiC50600	50	82	18
SiNiC75600	75	81	19
SiNiC100600	100	77	23

Results show that the nitrogen composition of the films increased with the nitrogen content of the sputter gas. This is as would be expected because of the increased nitrogen content of the system and is in agreement with the literature [2, 266, 277]. This trend contrasts the results for films grown on SiMgNi substrates (**Table 4.2.1**). Despite this reversal of trend it is only results for the films grown in 25 vol.% and 100 vol.% nitrogen atmospheres that are actually considerably different from each other. Erroneous results were eliminated as repeat testing on multiple samples was performed. The main difference between samples is the presence of the magnesium layer, although how that could have influenced the nitrogen uptake is unclear.

4.2.1.3.2 Raman analysis

Results of the Raman analysis of the carbonaceous films deposited on SiNi substrates at 600 °C are presented in **Table 4.2.9**. Additional Raman spectra for each sample run in this study can be found in **Appendix C**.

Table 4.2.7. Summary of the results of Raman analysis of CN_x films deposited on SiNi substrates.

	D peak position (cm ⁻¹)	G peak position (cm ⁻¹)	I _D /I _G ratio	I _G /I _N ratio
SiNiC0600	1350	1593	2.06	0.00
SiNiC25600	1372	1575	1.85	5.39
SiNiC50600	1385	1578	2.19	5.85
SiNiC75600	1385	1575	1.84	6.73
SiNiC100600	1371	1575	1.89	4.06

The results collected for samples deposited on SiNi substrates follow similar trends to those deposited on SiMgNi substrates (**Table**

4.2.4). The gap between the D and G peak positions was at its widest for SiNiC0600, which again showed no nitrogen peak. This time SiNiC0600's high I_D/I_G ratio well above 2 suggests a more amorphous structure than the one grown on the SiMgNi substrate [208].

Again there was no trend between nitrogen content of the sputter gas and the I_D/I_G or I_G/I_N ratios. The conflicting influences of nitrogen on growth and etching are the likely causes of these results (**Section 4.2.1.1.1**). The G peak position and the I_D/I_G ratio of the samples deposited in a nitrogen atmosphere were lower than for SiNiC0600 (except for the I_D/I_G ratio of SiNiC50600) suggesting an increase in graphitisation with the addition of nitrogen. Which of the many effects of nitrogen discussed in **Section 4.2.1.1** is responsible for the increase in graphitisation could not be identified in this study. There was a smaller variation between the results of the films grown on SiNi substrates (**Table 4.2.7**) than there was in the results for films grown on SiMgNi substrates (**Table 4.2.4**). This observation may be due to a change in the fractional distribution of carbon nanostructures present in the films, as will be discussed in the TEM analysis below.

4.2.1.3.3 TEM analysis

TEM analysis of the CN_x films grown on the SiNi substrates contained three distinct structures. They are exemplified in **Figure 4.2.13**.

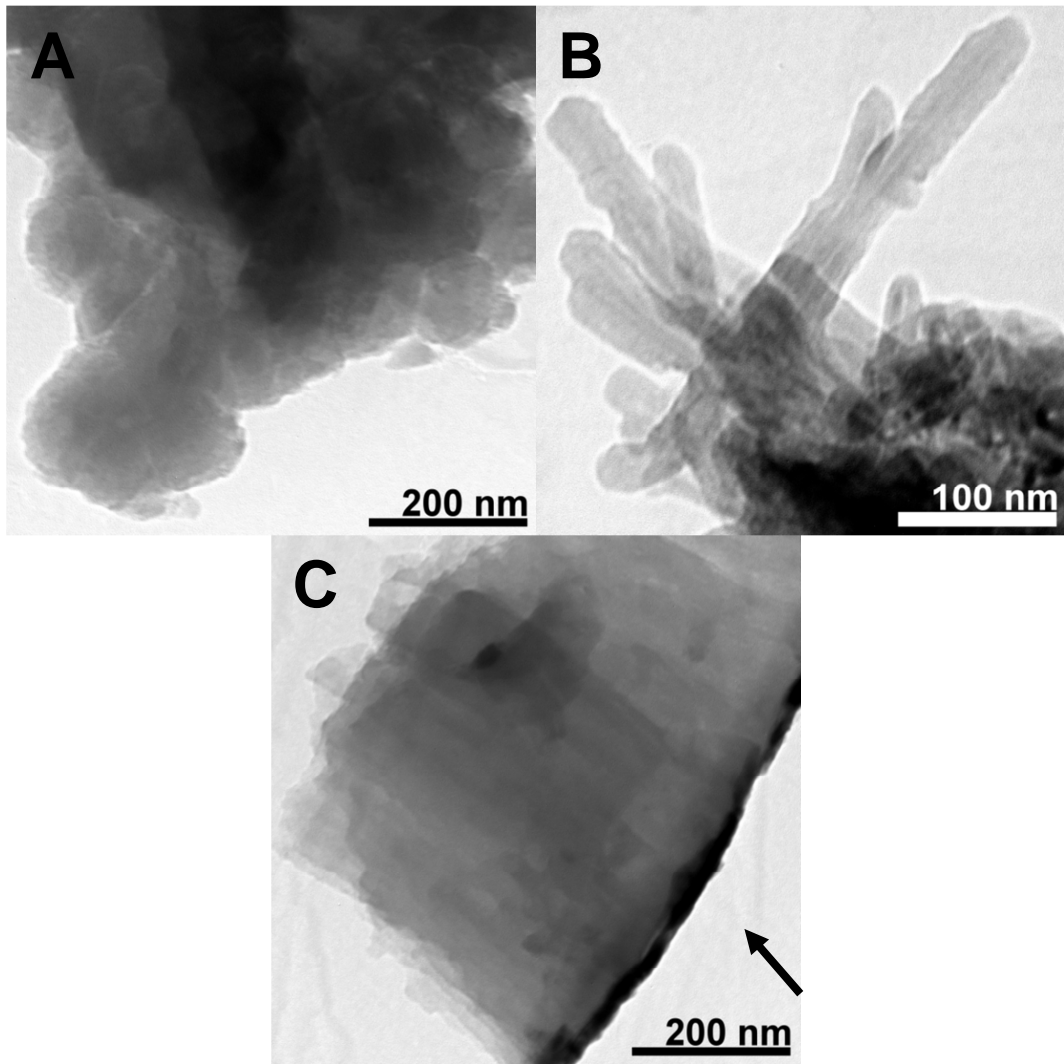


Figure 4.2.13. TEM images of carbonaceous species grown at 600 °C on a SiNi substrates. A) Amorphous carbon found in SiNi50600; B) Nanotubes found in SiNi75600. Black arrow identifies the nickel film attached to the base of the carbon structure; C) Ordered columnar structures found in SiNi100600.

Amorphous, nano-tubular and columnar structures, shown in **Figures 4.2.13A, 4.2.13B and 4.2.13C** respectively, were identified in all samples deposited in a nitrogen atmosphere. The SiNiC films were predominantly comprised of ordered columnar structures (**Figure 4.2.13C**) with a smaller fraction of nanotubes (**Figure 4.2.13B**) than in the SiMgNiC films. The nanotube fraction identified by TEM analysis again increased with nitrogen of the sputter gas content but tubes were shorter and narrower with average tube lengths no greater than 600 nm in any sample.

Evidence of amorphous carbon (**Figure 4.2.13A**) in all samples shows that the distribution of the nickel and the addition of nitrogen was still insufficient to homogenise ordered growth across the structure [210, 278].

SiC0600, grown in a nitrogen free atmosphere, showed no evidence of nanotubes and was comprised entirely of amorphous carbon and ordered columnar structures. The same was observed for SiMgNiC0600 showing that nitrogen was required for the curvature of the graphitic films for nanotube formation [2, 153].

Evidence of the type of nanostructures grown was used to determine the cause of the trends in film thickness and cluster size (**Figure 4.2.11**). The dispersion of the nickel film (**Figure 4.2.12**) promoted ordered growth despite the structure not meeting the expected requirements of a substrate as described in the literature [210]. From the ratio of nanocolumns to nanotubes identified in TEM analysis it appears growth was promoted because a different catalytic pathway was followed which promoted nanocolumn, rather than nanotube growth. Nano-islands dispersions described in the literature promote nanotube growth, however in this work nanotubes made up only a small fraction of the SiNiC films [277].

Nanocolumns were the most prolific material identified in TEM analysis of the SiNiC films. The growth of these structures appeared to be catalysed by a base-growth mechanism identified by the appearance of a dark metallic material at the base of the structures (**Black arrow in Figure 4.2.13C**). Whilst the nickel nano-island size is important for defining the width of a nanotube, nickel particle size does not appear to influence nanocolumn growth [270]. In light of this outcome, the magnesium layer seems to have functioned as intended- as a metal boundary layer to assist in the promotion of nanotube growth from nickel nano-islands dispersed on its surface- because nanotubes were more abundant in the films grown on SiMgNi rather than SiNi substrates. On SiMgNiC films, nanotubes were more prolific and longer suggesting that the magnesium layer has assisted in breaking down the nickel films into nano-islands for nanotube

promotion. The low propensity of CNTs identified in the SiNiC films indicates that not many nickel nano-islands of sufficient size to catalyse formation were generated during the nickel annealing step [210]. This outcome was corroborated by the film topography in **Figure 4.2.12**.

4.2.1.4 Analysis of CN_x films deposited at 600 °C onto silicon substrates under varying nitrogen atmospheres

The discussion below briefly outlines the results of the study of CN_x films grown directly onto the silicon substrate.

4.2.1.4.1 SEM and EDX analysis

SEM analysis of the topography of the CN_x films is presented in **Figure 4.2.14**. Thickness measurements were also collected by SEM but due to poor resolution of the films thickness analysis was instead collected by TEM analysis for these samples and will be discussed in **section 4.2.1.4.3**.

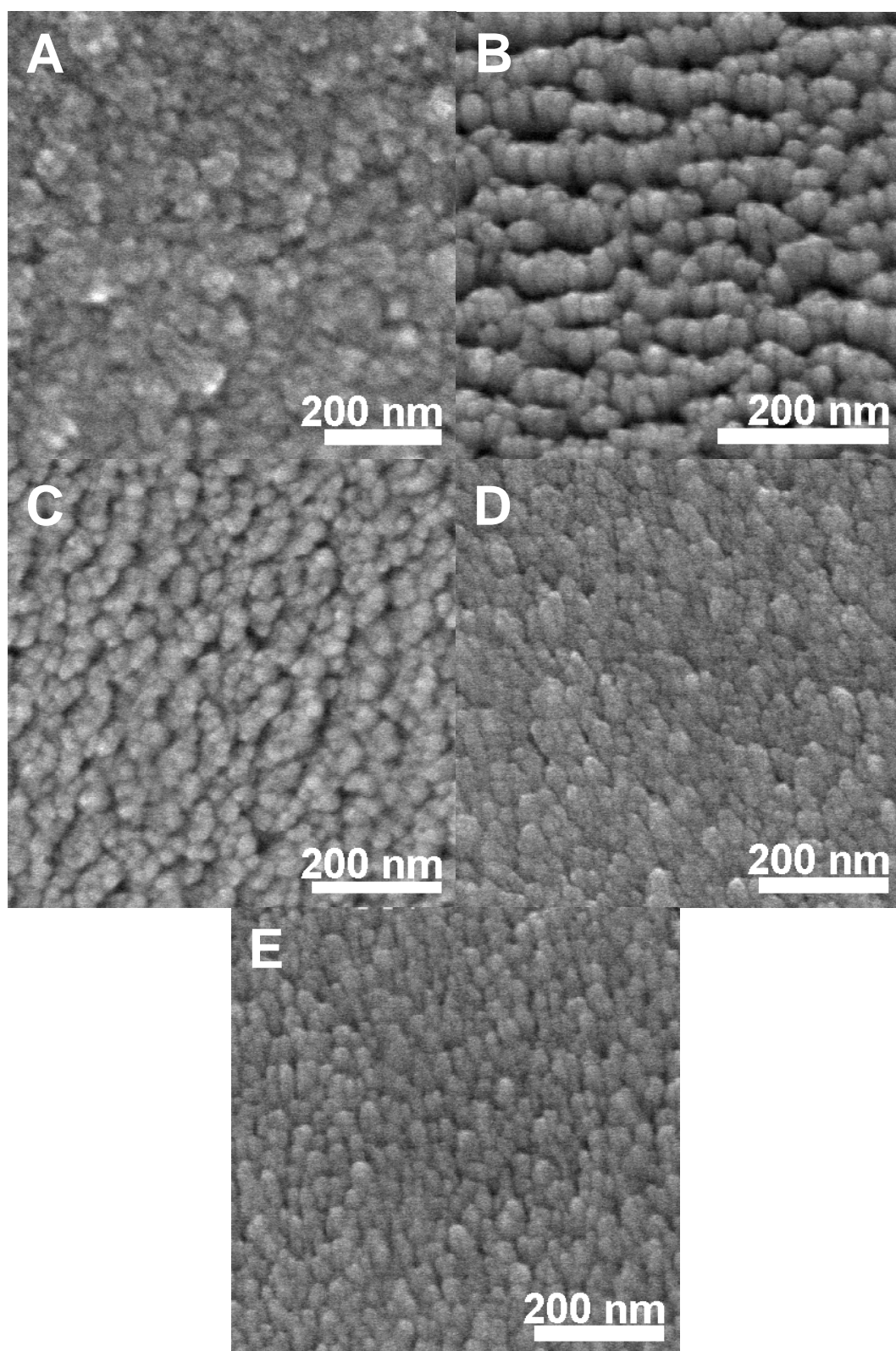


Figure 4.2.14. Topography of SiCN_x deposited at 600 °C in varying nitrogen atmospheres. A) SiC0600; B) SiC25600; C) SiC50600; D) SiC75600; E) SiC100600.

The topographical appearance of the films was drastically different to those of the films grown on SiMgNi substrates (**Figure 4.2.1**) or SiNi substrates (**Figure 4.2.10**). The ordered structures observed in this work lacked the tight clustered appearance seen in the other samples and instead appeared to form a dense forest of nanostructures similar in appearance to those found by Scalese *et al.* [154]. The film deposited onto silicon in a pure argon sputter atmosphere (**Figure 4.2.14A**) has a different topography to the films grown in the presence of nitrogen (**Figure 4.2.14B, 4.2.14C, 4.2.14D**). This change in appearance can be attributed to the lack of either nickel or nitrogen to promote the formation of a highly ordered structure in the film [152]. As the nitrogen content of the films increased the appearance of the ordered forest became less dense and each individual structure began to look less rounded and more elongated. The change in appearance is likely an effect of increasing nitrogen etching, as described in Section 4.2.1.1.1, damaging the growing structures [155, 266].

The EDX analysis was performed to analyse the C:N ratio of the deposited films. Results are presented in **Table 4.2.8**.

Table 4.2.8. C:N ratio of the films deposited under different nitrogen atmospheres onto Si substrates, measured by EDX analysis.

Sample	Sputter gas N ₂ content (vol.%)	Carbon composition (%)	Nitrogen composition (%)
C0600	0	100	0
C25600	25	89	11
C50600	50	88	12
C75600	75	86	14
C100600	100	86	14

The nitrogen loading of the CN_x films grown on silicon substrates matches the trends for the SiNiC films (**Table 4.2.6**) but at lower fractional

nitrogen loadings. This is likely because of the greatly reduced growth rate of these films as observed by their reduced film thicknesses. A reduced growth rate increases the time loosely bound volatile nitrogen species are given to escape from the structure before they are irreversibly locked within the structure as they react with freshly deposited carbons.

4.2.1.4.2 Raman analysis

Results of the Raman analysis of the carbonaceous films deposited on Si substrates at 600 °C are presented in **Table 4.2.9**. Additional Raman spectra for each sample run in this study can be found in **Appendix C**.

Table 4.2.9. Summary of the results of Raman analysis of CN_x films deposited on Si substrates.

	D peak position (cm ⁻¹)	G peak position (cm ⁻¹)	I _D /I _G ratio	I _G /I _N ratio
SiC0600*	1360	1580	2.47	0.00
SiC25600*	1394	1579	2.28	3.31
SiC50600**	1391	1579	2.10	5.30
SiC75600**	1381	1575	1.97	5.31
SiC100600*	1389	1579	2.13	3.39

Once again the film grown in the absence of nitrogen had a higher I_D/I_G ratio than the samples grown in a nitrogen atmosphere, and showed no N peak. No trend was observed in the I_D/I_G ratios of the films with increasing N₂ content of the sputter gas. The I_D/I_G ratio of these samples marked with an (*) were the highest recorded compared to those deposited on SiMgNi or SiNi substrates (**Tables 4.2.2** and **4.2.7**) and the samples marked ** were the second highest recorded. These increased values suggest that these films were the least graphitic of the structures

analysed. This is likely due to the absence of a catalytic metal fraction of the substrates to promote ordered growth [152, 154].

4.2.1.4.3 TEM analysis

TEM analysis of the CN_x films deposited onto silicon substrates at 600 °C in varying nitrogen atmospheres was performed to characterise the nanostructures observed in SEM analysis. The images in **Figure 4.2.15** are examples of the two types of structure identified.

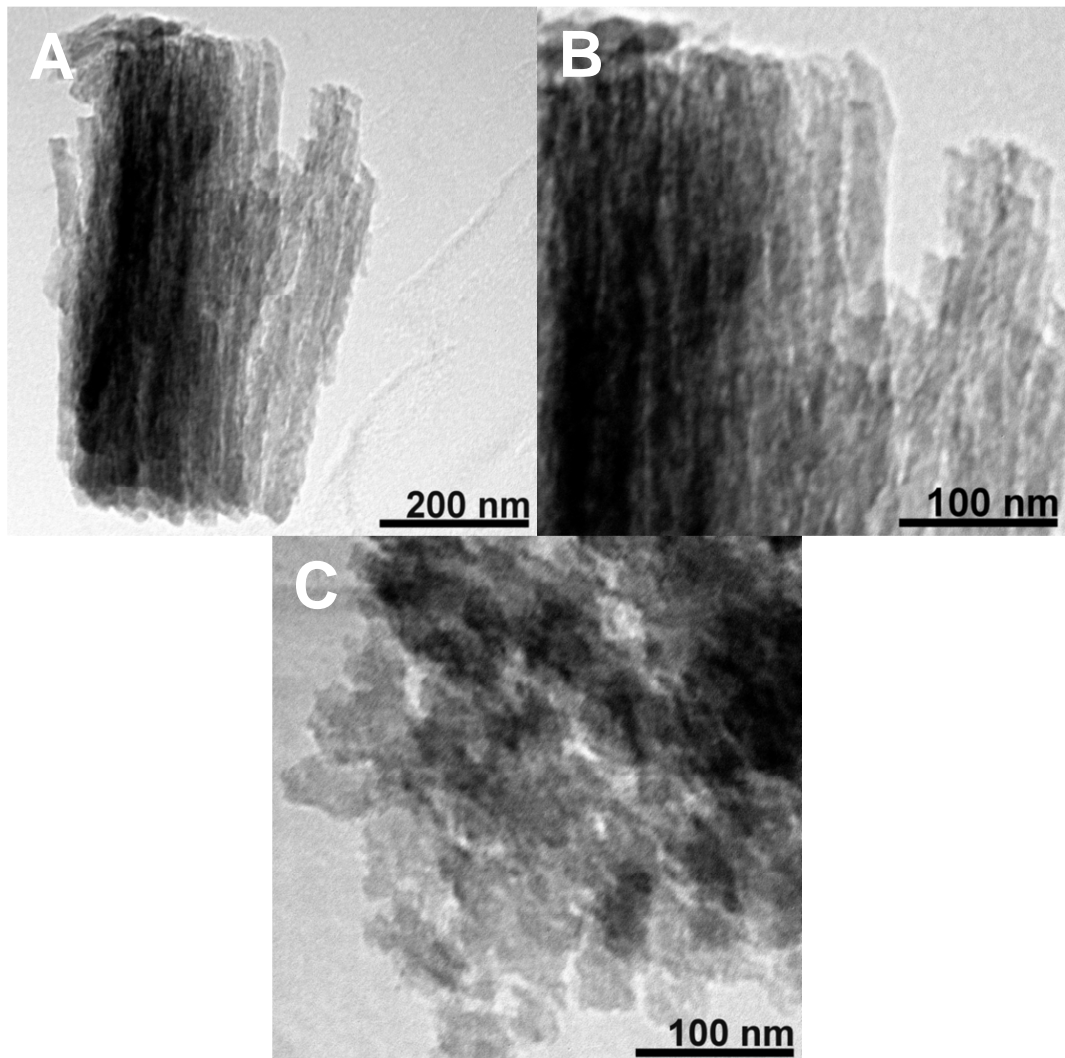


Figure 4.2.15. Examples of the structures identified in TEM analysis of SiC films. A) Structure of the ordered CN_x filaments identified in SiC75600 at low magnification; B) Closer examination of the same

nanofibers under higher magnification; C) Amorphous carbon films found in SiC0600.

From TEM analysis SiC0600 was entirely comprised of amorphous carbon structures similar to those in **Figures 4.2.15C** adding further evidence to the conclusion that ordered growth required nitrogen or nickel to reduce the energy barrier against ordered columnar growth [271]. Amorphous carbons were also identified in all the samples deposited in a nitrogen atmosphere. All samples deposited in a nitrogen atmosphere showed evidence of the ordered nanofibers identified in **Figures 4.2.15A** and **4.2.15B**. The appearance of the ends, and the lack of a resolvable core in the nanofibers observed in **Figures 4.2.15A** identifies that they are not nanotubes. Unlike the structures identified in the other samples these structures did not grow wider as they grew away from the substrate. The lack of column widening could either be a feature of the specific materials deposited or, given the packing density of the grown structures could be a result of van der Waals repulsive forces between growing columns [265].

Thicknesses of the carbonaceous films deposited on silicon substrates at 600 °C were measured using their TEM and SEM images. Results are presented in **Figure 4.2.16**.

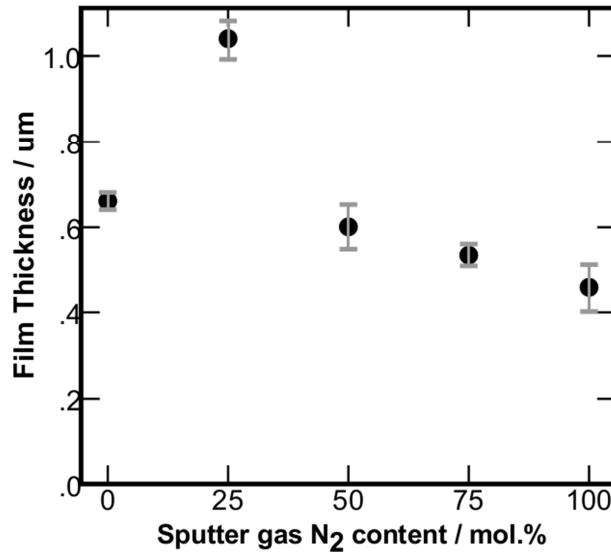


Figure 4.2.16. Variation in the film thickness (nm) with variation in the nitrogen content of the sputter gas (vol.%) of CN_x films deposited on silicon substrates at 600 °C. Error bars represent ± 1 SD from the average.

The total film thicknesses were far smaller for these materials than for films deposited on SiMgNi (**Figure 4.2.2**) or SiNi (**Figure 4.2.11**) substrates. The lack of nickel seems to severely inhibit the rate of growth, as evidenced by the reduced film thickness, identifying that the nickel layer catalytically promotes CN_x nanostructure formation and increases the rate of growth. The trend of an increase followed by a decrease in film thickness with nitrogen content of the sputter gas was again seen in these samples (**Figure 4.2.16**) showing the competing influences of nitrogen's incorporation, as discussed in **Section 4.2.1.1.1**, was still evident. The thickness of SiC0600 was calculated from SEM analysis because the direction of growth in the amorphous carbons imaged by TEM could not be verified. SiC0600 was similar in thickness to SiMgNiC0600 and SiNiC0600 showing that at equivalent rates of growth, without nitrogen effects such as etching or addition of curvature, the deposition rates remain similar.

4.2.2 Thermogravimetric analysis of hydrogen storage

At the time this work was performed, separation of sputtered films from the silicon substrates was not reliably achievable by any method that had been found in the literature without compromising the material integrity [273]. Furthermore, the deposited masses of the films were too small to provide adequate stability to the gravimetric balance's hang-down, preventing accurate measurement. To counter these problems the hydrogen storage capacities of the materials were measured still loaded on the silicon substrates. SEM cross-sectional images gave no impression that there was any alteration in the structure of the silicon materials after the deposition process so the variation in storage capacity is due entirely to the deposited film. The silicon substrate was a dead weight on the system and made up approximately 97 % of the total mass of the sample, yet despite its significant influence on the materials storage capacity results could still be used to determine trends in the influence of nitrogen sputter gas and the SiMgNi, SiNi or Si substrates on the deposited materials' hydrogen adsorption. The resolution of the apparatus balance was sufficient to accurately report the results despite the limited hydrogen uptake.

Isothermal data points collected below 50 mbar hydrogen and helium pressure were excluded from the results due to inaccuracy in the data collection methods. The reason for the inaccuracy related to the temperature and balance stabilisation of the thermogravimetric apparatus at low pressures. To calculate an accurate sample reading the balance requires time to stabilise and stop kinetic interference providing false results. At low pressure this takes longer as in a near perfect vacuum there are no opposing forces working against the balance to slow its movement. Unfortunately, when working at low temperatures and low pressures longer stabilisation times allow thermal conductance, presumably through the apparatus, to increase the temperature of the sample, disrupting the thermal accuracy of the data point. Despite attempts to improve accuracy, data below 50 mbar could not be accurately

collected at 77 K. Similar problems were not encountered at 298 K as thermal conductance was not as significant a problem allowing for longer stabilisation times.

4.2.2.1 Density correction and anomalous results

The IGA apparatus used to calculate hydrogen storage capacity measures the change in a sample's weight with a change in the pressure of the system. The sample balance is however not only influenced by the weight of the sample, it is also influenced by the gas pressure of the system, which depending upon the pressure can either increase or decrease the recorded weight of the balance and misinform the calculation of the materials storage capacity [227]. The influence of the gas on the balance can be corrected for using the buoyancy correction equation (not shown), which is performed automatically by the apparatus, to predict the correct material adsorption capacities. One of the key variables required for the buoyancy correction is the density of the sample [227].

Sample densities were initially estimated to be equivalent to that of pure silicon (2.329 g.cm^{-3}), but results obtained using this assumed value were inconsistent and unreasonably large.

Significant work was therefore undertaken to refine the sample densities. Of the different methods attempted, calculation of the actual sample density from helium isotherms, performed from 100-700 mbar at 77 K, provided the greatest accuracy. Despite this, analysis of the isothermal data presented in **Figures 4.2.18** and **4.2.19** still identified two anomalous isothermal trends for hydrogen uptake at 298 K. Hydrogen storage capacities of SiMgNi0600 at 298 K (\circ in **Figure 4.2.18B**) and SiMgNiC50700 at 298 K (\blacktriangledown in **Figure 4.2.18B**) are believed to be anomalous because they had higher hydrogen storage capacities at room temperature than at 77 K, and their storage capacities do not fit the trends observed by the other materials. The peculiarity of these results appears to be linked to their calculated densities and its influence on the ensuing

buoyancy correction to calculate the materials hydrogen storage capacity [227]. **Figure 4.2.17** shows the recorded densities for the samples.

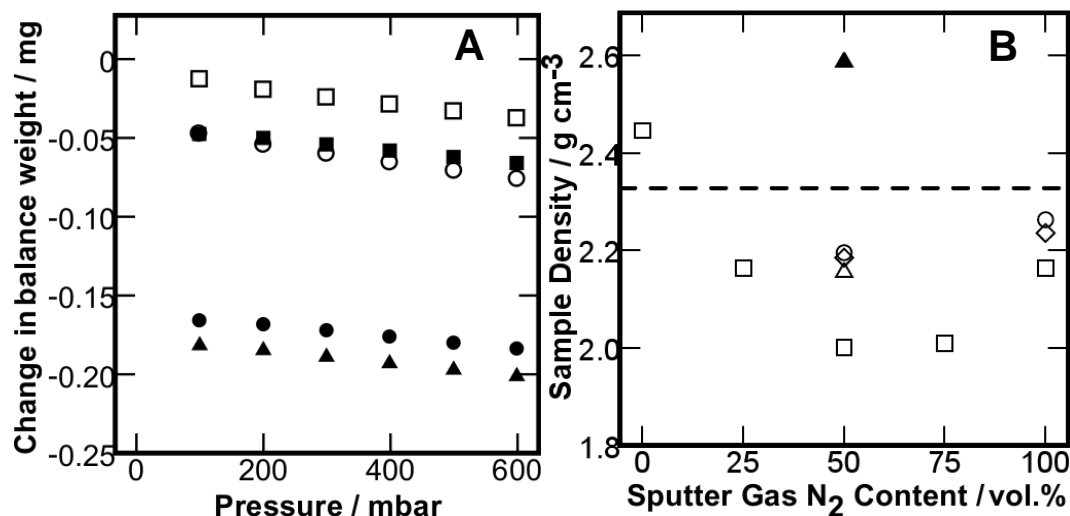


Figure 4.2.17. A) Example of He isotherms used for calculation of sample buoyancy. Key: (□) SiMgNiC0600; (●) SiMgNiC25600; (▲) SiMgNiC50600; (■) SiMgNiC75600; (○) SiMgNiC100600. B) Variation in the recorded sample densities (g.cm⁻³) with the nitrogen sputter gas fraction of the deposition process (vol.%). Key: (□) SiMgNiC600 films; (◇) SiNiC600 films; (○) SiC600 films; (Δ) SiMgNiC400 film; (▲) SiMgNiC700 film; (Dashed line) Density of silicon.

He isotherms in **Figure 4.2.17B** show the typical decrease in recorded sample weight with increasing pressure caused by the buoyancy effect. The linear gradient of the data points as should be expected for the data. The anomalies occurred in the two samples with densities that exceeded the density of silicon (2.329 g.cm⁻³; **dashed line** in **Figure 4.2.17**). For the work performed in previous and subsequent chapters of this thesis density calculation was found to be of less importance and had a smaller overall influence on the total storage capacity of the materials. The high impact of very small changes in sample density in this chapter is because of the limited total H₂ storage capacity of the materials when bound to the substrates.

No trend between estimated sample density and hydrogen storage capacity of the samples was found suggesting that the results presented

below are not being governed by inaccurate data collection and are in fact representative of the sputtered materials.

4.2.2.2 Hydrogen storage capacities of films deposited on SiMgNi substrates at 600 °C in varying nitrogen atmospheres

Figure 4.2.18 shows the hydrogen storage capacities of CN_x films grown on SiMgNi substrates in varying nitrogen atmospheres. Experimental results were modelled using the Toth equation (**Equation 3.31**) and the interpolation lines in the figures represent the best fit isothermal curves. They were included to assist interpretation of the results. The R^2 fit of the Toth model (**Equation 3.31**) exceeded 0.860 for all models, except SiMgNiC50700's isothermal run at 298 K. The reduced R^2 value, of 0.816, for this model was because of a hysteresis loop between the adsorption and desorption curves forcing the modelled data to sit between the two sets of results rather than closely follow either adsorption or desorption curve.

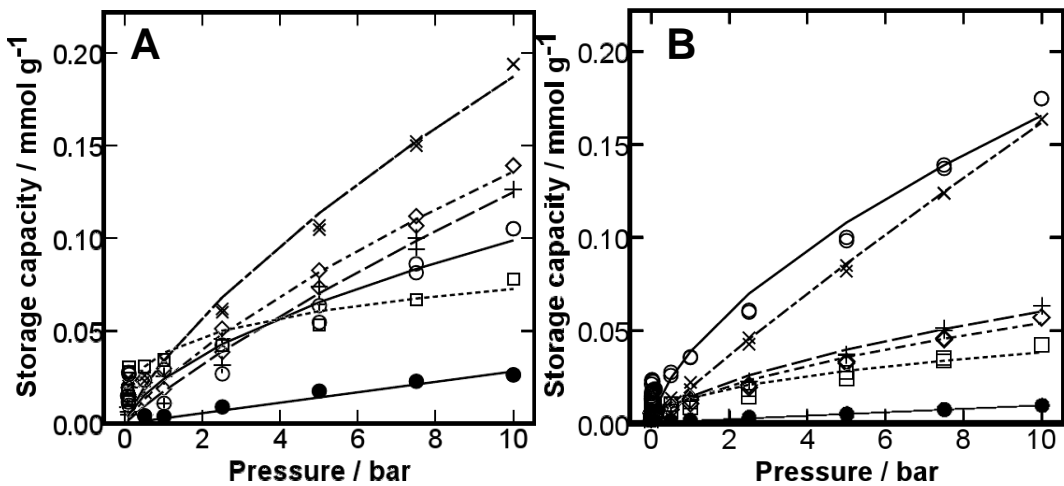


Figure 4.2.18. Isothermal H_2 storage capacities ($mmol.g^{-1}$) of SiMgNiC600 films with an increase in pressure (bar) at 77 (A) and 298 K (B). Key: (●) Silicon control; (○) SiMgNiC0600; (□) SiMgNiC25600; (◇) SiMgNiC50600; (+) SiMgNiC75600; (x) SiMgNiC100600.

Pure silicon unsurprisingly had the smallest storage capacity, $0.0312 \text{ mmol.g}^{-1}$ (0.0059 wt.%) and $0.0093 \text{ mmol.g}^{-1}$ (0.0019 wt.%) at 77 and 298 K respectively, (\bullet in **Figures 4.2.18A** and **4.2.18B**) as its surface had limited porous character. Addition of the carbon film increased hydrogen adsorption in all cases at least twofold and was likely due to the increase in material porosity provided by the carbon film serving as adsorption sites for H_2 . This conclusion is in agreement with the literature, but remains unverified as pore size analysis of these materials could not be performed whilst bound to the silicon. The deposited film with the highest combined storage capacities at both 77 and 298 K of $0.1942 \text{ mmol.g}^{-1}$ (0.0391 wt.%) and $0.1636 \text{ mmol.g}^{-1}$ (0.033 wt.%) respectively, was SiMgNiC100600 (\times in **Figures 4.2.18A** and **4.2.18B**). SiMgNiC75600 and SiMgNiC50600 performed similarly at both temperatures, outperforming SiMgNiC25600.

The high storage capacity of SiMgNi0600 (\circ in **Figure 4.2.18B**) at 298 K is believed to be anomalous for reasons described above. Discounting this anomalous result it appears that increasing nitrogen content of the sputter gas increases the performance of the deposited film as an adsorbent. No simple trend between the mass of the samples, the mass of the deposited films, the nitrogen contents of the films (**Tables 4.2.1**), the films carbon cluster sizes, or the film thicknesses (**Figures 4.2.2**) could be found to explain the trend in hydrogen adsorption. With no simple relationship apparent it seems likely that the complex relationship nitrogen had with film growth, as described in **Section 4.2.1.1.1**, is also responsible for the trends in hydrogen storage capacity. Whilst an accurate quantitative analysis could not be performed, the increase in the nanotube fraction of the films, seen to increase with nitrogen content of the sputter gas in TEM analysis (**Section 4.2.1.1.3**), bears the closest resemblance to the trends in hydrogen uptake.

4.2.2.3 Hydrogen storage capacities of films deposited at varying temperatures on SiMgNi substrates within a 50 vol.% nitrogen atmosphere

Figure 4.2.19 shows the hydrogen storage capacities of CN_x films grown on SiMgNi substrates deposited at different temperatures in a 50 vol.% nitrogen atmosphere.

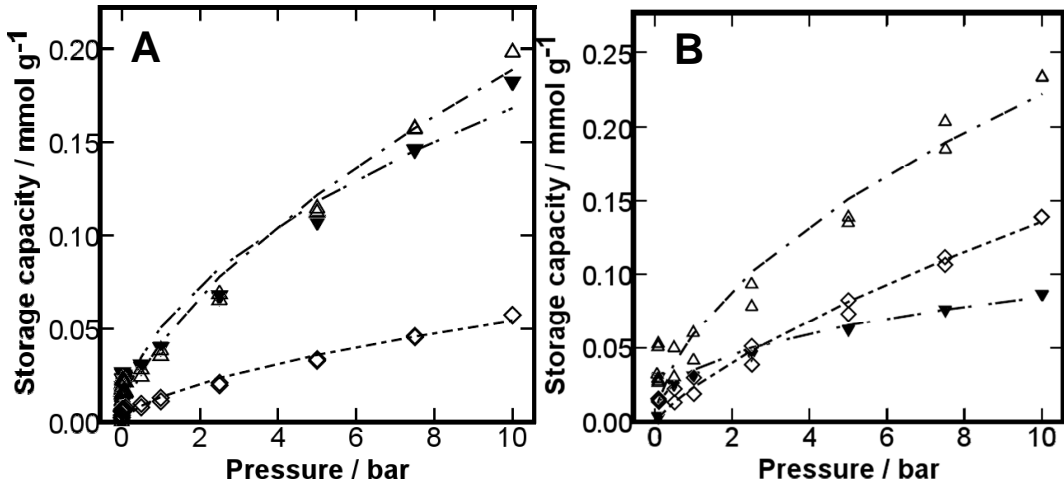


Figure 4.2.19. Isothermal H_2 storage capacities ($mmol.g^{-1}$) of SiMgNiC50 films with an increase in pressure (bar) at 77 K (A) and 298 K (B). Key: (Δ) SiMgNiC50400; (\diamond) SiMgNiC50600; (\blacktriangledown) SiMgNiC50700.

The highest storage capacities of $0.2335\text{ mmol.g}^{-1}$ ($0.0471\text{ wt.}\%$) and $0.1981\text{ mmol.g}^{-1}$ ($0.0399\text{ wt.}\%$) at 77 and 298 K respectively, were recorded for SiMgNiC50400. At 298 K, the isothermal result for SiMgNiC50700 (\blacktriangledown in Figure 4.2.19B) is thought to be anomalous for reasons described above. Discounting the anomalous result, at both 77 and 298 K, storage capacity was seen to decrease with the sputter deposition temperature. The closest correlation between trends in material structure and storage capacity was once again the prevalence of nanotubes which decreased as deposition temperature increased (Figure 4.2.9). Due to the variety of influences the nitrogen content of the sputter gas has had on the films growth it seems prudent to acknowledge that the relationship between nanotube prevalence and hydrogen uptake may or

may not be causal. The observed results may alternatively be due to influences such as the materials structure, density and nitrogen content working in combination. Inclusion of the silicon substrate was again responsible for the low storage capacities recorded.

4.2.2.4 Hydrogen storage capacities of films deposited on SiMgNi, SiNi or Si substrates at 600 °C in 50 or 100 vol.% nitrogen atmospheres

Only films deposited in 50 or 100 vol.% nitrogen atmosphere onto SiNi or Si substrates were tested for their hydrogen storage capacities. 100 vol.% nitrogen atmospheres were selected because they had the highest H₂ storage capacities for the SiMgNiC samples (**Figure 4.2.18**). 50 vol.% nitrogen atmospheres were selected because they deposited the thickest films (**Figures 4.2.2 and 4.2.11**). **Figure 4.2.20** compares the hydrogen storage capacities of the six CN_x films deposited in 50 or 100 vol.% nitrogen atmosphere onto SiMgNi, SiNi or Si substrates.

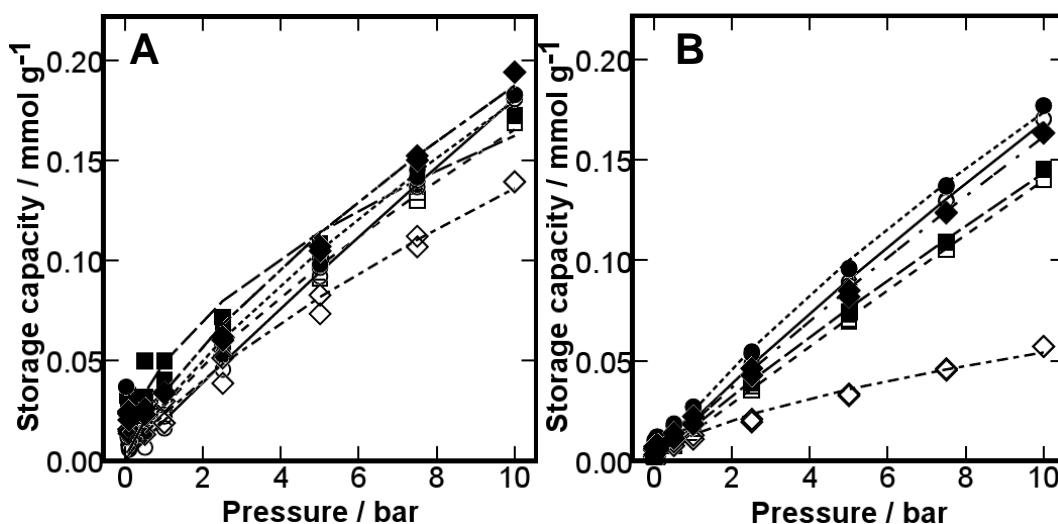


Figure 4.2.20. Isothermal H₂ storage capacities (mmol.g⁻¹) against pressure (bar) of CN_x films grown on different substrates in either a 50 or 100 vol.% nitrogen atmospheres at 77 (A) or 298 K (B). Key: (◇) SiMgNiC50600; (◆) SiMgNiC100600; (○) SiNiC50600; (●) SiNiC100600; (□) SiC50600; (■) SiC100600.

The highest storage capacity recorded at 77 K was $0.1942 \text{ mmol.g}^{-1}$ (0.0391 wt.%) for SiMgNiC100600, and at 298 K was $0.1772 \text{ mmol.g}^{-1}$ (0.0357 wt.%) for SiNiC100600. The storage capacity of the adsorbents deposited on SiNi and Si substrates were fractionally better when deposited in a 100 vol.% nitrogen atmosphere (Shaded markers in **Figure 4.2.20**). The minor variation in hydrogen uptake between films sputtered in 50 and 100 vol.% N_2 atmospheres, compared to the variation between the storage capacities of the SiMgNiC films (**Figure 4.2.18**) was due to the reduced variation in the nano-structural composition of the SiNiC and SiC films, resulting in similar material structures being deposited within different nitrogen atmospheres and smaller variation in the total hydrogen storage capacities. TEM analysis identified that SiMgNiC films varied from predominantly amorphous, to nano-columnar to a mix of nano-columns and nanotubes from low to high nitrogen loadings (**Figure 4.2.5**). Whilst the nanotube fraction of the SiNiC films (**Figure 4.2.13**) increased with nitrogen sputter gas content, the films remained predominantly nano-columnar in structure. Following addition of nitrogen, SiC films (**Figure 4.2.15**) were comprised almost entirely of densely packed nanocolumns.

The storage capacity of the films increased with a decrease in the isothermal temperature, but by comparison to the literature the extent of change in the capacity was very small [254]. Reduced variation in storage capacities at different temperatures was due to the low total uptake of the materials. Adsorption was still more prevalent at low temperatures as observed by the increased gradient of the isothermal trends in **Figure 4.2.20A** compared to those in **Figure 4.2.20B**.

Films deposited on SiNiC substrates and SiMgNiC100600 performed better than the films deposited in the Si substrates showing that ordered structures, whose growth was catalysed by nickel had an increased H_2 storage capacity at 10 bar.

As with the density checks, the validity of this data was considered by comparing the storage capacity profiles against the characteristics of

the materials. There was no correlation found between masses of the silicon substrates prior to deposition, or the masses of the deposited films and the trends in overall storage capacity. Nor, with the exception of the errors already discussed, was the density of the collected films seen to be primarily responsible for the results. The range of experimental weight data, collected within samples from low to high pressure was, at its smallest 180 times greater than the resolution limit of the apparatus showing that even within the experimental error of the scales the change in the sample mass was significant.

Attempts were made to extrapolate the storage capacities of the deposited films by subtracting the recorded storage capacity of silicon from the results and to re-evaluate the film mass based upon the difference between the mass of the substrate before and after deposition. Unfortunately an adequate model was not completed as factors such as how to accommodate for the buoyancy corrections influence on the materials, and how to assess the contribution of the metal underlayers could not be overcome.

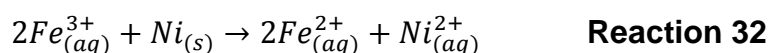
4.2.3 Adsorbent performance of cleaved CN_x films

As previously discussed, measuring the hydrogen storage capacities of the films was far from ideal whilst they were still loaded onto the silicon substrates. An additional test was devised to measure the hydrogen storage capacity of one of the films free from the dead weight of the silicon. The largest hydrogen storage capacity measured was for SiMgNiC50400 (Δ in **Figure 4.2.19**) so this material was selected. The process required mass production of the film to ensure that a reasonable quantity was recovered for testing. Sputter deposition was repeated on forty eight 1 cm² silicon wafers. The average mass of the deposited films from 48 samples was 0.189 mg. The full mass recorded for the deposited films, including the magnesium and nickel layers, was 9.08 mg after sputtering (but before cleavage).

4.2.3.1 Separation of the CN_x films from the substrate

The process required efficient cleavage of the film from the substrate. Several approaches were tested with varying degrees of success;

1. Scratch testing- scratching the films surface with a sharp blade was able to cleave the film from the substrate but was inefficient for removal of the entire film.
2. Sonication in acetone- Following sonication, evaporation of the acetone caused the films to bubble and peel and this increased the yield of film recovered compared to scratch testing. Performance however, was inconsistent from film to film.
3. Micromechanical cleavage [189]- films were coated with adhesive tape. Careful peeling of the tape at an angle horizontal to the substrate lifted the foil off the substrate. The foil was then separated from the tape by immersion in 25 ml pure benzene to dissolve the adhesive. This purification of the sample to remove the adhesive proved difficult and substantially reduced the yield of material recovered
4. Acid etching [198]- Immersion in 10 % hydrochloric acid or nitric acid solution effectively cleaved the film from the substrate but the oxidation of the metal generated hydrogen gas bubbles which fractured the film and made sample collection difficult.
5. Etching in acidified aqueous Iron (III) chloride [198]- This process relied upon the oxidative etching of the nickel (and magnesium) layers through **Reaction 32**.



This method digests the metal fraction of the substrate and whilst gaseous hydrogen was still produced, its formation was slower and less destructive to the film. Mild acidification prevented metal oxide precipitation onto the film which would contaminate the sample.

Etching in acidified aqueous Iron (III) chloride allowed cleavage of full undamaged CN_x films from the substrates so was used for the mass separation of the SiMgNiC50400 film. **Figure 4.2.21** illustrates the separation process.

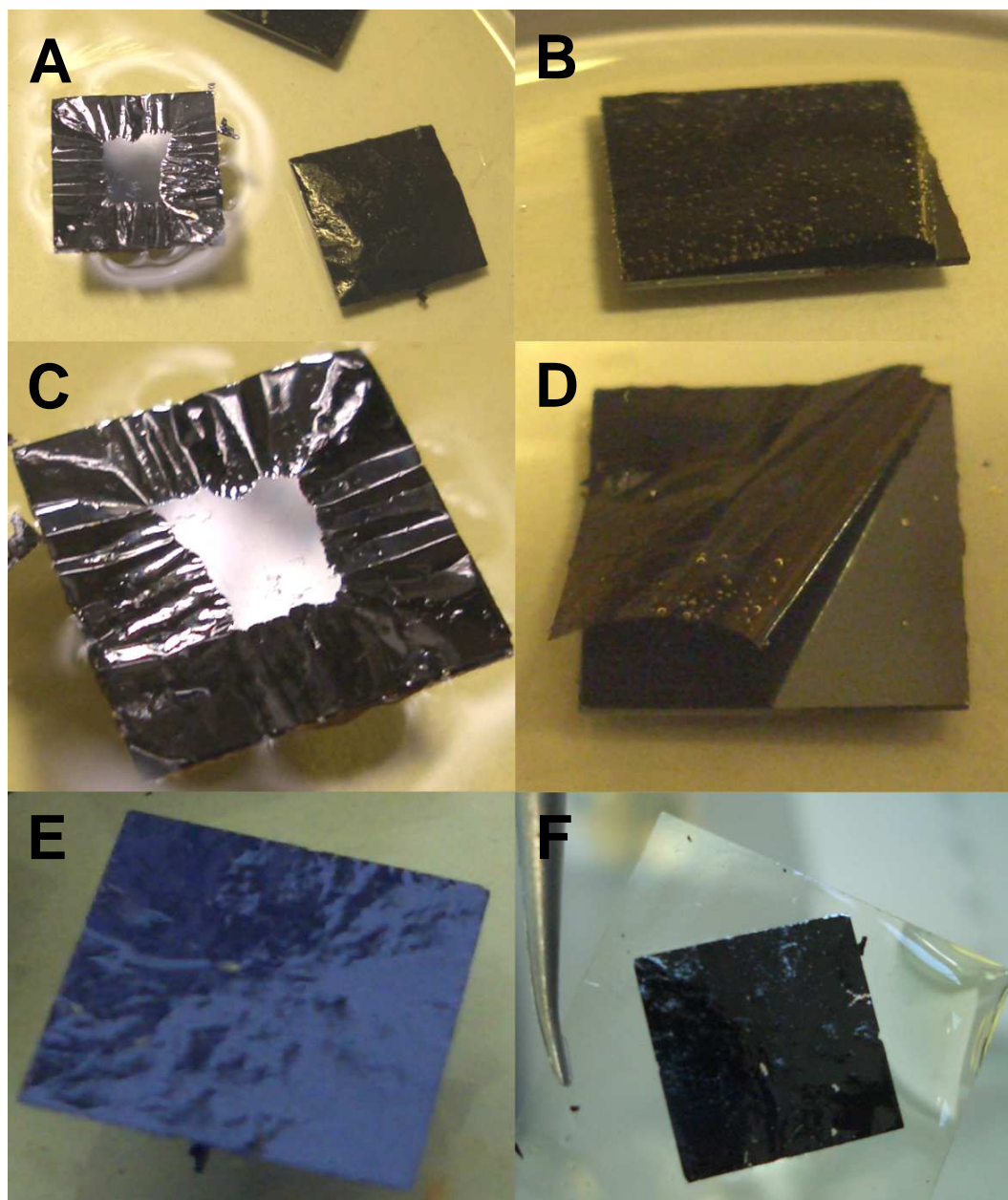


Figure 4.2.21. Foil separation tests. A) Samples balanced on the surface or immersed in the solution. B) Bubble formation on the immersed foils. C) The different separation processes for surface or immersed samples. D) Separated foils on the surface of the solution and collected on a glass slide. E) Separated film floating on the

surface of the solution. F) Separated film transferred onto a glass slide.

It was observed that samples immersed in the solution would separate from the substrate far faster than those balanced on the surface but during the digestion of the metal film small gas bubbles would escape through the carbon layer (**Figure 4.2.21B**) and in some cases the foil would curl up (**Figure 4.2.21C**). Subsequent separation tests were performed on the surface of the solution to prevent potential damage to the films by the bubbles and to improve the ease of foil collection. Foil collection could also be performed without causing any damage but only after several failed attempts. The separated foils were strong and flexible for their size but can be easily dispersed when sonicated within a solution.

The recovered mass after film separation was approximately 6 mg compared to the estimated total content of 9 mg (see above). Variation between the deposited and collected masses was due to in part to CN_x foil lost in separation and also due to the removal of the now digested metal layers. EDX analysis revealed that the foils were 97.5 % carbon, nitrogen and oxygen (hydrogen content cannot be detected by EDX) confirming that the metal content of the films had been removed and that metal oxide impurities from the separation process were limited to trace levels [198]. TEM and SEM analysis of the separated foils was not performed as they were assumed to be analogous to those in **Section 4.2.1.2**.

4.2.3.2 Volumetric analysis of the separated foils

As each of the forty eight separated foils had an apparent surface area in excess of 2 cm^2 (1 cm^2 on the top and bottom of the foils) this material potentially has a surface area in excess of $9600 \text{ m}^2\text{g}^{-1}$. The actual material characteristics are listed in **Table 4.2.10**. The isothermal curve (**Figure 4.2.22A**) was classified as a Type VI isotherm, indicative of stepwise multilayer adsorption, with Type 3 or 4 hysteresis identifying slit-shaped pores [223, 286].

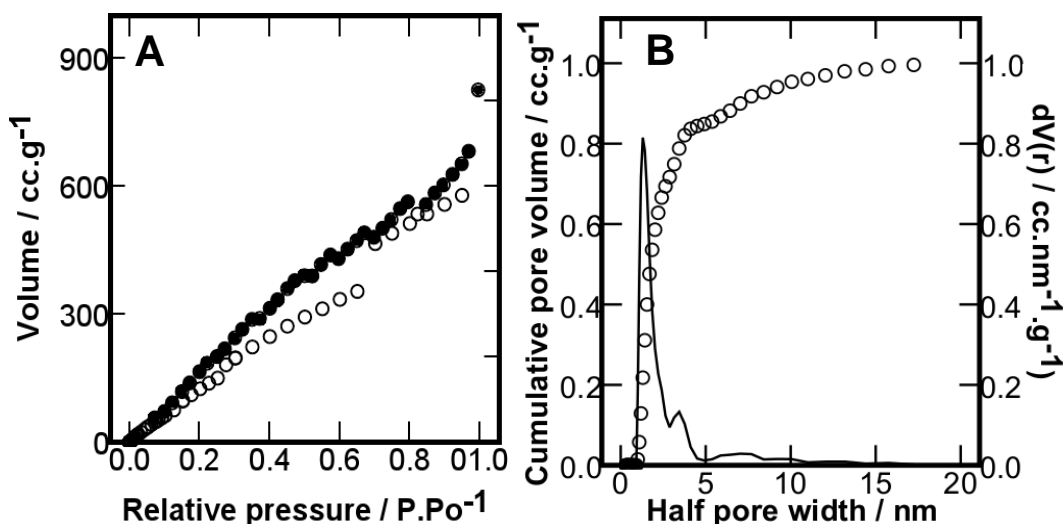


Figure 4.2.22. Volumetric characterisation of MgNiC50400 foil structure. A) isothermal results at 77 K; (○) Adsorption data; (●) Desorption data. B) Results of DFT analysis; (black line) Pore size distribution; (○) cumulative pore volume.

Table 4.2.10. Physical attributes of MgNiC50400 foil.

Surface Area (m ² .g ⁻¹)		DA Micropore volume (cc.g ⁻¹)	Pore Volume (cc.g ⁻¹)		Mode Pore Radius (nm)	
BET	BHJ		BHJ	DFT	BHJ	DFT
952	815	0.542	1.211	0.996	1.0901	1.3

The surface area is smaller than predicted but is still almost a three-fold improvement upon the BET surface area of any adsorbent measured in this thesis. The same is true of the pore volume. The large mode pore radius in **Table 4.2.10** and the spread of the tallest peaks in the DFT analysis of pore size distribution (**Figure 4.2.22B**) identify the material as mesoporous but with considerable microporous character [211]. DA analysis showed that the micropore volume was shy of half of the total pore volume. A mode pore radius between 1.0 and 1.3 nm (depending upon the model used) is above the ideal pore width, reported

as a diameter of 0.7 or 0.92 nm, which corresponds to a double layer of hydrogen [38, 46]. DA analysis identifies a pore volume of 0.02 cc.g^{-1} between 0.7 and 0.92 nm however the large pore volume or surface area of the foil still provides plenty of surfaces for hydrogen to adsorb onto and may compensate for the larger than ideal mode pore width.

4.2.3.3 Gravimetric H₂ storage capacity of the MgNiC50400 foil

H₂ storage capacity of the separated foil was calculated at 77 and 298 K. Results are presented in **Figure 4.2.23**. A sample density of 3 g.cm^{-3} was used for buoyancy correction because it was a mean value collected from the spread of sample densities calculated from the range of different density calculation approaches tested. As the wt.% of hydrogen adsorbed was so high the fine accuracy required for sample density calculation was less of an issue for buoyancy correction of this material compared to the materials loaded on the silicon substrates (**Section 4.2.2.1**). The reduced influence of sample density on the buoyancy correction with increased material adsorption capacity was observed in the density calculation of the other samples studied in this thesis. Lines of best fit represent the results of the Toth model. The R² fit between the modelled and experimental data was 0.980 and 0.915 at 298 and 77 K, respectively.

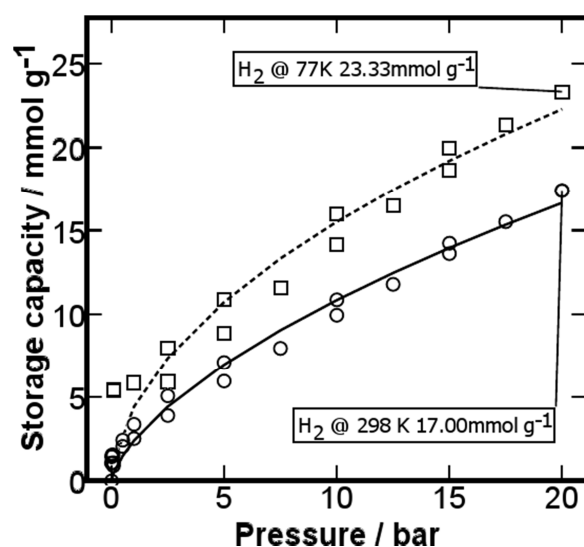


Figure 4.2.23. Isothermal H₂ storage capacities (mmol.g⁻¹) of MgNiC50400 foil against pressure (bar) at 77 (□) and 298 K (○).

H₂ storage capacities of 23.33 and 17 mmol.g⁻¹ convert to 4.7 and 3.5 wt.%, respectively. The gradient of the isothermal curves in **Figure 4.2.23** do not appear to be levelling off by 20 bar suggesting that the material storage capacity would continue to climb as the system pressure increased. Whilst this total still falls short of the DOE objectives of 5.5 to 7.5 wt.% it is a step in the right direction [48]. Storage capacities as high or higher than this have been claimed before but not been substantiated [67]. The validity of these results was scrutinised closely. Each isotherm was repeated three times with freshly loaded sample. The capacity at 77 K varied by 3 mmol.g⁻¹ and the Capacity at 298 K varied by 5 mmol.g⁻¹. Values reported are the median uptakes. The lowest recorded capacities still exceed 4.5 and 2.5 wt.% at 77 and 298 K respectively. Variation could come as a result of the mass of the sample loaded, and due to the heterogeneous nature of the material, as shown in **Section 4.2.1.2.3**, different material compositions were studied in each loading of the sample. The high surface area and pore volume of the sample (**Table 4.2.10**) does help to substantiate the results, as does the adsorbent performance of the film when measured still bound to the silicon substrate (**Figure 4.2.19**). Whilst SiMgNiC50400's storage capacity was low, the fractional increase in capacity compared to pure silicon following the addition of only

0.189 mg of sample was proportionally very high. Time limitations on the project prevented further analysis of the material.

Isosteric Heat of H_2 adsorption for the MgNiC50600 foil was calculated from the Clausius-Clapeyron equation (**Equation 3.36**). Results are shown in **Figure 4.2.24**.

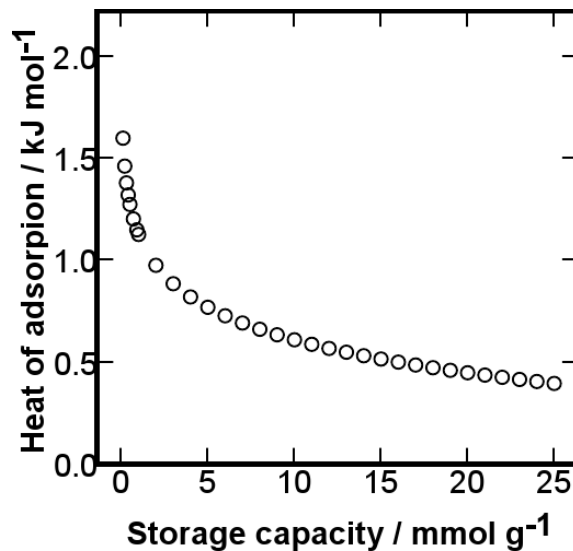


Figure 4.2.24. Isosteric heats of adsorption ($\text{kJ}\cdot\text{mol}^{-1}$) and its variation with storage capacity ($\text{mmol}\cdot\text{g}^{-1}$) for MgNiC50400 foil.

The isosteric heat of adsorption for the material was small suggesting weak binding. This result is as expected given the difference between the mode pore width of the sample and the ideal pore width for hydrogen storage (**Section 4.2.3.2**). Judging by the gradient of the heat of adsorption curve at high storage capacities it appear that adsorption will continue to occur spontaneously ($-\Delta H_{\text{ads}} > 0$) up to far higher storage capacities. Predicting how high the storage capacity could go is unadvisable as the Clausius-Clapeyron equations accuracy falls at very high pressures [238]. This prediction that adsorption capacity would continue to increase with pressure is in agreement with trend of the isothermal curves in **Figure 4.2.23**.

4.2.3.4 Gravimetric CO₂ storage capacity of the MgNiC50400 foil

CO₂ storage capacity of the separated foil was calculated at 273 and 298 K. Results are presented in **Figure 4.2.25**. A sample density of 3 g.cm⁻³ was used again for the reasons described above. Lines of best fit represent the results of the Toth model. The R² fit between the modelled and experimental data was 0.989 and 0.981 at 298 and 273 K, respectively.

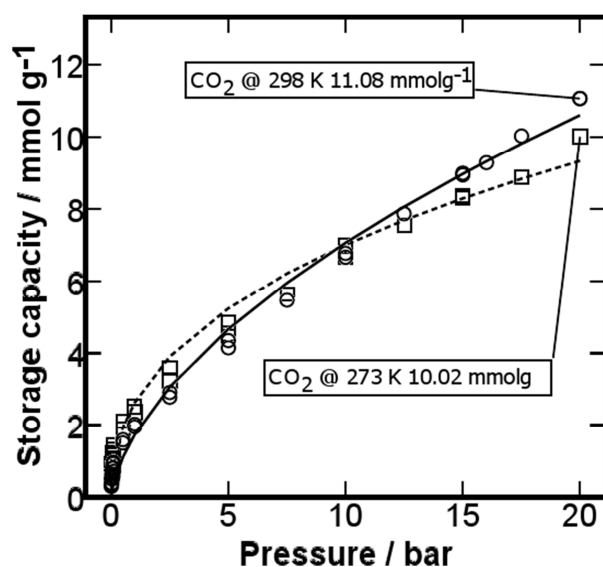


Figure 4.2.25. Isothermal CO₂ storage capacities (mmol.g⁻¹) of MgNiC50400 foil against pressure (bar) at 273 K (□) and 298 K (○).

As discussed previously in **Section 3.6.6.1**, error intrinsic to buoyancy correction of CO₂ gravimetric analyses will result in a slight inaccuracy in the output data in this section, CO₂ storage capacities of 11.08 and 10.02 mmol.g⁻¹ convert to 48.76 and 44.1 wt.%, respectively. Once again the isothermal gradient of the sample does not appear to be levelling off so adsorption would be expected to increase further with increased pressure. The results are once again promising for an adsorbent material. Comparison to the literature will be reserved for the conclusions section. One of the more peculiar results was that the storage capacity at low temperature drops below the storage capacity at high temperatures. This same shift was observed regardless of the experimental density used for buoyancy correction. There are two possible explanations for this.

Firstly there is a problem with the density calculation as was discussed in **Section 4.2.2.1**. Secondly, a hysteresis loop was observed in the volumetric analysis of the sample (**Figure 4.2.22A**) identifying that the sample contains slit shaped pores that require a gas to diffuse into them along or past low energy binding sites. At reduced temperatures the strength of adsorption between CO₂ and the mouths of the pores could be responsible for blocking pore mouths and preventing diffusion into the complete pore volume. This reduction in pore volume available for use in adsorption would result in a reduction in the storage capacity at higher pressures. Once again the high surface area and pore volume of the material, as identified in **Section 4.2.3.2**, help to substantiate the results. An opportunity to repeat the results is highly recommended before reporting the data within a scientific journal.

Isosteric Heat of CO₂ adsorption for the MgNiC50600 foil was calculated from the Clausius-Clapeyron equation (**Equation 3.36**). Results are shown in **Figure 4.2.26**.

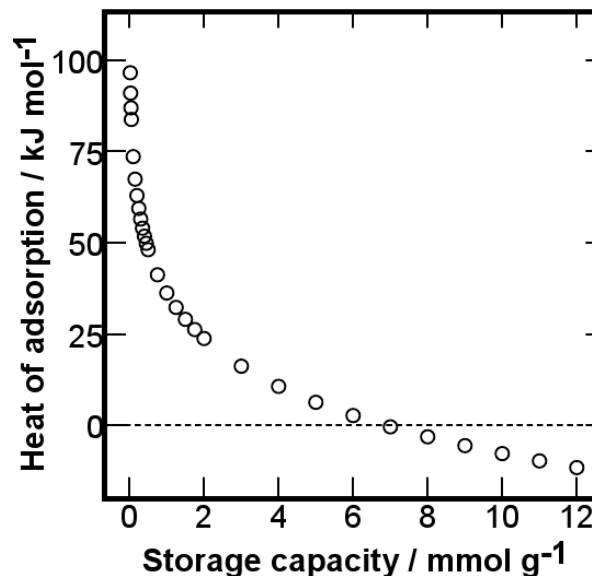


Figure 4.2.26. Isosteric heats of CO₂ adsorption (kJ.mol⁻¹) and its variation with storage capacity (mmol.g⁻¹) for MgNiC50400 foil.

The isosteric heat calculated at low pressures is higher than is seen in the literature but falls into the expected values above 1 mmol.g⁻¹. The

heat of adsorption becomes negative at approximately 7 mmol.g^{-1} , occurring at an equivalent storage capacity to the pressure at which the isothermal curves at 273 and 298 K crossed over in **Figure 4.2.25**

Selectivity of the adsorbent for H_2 or CO_2 adsorption was performed (**Section 3.3.6.4**) Selection was found to favour CO_2 adsorption, with a selectivity of 9.5. The increased selectivity may relate to the pore size distribution of the sample. Average pore size was found to be too large for strong H_2 adsorption. CO_2 is a fractionally wider molecule so would fit better in slightly wider pores.

4.2.4 Conclusions

Control of the nitrogen content is of paramount importance to control the structure of the film grown. Nitrogen was required to promote ordered growth of nanotubes or nanocolumns. Increasing the nitrogen content of the atmosphere increased the carbon deposition rate and the fraction of ordered growth. When the nitrogen content of the sputter gas exceeded 50 vol.%, nitrogen enhanced etching rates began to reduce the thickness and deposited mass of the film.

Nickel nano-islands were responsible for the catalysis of the nanotubes and were likely responsible for enhanced nanocolumns seeding. Higher temperature annealing and deposition was responsible for improved nano-island formation, providing additional energy to fragment nickel into smaller particles.

Increasing the deposition temperature had little influence on carbonaceous growth below $600 \text{ }^\circ\text{C}$. At $700 \text{ }^\circ\text{C}$ the extent of ordered growth increased greatly suggesting that an activation energy barrier against ordered growth was overcome between these two temperature regions. The presence of the mix of amorphous, nano-tubular and

nano-columnar structures identifies that the base layer preparation was insufficient for the synthesis of one homogeneous nanostructure across the film.

Separation of the deposited films could be achieved by oxidative etching of the metal layer using aqueous ferric chloride (III) solution.

SiMgNiC50400 was mass produced and the CN_x film was separated from the SiMgNi substrate. The collected film was comprised of nanotubes of varying length and width as well as an abundance of carbon nanocolumns. Despite having a large surface area and pore volume only a very small fraction was distributed within the pore size believed to be ideally suited for hydrogen adsorption. The hydrogen storage capacity of the material was repeatedly tested and found to be approximately 4.7 wt.% by 20 bar and at 298 K. The result suggests that the material is highly promising as an adsorbent but should, for the moment, still be regarded with caution until verified by further work.

The outcome of this study suggests that further research to refine and improve upon the work performed above could be of considerable value for developing a material to meet the DOE objectives [48]. This first principle study has identified some of the logistical stumbling points encountered when trying to generate adsorbents by magnetron sputtering, such as film separation, and should be used to inform and improve future projects.

4.3 A study of magnetron sputtering as a means to compositionally dope carbon nanotubes with cerium and nickel and its influence on H₂ storage capacity

This section discusses sputter deposition of cerium and nickel onto pre-prepared CNTs. The main objective of this work is to identify whether cerium can act as an effective catalyst for improving H₂ storage capacity and also to determine the viability of sputter deposition as a doping process. The background to this work is presented in **Section 2.4.3** and the experimental process is described in **Section 3.4.3**. Samples were named after the molar percentage of the deposited material in the sample. A list of sample names and compositions is presented in **Appendix B**.

4.3.1 Preparation

4.3.1.1 Tuning sputter deposition conditions

Argon was selected as the sputter gas because of its inert nature and its high atomic mass. Sputter excitation is best promoted by ions of similar mass to the target material [140, 142]. **Figures 4.3.1 and 4.3.2** show the results of the sputter rate tests calculated *in situ* using the apparatus' crystal rate monitor. It is worth remembering that sputter rate relates to the rate of excitation from the target whilst deposition rate relates to the rate of mass deposited and can be affected by factors such as etching.

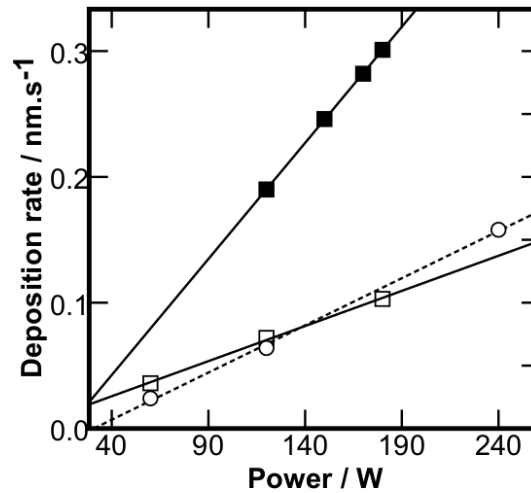


Figure 4.3.1. *In situ* sputter rate ($\text{nm}\cdot\text{s}^{-1}$) determination based upon sputter power ($\text{W}\cdot\text{cm}^{-2}$). Key: (\circ) RF deposited Ni; (\blacksquare) DC deposited Ce; (\square) RF deposited Ce.

A linear correlation between sputter power ($\text{W}\cdot\text{cm}^{-2}$) and sputter rate ($\text{nm}\cdot\text{s}^{-1}$) was observed for all materials within the desired range. R^2 values for the linear fits exceeded 0.99 in all cases. Despite DC powers increased deposition rate as observed in **Figure 4.3.1**, RF power was selected for doping CNTs with pure cerium because of the increased plasma stability provided by the RF power source. A RF power level of $5.92 \text{ W}\cdot\text{cm}^{-2}$ was arbitrarily chosen for lone cerium deposition based upon experience gathered from apparatus use. $11.84 \text{ W}\cdot\text{cm}^{-2}$ RF power was selected for lone nickel deposition. DC sputtering of nickel was not an option due to nickel's strong magnetic character preventing plasma ignition.

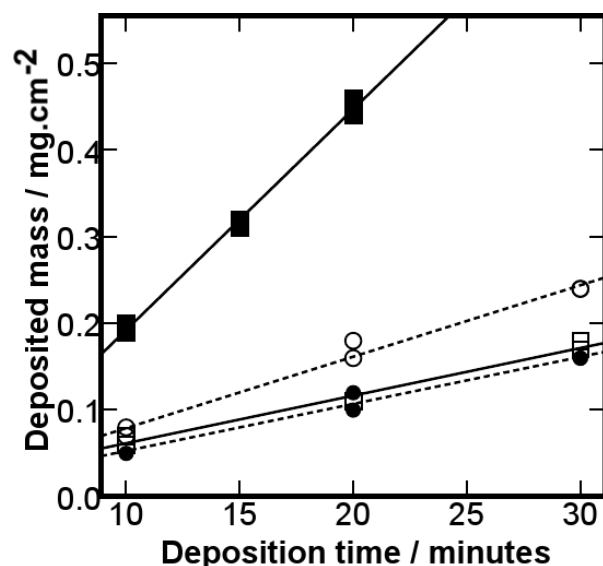


Figure 4.3.2. *Ex situ* deposition rate ($\text{mg}\cdot\text{cm}^{-2}$) determination from the deposition time (minutes). (●) Ni deposited at $5.92 \text{ W}\cdot\text{cm}^{-2}$ RF power, (○) Ni deposited at $11.84 \text{ W}\cdot\text{cm}^{-2}$ RF power, (■) Ce deposited at $8.88 \text{ W}\cdot\text{cm}^{-2}$ DC power (□) Ce deposited at $5.92 \text{ W}\cdot\text{cm}^{-2}$ RF power.

Deposited mass increased linearly with deposition time within the desired range, with R^2 fitting values exceeding 0.97 (**Figure 4.3.2**). Experimental deposition times for powder coating experiments were extrapolated from these tests. Sputter rates are summarised in **Table 4.3.1**.

Table 4.3.1. Summary of material sputter rates under different conditions

	In situ sputter rate ($\text{nm}\cdot\text{min}^{-1}$)	Mass deposition rate ($\text{g}\cdot\text{min}^{-1}\text{cm}^{-2}$)	Deposition rates for powder coating tests ($\text{g}\cdot\text{s}^{-1}$)
Ni $5.92 \text{ W}\cdot\text{cm}^{-2}$ RF	3.8	5.42×10^{-6}	2.88×10^{-5}
Ni $11.84 \text{ W}\cdot\text{cm}^{-2}$ RF	9.5	7.96×10^{-6}	4.23×10^{-5}
Ce $5.92 \text{ W}\cdot\text{cm}^{-2}$ RF	6.9	5.96×10^{-6}	3.17×10^{-5}
Ce $8.88 \text{ W}\cdot\text{cm}^{-2}$ DC	18.1	2.17×10^{-5}	1.12×10^{-4}
Ni $7.59 \text{ W}\cdot\text{cm}^{-2}$ RF	4.64	6.16×10^{-6}	3.27×10^{-5}

The *in situ* sputter rate data was collected from the crystal rate monitor (**Figure 4.3.1**). The mass deposition rate was calculated by dividing the deposited mass by the deposition time (**Figure 4.3.2**). The deposition area for powder coating experiments was a 5.314 cm² circular holder. So the actual rate at which metal dopants would be added to the PCNT sample is listed in the “deposition rates for powder coating tests” column. For co-deposition tests it was decided that the deposition times for both materials should be identical. As the desired molar ratio of Ce:Ni was 1:0.7, extrapolating the desired rates from the data plotted in **Figure 4.3.2**, deposition was performed at 8.88 W.cm⁻² DC power for cerium and 7.59 W.cm⁻² RF power for nickel. Sputter rates are included in **Table 4.3.1**.

4.3.1.2 Target melting during co-deposition

Co-deposition of nickel and cerium for more than ten minutes led to melting of the cerium target, a process which can prove catastrophic for the sputter apparatus. Evidence of melting was apparent from the change in the cerium targets appearance and its plasma shape during deposition. The target core was observed to sag and balloon down from the magnetron. Target melting was likely due to alloying of the cerium target with “stray” sputtered nickel particles. Alloying of cerium with nickel is known to reduce cerium’s melting temperature from 1068 K to below 760 K [287, 288]. Apparatus failure was eliminated as an explanation when melting was again observed using a fresh target and magnetron. To compensate for these problems deposition times in co-sputtering tests was limited to five minute bursts followed by five minute rest periods to prevent overheating of the cerium target. A fresh cerium target was used for any lone cerium deposition as the cerium target used for co-deposition became tainted with low levels of nickel that would contaminate pure cerium samples.

4.3.2 Material characterisation

4.3.2.1 Purification of CNTs

Purification of the as-received CNTs was required as they were still saturated with their growth catalyst $\text{Ni}_x\text{Mg}_{x-1}\text{O}$. The purification step involved immersion of the RCNT powder in a HNO_3 solution which was continuously stirred at 353 K for six hours (**Section 3.4.3.1.1**) [244]. XRD results are presented in **Figure 4.3.3**. Comparison of the raw and pure diffraction patterns identifies that purification successfully eliminated crystalline magnesium and $\text{Ni}_x\text{Mg}_{x-1}\text{O}$ particles from the nanotubes. The nickel content of the sample is significantly reduced but due to overlap between broad CNT peaks and narrow Ni peaks at 44.5° and 52° it is unclear whether nickel has been entirely eliminated.

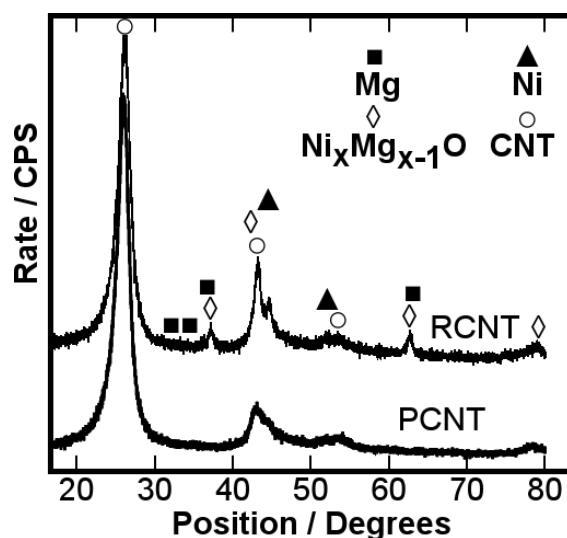


Figure 4.3.3. X-ray diffraction patterns for raw and purified CNTs.

Typical Raman spectra for RCNTs and PCNTs are provided in **Figure 4.3.4**. The averaged peak information for each sample is presented in **Table 4.3.2**.

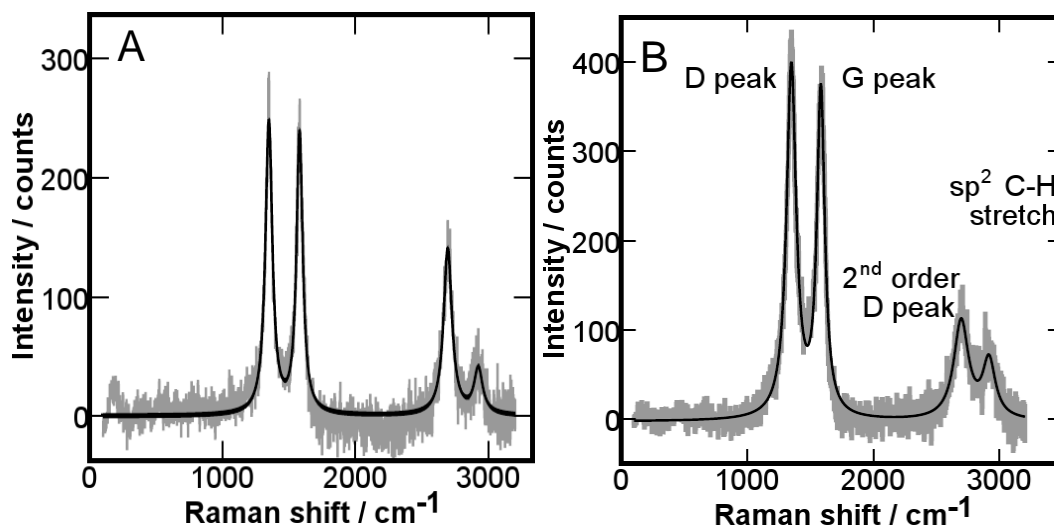


Figure 4.3.4. Raman spectra for the raw (A) and purified (B) CNTs. (Grey lines) background corrected experimental spectra; (Black lines) modelled peak data.

Table 4.3.2. Raman data for RCNT and PCNT samples

	RCNT		RCNT	
	Peak Position / cm^{-1}	SD	Peak Position / cm^{-1}	SD
D Peak	1346	1.4	1349	1.7
G peak	1577	2.6	1581	4.2
2 nd order D peak	2689	4.3	2695	4.7
sp ² C-H Stretch	2919	2.6	2926	8.3
	Value	SD	Value	SD
I _D /I _G ratio	1.18	0.02	1.26	0.14

The Raman spectra are similar to that of other CNTs from the literature [209, 210, 261, 280]. The presence of well-defined second order peaks in the spectra is indicative of highly graphitic materials [208]. The 2nd order G peak, usually observed at 3100 cm^{-1} , was too close to the top end of the apparatus' data collection range to resolve properly. The I_D/I_G ratio, when looked at in conjunction with the position of the D peak

provides a measure of order within the system. Based upon the I_D/I_G ratio it appears that the purification process not only had no detrimental influence on the CNTs, it also increases the graphitic purity of the sample, increasing the G peak position above 1580 cm^{-1} and decreasing the relative intensity of the first and second order D peaks. This is likely due to the removal during washing of amorphous carbon or nanocrystalline graphitic deposits loosely bound to the CNTs or bound on or in the metal catalysts [270]. The presence of G peaks above 1580 cm^{-1} and an I_D/I_G ratio of 1.26 suggest that the PCNT sample contains highly ordered graphite and nanocrystalline graphite [208]. By comparison, it is worth noting that an amorphous material would have a far higher I_D/I_G ratio and the G peak position would fall, potentially as low as 1520 cm^{-1} , because as the sp^3 fraction of the material increased the D peak intensity would increase proportional to the G peak, and a growing sp^3 fraction in the film softens the sp^2 vibrational modes, lowering the peak position [208].

TEM images in **Figure 4.3.5** provide an overview of the artefacts observed during material analysis and help chronicle the changes undergone during purification. Tube diameters were assessed quantitatively from TEM results [152, 209, 210, 276]. However, the other observations from the TEM analysis discussed below were quantified by XRD and Raman analysis. Discussing XRD and Raman findings along with TEM images provides a more tangible interpretation of the results.

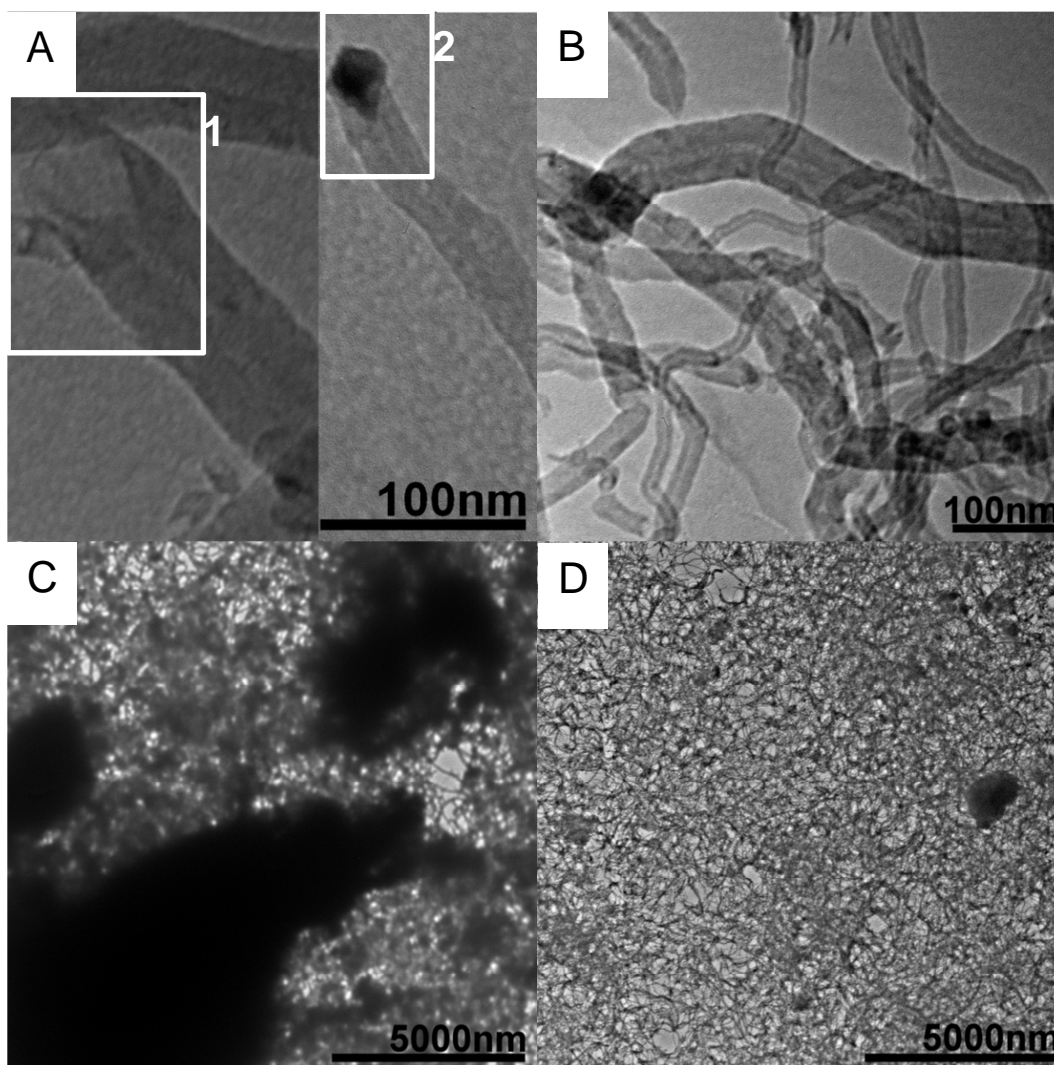


Figure 4.3.5. TEM images indicative of the raw and purified CNTs. A) Open (1) and blocked (2) RCNT tube ends. B) A dispersion of PCNTs. C) RCNT contamination with metal impurities. D) PCNTs contamination with metal impurities

TEM analysis did not reveal any significant differences in the appearance of the nanotubes before and after purification. This result combined with the Raman results indicate that the purification process was not harmful to the CNT structures. Comparison of **Figures 4.3.5C** and **4.3.5D** show the reduction in the abundance of large metal clusters following purification as was also observed from XRD analysis. The number of tube ends blocked by catalyst particles (**Box 2** in **Figure 4.3.5A**) decreased following purification leaving open tube ends (**Box 1** in **Figure 4.3.5A**) thus opening up pore spaces down nanotube lengths.

Multi-walled carbon nanotubes (MWCNTs) were abundant throughout the material with an average outer tube diameter of approximately 50 nm (SD \approx 25 nm). The inner tube diameters were approximately 8.97 nm with a smaller standard deviation (SD \approx 3.15 nm) suggesting less variability. Tube lengths were variable and could not be measured accurately because bundling of tubes obscured clear definition of which tube was which. The appearances of tube ends, as in **Square 1** of **Figure 4.3.5A**, are indicative of a tip growth mechanism catalysed by pear shaped metal catalysts (**Square 2** in **Figure 4.3.5A**), in this case nickel [152, 270, 277, 289]. CNTs possess a bamboo-like structure with an inner core compartmentalised by thin graphitic planes. These planes form around the base of the pear shaped catalyst particle when tube propagation slows and carbon precipitates out the bottom of the catalyst particle [209]. Purification may have removed catalyst particles blocking the nanotube ends, but the presence of the graphite planes throughout the tubes mean that an increase in pore volume with purification is unlikely to be proportional to the total volume of the nanotube core. Isothermal data for the raw and purified CNTs are displayed in **Figure 4.3.6**.

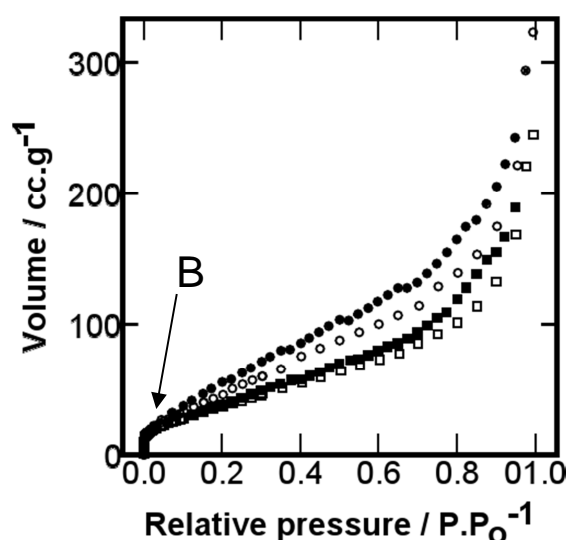


Figure 4.3.6. Isothermal N_2 adsorption ($cc.g^{-1}$) for the raw and purified CNTs with pressure (P/P_0). Key: (\square) RCNT adsorption; (\blacksquare) RCNT desorption; (\circ) PCNT adsorption; (\bullet) PCNT desorption.

Normalisation of the sample surface area and pore volume data to give the values relative to carbon content (**Equations 4.1 to 4.5**) was not performed on these samples. A number of factors influenced this decision. Firstly, appropriate estimations of the metal impurities mass and specific surface area could not be made. Secondly, the recovered mass of PCNT was greater than 90 % of the RCNT. Accounting for materials losses, this reduces the impurity content below 5 %. As was discovered in **Section 4.1**, normalisation against dopants of such small content provided results almost identical to the collected data. It was therefore decided to stick with the collected results. All samples generated type IV isotherms, indicative of capillary condensation in mesopores [223, 245]. Type H3 hysteresis loops (IUPAC nomenclature) suggest capillary condensation occurs in slit-shaped pores [245]. These observations were considered when determining the correct parameters for DFT analysis. The size of the hysteresis gap between the adsorption and desorption plots of the two isotherms suggests that the purification process opened up previously sealed slit-shaped mesopores [290]. Given the P/P_0 range where divergence between RCNT and PCNT isotherms begins (0.1 P/P_0) it would appear that the purification has its largest influence on the mesopore region. As the purification process was shown to have unblocked nanotubes by digesting the catalytic particles found at their tip (**Figure 4.3.5A**), the increase in mesopore volume can likely be attributed to the volume down to core of the nanotubes.

The presence of hysteresis extending below 0.3 P/P_0 indicates some micropores character within the sample [245]. As the intensity of the “Knee” in the isotherm (**point B** in **Figure 4.3.6**) was similar for both materials it appears the purification step had neither a positive nor detrimental effect on the micropore fraction of the material [249]. Regions of microporosity can be imagined as damaged or broken walls on the outside of MWCNTs, porous spaces between tightly packed nanotube bundles (**Section 2.2.2.2.2**) [111], cracks on the surface of amorphous deposits within the sample or, given that the nanotube diameter was found to be highly varied, microporosity could have existed within very narrow

CNTs. Another region with a fractional influence on the microporosity of the sample would be within the bamboo cones within the nanotubes.

Mesoporous materials with some microporous character are best analysed by DFT and BHJ analysis (**Section 3.3.5**) [223, 290]. Whilst BHJ analysis of mesoporous materials classically studies the desorption profile of the hysteresis loop, combined micropore and mesopore analysis could only be performed during the adsorption step of the experimental process. BHJ modelling was applied to the adsorption profile to incorporate the full spread of pore sizes [290]. Similarly DFT analysis was confined solely to the adsorption curve to incorporate the entire pore range. Adsorption and desorption were not studied simultaneously due to the hysteresis loop.

Monolayer coverage in Type IV isotherms is achieved by point B in **Figure 4.3.6**, representing the beginning of the linear central section of the isotherm [245]. Monolayer coverage data is useful in the determination of the materials surface area, popularly extrapolated using the BET equation. Point B for all samples analysed was achieved around 0.01 P/P_0 , earlier than the data collection range for the BET model (0.05 to 0.35 P/P_0) [223]. These samples do not meet the BET models assumptions of monolayer adsorption as monolayer coverage had already been achieved below the BET data collection range, rendering the technique redundant [223]. BET results are however included for comparison with literature where similar discrepancies are often overlooked. Surface area, extrapolated from BHJ analysis is likely to be more representative of the material. **Figure 4.3.7** highlights difference between the results used by the two approaches to calculate surface area.

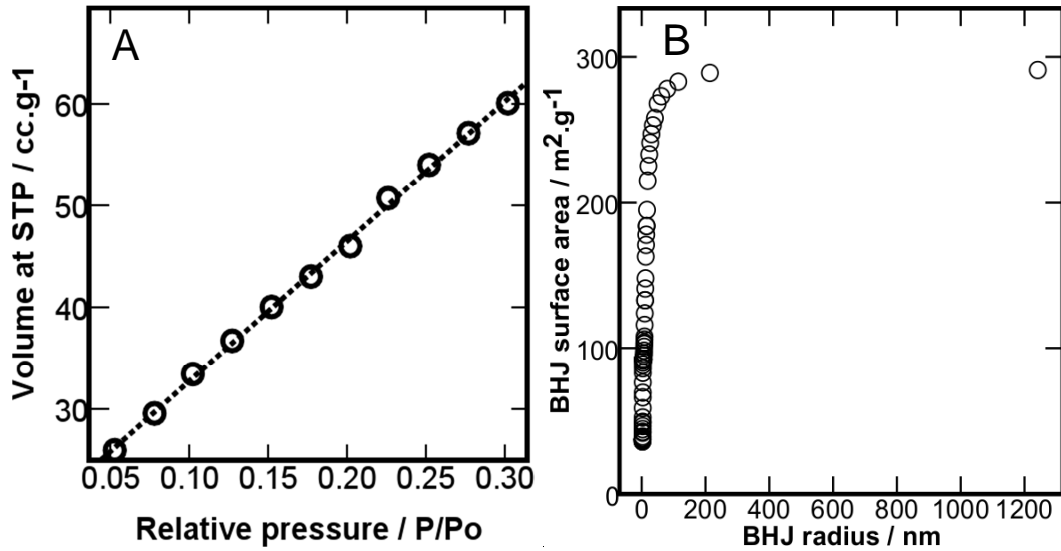


Figure 4.3.7. Comparison of approaches for surface area calculation. A) BET plot for PCNT, (○) Adsorption data points; (----) BET model. B) BHJ plot for PCNT, (○) Adsorption data points.

The BHJ method samples a larger, more representative fraction of the recorded isothermal data and the recorded surface area is collected from a plateau in the results rather than a snapshot of the isothermal gradient elected for in BET analysis. Physical characteristics of RCNTs and PCNTs are displayed in **Table 4.3.3**.

Table 4.3.3. Physical attributes of RCNTs and PCNTs

Sample	Surface Area (m ² /g)		Micropore Volume (cc/g)	Pore Volume (cc/g)		Mode Pore Radius (nm)	
	BET	BHJ	DA	BHJ	DFT	DA	DFT
RCNT	128	248	0.09	0.33	0.30	1.0	1.0
PCNT	177	291	0.13	0.44	0.40	10.	1.1

Table 4.3.3. shows that the purification process increased the surface area and pore volume of the materials. This outcome can have been achieved in two ways. Firstly, as observed in the TEM images, residual large metal clusters, and the dead weight they represented, were

removed during purification. Secondly, unblocking of the pore ends, capped with small metal particles will have increased the exposed surface area or pore volume [247]. Purification shifted the mode pore radius from a microporous region to a mesoporous region. Closer scrutiny of the influence of the purification step in the pore volume and its distribution was carried out comparing the DFT pore size distributions of the two materials. Results are shown in **Figure 4.3.8**.

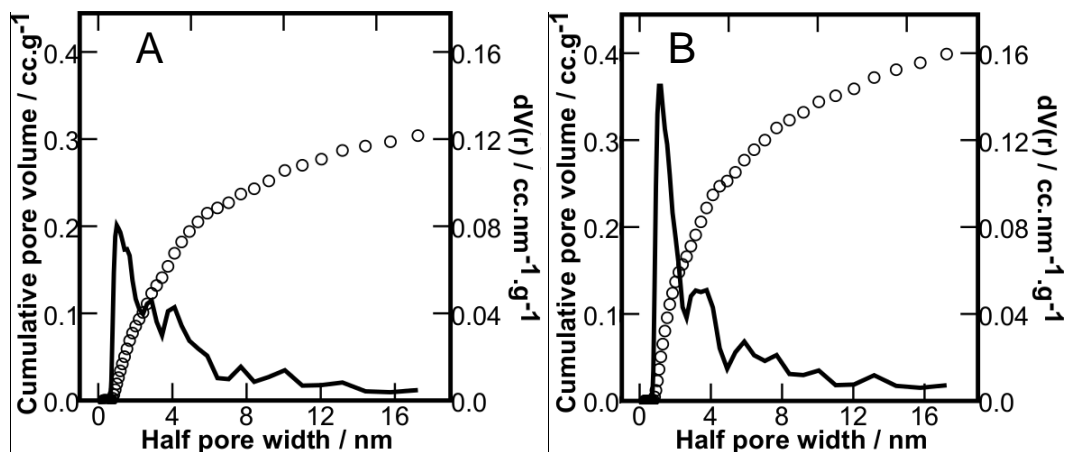


Figure 4.3.8. Change in the pore size distribution ($\text{cc.nm}^{-1}.\text{g}^{-1}$) and cumulative pore volume (cc.g^{-1}) with half pore width (nm) of RCNT (A) and PCNT (B) calculated from DFT analysis. Key: (○) cumulative pore volume, (-) pore size distribution

The increase in $dV(r)$ is consistently larger for PCNT except between 2.5 and 2.8, and 4.1 to 5.3 nm half pore widths. Variation between the $dV(r)$ trends suggest that the purification process not only removed excess weight from the sample but also opened up previously sealed pores. Were the increase in pore volume reliant solely on the removal of excess catalyst material that was not blocking pore but acting as a dead weight then the trend in $dV(r)$ would have been analogous for both samples but with a varying intensity. The greatest increase in the PCNTs pore volume compared to RCNTs was between 0.8 and 2.0 nm half pore widths, spanning the upper micropore and lower mesopore region. This increase made up over half of the total increase in pore volume. The purification process increased the micropore volume by 0.04

cc.g⁻¹ or 0.004 cc.g⁻¹ by DA or DFT analysis, respectively. In spite of this, for RCNTs the micropore region (pore volume below 1.0 nm half pore width [249]) contributed 6 % of the total pore volume, while for the PCNTs this fraction dropped to 5 %, indicating that the purification process had its greatest influence on the mesopore region. As reported above, this increase in the mesopore volume is likely the result of the purification process opening up previously sealed nanotubes. The average PCNT inner tube radius recorded from TEM analysis was 4.5 nm with a standard deviation of 1.6 nm. The pore volume within this region (between 2.9 and 6.1 nm) made up 28 % of the total pore volume of the PCNTs whilst being only one fifth of the spread of pore width analysed. By comparison, the fractional contribution to the total pore volume from pores with a radius smaller than 2.91 nm (the average nanotube width minus the SD) was 42 % from only 15 % of the total spread of pore width analysed. Such a result could be taken to suggest that opening of the CNT core by unblocking tubes was not the predominant cause for the increase in pore volume. However, the internal tube diameter results collected by from TEM analysis may be misleading as the recorded inner tube diameter was subject to the resolution of the TEM apparatus. Smaller tube diameters that could not be resolved for analysis are likely to have been opened and have played a part in the increased pore volume. Whilst pore opening remains the most likely cause for the increase in pore volume, despite TEM results, porosity may have been contributed to by other factors. Removal of excess amorphous deposits during purification could have led to closer packing of nanotubes and formation of narrow porous spaces between bundles or ropes [111].

In summary, the purification process increased the micro- and meso- pore volumes of the PCNT material by opening up previously sealed pores (**Figure 4.3.5**), removing dead weight and generating new pore spaces within closer bound CNT bundles. The PCNT material is predominantly mesoporous with the greatest increase in pore volume compared to the RCNT in the region between 0.8 and 2.0 nm half pore width.

4.3.2.2 Powder sputtering of lone metals

Figure 4.3.9 provides an overview of the XRD results for nickel or cerium doped CNTs.

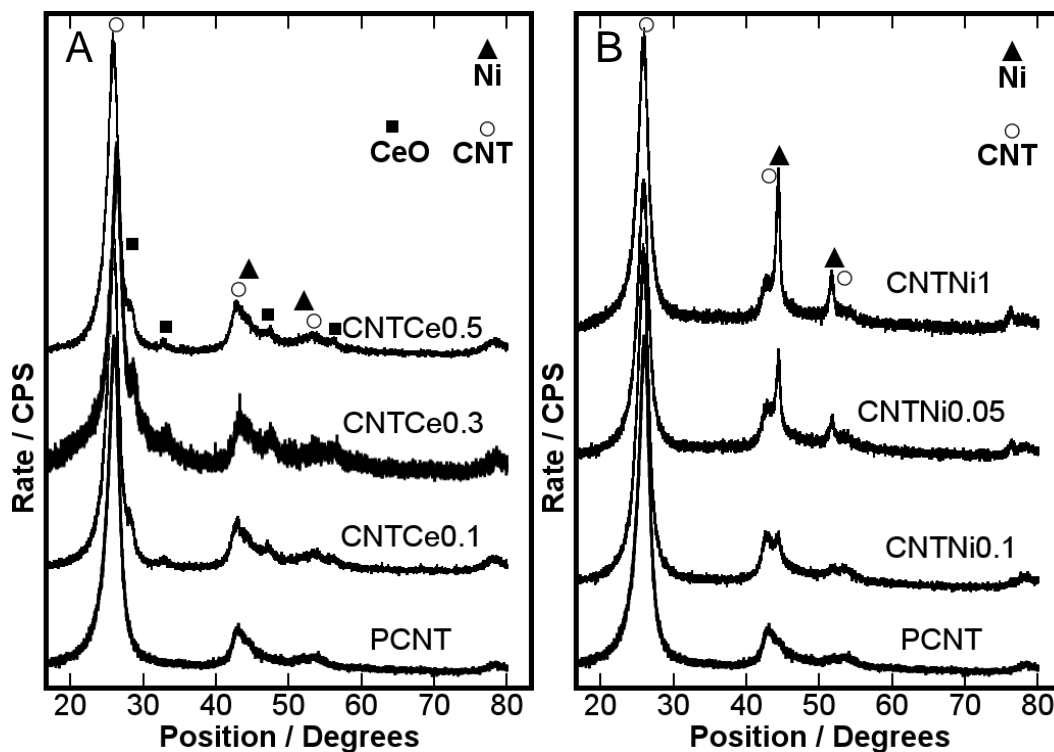


Figure 4.3.9. A) Comparison of X-ray Diffraction patterns for PCNT and cerium doped CNTs and (A) PCNT and nickel doped CNTs (B).

Sputter coating of the nanotubes with increasing volumes of nickel lead to a steady increase in the appearance of the Ni diffraction peaks relative to the CNT peaks. Whilst the trend in peak height ratio correlated with the expected experimental outcomes, using XRD for quantitative analysis of the CNT:Ni ratio was not possible. XRD is only able to quantitatively analyse crystalline phases [291]. 100 % crystallinity in the nickel could not be assumed and could not be expected of the CNTs. Whilst the intensity of the Ce peaks was a fraction of those of the Ni peaks, the Ce peak intensity was also seen to increase with deposited amount. Cerium peaks were better resolved in Raman analysis (discussed below). Diffraction patterns matched CeO spectra rather than pure cerium. This is due to XRD being performed exposed to air and cerium's readily

oxidisable nature [167]. Hydrogen storage tests and volumetric analysis was performed prior to other analytical studies to keep the ceria (CeO_2) fraction of the samples during these tests to a minimum.

Raman analysis was performed to see if the doping process influenced the structure of the carbon samples. **Figure 4.3.10** shows a typical Raman spectra for a cerium doped CNT.

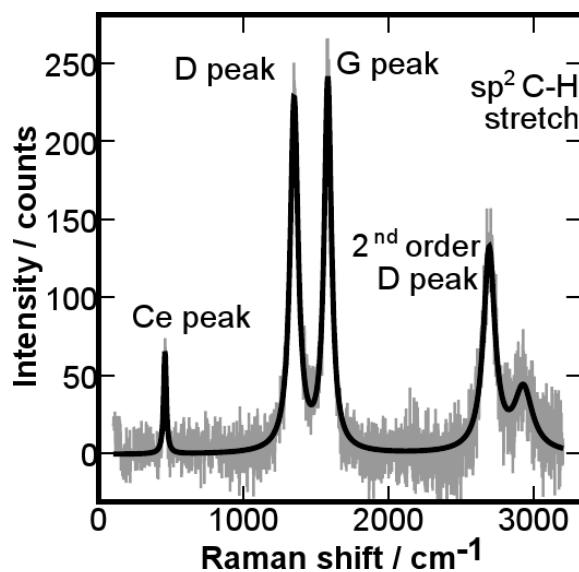


Figure 4.3.10. Raman spectra for CNTCe0.1. (Grey line) experimental data, (Black line) peak modelled data.

Additional secondary carbon peaks not present in **Figure 4.3.10** appeared in some spectra, including a peak at 1855 cm^{-1} identified as in plane C-C stretching along a tube and a peak at 2100 cm^{-1} attributed to sp^1 carbon vibration [208]. An additional peak at 454 cm^{-1} , attributed to cerium, was identified in all samples [292]. There was a standard deviation of 2.1 cm^{-1} in the 454 cm^{-1} peak position with variation in the deposited cerium content but no trend in the average peak position could be seen. **Table 4.3.4** summarises the Raman results for the samples tested.

Table 4.3.4. Raman results for cerium doped CNTs

	D peak (cm ⁻¹)		G peak (cm ⁻¹)		I _D /I _G ratio	Ce peak (cm ⁻¹)	
	Position	SD	Position	SD		Position	SD
CNT Ce0.1	1348	1.8	1578	1.8	1.07	455	0.9
CNT Ce0.2	1348	0.6	1579	1.9	1.05	454	1.5
CNT Ce0.3	1348	1.9	1580	4.9	0.84	451	1.7
CNT Ce0.4	1350	4.1	1581	4.3	0.87	453	1.7
CNT Ce0.5	1351	5.9	1581	4.9	1.08	455	0.9

A minor shift was observed in the peak positions of both the D and G peaks along with a broadening of their standard deviation with increasing Ce content. The increase in the position of the G peak suggests an increase in the order of the material, a result supported by the drop in the I_D/I_G ratio [2, 208]. A decrease in the I_D/I_G ratio comes as a result of an increase in the ordered, sp², fraction of the film. Strong definition of the second order D peak helps substantiate that the material remains highly ordered. The apparent increase in order could come as a result of etching of loosely bound amorphous carbons bound to nanotube exteriors by oxygen during sputtering. Trace oxygen levels within the sputter chamber, energized by the sputter plasma could have reacted with the carbon leading to its expulsion as carbon monoxide [273]. Alternatively, these carbonaceous deposits could have been adsorbed into the cerium structures during deposition.

TEM images indicative of the changes in morphology with increased deposition of cerium are shown in **Figure 4.3.11**.

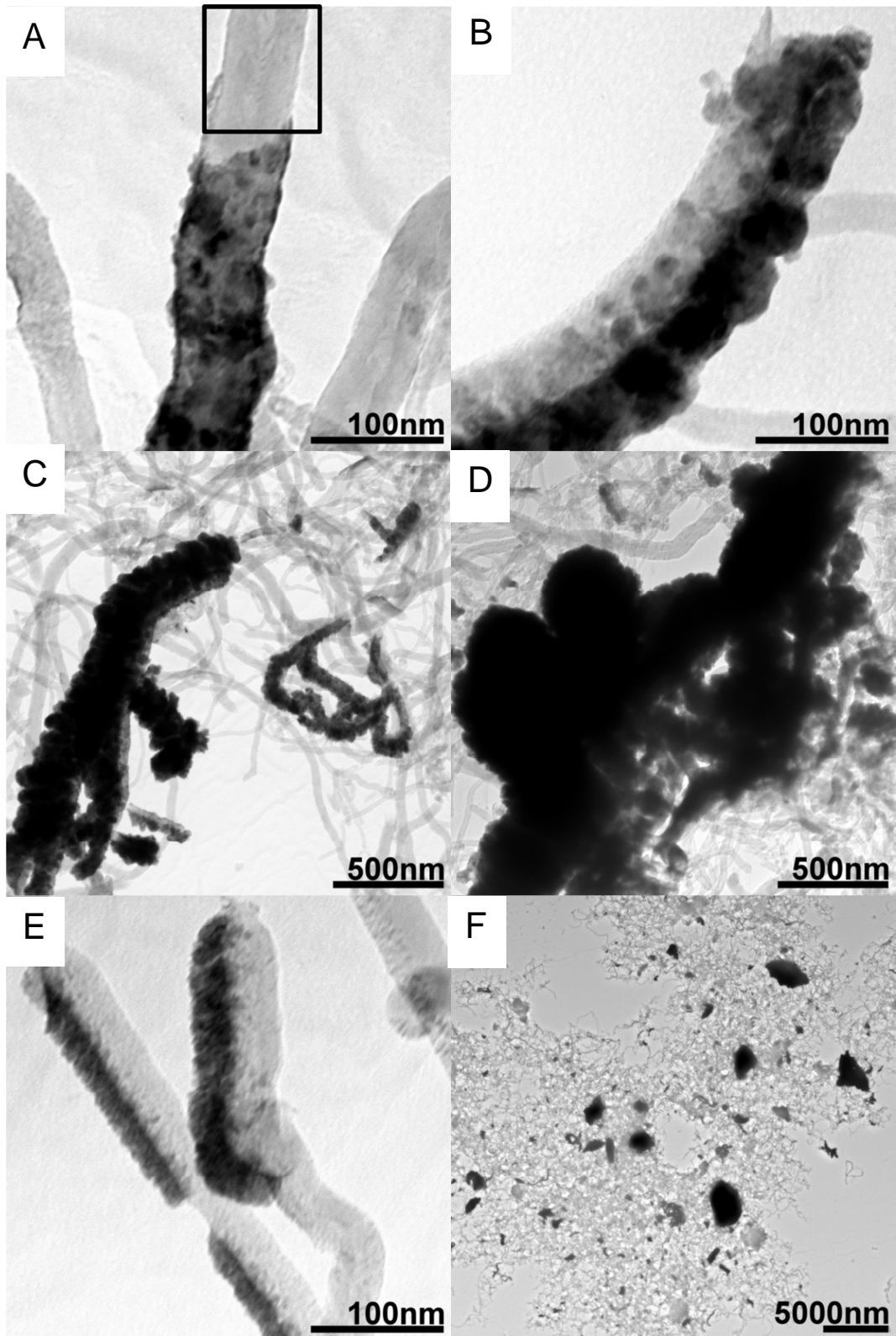


Figure 4.3.11. TEM images representative of the cerium (dark regions) coated CNTs (grey tubes). A) CNTCe0.25 displaying cerium coating around a CNT. B) CNTCe0.125 showing cerium coating down one side of a CNT. C) CNTCe0.05 showing the lack of homogeneity in

cerium distribution. D) CNTCe0.4 showing a large cerium covered CNT cluster. E) CNTCe0.025 displaying cerium coating down one side of a CNT. F) CNTCe0.5 showing metal distribution and cluster size.

The boxed area in **Figure 4.3.11A** shows evidence of bamboo-like structure in the CNTs as described in the TEM analysis of the raw and purified CNTs (**Section 4.3.2.1**). The deposition process could not have been responsible for bamboo structure formation because, amongst other reasons, the bamboo structures run down the inner tubes, whilst cerium was coated on the outer tubes. The bamboo structure must therefore be as a result of the CNT growth process.

The deposited metals were identified by their darker appearance down the sides of the samples (**Figures 4.3.11A and 4.3.11B**). Their identity as the metal could not be confirmed but similar deposits were absent from the RCNT and PCNT samples. The deposited cerium was heterogeneously spread throughout the CNTs with some nanotubes heavily coated and some unchanged (**Figure 4.3.11C and 4.3.11D**). This was a consequence of not sonicating the samples during deposition [174-176]. Coatings were identified predominantly along the outer walls of the nanotubes. Thicknesses of the deposited cerium were inconsistent within each sample but average thickness did increase with deposition time. Longer sputtering times increased the aggregation of the tubes, with the metal binding nanotubes together to form clusters (**Figure 4.3.11C and 4.3.11D**). Even after the longest deposition time the size of the deposited clusters were significantly smaller than the metal impurities identified in the raw CNTs (**Figure 4.3.11F**). As clusters grew broader, they seemed to remain relatively flat as the axial variation (depth of field) was smaller for the doped samples than for the RCNTs (raw CNTs). It appears that in cases where deposition time was short there was very little movement or spreading in the deposited material. This was evidenced by build-ups occurring on only one side of the nanotube (**Figure 4.3.11E**), and also due to a lack of uniformity in the thicknesses across a nanotube. Small dopant

particle size is a highly desirable trait because maximising dispersion increases the activity of the dopant [46, 293]. Also smaller particle sizes tend to show increased activity due the smaller crystallite sizes and the higher energy surface conformations present.

There appeared to be an ordered growth structure in some of the cerium deposits. Evidence of the order was more apparent after prolonged deposition when dopants had longer to grow and develop their structure (**Figures 11B and 11E**). The ordered structure had an uneven surface with cracks and pores along its structure. The influence of the surface topography of the dopant will be discussed in the volumetric analysis of the samples.

Intimacy of binding between dopant and adsorbent seemed high as identification of lone metal particles separated from a nanotube surface were rare and such particles were small. Such a result suggests that, although this experimental procedure requires refining to generate desirable homogeneous dopant dispersions, the process does generate intimately bound dopants and adsorbates [142]. This is a highly desirable trait for optimising the activity of an adsorbent-dopant mix; a trait not shared by dopant processes such ball milling or some wet chemistry approaches [97].

The distribution of the metals on the CNTs was predominantly along the tube length as opposed to around the tube ends. This is because the sputter process deposits the metal dopant indiscriminately with binding occurring on any surface exposed to the sputter beam [142]. By comparison, Wet chemistry doping processes tend to bind the catalyst at strong binding sites, such as pore ends, due to the added chelative influence offered by multiple points of contact between the catalyst particle and the tube walls [96]. As tube ends are commonly thought to be the best sites for gas adsorption leaving pore ends exposed would be advantageous [67]. This suggests that the sputter deposition of a catalyst may prove more effective for preserving an adsorbents pore volume than wet chemistry doping alternatives. The sputter process also has the

advantage of not requiring purification steps to remove catalyst precursors that some wet chemistry approaches need.

The appearance of the nickel coated nanotubes and the variation in the deposited film thicknesses were analogous to the cerium coated samples. The explanation for their appearance is analogous to the above discussion for cerium deposition

Volumetric analysis was performed to characterise the surface area and pore size distributions of both the cerium doped and nickel doped CNTs. The typical shape for all the sample isotherms was again a type IV curve, as observed for samples RCNT and PCNT (**Figure 4.3.6**) so the same analytical processes were performed. Results of volumetric analysis are arranged in **Table 4.3.5**.

BET surface area results were spread across a range of 150 to 250 m^2g^{-1} . BHJ analysis increased this spread from 200 to 400 m^2g^{-1} . Despite the increased spread, there is a smaller SD between the BHJ results. There was no trend between SA and doped amount but results from both materials followed a similar pattern that will be discussed below.

Table 4.3.5. Physical attributes of cerium or nickel doped CNTs

Sample	Surface Area (m^2g^{-1})		Micropore Volume (cc.g^{-1})	Pore Volume (cc.g^{-1})		Mode Pore Radius (nm)	
	BET	BHJ	DA	BHJ	DFT	DA	DFT
CNTCe0.5	199	325	0.13	0.73	0.58	1.1	1.5
CNTCe0.4	201	340	0.14	0.54	0.38	1.0	1.85
CNTCe0.3	165	223	0.11	0.52	0.43	1.1	1.4
CNTCe0.2	151	340	0.12	0.49	0.41	1.0	1.6
CNT Ce0.15	188	280	0.14	0.47	0.43	1.1	1.2
CNT Ce0.125	209	263	0.15	0.52	0.47	1.1	1.3
CNTCe0.1	160	255	0.12	0.36	0.34	1.1	1.2
CNT Ce0.075	165	280	0.13	0.45	0.40	1.0	1.1
CNT Ce0.05	218	264	0.14	0.54	0.46	1.1	1.4
CNT Ce0.025	202	217	0.08	0.49	0.39	1.1	1.5
CNTNi1	265	299	0.12	0.55	0.51	1.2	1.4
CNTNi0.5	135	279	0.10	0.42	0.35	1.0	1.3
CNTNi0.1	121	257	0.10	0.42	0.35	1.0	1.6
CNT Ni0.05	227	273	0.15	0.54	0.48	1.1	1.4
CNT Ni0.01	172	260	0.12	0.47	0.39	1.0.	1.1

Both DFT and BHJ pore volumes remained relatively constant as doped mass increased. The lowest pore volume recorded by both models was 0.3 cc.g^{-1} for RCNT confirming that the doping process was less destructive to the CNTs pore space than the purification process had been

beneficial, even when doped mass exceeded the impurity fraction of the RCNTs. The dopant must therefore be more evenly distributed than the metal catalysts, reducing its negative influence on the CNTs porosity. A possible explanation for this was observed from TEM analysis. RCNT material impurities blocked tube ends, dopant materials coated tube sides as discussed above. Despite there being no particular peculiarities in its isothermal results compared to the other samples, CNTCe0.5 had a larger pore volume than any of the other materials when modelled by either process. No explanation for this can be found. Excluding CNTCe0.5's result from both comparisons the DFT model had a narrow spread of pore volumes between 0.3 and 0.5 cc.g⁻¹ with a slight trend for decreasing pore volume with dopant amount. BHJ pore volumes had a slightly wider spread from 0.3 to 0.55 cc.g⁻¹ and tended toward the larger volume compared to DFT results but with occasional departures from this trend. Variation can be ascribed to differences in the two models assumptions as discussed in **Section 3.3.5**.

Trends in the mode pore width with increasing dopant mass were different for DA and DFT models, however both processes limit the half pore width or mode pore radius to a region between 1.0 and 1.8nm confirming that the majority of the sample volume is shared between the micropore and lower mesopore region [249]. Comparing the change of pore volume with pore size, $d(V)r$, calculated by DFT analysis provides some clues about how the dopant has affected the pore size distribution. **Figure 4.3.12** exemplifies this point by comparing the pore size distribution of three of the cerium doped samples to the PCNT.

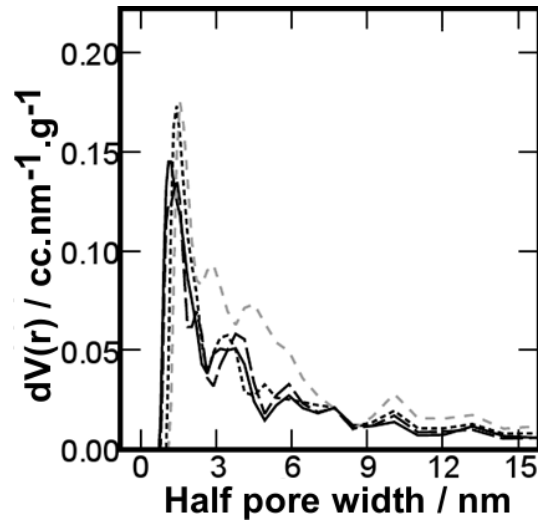


Figure 4.3.12. DFT pore size distribution of cerium doped CNTs. Key: PCNT (black line), CNTCe0.1(black dashed line), CNTCe0.3 (Black dotted line), CNTCe0.05 (grey dashed line).

Figure 4.3.12 shows that there was very little change in the pore size distribution between doped samples and PCNT for pore sizes greater than 7.5 nm, confining the dopants influence on pore size to the meso and micropore regions. As dopant levels increased the fraction of pores identified by DFT with a radius below 1.5 nm decreased and pore volumes in the region between 4.5 and 6.0 nm increased. Heavily doped samples had an increased pore volume between 1.0 and 3.0 nm as well. There are two possible explanations for this. Firstly, were the doping process homogeneous it could be concluded that the dopant had blocked the narrowest micropores [96]. As TEM analysis has shown an uneven distribution of dopant on the CNTs it seems more reliable to state that increasing the dopant mass reduces the pore volume per gram of the smallest pores to negligible levels. This reduction in resolution would increase the observed mode pore width of the materials with increased doped amount. Secondly, PVD is non-destructive process so explanations such as pore opening or adsorbent damage to increase porosity of the adsorbent are unlikely to be responsible [247]. Considering the texture of the dopant observed by TEM (**Figures 4.3.11A** and **4.3.11F**) it could be that the increased pore volume in these regions is due to crevices or pores on the surface of the cerium particles. Dopant materials generating pore

sizes similar to those of the adsorbent seem wholly feasible when considering that they are growing on structures nanometres in width. Such a conceptual model also helps explain how a doped material can maintain a constant pore volume in cc.g^{-1} even as the density of the samples increases.

The mode pore widths recorded by the DA model were between 1.0 and 1.1 nm. The outcome is lower than the results reached by DFT model but is consistent with their conclusions that the majority of the doped CNTs volume is in pore spaces bridging the upper micropore and lower mesopore region. Whilst the DA model is designed to measure micropore volume, the model extends to pore widths of 3.0 nm, a range greater than the recorded half pore widths from DFT analysis confirming that the outcomes are not being restricted by the models range. DA pore volumes mirror the recorded volume at point B (**Figure 4.3.6**) in the isothermal plots. Whilst no overall trend was observed in the DA results, comparison of the isothermal plots showed that point B occurred at lower adsorbed volumes as the doped mass increased.

4.3.2.3 Mixed metal powder sputtering

Figure 4.3.13 shows the XRD spectra for the co-deposited CeNiCNT samples.

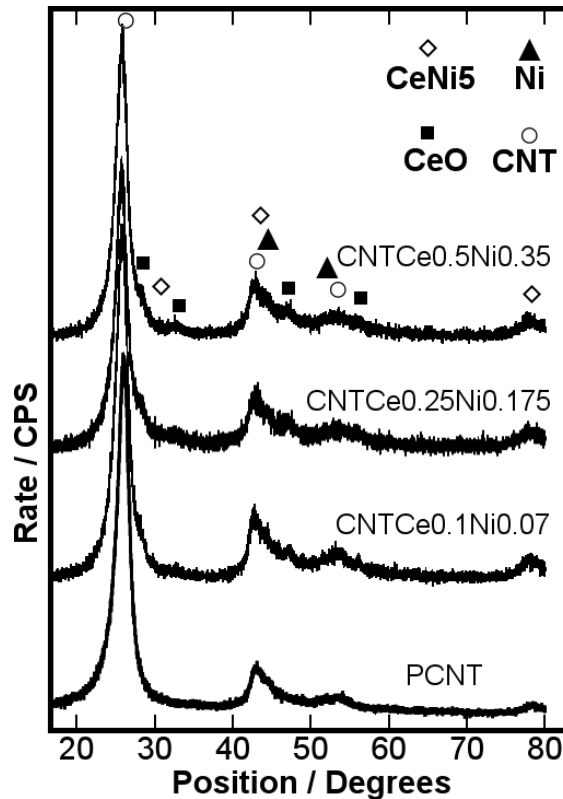


Figure 4.3.13. Comparison of PCNT and CeNi doped CNT Diffraction patterns.

The heights of the nickel and cerium peaks were severely subdued in the co-deposited samples relative to the intensities recorded in the CNTs doped with the pure metals. As XRD can only identify crystalline materials, the low peak abundances suggest either a lack of metal dopant or amorphous metal deposits. The metal content of the samples was clear from TEM inspection (**Figure 4.3.15**) so a highly amorphous metal phase is not only more likely, it was also predicted as a consequence of the deposition process (**Section 2.4.3**). Mismatch between nickel and cerium atomic diameters makes crystallisation difficult [163]. Weak peaks for CeNi_5 were identified (**Figure 4.3.13**) showing that some crystallisation of CeNi alloys has occurred. Alloy formation, reducing the cerium crystallinity was the goal of the co-deposition as it has been shown to improve cerium and nickel's catalytic activity toward methane tri-reforming [159, 160]. In that respect, the co-deposition process was successful.

TEM analysis of the co-deposited samples showed the same structural artefacts as were identified in the pure metal deposited samples (**Figure 4.3.10**). The most significant difference was what appeared to be a textural change in the appearance of the deposited material. The co-deposited metals had a rounder, more bobbled texture as shown in **Figures 4.3.14A** and **4.3.14B**.

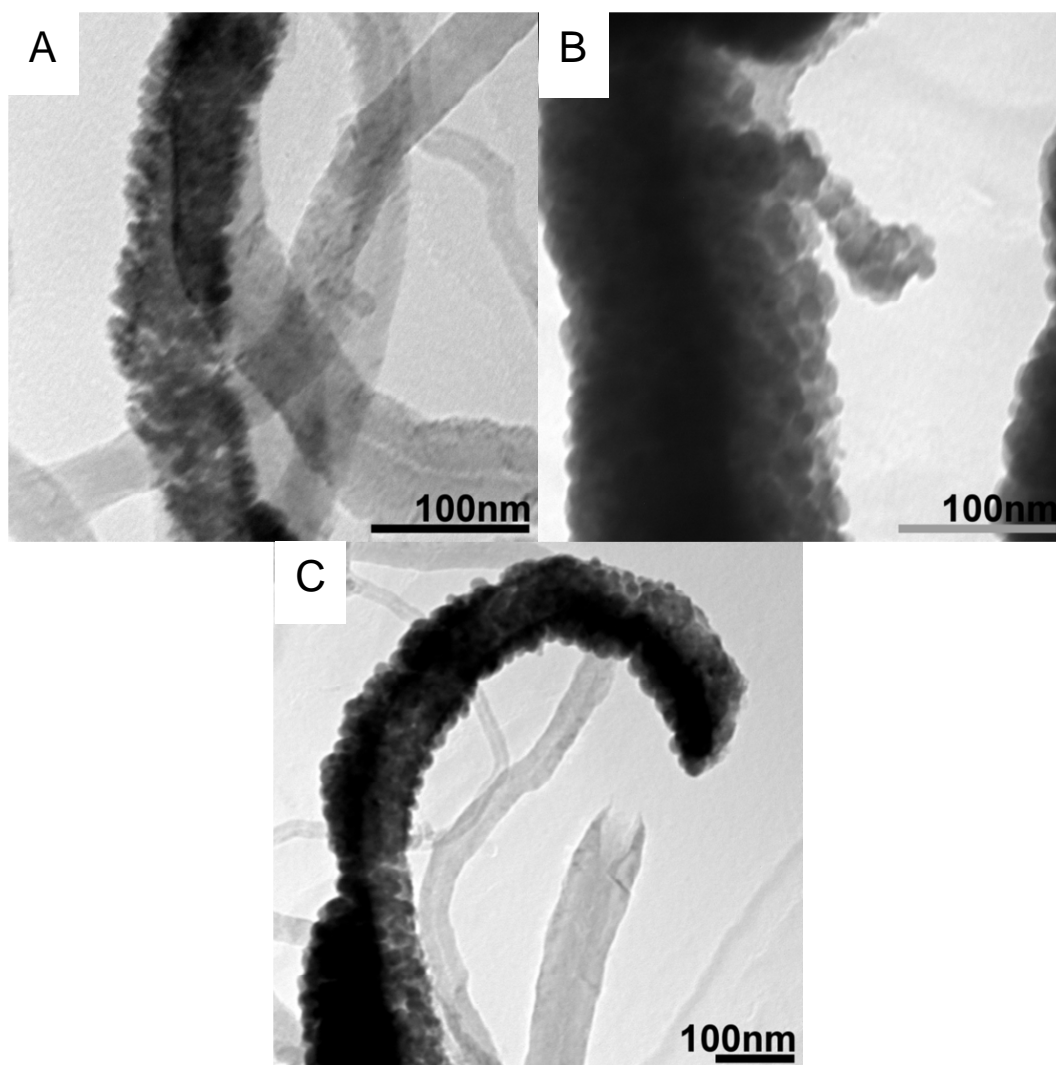


Figure 3.3.14. TEM images of textured CeNi doped CNTs. A) CNTCe_{0.1}Ni_{0.07}. B) CNTCe_{0.25}Ni_{0.2175}. C) CNTCe_{0.5}Ni_{0.35}.

The textural variation may come as a result of the interaction between the two metals. Volumetric analysis results for the samples are shown in **Table 4.3.6**

Table 4.3.6. Physical attributes of cerium and nickel doped CNTs.

	Surface Area (m ² /g)		Micropore Volume (cc/g)	Pore Volume (cc/g)		Mode Pore Radius (Å)	
	BET	BHJ	DA	BHJ	DFT	DA	DFT
CNT Ce_{0.1}Ni_{0.07}	241	333	0.16	0.55	0.51	1.0	1.0
CNT Ce_{0.25}Ni_{0.18}	166	250	0.12	0.44	0.40	1.0	1.2
CNT Ce_{0.5}Ni_{0.35}	185	165	0.05	0.48	0.35	1.1	1.8

Once again, the pore volume and surface area of these samples were greater than those of the RCNTs and PCNTs (**Table 4.3.3**). Comparable surface areas, pore volumes, pore radii and half pore widths are found when compared to the single metal doped samples (**Table 4.3.5**).

4.3.3 Gravimetric hydrogen storage capacity

4.3.3.1 Density calculation

Density correction played a major role in finding the correct hydrogen storage capacities of the materials in **Section 4.2** due to density's influence on the buoyancy correction process for correcting for pressure effects on the balance [227]. Added care was taken when calculating density for the samples considered in this chapter although the precautions taken were found to be overcautious. Helium isotherms, collected from 30 to 600 mbar at 77 K, were used for calculating sample density. Three densities were extracted from each isotherm using different data collection ranges; 30-600, 100-600 and 200-600 mbar, respectively. Erroneous results provided by the inaccurate data collected at very low

pressures meant that these values could generate densities that varied by up to 3 g.cm^{-3} . Unlike results in the previous chapter, such variation – explored out of curiosity- was found to have only a nominal impact on the final hydrogen storage capacities of the samples when compared to the variation in hydrogen storage between materials. For example, changing CNTCe0.2's sample density by 3 g.cm^{-1} only changed the hydrogen storage capacity of the sample by 0.06 wt.%. Whilst not insignificant, a change of such proportions in any of the materials would not change the overall trend in isothermal results between samples. The reason for the depleted influence of density in these tests is due to the increased fractional uptake of hydrogen on the samples. These materials are recording hydrogen uptakes ten times greater than **Chapter 4.2's** samples. Across the spread of densities collected, each sample had one density of approximately 3.26 g.cm^{-1} . These densities were selected for the subsequent analysis of the hydrogen storage capacities.

RCNT, PCNT and all CNTs doped with nickel, cerium or CeNi alloys were found to have sample densities of approximately 3.26 g.cm^{-1} with a SD of 0.19 g.cm^{-1} .

4.3.3.2 Raw and pure CNTs

Isothermal results for the hydrogen storage capacity of the raw and purified CNTs are shown in **figure 4.3.15**. The data points represent the experimental results whilst the curve is the modelled best fit based upon the Toth equation (**Section 3.3.6.2**) [230]. This modelled fit helps better visualise the isothermal shape and is also a required step to calculate the heats of adsorption [234].

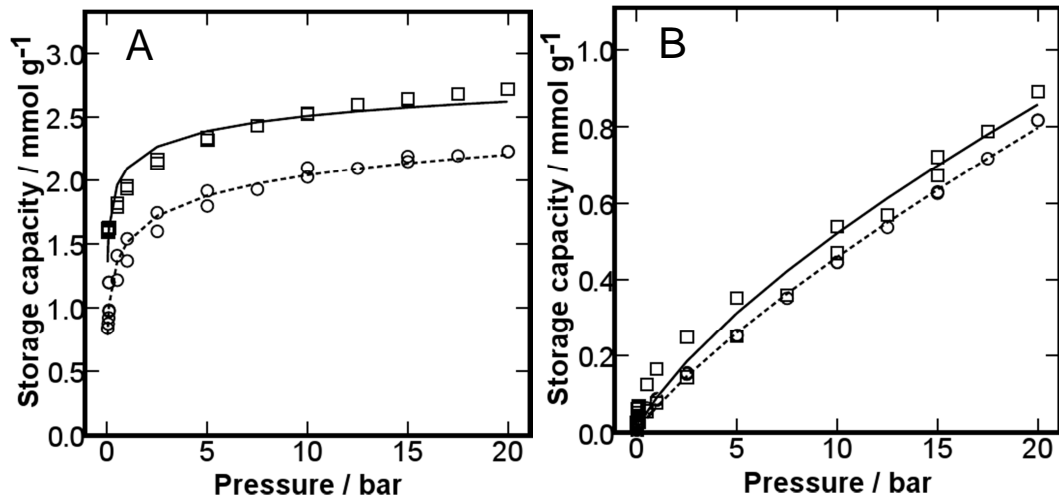


Figure 4.3.15. Isothermal H₂ storage capacities (mmol.g⁻¹) for RCNT (○) and PCNT (□) with pressure (bar). A) Isothermal results at 77 K. B) Isothermal results at 298 K.

The H₂ storage capacity for PCNT at 20 bar was 2.72 mmol.g⁻¹ (0.55 wt.%) at 77 K and 0.89 mmol.g⁻¹ (0.18 wt.%) at 298 K. The hydrogen storage capacity of the CNTs increased at both isothermal temperatures after purification. Not only did the storage capacity increase, so too did the kinetics as evidenced by the consistently steeper gradient in the PCNT isotherm compared to the RCNT isotherm. Type 3 hysteresis was observed for both samples again indicating adsorption in slit shaped pores [245]. The Toth based model (**Equation 3.31**) fitted to the experimental data with ANOVA R² value greater than 0.92 for all isotherms. The increase in the hydrogen storage capacity with purification can be ascribed to an increase in pore volume as evidenced by volumetric analysis and a decrease in dead weight as evidenced by the reduction in metal catalyst.

At 298 K (**Figure 4.3.15B**) variation in the isothermal trends between the samples did not become appreciable until around 1 bar suggesting that the purification had no effect on the fraction of binding site with the strongest hydrogen affinity. At 77 K (**Figure 4.3.15A**) the significant increase in hydrogen uptake at pressures below 500 mbar can most likely be ascribed to the increase in pore volume in the micropore and lower mesopore regions as described by volumetric analysis. The half

pore widths that saw the greatest fractional increase with purification were 0.9 to 2.4 nm, a region well documented to assist hydrogen adsorption [38, 46, 72]. The variation between storage capacities of PCNT and RCNT increased with pressure suggesting that the increases in total pore volume during purification contributed to the higher overall hydrogen uptake. DFT results from the volumetric analysis of these materials showed that in the regions between 2.5 and 2.8, and 4.1 to 5.3 nm half pore widths RCNT had a greater pore volume. Given that the hydrogen storage capacity and kinetics of the RCNTs was worse than that of the PCNTs it would suggest that these pore volumes do not play a significant role in hydrogen adsorption. The fractional increase in storage capacity with purification was 22 %. This is lower than the fractional increase in pore volume or surface area with purification further identifying that some of the newly exposed surfaces do not bind effectively with hydrogen.

The first isothermal data points collected for the samples at 77 K could not be made until the storage capacity had already exceeded 0.8 mmol.g⁻¹ and 1.6 mmol.g⁻¹ for RCNT and PCNT, respectively. This was due to the same apparatus problems described in **Section 4.2.2.1**. In overview, data points collected in this region had insufficient time to stabilise either gravimetrically or thermally and as a result gave inaccurate readings.

The total storage capacity of the PCNTs was 0.55 wt.% which, by comparison to the literature available for H₂ storage on CNTs (**Section 2.2.2**) is not particularly impressive. The observed storage capacities are however sufficient to allow an evaluation of the dopants influence on the storage capacity. Given the low storage capacity of the CNTs it is unlikely that the storage capacities of the doped samples will approach the DOE goals. It is instead the activity of the dopants and their influence on adsorption that is the focus of this work. The low storage capacity of the CNTs can be ascribed to a number of physical traits observed during material characterisation. Firstly, TEM analysis confirmed that the CNTs had multiple walls (**Figure 4.3.5B**). As the space between walls is typically

too small to allow for H₂ diffusion between them, then each tube wall except the innermost and outermost tubes provides no contribution toward the adsorption process and is effectively dead weight reducing the gravimetric storage capacity [67]. Secondly, TEM analysis also confirmed that the CNTs have a bamboo structure (**Figure 4.3.11A**). As described above a bamboo knot is a thin graphitic sheet formed during synthesis that compartmentalises the inner tube into segments. Any inner tube pore volume sealed at both ends by bamboo knots also provides no contribution toward the adsorption process [247]. The carbon mass that surrounds these sealed pore volumes is effectively dead weight further reducing the gravimetric storage capacity.

Isosteric Heat of adsorption for the raw and purified CNTs was calculated from the Clausius-Clapeyron equation (**Equation 3.36**) [234]. Results are shown in **Figure 4.3.16**.

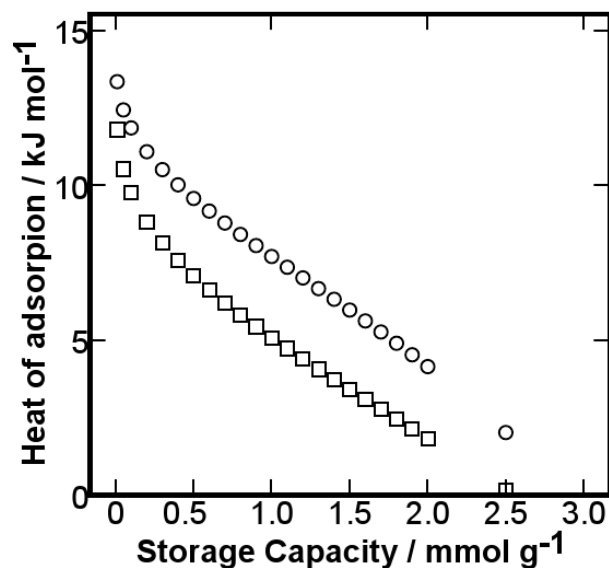


Figure 4.3.16. Isosteric heat of adsorption (kJ mol⁻¹) for RCNT (□) and PCNT (○), and its variation with storage capacity (mmol.g⁻¹).

The heats of adsorption recorded at low storage capacities (below 0.5 mmol.g⁻¹) in **Figure 4.3.16** will be overestimations due to limitations of the Clausius-Clapeyron equation in the Henry's law region [239]. The trend in the heats of adsorption curves show that binding strength was quite strong at 0.5 mmol.g⁻¹, suggesting at least a small fraction of the CNTs

contained pore sizes strongly suited for H₂ adsorption. The steep gradient of the trends shows that the availability of strong binding sites drops off rapidly. Based upon the shape of the Toth modelled adsorption capacities of RCNT (dashed line of best fit in Figure 4.3.15) which were used to generate the data points for the Clausius-Clapeyron equation, adsorption will not exceed 2.5 mmol.g⁻¹ without a shift in temperature or pressure. Comparison of the RCNT to the PCNT results (Figure 4.3.16) shows that the purification process has increased the storage capacity of the materials, in part by generating fresh surfaces that bind strongly with hydrogen, thus the increase in heat of adsorption across the range of storage capacities.

4.3.3.3 Powder sputtering of lone metals

Figure 4.3.17 shows the isothermal results for the materials doped with nickel.

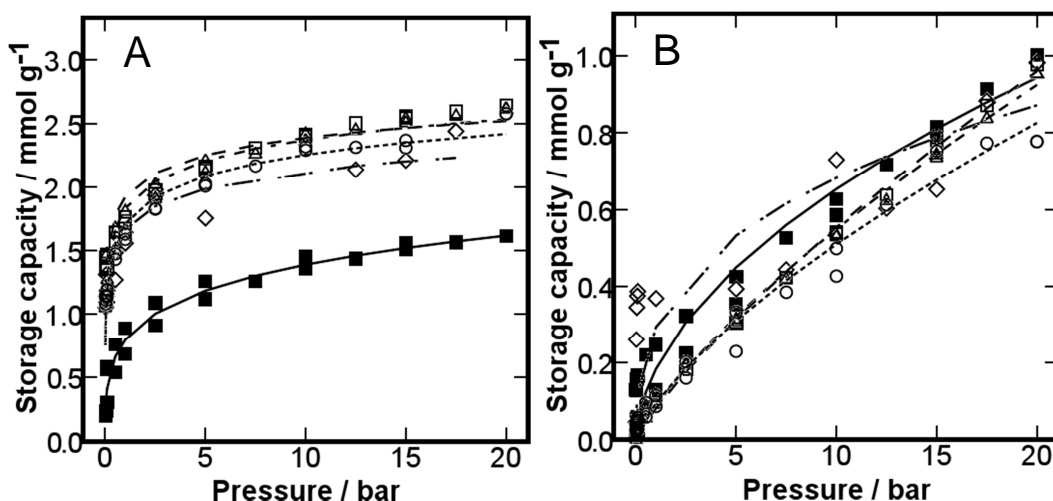


Figure 4.3.17. Hydrogen storage capacities (mmol.g⁻¹) for nickel doped CNTs up to 20 bar at 77 (A) and 298 K (B). Key: CNTNi0.01 (○), CNTNi0.05 (□), CNTNi0.1 (△), CNTNi0.5 (◇), CNTNi1 (■).

The highest H₂ storage capacity recorded at 77 K and 20 bar was 2.64 mmol.g⁻¹ (0.53 wt.%) for CNTNi0.05. The highest H₂ storage capacity recorded at 298 K and 20 bar was 1.00 mmol.g⁻¹ (0.2 wt.%) for CNTNi1. At

77 K there was very little variation in the hydrogen storage capacity of these materials compared to the PCNTs except for CNTNi1. The decrease in the storage capacity for CNTNi1 is likely due to the additional mass of the material provided by the excess of doped nickel. CNTNi1 also had a slightly smaller gradient in its isothermal knee (the region equivalent to point B in **Figure 4.3.17**), a feature attributable to a decrease in the availability of strong adsorption sites. ANOVA R^2 results for the Toth modelled fit exceeded 0.9 for all samples, except for CNTNi0.5 at 77 K, where the collected data was skewed due to apparatus failure during the run and R^2 dropped to 0.76.

According to XRD results the nickel contents of CNTNi0.05, CNTNi0.1 and CNTNi0.5 were all higher than the nickel content of RCNT. Despite this their hydrogen storage capacities continue to outperform the RCNTs suggesting that in these samples the nickel content is better distributed, and whilst not particularly beneficial as a catalyst, its additional mass was not especially detrimental. This conclusion provides further merit to the hypothesis from the TEM analysis; that dopant material coats the outer walls whilst catalytic waste material blocks the ends and that the metal distribution in the doped CNTs is less detrimental to the porosity of the adsorbent.

At 298 K the materials with larger doped masses had improved hydrogen storage capacities. Whilst the overall storage capacity is only fractionally larger than that of PCNT, given the added mass provided by the dopant, especially in samples CNTNi1 and CNTNi05, the actual mass of hydrogen per gram of CNT is larger. The presence of the isothermal knee became more pronounced as the dopant mass increased. This trend identifies catalytic activity promoting hydrogen adsorption in these samples, most likely through the spillover process (**Section 2.2.2.2.1**) [97]. The redistribution of pore sizes due to the presence of the dopant, as observed by DFT and BHJ analysis (**Table 4.3.5**), could also influence the adsorbed capacity. However, given the range within which pores sizes

were seen to increase are not pore sizes typically associated with strong hydrogen binding, the increase due to this effect would probably be small.

The maximum hydrogen adsorbed mass was only fractionally larger with increased doped mass despite the difference in isothermal shape indicating that the catalytic advantage provided by the nickel is negated by 20 bar. For example, in **Figure 4.3.17B** it can be seen that CNTNi1 (\blacksquare in **Figure 4.3.17B**) achieve a hydrogen uptake of 0.3 mmol.g^{-1} at a pressure approximately 2.5 bars lower than was required for CNTNi0.1 (Δ in **Figure 4.3.17B**) to achieve the same loading. By 20 bar both samples stored equivalent hydrogen masses.

Isosteric Heat of adsorption for the nickel doped CNTs was calculated from the Clausius-Clapeyron equation (**Equation 3.36**). Results are shown in **Figure 4.3.18**.

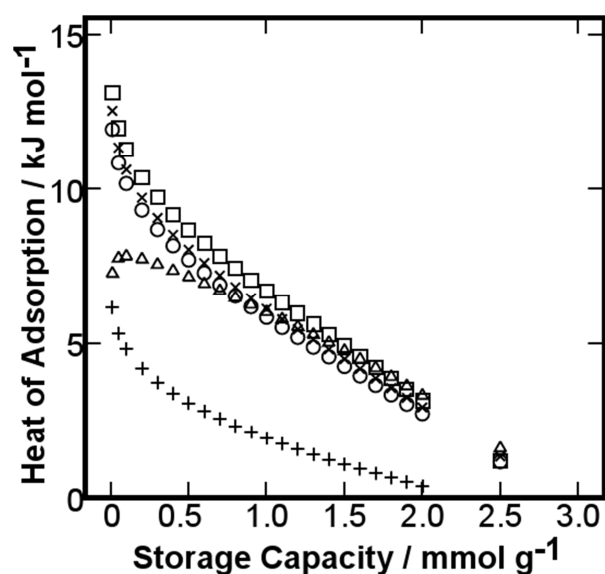


Figure 4.3.18. Isosteric heats of adsorption (kJ mol^{-1}) and its variation with storage capacity (mmol.g^{-1}) for nickel doped CNTs. Key: CNTNi0.01 (\square), CNTNi0.05 (\circ), CNTNi0.1(\times), CNTNi0.5 (Δ) and CNTNi1 ($+$).

Following the trend in the curve of the five sets of results, all samples would require additional energy input to exceed a storage

capacity of 3 mmol.g^{-1} . CNTNi1 (+ in **Figure 4.3.18**) has a lower heat of adsorption per gram of adsorbent due to the excessive loading of nickel that was shown to reduce the storage capacity. Unlike all the other samples, the results for CNTNi0.5 (Δ in **Figure 4.3.18**) curve downward in the low storage capacity region. This was due to problems fitting the isothermal curve at 298 K leading to an overestimation of storage capacity. As the Clausius-Clapeyron equation tends to overestimate heat of adsorption data in the low storage capacity region, these anomalous results below 0.5 mmol.g^{-1} for CNTNi0.5 should be ignored. At higher storage capacities there does not appear to be a problem with CNTNi0.5's data as the results follow a trend very similar to the other materials.

The maximum heat of adsorption recorded for these nickel doped CNTs does not exceed the maximum heat of adsorption of PCNT because none of the results for H_2 adsorption at 77 K outperform PCNT and because the Clausius-Clapeyron equation used to calculate the heat of adsorption does not seem an adequate method to express the heat of adsorption for a spillover material. The Clausius-Clapeyron equation is expressed as [234]:

$$-\Delta H_{ads} = \left[\left(\ln \frac{P_2}{P_1} \right) \left(\frac{RT_2 T_1}{T_2 - T_1} \right) \right]_W \quad \text{Equation 3.36}$$

Where T_1 , P_1 , T_2 , and P_2 are the respective temperatures and pressures of isotherms 1 (77 K) and 2 (298 K) at equivalent adsorbed quantities (W) and R is the ideal gas constant. The bigger the difference between pressures P_2 and P_1 , the larger the heat of adsorption. The advantageous nature of nickel as a spillover catalyst was it increased the storage capacity at 298 K but not 77 K, reducing the pressure difference P_2 and P_1 to achieve W and conflicting with the requirements of the equation. These results mean the Clausius-Clapeyron equation is incapable of expressing the contribution of a spillover catalyst.

Figure 4.3.19 shows the isothermal results for the preliminary cerium doped CNTs along with their Toth modelled experimental fits.

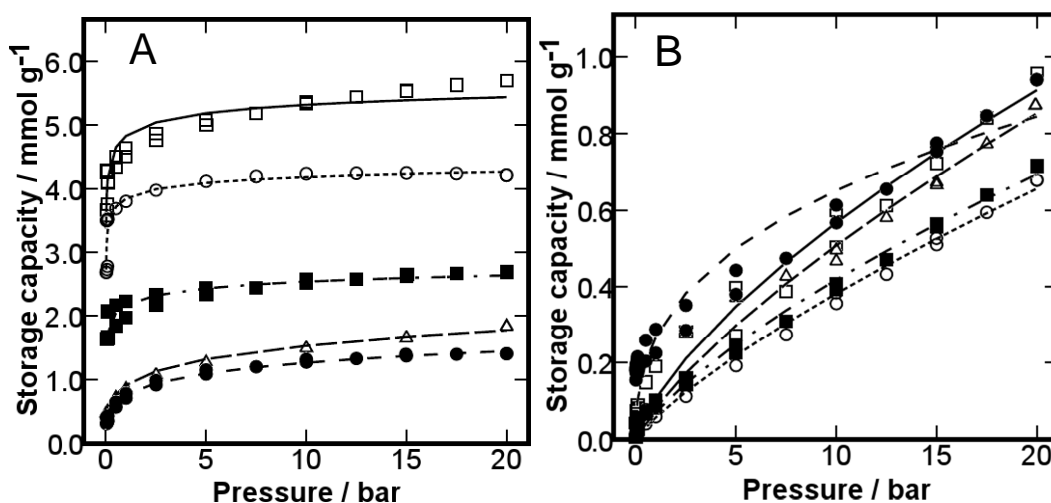


Figure 4.3.19. Hydrogen storage capacities (mmol.g⁻¹) for cerium doped CNTs up to 20 bar at 77 (A) and 298 K (B). Key: CNTCe0.1 (□), CNTCe0.2 (○), CNTCe0.3 (△), CNTCe0.4 (●), CNTCe0.5 (■).

The highest H₂ storage capacity recorded at 77 K and 20 bar was 5.7 mmol.g⁻¹ (1.15 wt.%) for CNTCe0.1. The highest H₂ storage capacity recorded at 298 K and 20 bar was 0.96 mmol.g⁻¹ (0.19 wt.%) also for CNTCe0.1. At 77 K, additions of small quantities of cerium, below 0.2 mole %, were able to significantly increase the adsorption capacity of the CNTs (○ and □ isotherms in Figure 4.3.19A). For loadings greater than 0.3 the storage capacities of the doped materials became smaller than the results for the purified materials indicating that the beneficial effects of the cerium were undermined by the additional mass fraction added to the samples. CNTCe0.1 had a storage capacity effectively double that of the PCNT. ANOVA R² values for the model fitting were better than 0.832 for all samples. No significant improvement or trend in results was observed in the hydrogen storage capacity at 298 K for any of the cerium doped samples. Given the high storage capacities at low loadings additional tests were performed with different cerium loadings. These tests focused on dopant loading volumes around 0.1 mol%. Their results are summarised in Figure 4.3.20.

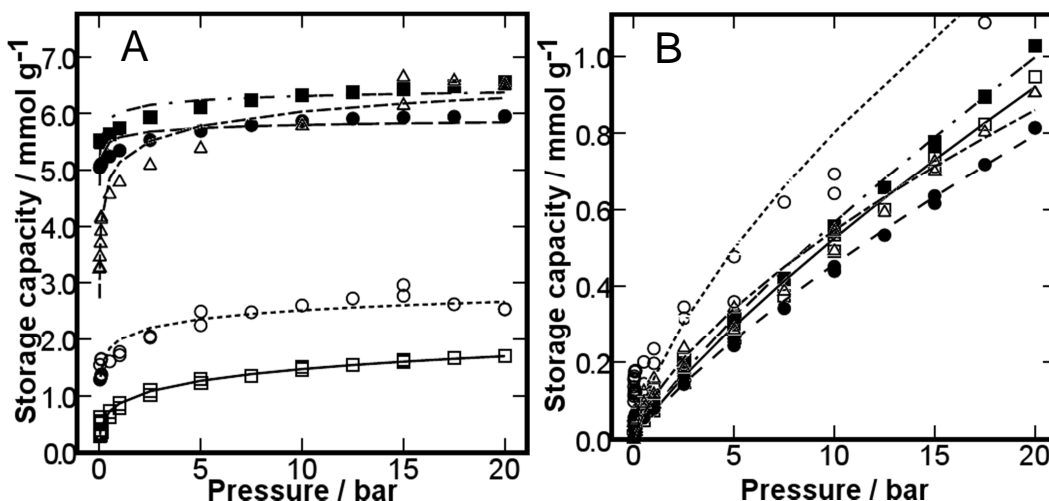


Figure 4.3.20. Hydrogen storage capacities (mmol.g⁻¹) for additional cerium doped CNTs up to 20 bar at 77 (A) and 298 K (B). Key: CNTCe0.025 (□), CNTCe0.05 (○), CNTCe0.075 (Δ), CNTCe0.125 (●), CNTCe0.15 (■).

The highest H₂ storage capacity recorded at 77 K and 20 bar was 6.6 mmol.g⁻¹ (1.32 wt.%) for CNTCe0.15. The highest H₂ storage capacity recorded at 298 K and 20 bar was 1.4 mmol.g⁻¹ (0.28 wt.%) for CNTCe0.05 however, as discussed below, this result was believed to be anomalous. These results support the findings from **figure 4.3.19** and show that cerium loading around the 0.1 % mol mark increase the storage capacity at 77 K. At 298 K (**Figure 4.3.20B**), with the exception of sample CNTCe0.05, all results had similar storage capacities to the previous cerium doped samples (**Figure 4.3.19B**) or the purified CNT samples (**Figure 4.3.15B**). CNTCe0.05 at 298 K seems like an anomalous result. Fitting the Toth equation to the collected isothermal data for CNTCe0.05 at 298 K proved difficult suggesting that there was an error during the experimental run. Given the trend observed in all other samples it seemed fruitless to repeat the CNTCe0.05 sample run as it was unlikely to contribute massively to the conclusions. R² ANOVA results were above 0.832 for all samples.

Heats of adsorption for the cerium doped samples are shown in **Figure 4.3.21**.

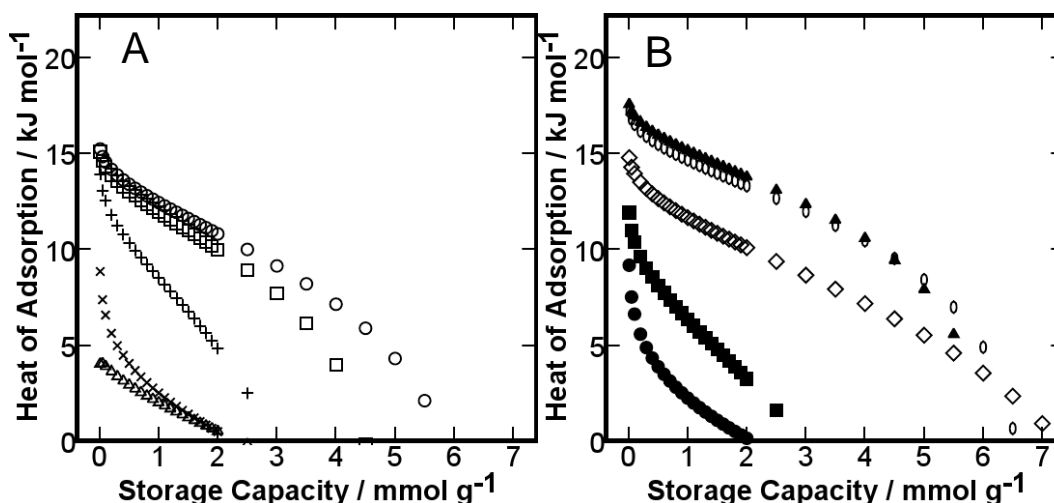


Figure 4.3.21. Isothermic heats of adsorption (kJ mol^{-1}) and its variation with storage capacity (mmol.g^{-1}) for cerium doped CNTs. Key: A) CNTCe0.1 (\square), CNTCe0.2 (\circ), CNTCe0.3 (\times), CNTCe0.4 (Δ) and CNTCe0.5 ($+$). B) CNTCe0.025 (\bullet), CNTCe0.05 (\blacksquare), CNTCe0.075 (\diamond), CNTCe0.125 (\blacktriangle) and CNTCe0.15 (\circ).

Addition of cerium not only increased the maximum heat of adsorption the system achieved compared to PCNT (Figure 4.3.16) it also increased volume of adsorbent that could be loaded exothermically (whilst the heat of adsorption remained positive). CNTCe0.025, CNTCe0.05, CNTCe0.3 and CNTCe0.5 (\bullet and \blacksquare from Figure 4.3.21A, and \times and $+$ from Figure 4.3.21B) all had similar isothermal heat of adsorption trends to PCNT, with the maximum storage capacity before the heat of adsorption becomes negative being between 2 and 3 mmol.g^{-1} . Variation in the calculated heat of adsorption became more apparent as the storage capacity increased. CNTCe0.1, CNTCe0.2 and CNTCe0.075, (\circ and \square from Figure 4.3.21A, and \diamond from Figure 4.3.21B) all had similar maximum heats of adsorption to PCNT of approximately 15 kJ mol^{-1} but the drop off in heat of adsorption with storage capacity was more gradual. Assuming that cerium acted to polarise some of the adsorbent surface, tube sides would be the likely sites of polarisation because of where cerium was observed to deposit from TEM results (Figure 4.3.11). Outer tube with no close proximity to other CNTs are known to be the worst sites for binding as they provide only one point of contact between the

adsorbate and the adsorbent [73]. Polarisation of these walls (see below) may have been sufficient to increase the hydrogen binding on tube outer walls to a level that increased the observed storage capacity. but not with a binding strength greater than chelative adsorption at tube ends, which is why the maximum heats of adsorption barely change [46]. No trend was apparent for maximum storage capacities of the materials that exceeded a storage capacity of 3 mmol.g^{-1} . This may be as a result of cerium dopant distribution as discussed below.

Volumetric analysis identified that additional dopant mass did not compromise pore volume. Furthermore, as no clear trend between the pore size distribution and storage capacity can be identified, variation in storage capacity and heat of adsorption must be attributable to the presence of the cerium. The mechanism by which cerium promotes hydrogen uptake is believed to be by donation of charge to the surrounding substrate, increasing the polarisability of the adsorbent and increasing the attraction between the adsorbent and the adsorbate [46]. There is very little insight available from this study to categorically confirm that this is the mechanism being followed; however, some of the observations discussed below strongly support it.

Three of the most important considerations for optimisation of dopant performance are the quantity added, the dispersion of the dopant and the average dopant particle size [97, 103]. The intertwined relationship between these considerations heavily influences catalyst activity. Issues with this sputter technique providing inadequate dispersions of the metals have already been discussed in **Section 4.3.2.2.**, here they will be further scrutinised to explain the observed changes in adsorbent performance. Cerium doped CNTs with a high H_2 storage capacity had a dopant wt.% equivalent to the wt.% H_2 storage capacity. For example CNTCe0.1 stored 1.148 wt.% H_2 and was doped with 1.153 wt.% cerium. Additionally, TEM analysis showed that the average cerium particle size for these samples was within the nanometre range with very little agglomeration between tubes (**Figure 4.3.11C**).

Conditions well suited for dopant distribution [97, 103]. Cerium doped CNTs with a low H₂ storage capacity had a dopant wt.% greater than the highest wt.% H₂ storage capacities of any sample. CNTCe0.3 contained 3.38 wt.% cerium, nearly triple the H₂ wt.% stored on CNTCe0.15. Additionally, TEM analysis revealed that the increased cerium mass had begun to encase whole nanotubes and agglomerate nanotube bundles together (**Figure 4.3.11D**). The activity of cerium in the WGS reaction, as discussed in the introduction, is closely influenced by the average cerium crystallite size, manipulated by alloying with nickel [157]. Crystallites of cerium are more inclined to share their electron positivity with their environment when they are smaller [293]. Larger particles internalise their charge distribution by sharing with encapsulated atoms [97, 160, 163]. The decrease in hydrogen adsorption with increased dopant mass is likely caused by three factors. Firstly, internalisation of charge distribution caused by increased particle size reduces cerium's charge sharing "influence" on the adsorbent [157, 158]. Secondly; agglomeration will have decreased the fraction of the dopant active in hydrogen physisorption as increasingly thick layers prevent encapsulated cerium atoms from interacting with the adsorbent or the gas. The ratio of active dopant atoms to mass of dopant will fall as agglomeration increases, reducing the effectiveness of the catalyst and increasing the dead weight of the system from the surplus mass of buried catalyst. Such an explanation fits the trend observed in the results, as shown in a summary of all isothermal results in **Figure 4.3.25**. Thirdly, as the dopant mass increases so too does the total mass of the adsorbent. This reduces the proportional adsorbed mass of hydrogen in terms of mol/g⁻¹.

Observations from the TEM analysis (**Figure 4.3.11**) that show cerium was not homogeneously distributed throughout the samples suggest that higher dopant masses, better distributed across the sample may be able to further improve the total storage capacity of the system.

4.3.3.4 Mixed metal powder sputtering

Figure 4.3.22 show the hydrogen storage capacities of the co-deposited CeNi alloys onto the CNTs.

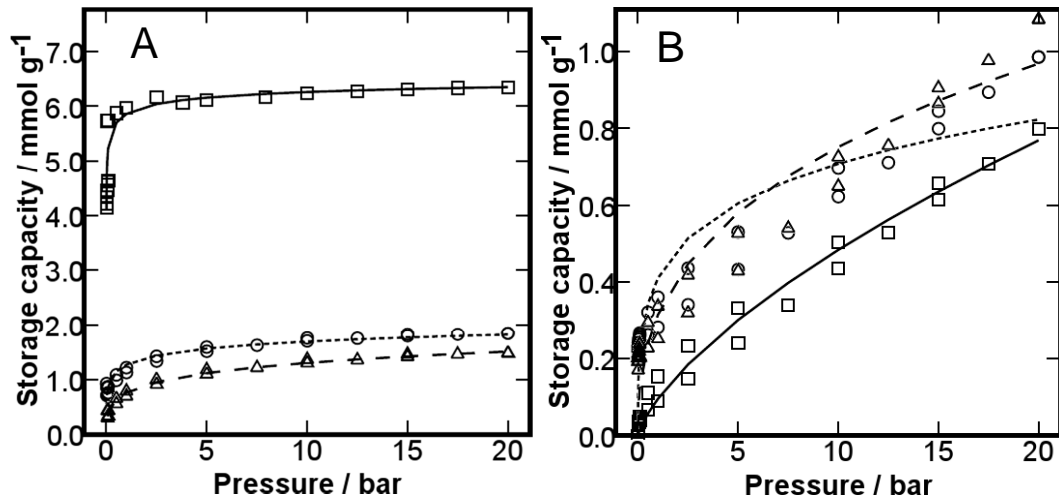


Figure 4.3.22. Hydrogen storage capacities for CeNi co-doped CNTs up to 20 bar at 77 (A) and 298 K (B). Key: CNTCe0.1Ni0.07 (□), CNTCe0.25Ni0.175 (○), CNTCe0.5Ni0.35 (△).

The highest H₂ storage capacity recorded at 77 K and 20 bar was 6.4 mmol.g⁻¹ (1.28 wt.%) for CNTCe0.1Ni0.07. The highest H₂ storage capacity recorded at 298 K and 20 bar was 1.08 mmol.g⁻¹ (0.22 wt.%) for CNTCe0.5Ni0.35. These co-doped samples displayed the combined beneficial properties of the individual metals. At 77 K the CNTCe0.1Ni0.07 performed best with a comparable storage capacity to CNTCe0.1. The performance at low temperatures must have been catalysed by cerium as nickel showed no activity at 77 K. Addition of further CeNi alloy reduced the storage capacity as was observed in both the lone Ce and lone Ni tests. At 298 K, as doped amount increased so too did the hydrogen storage capacity, as was found for the nickel doped CNTs. ANOVA R² results for the Toth fitting models were greater than 0.741 for all samples. The explanations for why each individual outcome occurs have already been covered above in the discussions about lone cerium and lone nickel deposition. As XRD analysis showed that the metal content was predominantly amorphous (Figure 4.3.13) the combined appearance of

the beneficial effects of both dopants in these samples (cerium's increase in storage capacity at low temperatures, nickel's increase in adsorption capacity at high temperatures) is likely due to each material acting independently in its amorphous form, rather than an effect of CeNi_5 crystalline alloys. Heats of adsorption for the CeNi doped samples are shown in **Figure 4.3.23**.

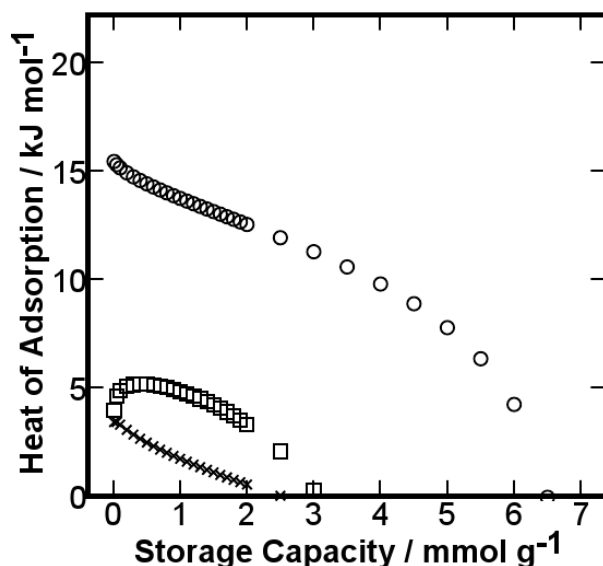


Figure 4.3.23. Isosteric heats of adsorption (kJ mol^{-1}) and its variation with storage capacity (mmol.g^{-1}) for CeNi co-doped CNTs. Key: $\text{CNTCe}_{0.1}\text{Ni}_{0.07}$ (\square), $\text{CNTCe}_{0.25}\text{Ni}_{0.175}$ (\circ), $\text{CNTCe}_{0.5}\text{Ni}_{0.35}$ (\times).

Once again the error in the trend of $\text{CNTCe}_{0.25}\text{Ni}_{0.175}$ (\circ in **Figure 4.3.23**) in the low pressure region is due to poor isothermal fitting of the Toth equation to the low pressure storage capacity of the sample at 298 K. Improvements to the model fits were attempted but to no avail. Explanations for the behaviours and trends observed can again be found in the discussion of the lone deposited samples.

4.3.3.5 Summary of all hydrogen storage results

Figure 4.3.24 compares the maximum storage capacities of all the materials at 77 K.

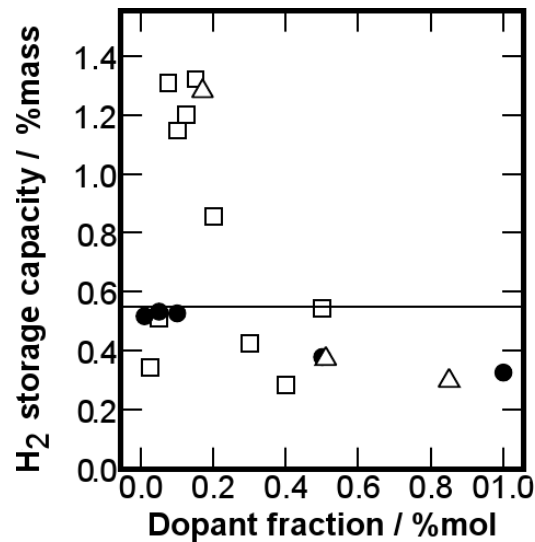


Figure 4.3.24. Comparison of the maximum hydrogen storage capacities (wt.%) at 77 K and 20 bar mol.% for cerium doped samples (□), nickel doped samples (●) and CeNi doped samples (Δ). The black line represents the maximum storage capacity of PCNT

A trend in the data for the cerium doped materials can be seen to increase around the CNTCe0.125 point then decrease. Similar results were found for the CeNi co-doped samples. No significant performance enhancement of PCNT could be measured for nickel doped samples and their capacity did decrease as the doped fraction increased.

4.3.4 Conclusion

The purification process worked effectively to remove the impurities in the material without compromising the structure of the CNTs. The process increased the pore volume by removing catalytic growth particle caps from sealed nanotubes. Volumetric analysis identified that these nanotube cores were predominantly mesoporous in size.

Doping samples through powder sputtering was an effective way to distribute dopant indiscriminately across an adsorbent. However, to truly optimise the dopants performance the process requires modification to homogenise the distribution.

Cerium was found to increase the storage capacity of PCNTs at low temperatures most likely through polarisation of the adsorbent surface. Longer deposition times increased the dopant particle size and the catalytic influence decreased. This is likely attributable to internalisation of the catalysts charge in thicker deposits and due to the added dead weight of unreactive dopant reducing the gravimetric efficiency of the system.

Nickel was found to increase the storage capacity of PCNTs at high temperatures through a spillover mechanism. Increasing the deposited mass of nickel seemed to further promote the catalytic influence within the fractional dopant masses tested.

Co-sputtering, although difficult to perform due to magnetron target melting, is an efficient way to optimise the distribution of the CeNi metals and reduce the formation of crystallites of either metal or an alloy. The amorphous structure of the dopant was thought to be beneficial for preserving the catalytic activity displayed by each material individually. The co-sputtered sample with the highest hydrogen storage capacity (CNTCe_{0.1}Ni_{0.07}) outperformed PCNT at both 77 and 298 K due to individual catalytic performances of cerium and nickel at the two temperatures, respectively.

4.4 Exploring the synthesis of graphene by magnetron sputtering

This section discusses the attempted synthesis of copper or nickel catalysed graphene films by magnetron sputtering. The background to this work is presented in **Section 2.4.4** and the experimental process is described in **Section 3.4.4**. Samples were named based upon their metal underlayer, the letter “G” to indicate that this was a graphene tests and then the deposition time. A list of sample names and compositions is presented in **Appendix B**.

4.4.1 Results and discussion

4.4.1.1 Visual inspection of the films

The deposited films were photographed to contrast their appearance, texture and transparency. Results are displayed in **Figure 4.4.1**.

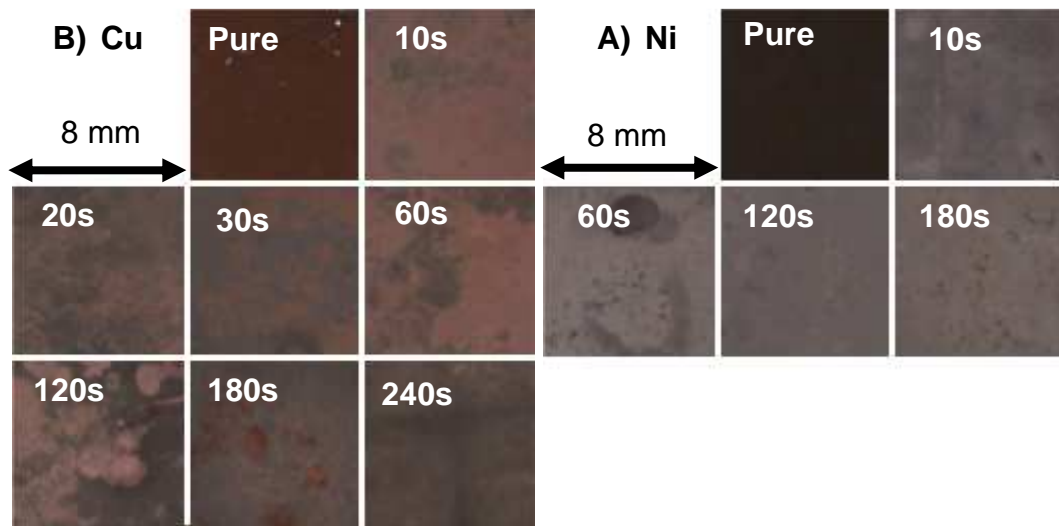


Figure 4.4.1. Changes in a films appearance with carbon deposition time. A) Variation in a Cu films appearance with carbon deposition time at 800 °C, B) Variation in a Ni films appearance with carbon deposition time at 800 °C.

Few-layer graphenes become less transparent by approximately 2.3 % with the addition of each additional graphitic layer [294]. In this work, the transparency of the carbon film decreased with deposition time on both metal underlayers. The pure copper film had a smooth, metallic coppery appearance evenly distributed across the grid. Following ten seconds deposition the films metallic appearance became matted and dim but still with a coppery reddish brown colour; suggesting that complete carbonaceous coverage across the substrate was achieved despite the short deposition time. The coppery appearance was mottled by randomly orientated grey patches suggesting inconsistency in the film thickness. As the deposition time increased the fraction of the film with a coppery brown colouring decreased and following four minutes deposition the grey coverage was almost complete with some sections beginning to appear black. The shift in the carbonaceous films appearance from transparent to black signifies the increase in the film thickness as carbon becomes less transparent as thickness increases. The coppery appearance remained prominent in samples sputtered for less than 120 seconds suggesting that they were coated in uneven FLG or very thin graphitic films. Similar changes in appearance were observed with the nickel deposition. The patchy and mottled appearance of the carbon films suggest that if any graphene materials have been synthesised then it is not as a single homogenous monolayer film across the whole substrate as such a film would have a homogeneous surface appearance. The deposition process requires refining to improve the homogeneity of the film.

4.4.1.2 Raman analysis

The key characteristics of a Raman spectra for characterising graphene films are the ratios between the full width at half maximum (FWHM) of the D peak at $\approx 1350 \text{ cm}^{-1}$ (breathing mode of sp^2 atoms in rings) and the G peak at $\approx 1580 \text{ cm}^{-1}$ (sp^2 bond stretching) referred to as the I_D/I_G ratio [208], and the 2D peak at 2680 cm^{-1} (double resonance of

the sp^2 atoms in the ring) and the G peak referred to as the I_{2D}/I_G ratio [192, 201]. Ideally the I_{2D}/I_G ratio should be ≤ 0.3 .

Significant variations between the Raman spectra collected across each carbon film, deposited on either copper or nickel, confirm that the deposited layers were not homogeneous in structure.

Amongst all the Raman spectra collected for the copper coated films, only one of the eight spectra collected from sample CuG30 (**Figure 4.4.2A**) was indicative of the graphene spectra from the literature. The other collected spectra for most samples were reminiscent of highly ordered graphite, such as the spectra for CuG180 in **Figure 4.4.2B**.

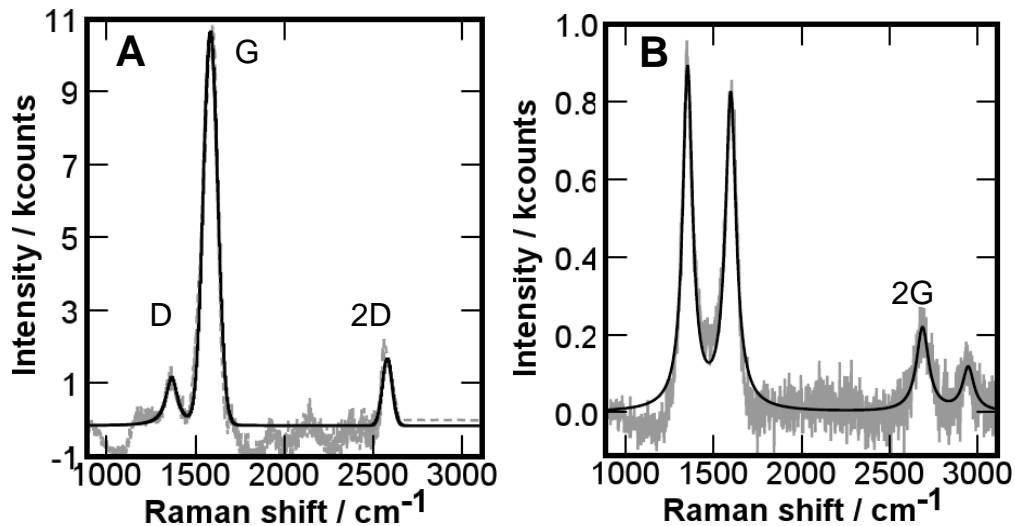


Figure 4.4.2. Raman spectra for carbon coated copper films. (Grey lines) base-line subtracted experimental data, (Black lines) modelled best fit. A) CuG30; B) CuG180.

The spectrum in **Figure 4.4.2A** shows a strong G peak, a weak D peak and an intermediate 2D peak. The I_{D2}/I_G ratio of the sample was 0.68, which is higher than is ideal for graphene [191, 194]. With longer deposition times, as in **Figure 4.4.2B**, the strength of the 2D peak decreased suggesting a drop-off in the ordered structure or an increase in the graphitic thickness [187]. The additional peak present at 2900 cm^{-1} is the carbon 2G peak. No high purity graphene films were identified on the copper coated substrates.

The mechanism for carbon deposition in this study was obviously different from the literature, as one process was PVD and the other CVD, but it was hoped that the graphene/FLG/graphite synthesis mechanism may be similar regardless of the deposition process. However, as discussed in **Section 2.4.4.2**, the copper mechanism for graphene synthesis should not be able to generate graphite as it is a self-limiting process [194], and because of copper's low carbon solubility, graphite synthesis via surface segregation followed by precipitation is also not possible [187, 194]. This means that the graphitic structures identified by Raman analysis above must have been synthesised by an alternative mechanism. Two alternative mechanisms can be imagined.

The first involves the deposition of amorphous carbon onto the copper surface, and due to additional energy provided by the temperature of the substrate and the energy of the impinging particles, subsequent carbon deposited onto the amorphous layer forms graphitic structures. By this mechanism copper played no role in the synthesis and graphene was never formed. This process seems unlikely because low I_D/I_G ratios observed in the Raman spectra suggest highly ordered systems that would not be present were graphite grown on amorphous carbon.

The second mechanism, which fits better with the observed results, is template growth of graphene on top of other graphene sheets [295, 296]. In this mechanism graphene would grow across some or all of the copper film. Additional sputtered carbon particles, deposited atop the graphene film and lacking sufficient energy to find the edge site, nucleate on top of the graphene film. They in turn grow and are once again nucleated on top of if sufficient sputtered carbon precursor is still present. This layering of graphene on graphene fits better with the highly ordered graphitic structures identified by Raman analysis and also explains what happens to additional sputtered carbon deposited onto graphene sheets. Three important factors to consider during template growth are [296]:

1. Selection of an adequate templating surface. Graphene/graphite is an ideal surface for templating graphene as it suppresses the formation of deviations from the graphitic structure. Copper is also a suitable template as proven by the growth of graphene on its surface by CVD [186]. This factor would seem to be adequately controlled by the experimental sputter process as graphene/graphite or copper are the two surfaces that sputtered particles should be impacting on.
2. Well annealed carbon addition [296]. Removal of carbons deposited in any configuration other than that required for graphene is essential for graphene propagation. Templating assists this cause and so does annealing at high temperatures. Carbon conformations not corresponding to pristine graphene formation are more kinetically reactive so are easier to remove by thermal excitation or etching, but the rate of carbon addition (rate of deposition in this case) needs to be low enough to allow annealing of the defect conformations otherwise defective carbon lattices would propagate. Better control over this parameter could be studied by refining the synthesis process, using higher substrate temperatures or lower sputter rates.
3. Nucleation suppression [295]. In CVD this involves limiting the sooting potential by keeping the carbon precursor levels at low partial pressures and temperatures to prevent formation of fresh nucleation sites on top of graphene sheets. In sputtering this is a far harder issue to suppress as carbon is activated before it reaches the target, and where it binds on the surface cannot be controlled.

Table 4.4.1 outlines the key Raman results collected for the carbonaceous films deposited on copper. Isolation of the carbon spectra was difficult for the shorter deposited films due to low intensity signals from the carbon films and saturation of the spectral background by the copper plasmon [201].

Table 4.4.1. Key Raman results from analysis of carbon coated copper films.

Sample	D peak		G Peak		* FWMH full width at half maximum
	Average Shift (cm ⁻¹)	Range FWMH*	Average Shift (cm ⁻¹)	Range FWMH	
CuG10	1352	65 160	1589	31 98	
CuG20	1364	39 182	1591	72 105	
CuG30	1360	69 93	1591	70 125	
CuG60	1355	48 107	1600	51 93	
CuG120	1355	70 110	1597	63 86	
CuG180	1353	39 117	1596	50 85	

Sample	2D Peak		Spread of I _D /I _G ratio		Spread of I _{2D} /I _G ratio	
	Average Shift (cm ⁻¹)	Range FWMH	Low	High	Low	High
CuG10			1.63	2.10		
CuG20	2586	236 322	1.21	1.61	3.03	4.46
CuG30	2575	65	0.56	1.24	0.69	
CuG60			0.72	1.27		
CuG120			0.97	1.27		
CuG180	2686	41 143	0.79	1.44	0.61	2.05

The Raman analysis of all films showed both the D and G peaks in varying strengths but no trend with sputtering time could be found with their average shift or FWMH. Variation in the I_D/I_G ratio showed that carbonaceous deposits, ranging from graphite (I_D/I_G ratio of 0.5-1.5) to nano-crystalline graphite (I_D/I_G ratio above 1.5) were synthesised [208]. I_D/I_G ratios below 1.0 with a G peak position above 1580 cm⁻¹ indicate the presence of highly ordered graphitic structures [208]. The presence of the 2D peak at 2680 cm⁻¹ was identified in a number of the samples but not in

all spectra and not consistently in all films. The 2D peak intensities were significantly less intense and wider than would be expected for graphene suggesting that graphene or FLG was not synthesised [191]. The 2D peaks presence does however compliment the assessment that highly ordered graphitic structures dominated in the carbon film, as 2D peaks are not present in amorphous films.

Figure 4.4.3 provides two examples of the Raman spectra collected for the carbon coated nickel samples and **table 4.4.2** outlines the key results from the Raman analysis of the carbon coated nickel films.

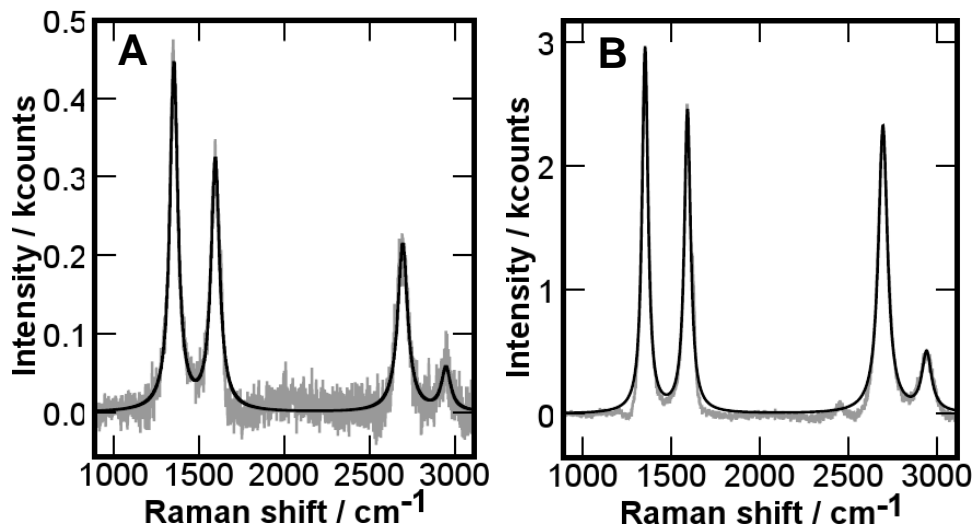


Figure 4.4.3. Raman spectra for carbon coated nickel films. (Grey lines) base-line subtracted experimental data; (Black lines) modelled best fit. A) NiG60; B) NiG120.

As the deposition time increased the intensity of the 2D peaks in the Raman spectra increased compared to the G peaks, as is seen in the comparative increase in the 2D peak intensities between **Figure 4.4.3A** and **4.4.3B**, and in **Table 4.4.2**.

Once again D and G peaks were identified in all samples. The G peak remained above 1580 cm^{-1} suggesting that regardless of I_D/I_G ratio the materials grown were predominantly graphitic [208]. The strength of the 2D peak increased with carbon deposition time until, following three minutes carbon deposition, the 2D peaks abruptly disappeared in all but

one of the NiG180 spectra. The I_{2D}/I_G ratio for all these samples was between 0.79 and 1.88 once again identifying a highly ordered but not graphene based film [191].

Table 4.4.2. Key Raman results from analysis of carbon coated nickel films.

Sample	D peak		G Peak	
	Average Shift (cm ⁻¹)	Range FWHM*	Average Shift (cm ⁻¹)	Range FWHM
NiG30	1351	69 110	1592	65 137
NiG60	1353	48 132	1595	60 85
NiG120	1347	40 79	1592	42 55
NiG180	1352	89 118	1597	65 95

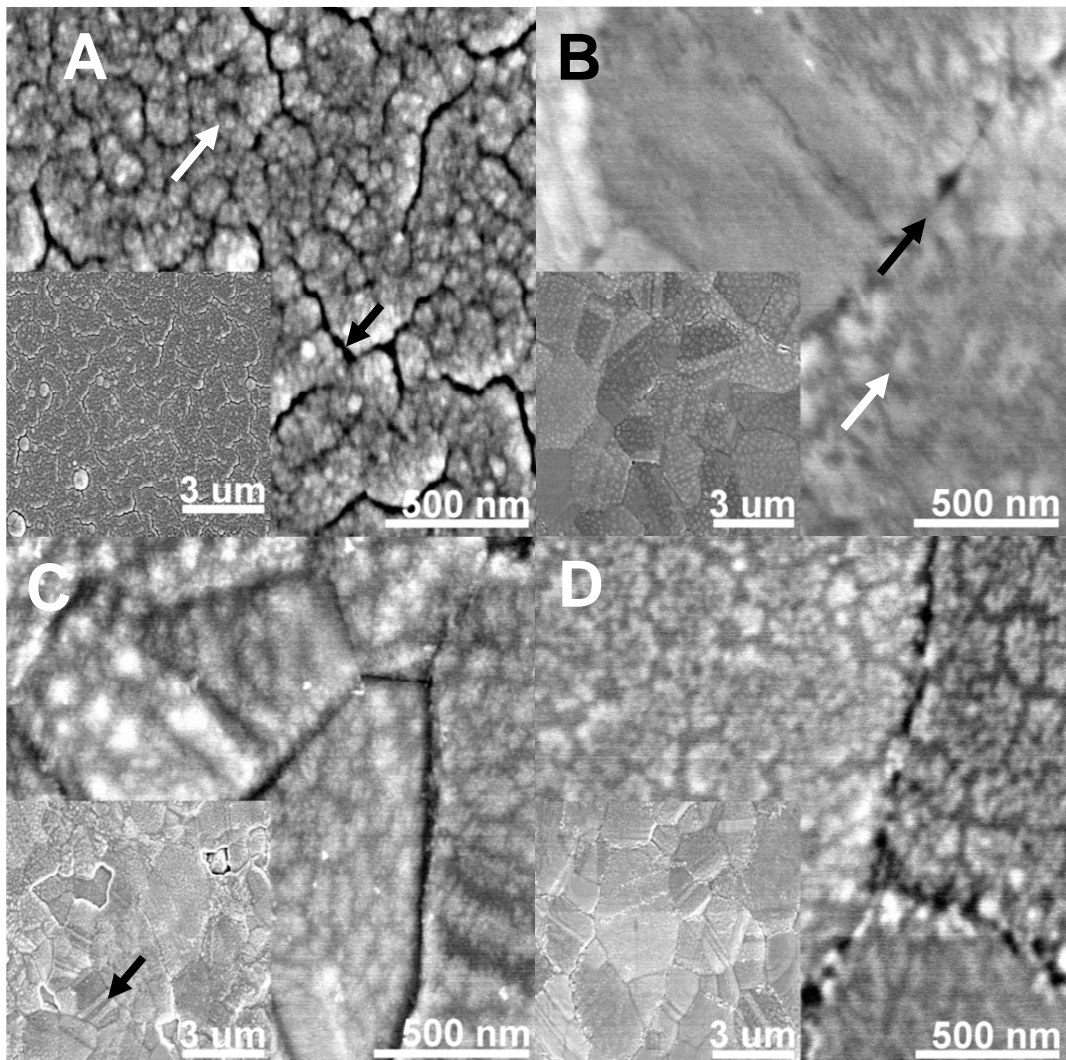
Sample	2D Peak		Spread of I_D/I_G ratio		Spread of I_{2D}/I_G ratio	
	Average Shift (cm ⁻¹)	Range FWHM	Low	High	Low	High
NiG30	2688	70	0.80	1.51	0.94	
NiG60	2695	64 81	0.79	1.55	0.79	1.28
NiG120	2694	57 80	0.88	1.59	1.09	1.88
NiG180	2717	79	1.17	1.74	1.14	

The range between an individual samples largest and smallest I_D/I_G ratio (**Tables 4.4.1** and **4.4.2**) was frequently larger for nickel samples than for copper samples implying less homogeneity in the nickel synthesised films. This seems consistent with the different film appearances as discussed in the SEM analysis (**Section 4.4.2**). The highest I_D/I_G ratios, identifying the most ordered carbon deposits, were predominantly found from nickel, rather than copper samples. This suggests that the growth mechanism for sputtered carbons on nickel was better suited for the synthesis of ordered carbon structures, within the experimental conditions

tested, than on copper. Refinement of the carbon sputtered on nickel, rather than copper, process seems more likely to yield graphene because of the increased crystalline order seen in the deposited films.

4.4.1.3 SEM analysis

The appearance of the deposited films was recorded by SEM analysis. Topography of the deposited carbonaceous materials grown on a copper underlayers are shown in **Figure 4.4.4**.



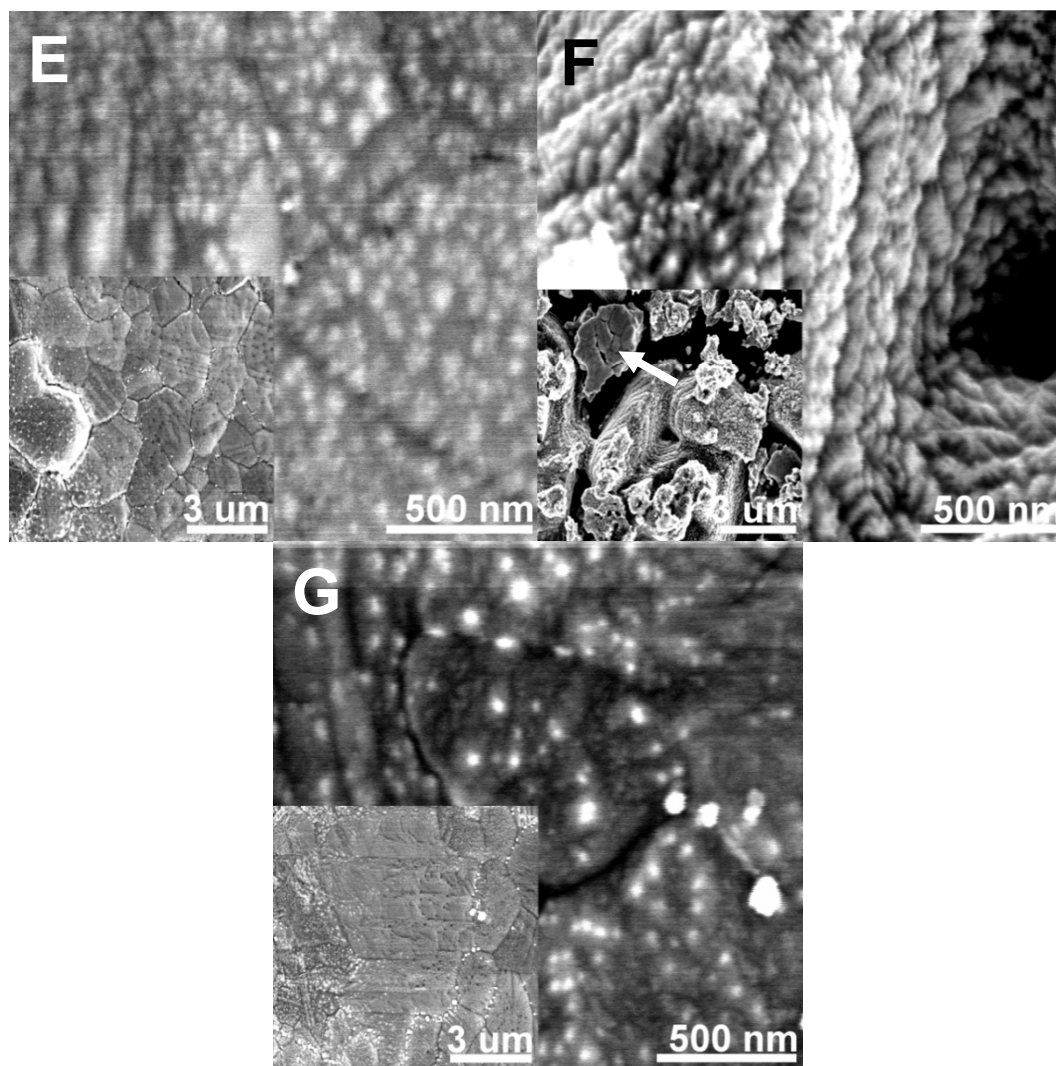


Figure 4.4.4. Surface topography at different magnifications of copper and carbon films deposited at 800 °C over varying deposition times. A) Pure Cu. Black arrow denotes a macroscopic crack in the film, White arrow denotes the microscopic features of the film; B) CuG10. Black arrow denotes a Grain boundary. White arrow denotes an uncharacterised star-like structure; C) CuG20. Black arrow denotes a contrast in film brightness with a single grain boundary; D) CuG30; E) CuG60; F) CuG120. White arrow denotes an area of planar carbon growth similar to the other carbon films; G) CuG180.

It seems prudent to note that the SEM images were taken following cooling of the metal later from 800 °C to room temperature. The cooling process may have caused cracking or crystallisation of the metal layer and therefore the topography shown in **Figure 4.4.4A** may be different to the

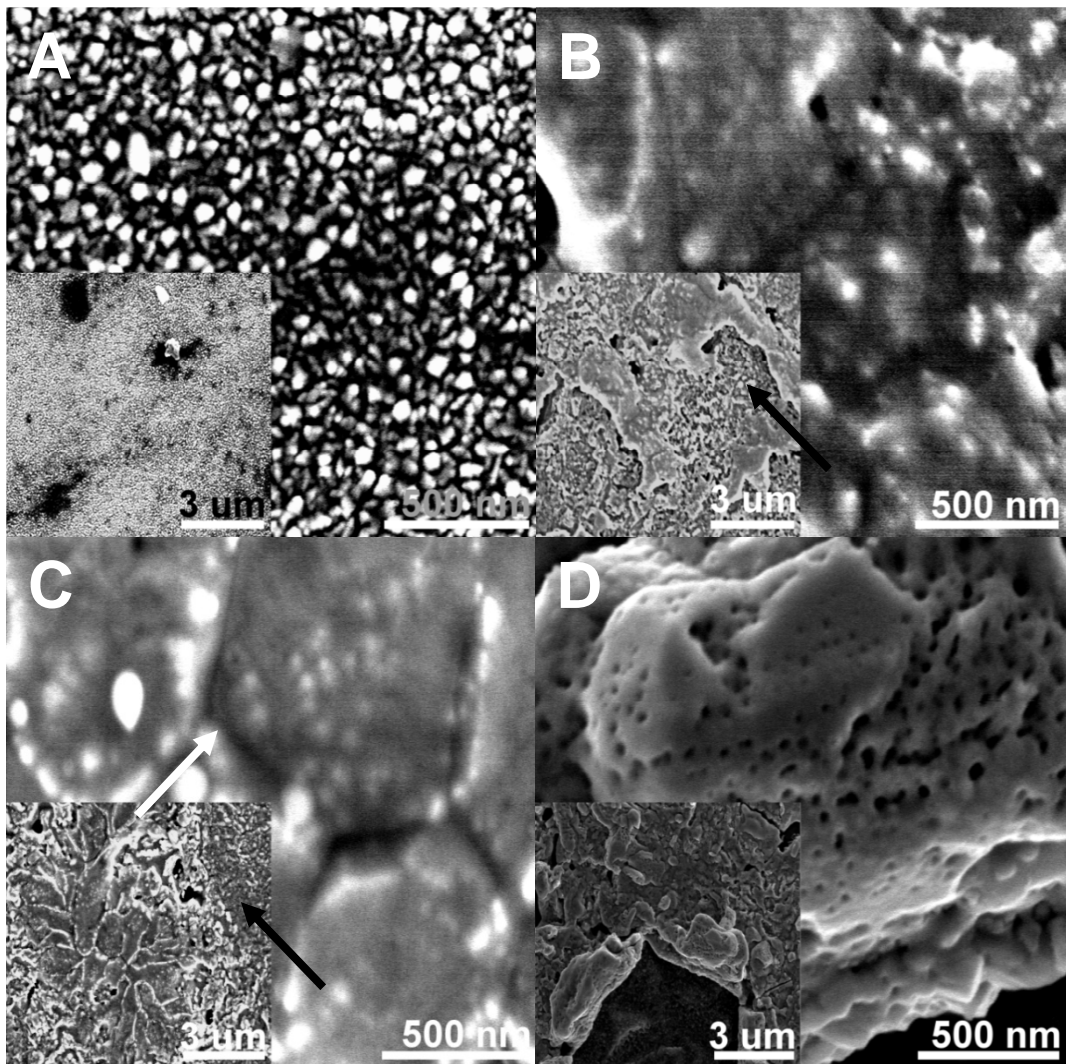
topography that carbon was actually deposited onto. The pure copper film (**Figure 4.4.4A**) has a cracked surface structure. The macroscopic cracks (**Black arrow in Figure 4.4.4A**) relating to the deepest troughs in the film may be the result of thermal mismatch between the copper and silicon layers and could have formed during the cooling step after copper deposition and would not necessarily have been present during deposition. The microscopic features (**White arrow in Figure 4.4.4A**) may have been caused by unaligned crystalline phases rearranging themselves to their lowest energy conformations and forming grain boundaries. The rough surface appearance of the metal underlayer (**Figure 4.4.4A**) is consistent with the appearance of metal underlayers for graphene synthesis from the literature [202]. Both SEM images and graphene mechanistic diagrams have depicted uneven metal underlayers being adequate for the synthesis of FLG structures. The mechanistic growth process described by Obratsov *et al.* suggests that the uneven troughs in the metal underlayer fill with amorphous and FLG structures allowing for flat growth of graphene or FLGs across the rest of the even metal surface [195].

The appearance of the film surface changes dramatically following 10 seconds of carbon deposition (**Figure 4.4.4B**). A flatter film (as established by the depth of field during focusing) has formed on the metals surface. The film appears to be made up of multiple nucleation sites identified by the grain boundary lines (**Black arrow in Figure 4.4.4B**). Their appearance is reminiscent of graphene films within the literature [202, 297]. Whilst the shape of the different nucleated films is irregular their boundary edges are straight and frequently fork off at an angle of 120° suggesting the propagation of a hexagonal lattice. Within some of the planes a contrasting brightness can be seen running parallel the grain boundaries (**Black arrow in figure 4.4.4C**). This contrast in structure could be the result of the formation of secondary layers, either through direct nucleation of a second layer on top of another film, or overlap interfacing as described in the introduction (**Figure 2.18**) [190]. The brighter areas of a film may also represent an area with significant

alignment between a stack of graphitic planes in their Z axis [186]. The film surface was also decorated with star-like patterns (**White arrow in Figure 4.4.4B**) which appear to have a hole in their middle in the larger specimens. Their appearance on film surfaces appears to be unique to this work so may be a consequence of the sputter process. They appear to grow larger in both width and thickness as deposition time increased. By three minutes deposition their presence could not be identified. Similar structures were observed growing on the nickel films and will be described below. As deposition times increase, the low magnification ($> 3 \mu\text{m}$) appearance of the films remained similar whilst on the high magnification ($< 500 \text{ nm}$) appearance of the star structures appeared to expand. The images in **Figure 4.4.4F** for sample CuG120 were taken where the copper underlayer appeared to have not been uniformly coated during deposition, leaving a rough surface structure over a fraction of the film. Some plateaus in the copper film showed signs of the planar carbon film growth (**White arrow in Figure 4.4.4F**) but no propagating film could be identified on the steep edges of the copper cracks. They were however coated in the star-like nanostructures as observed on all the other films. Based upon the graphene literature, these star-like structures could be Cu-Si-O particles that have adsorbed or migrated through the carbon layer and precipitated on the surface [191]. However, this composition seems unlikely due to their presence on the nickel films, where no copper was present, and their absence at grain boundaries in the copper coated samples. Alternatively they could be wrinkles in the graphitic structure caused by thermal mismatch of the individual films during cooling although their spacing is considerably closer than could be explained by thermal shrinkage [195]. As the star-like structures appearance was not observed in the pure copper film and was apparent on the surface of the propagating carbon layers it would appear they are carbon based materials and may be evidence of seed points for either nanotubes or the nanocolumns as described in **Section 2.4.2** [153, 264]. Recent research performed by Rao *et al.* has indicated that nanotubes can be synthesised across a graphene surface [298].

As near complete surface coverage with graphitic films was achieved across the copper substrate, even after 10 seconds deposition, future attempts to deposit graphene would benefit from shorter deposition times to further reduce the quantity of carbon deposited and reduce the opportunity for thicker carbon films to form.

Figure 4.4.5 shows the surface structure of the carbonaceous films grown on the nickel surface.



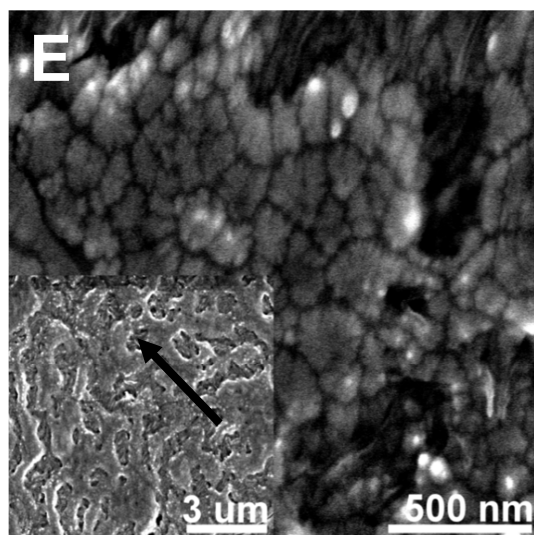


Figure 4.4.5. Surface topography at different magnifications of nickel and carbon films deposited at 800 °C over varying deposition times.

A) pure Ni; B) NiG30. Black arrow denotes exposed nickel underlayer; C) NiG60. White arrow denotes a hexagonal carbon film, Black arrow denotes exposed nickel underlayer; D) NiG120; E) NiG180. Black arrow denotes exposed nickel underlayer.

The pure nickel surface, as shown in **Figure 4.4.5A**, had an even rougher topography than the copper surface. This film however did not have deep troughs propagating through it. Following 30 seconds of carbon deposition (**Figure 4.4.5B**) a smoother carbonaceous layer had formed patchily across the surface. The surface was mottled with either the carbonaceous film or exposed underlayer that still resembled the nickel structure. The deposited carbon layers did not have smooth, angular edges where the carbon film met the underlayer but evidence of grain boundary interference, as observed in **Figure 4.4.4B**, could be identified within the carbon layer, as shown in **Figure 4.4.5B**. These carbon films were observed in all samples regardless of deposition time except time zero. Unlike the carbon coated copper samples, complete surface coverage with the planar carbonaceous film was not achieved within the deposition times tested, although the fractional coverage did increase. This was shown by the topographical appearance of nickel structures in SEM images at high magnifications (**Black arrows in Figures 4.4.5B,**

4.4.5C and **4.4.5E**) The results for NiG60 show a hexagonal carbon film structure (**white arrow in Figure 4.4.5C**) identifying that graphitic structures have been formed over at least a fraction of the films surface. Raman analysis however confirmed that these graphitic phases were not thin enough to be graphene or FLGs. NiG120 (**Figure 4.4.5D**) shows another area where the surface structure of the metal underlayer appeared more fragmented than the rest of the film. In these regions the nickel appeared to be coated in a smooth and porous carbon layer. No grain boundaries were apparent in the structure and the pore size distribution was irregular. Comparison of carbonaceous materials grown on areas with evenly distributed Cu or Ni underlayers compared to materials grown on regions with poor metal distributions (**Figures 4.4.4F and 4.4.5D**) suggests that despite the pure Cu and Ni films slightly irregular appearance and surface texture (**Figures 4.4.4A and 4.4.5A**) they were still sufficiently flat for the precipitation of planar ordered carbonaceous films. The star-like structures were also present in the carbon coated nickel films and are most apparent in **Figures 4.4.5B, 4.4.5C and 4.4.5E**.

Carbon coverage of the nickel film was incomplete even after three minutes deposition suggesting that carbon oversaturation was not responsible for preventing graphene synthesis. As graphite was heterogeneously distributed over the nickel surface, then assuming the carbon-nickel adsorption/precipitation mechanism was followed in the tests, the adsorbed carbon that diffused into the nickel layer at high temperature was equally poorly distributed (**Section 2.4.4.3**). Prolonged heating of the substrate after deposition could improve carbon distribution within the nickel layer by increasing the time available for carbon diffusion to homogenise to an equilibrium concentration, increasing the likelihood of homogeneous precipitation.

4.4.2 Conclusions

Based upon the available evidence, the copper and nickel underlayers prepared were sufficient for the synthesis of graphene as their appearance matched examples from the literature [202]. Raman analysis concluded that graphene was not synthesised, but highly ordered graphite and nano-crystalline graphite was.

The presence of graphite on the copper films directly contradicts the copper catalysed graphene synthesis mechanism, described in **Section 2.4.4.2**, identifying that an alternative growth mechanism for graphite synthesis by magnetron sputtering must be occurring preferentially.

The crystallinity of the carbon films, compiled from the I_D/I_G ratios of carbon spectra, were greater for materials grown on nickel (**Tables 4.4.2**) than those grown on copper (**Table 4.4.1**), suggesting that nickels presence assisted ordered growth of graphitic films. It was not established whether this was by the same mechanism as graphene synthesis on nickel (**Section 2.4.4.3**) but with excess precipitation of carbon resulting in graphite precipitation, or by a different process.

Unique nano-sized star-like surface moieties were identified on the carbon films. They appear to be carbonaceous and following a review of the literature are most likely nano-seeds from which an array of different carbon nanostructures would have grown had deposition continued.

Shorter carbon deposition times onto copper or prolonged substrate heating following deposition onto nickel may increase the chances of single or few-layer graphene formation.[1]

CHAPTER 5: JOINT DISCUSSION

5.1 Comparison to the literature

5.1.1 Hydrogen storage

The Ce doped CNTs storage capacities were very low as a result of the pure CNT materials poor storage capacity (**Section 4.3.3.2**). They underperform compared to the literature and as such do not require further comparison. The same is true for the CN_x films tested still loaded on the silicon underlayer (**Section 4.2.2**). AC30, AC120 from the ball milling test and the MgNiC50400 foil from the sputtered adsorbent tests were selected for comparison to the literature as they displayed the highest H₂ storage capacities of the samples prepared in their individual tests.

Table 5.1 details the H₂ storage capacities of some of the alternative adsorbents from the literature. The units for expressing adsorbed quantity have been swapped from mmol.g⁻¹ to wt.% to allow direct comparison.. Whilst higher H₂ storage capacities have been claimed by several groups, their results have not been substantiated and were therefore not included in **Table 5.1** [299].

Table 5.1. List of H₂ storage capacities from the literature.

	Material	Ref.	H ₂ storage capacity (wt.%)	Temp (K)	Pressure (bar)
1	ITIM-1	[300]	4.2	77	20
2	MIL-101	[301]	5	77	20
3	Al-TCBPB	[302]	4	77	20
			≈0.1	298	20
5	Ni0.1-MCM	[303]	0.04	298	1
6	MOF-177	[304]	0.62	298	100
7	PtAC-MOF177	[304]	1.5	298	100
8	O-AC	[305]	2.6	77	10
9	AC	[299]	≈2	77	10
10	AC25_0.0	[306]	≈4.5	77	20
11	AC	[299]	0.1	298	10
12	AC31_10	[306]	≈0.26	298	20
13	Pd-AC	[305]	0.7	303	6
14	H16-Ni/AC	[307]	0.7	303	10
	AC30	4.1	1.98	77	10
	AC120	4.1	0.46	298	10
	MgNiC50400 foil	4.2	4.7	77	20
			3.5	298	20

The performance of the ball milled activated carbon samples in this work were equivalent to, or smaller than those reported in the literature (**Samples 8-14** in **Table 5.1**) at 77 K. Their performance at room temperature was more promising as the capacity was in the middle of the comparative data ranges. Poor performance at 77 K can be attributed to the low BET surface area/ pore volume of the activated carbons, limiting their total storage capacity at low temperatures. This is typically characterised by a reasonable correlation between BET surface area and hydrogen storage capacity at 77 K and above 50 bar [73]. The strong

performance at 298 K was likely because of the high fraction of microporous character identified within the samples that strongly bind to hydrogen, as described in **Section 4.1.1**, increasing their actual storage capacity. Designing a material to have a large SA is no guarantee of strong binding interaction. Small surfaces with stronger binding would outperform large surfaces with weak binding under immoderate conditions (such as high temperatures or low pressures); as observed for the AC samples milled for 15 and 120 minutes and their variance between storage capacities at 298 K (**Section 4.1, Figure 4.7B**).

The MgNiC50400 foil presented results equivalent to one of the AC samples and most of the metal organic framework (MOF) materials at 77 K (**Table 5.1**). The foils narrow pore size distribution, bridging the upper micropore and lower mesoporous region, will have assisted in maximising the performance. The MgNiC50400 foils performance at 298 K outstrips the H₂ storage capacity of all examples from the literature presented in **Table 5.1**. Assuming that the sample data collected for the MgNiC50400 foil was accurate, there are two explanations for the foils increased performance at 298 K compared to the literature. They will be discussed by comparing the MgNiC50400 foil to the MOF material Al-TCBPB [302]. Firstly, DFT analysis of Al-TCBPB's pore size distribution identified that most of the materials pore volume was distributed between two pore sizes. The smaller pore volume had a mode radius of 1.18, the larger pore volume had a mode radius of 2.0 nm [302]. The DFT mode pore radius of the MgNiC50600 foil was 1.3 nm which is narrower than the dominant pore width in the zeolites structure, and approximately the same as the zeolites smaller peak width. All pore sizes are greater than the theoretical ideal pore width for hydrogen adsorption of 0.7 nm [46], but the smaller mode pore width of the MgNiC50400 foil will have promoted stronger binding on its surface than in the zeolites wider pores, increasing the foils storage capacity relative to the zeolite. Secondly, storage capacity is being reported in wt.% and is therefore relative to the mass of the adsorbent. The MgNiC50400 foil, as identified by EDX analysis, is predominantly carbon whilst the Al-TCBPB contains carbon, oxygen and aluminium [302].

The increased mass of the Al-TCBPB adsorbent will have reduced the relative adsorption capacity of the zeolite. It is therefore possible that both materials adsorb the same volume of hydrogen when compared by another significant unit, such as pore volume within a specific range of pore sizes, but because the MgNiC50400 foil has a smaller mass its reported capacity is higher.

5.1.2 Carbon dioxide storage [1]

Ball milled AC15, and the MgNiC50400 foil (**Section 4.2**) will have their storage capacities compared to the literature. AC15 was selected from the ball milled samples because it recorded the highest CO₂ storage capacities at 10 bar and 298 K. **Table 5.2** details the CO₂ storage capacities of some alternative adsorbents from the literature. Materials 1-4 are silica based adsorbents, 5-8 are MOF's and 9-12 are activated carbons.

Table 5.2. List of CO₂ storage capacities from the literature.

	Material	Ref.	CO ₂ storage capacity (mmol.g ⁻¹)	Temp (K)	Pressure (bar)
1	Zeolite X13	[308]	1.77	293	1
2	MCM-41	[309]	≈0.49	298	1
3	Aminated MCM-41	[309]	1.1	298	1
4	Colloidal silica	[310]	≈2.8	298	20
			≈2.7	298	10
			≈2.2	298	1
5	MOF-505	[311]	3.3	298	1
6	Norit RB2	[228]	≈9	298	20
			≈7	298	10
			2.5	298	1

7	IRMOF-11	[228]	≈14	298	20
			≈11	298	10
			1.8	298	1
8	MOF-177	[228]	≈26	298	20
			≈12	298	10
			≈2	298	1
9	N-AC	[229]	≈21	298	20
			≈15	298	10
			3.75	298	1
10	AC	[229]	≈18	298	20
			≈12.5	298	10
			2.92	298	1
11	Coconut-AC	[312]	2.49	293	1
			3.41	273	1
12	Coal-AC	[312]	2.13	293	1
			2.61	273	1
AC15		4.1	4.62	298	10
			2.09	298	1
			5.25	273	10
			2.79	273	1
MgNiC50400 foil		4.2	11.08	298	20
			9.04	298	10
			1.95	298	1
			10.02	273	20
			6.79	273	10
			2.52	273	1

Table 5.2 continued. List of CO₂ storage capacities from the literature.

Ball milled sample AC15 has a storage capacity equivalent to most of the silicates and MOFs in **Table 5.1** at 1 bar and 298 K but it underperforms compared to the activated carbons listed. By 10 bar AC15's performance is far lower than any of the materials listed in the table except

colloidal silica. As discussed in **Section 5.1**, variation in performance can be attributed to the variation in total pore volume and the pore volume distribution between pores of specific widths which promote CO₂ adsorption. 0.7 nm is believed to be the ideal half pore width for CO₂ adsorption [312].

AC15's smaller CO₂ uptake compared to the AC materials in **Table 5.2**, along with the variation in the performances of the different AC's in **Table 5.2**, highlights the importance of selecting of an appropriate adsorbent precursor. As discussed in **Section 4.1.1**, the ball milling process improves pore size distribution, and the eventual adsorption capacity of the adsorbent, by breaking apart larger particles and opening up previously sealed pores. Milling's ability to generate fresh pores is limited, and therefore, whilst the process is able to improve an adsorbents performance, the improvement in capacity is limited by the structure of the initial adsorbent. A similar result was observed in **Section 4.3**. The H₂ uptake of the cerium or nickel doped CNTs was poor compared to the literature regardless of the mass of dopant as the CNT adsorbents performance was poor to begin with.

The MgNiC50400 foil, a novel adsorbent synthesised in this work, had a lower CO₂ storage capacity at 1 bar than the ball milled sample AC15. Compared to the adsorbents in **Table 5.2**, its performance was similar to that of the silicates and MOFs but smaller than the ACs. By 10 bar its performance exceeded that of the AC15, but by 20 bar its performance was smaller than most of the comparative literature.

Given the MgNiC50400 foils exceptional performance as a H₂ adsorbent compared to the literature, especially at 298 K, but its average performance as a CO₂ adsorbent, future study of these foils should focus on improving the foils H₂ adsorption capacity.

5.2 The catalytic performance of nickel

The catalytic performance of nickel for promoting H₂ storage was analysed in two separate tests; Nickel was dispersed throughout an activated carbon sample by mechanical milling in **Section 4.1**, and nickel was coated onto CNTs by magnetron sputtering in **Section 4.3**. The tests are not directly analogous because the milling process modifies the adsorbent structure and distributes the nickel catalyst (**Section 4.1.1**) whilst the sputtering process distributes the nickel catalyst without damaging the adsorbents (**Section 4.3.2.2**). With this in mind, conclusions drawn from the comparison of these processes were carefully considered. For both tests, the doped samples have an increased sample mass and saw a change in their pore size distribution compared to their pure counterpart following the addition of nickel. Results identified that at 298 K sputtered nickel increased the H₂ storage capacity of the CNTs, and ball milled nickel reduced the H₂ storage capacity compared to the pure milled activated carbon. Nickel increases adsorption through the spillover process (**Section 2.2.2.2.1**) [103], and from these results it appears that dispersion of the catalyst by sputter deposition was better suited for promoting the catalytic spillover performance than ball milling. Precise causes for the increase could not be established from the collected data, but possible explanations include;

The distribution mechanism [103]. As discussed previously (**Sections 4.1.1** and **4.3.2.2**), the distribution of the catalyst on the adsorbent differed between the two processes. Nickel addition to the AC material blocked pores, reducing the total pore volume, whilst sputter deposition coated tube sides which was seen to have a lesser impact on the samples total pore volume. Sputter deposition therefore was less detrimental to the physical structure of the adsorbent.

Intimacy of binding [97]. In sputtering, intimacy between the catalyst and adsorbent will be high as the process involves atomic deposition and growth of one material directly on and around the other. TEM analysis of cerium deposited on CNTs (**Figure 4.3.11**), with a dopant

dispersion and structure comparable to that of the nickel coating, showed intimate contact between the catalyst and adsorbent with little to no lone cerium particles identified in the sample. The dopant material followed the shape of the adsorbent nanotubes, identifying that they were in close physical contact and in some cases wrapped around the nanotubes outer wall. Identification of the ball milled nickel on the surface of the AC structures by TEM analysis was less clear as nickel particles were difficult to differentiate against the denser activated carbon structure. It is however understood that contact during milling is promoted through either cold-welding or physical pulverisation of the two particles against one-another [143]. As particles of both nickel and carbon will have been amorphous, promotion of alignment and close intimacy by ball milling will have been low. Intimacy of contact facilitates transfer of the disassociated hydrogen from the catalyst to the adsorbent. The above arguments demonstrate that sputtering had a mechanistic advantage for improving intimacy that milling could not match.

It seems that between these two factors, and a number of others, the sputter process was able to increase the efficiency of the spillover process and improve the adsorbents hydrogen storage capacity. Sputtering therefore is a useful process for catalyst dispersion and its qualitative performance compared to other doping processes deserves further investigation. Given sputtering's slow deposition rate the process may not find application industrially. However, as within much of the work within this study, the process may be of benefit for academic research due to the fine control the process provides.

5.3 The role of sputtering for adsorbent design

Given that this is the first example that could be found of sputtering being used to synthesis or dope adsorbents for H₂ or CO₂ storage applications it seems prudent to assess the viability of the process for these tasks.

Firstly, given the discussion in **Section 5.2**, it seems clear that sputter deposition could be advantageous for doping applications. Sputtering promotes many of the desirable qualities of a dopant, such as intimate binding (**Figure 4.3.11**) and could be used to control particle size and distribution [103]. Additionally, the process was found to be non-destructive to the adsorbents structure, as discussed in **Section 4.3.2.2**. Compared to alternative techniques, sputter deposition does not require a purification step (required in some wet chemistry processes) [133] and, as sputtering is performed from a pure source, complex and expensive organometallic precursors, required for wet or vapour deposition processes, are not required.

The feasibility of using sputter deposition for the growth of adsorbents is a far more complex argument. Whilst the process does allow for fine control over the adsorbent structure grown, and results of the H₂ and CO₂ storage capacities of the deposited films seemed very promising (**Section 4.2.3.3** and **4.2.3.4**), the process was very slow and the yield of film recovered was small. Additionally, the ability to generate the material in a one-pot synthetic process, generating the catalytic underlayer and depositing the film all within the same environment, without exposing the sample to the atmosphere is an appealing prospect, and as already discussed, preparing the catalyst from their pure metal precursor saves on costs and some mechanistic conflicts. However processing and generation of pure carbon targets for sputtering are more expensive than the gaseous carbon precursors, such as methane, used in CVD or PA-CVD. Overall, limitations, such as slow rate of synthesis, provide a justifiable argument for why magnetron sputtering has not received much attention within the adsorbent synthesis field. However, the fine control sputtering offers over the synthesised structures make it a powerful tool for lab based adsorbent research and development.

CHAPTER 6: CONCLUSIONS

Ball milling increases pore volume and adsorbent storage capacity through a reduction in the average particle size by breaking apart larger particles and opening up previously sealed pores (**Section 4.1.1.2**). Milling was an inappropriate process for the addition of a spillover catalyst as it was unable to promote intimate adsorbent-catalyst binding to facilitate a high spillover rate (**Section 5.3**).

Powder sputtering was an effective doping technique to distribute dopant indiscriminately across an adsorbent and provide sufficient intimacy in the binding to promote spillover (**Section 4.3**). Further work is required to optimise dopant distribution.

Sputter deposited cerium was found to improve the adsorption capacity of an adsorbent (**Section 4.3**). The mechanism of action is believed to be charge sharing increasing the polarisability of the adsorbent. Intimacies of contact between the catalyst and the adsorbent and the small catalyst particle sizes, both promoted by the sputter deposition process, were believed to have assisted the catalytic performance.

Sputtering of carbon onto nickel or copper films at high temperatures promotes the formation of highly ordered carbonaceous materials but as of yet there is no evidence to suggest that the process can be used to synthesise graphene (**Section 4.4**).

MgNiC50400 foil, synthesised by magnetron sputtering appears to be a promising adsorbent for both H₂ and CO₂ adsorption and whilst it does not meet the DOE guidelines it is heading in the right direction [48]. Further testing is required to confirm the results but the methods developed across this project, discussed in **Section 4.2**, should make material synthesis and data collection simpler and more accurate in future.

The control magnetron sputtering provides for synthesis of highly ordered materials makes it an ideal technique for adsorbent design and catalyst doping. Whilst limitations of the technique were identified in this project some could have been overcome with different equipment set-ups. Deposition rate was the major limitation of the process and is likely to limit the feasibility of sputtering to research and development tasks, rather than industrial mass production of adsorbents applications.

The materials tested in this paper did not achieve the goals laid out by the DOE for materials for vehicular H₂ storage. Some of the outcomes however can be used to inform design of improved adsorbents, increasing the likelihood of achieving the targets.

CHAPTER 7: FUTURE WORK

From the investigations performed in this study a number of avenues for future research were uncovered. Developments of particular interest include:

1. Additional research into the H₂ storage capacity of the separated films presented in **Section 4.2.3**. The storage capacity of the collected MgNiC50600 foil was high but additional testing is recommended to confirm that the storage capacities recorded were valid and repeatable. Work would involve repeating the test performed with freshly synthesised foils.
2. Highly porous carbon materials, Such as those designed in **Section 4.2**, are a valuable commodity as carbon electrodes for improving the performance of lithium batteries [290]. Electrochemical analysis, through galvanostatic charge/discharge measurements in a Li/O₂ cell could identify if such carbon foils are industrially valuable for battery design.
3. Given that CeNi alloyed catalysts deposited by magnetron sputtering were shown to enhance the H₂ storage capacity of CNT adsorbents (**Section 4.3.3.4**), additional trials to improve catalyst distribution, using a sonicating sample mount, would provide further insight into ideal catalyst loadings and how to optimise an adsorbents storage capacity.
4. A study combining the highest performance adsorbent synthesised by magnetron sputtering (**Section 4.2**) and the highest performance adsorption catalyst dispersed by magnetron sputtering (**Section 4.3**) would provide further insight into the applicability of magnetron sputtering for adsorbent synthesis.
5. Based upon the outcomes of **Section 4.4**, synthesis of graphene using a nickel catalyst may merit further study. Reduction in the carbon deposition time and an increase in the film annealing time may promote graphene formation through a similar mechanism to that followed for CVD synthesis [194]. Should a mechanism for

synthesis be found, sputtering's advantages, as discussed in **Section 2.4.4.4**, may provide a lower energy, more cost effective graphene synthesis process.

6. XRD analysis of CeNi alloys (**Section 4.3.2.3**) identified very little crystallinity within the samples suggesting a highly amorphous material made up of very small clusters of each metal. Small particle size was identified as a desirable trait of CeNi catalysts for methane tri-reforming reactions [159]. Comparison of the structure and catalytic performance of CeNi alloys synthesised by magnetron sputtering to alternative approaches such as, electrolysis [170], may identify alternative applications for these materials in methane decomposition catalysis.
7. The catalytic nano-island distribution is known to influence the growth of carbon nanostructures across a substrate [210]. Annealing time and temperature in turn influence the nano-island distribution. The influence of the carbon deposition step, in its first few seconds, on the nano-island distribution is unknown. Exploration of factors such as carbon deposition rate and the carbon source (PVD or CVD, or, carbon precursor) may also influence the nano-island distribution and the structure of the eventual carbon film.

REFERENCES

1. *Technical System Targets: Onboard Hydrogen Storage for Light-Duty Fuel Cell Vehicles*. [PDF] 2011 26th June 2011 [cited 2013 16 July]; Available from: http://www1.eere.energy.gov/hydrogenandfuelcells/storage/current_technology.html.
2. Scalese, S., et al., *Growth of aligned CN_x nanocolumns on silicon by RF-magnetron sputtering*. Carbon, 2006. **44**(14): p. 3123-3126.
3. EIA/AER, *Annual Energy Review 2003*, E.I. Administration, Editor 2004, U.S. Department of Energy.
4. Keeling, C.D. and T.P. Whorf, *Atmospheric CO₂ records from sites in the SiO air sampling network*, in *Trends: A Compendium of Data on Global Change 2005*, Carbon Dioxide Information Analysis Center, Oak Ridge National Laboratory: TN, USA.
5. Bradford, M.C.J. and M.A. Vannice, *CO₂ Reforming of CH₄*. Catalysis Reviews: Science and Engineering, 1999. **41**(1): p. 1 - 42.
6. Wang, S., G.Q. Lu, and G.J. Millar, *Carbon Dioxide Reforming of Methane To Produce Synthesis Gas over Metal-Supported Catalysts: State of the Art*. Energy & Fuels, 1996. **10**(4): p. 896-904.
7. Yang, H., et al., *Progress in carbon dioxide separation and capture: A review*. Journal of Environmental Sciences, 2008. **20**(1): p. 14-27.
8. Song, C., *Global challenges and strategies for control, conversion and utilization of CO₂ for sustainable development involving energy, catalysis, adsorption and chemical processing*. Catalysis Today, 2006. **115**(1-4): p. 2-32.
9. Khalilpour, R. and A. Abbas, *HEN optimization for efficient retrofitting of coal-fired power plants with post-combustion carbon capture*. International Journal of Greenhouse Gas Control, 2011. **5**(2): p. 189-199.
10. Fichman, B.T., *Annual Energy Review 2011*, in *Annual Energy Review*, U.S.E.I. Administration, Editor 2012, U.S. Energy Information Administration: Office of Survey Development and Statistical Integration. p. 3.
11. Hall, P.J., *Energy storage: The route to liberation from the fossil fuel economy?* Energy Policy, 2008. **36**(12): p. 4363-4367.
12. Nautiyal, H., *Progress in renewable energy under clean development mechanism in India*. Renewable and Sustainable Energy Reviews, 2012. **16**(5): p. 2913-2919.
13. Krozer, Y., *Cost and benefit of renewable energy in the European Union*. Renewable Energy, 2013. **50**(0): p. 68-73.
14. Haryanto, A., et al., *Upgrading of syngas derived from biomass gasification: A thermodynamic analysis*. Biomass and Bioenergy, 2009. **33**(5): p. 882-889.
15. Kuchler, M. and B.-O. Linnér, *Challenging the food vs. fuel dilemma: Genealogical analysis of the biofuel discourse pursued by international organizations*. Food Policy, 2012. **37**(5): p. 581-588.

16. Waller, I., *5.08 - Ethics of Biofuel Production*, in *Comprehensive Renewable Energy*, S. Editor-in-Chief: Ali, Editor. 2012, Elsevier: Oxford. p. 99-108.
17. Florin, N.H. and A.T. Harris, *Enhanced hydrogen production from biomass with in situ carbon dioxide capture using calcium oxide sorbents*. *Chemical Engineering Science*, 2008. **63**(2): p. 287-316.
18. Farrelly, D.J., et al., *Carbon sequestration and the role of biological carbon mitigation: A review*. *Renewable and Sustainable Energy Reviews*, 2013. **21**(0): p. 712-727.
19. Choi, S., J.H. Drese, and C.W. Jones, *Adsorbent Materials for Carbon Dioxide Capture from Large Anthropogenic Point Sources*. *ChemSusChem*, 2009. **2**(9): p. 796-854.
20. Leduc, P., et al., *Downsizing of gasoline engine: An efficient way to reduce CO₂ emissions*. *Oil and Gas Science and Technology*, 2003. **58**(1): p. 115-127.
21. Sartore, J.J., Chris., *Repowering The Planet. Energy For Tomorrow*, in *National Geographic* 2009, National Geographic Society USA. p. 67.
22. Mikkelsen, M., M. Jorgensen, and F.C. Krebs, *The teraton challenge. A review of fixation and transformation of carbon dioxide*. *Energy & Environmental Science*, 2010. **3**(1): p. 43-81.
23. Iwan, A., et al., *High temperature sequestration of CO₂ using lithium zirconates*. *Chemical Engineering Journal*, 2009. **146**(2): p. 249-258.
24. Balat, H. and C. Öz, *Technical and Economic Aspects of Carbon Capture and Storage – A Review*. *Energy, Exploration & Exploitation*, 2007. **25**(5): p. 357-392.
25. Haszeldine, R.S., *Carbon Capture and Storage: How Green Can Black Be?* *Science*, 2009. **325**(5948): p. 1647-1652.
26. Posch, S. and M. Haider, *Optimization of CO₂ compression and purification units (CO₂CPU) for CCS power plants*. *Fuel*, 2012. **101**(0): p. 254-263.
27. Stadler, H., et al., *Oxyfuel coal combustion by efficient integration of oxygen transport membranes*. *International Journal of Greenhouse Gas Control*, 2011. **5**(1): p. 7-15.
28. Habib, M.A., et al., *Computational fluid dynamic simulation of oxyfuel combustion in gas-fired water tube boilers*. *Computers & Fluids*, 2012. **56**(0): p. 152-165.
29. Davison, J., *Performance and costs of power plants with capture and storage of CO₂*. *Energy*, 2007. **32**(7): p. 1163-1176.
30. Rao, A.B. and E.S. Rubin, *A technical, economic, and environmental assessment of amine-based CO₂ capture technology for power plant greenhouse gas control*. *Environmental Science and Technology*, 2002. **36**(20): p. 4467-4475.
31. Cifre, P.G., et al., *Integration of a chemical process model in a power plant modelling tool for the simulation of an amine based CO₂ scrubber*. *Fuel*, 2009. **88**(12): p. 2481-2488.
32. Campen, A., K. Mondal, and T. Wiltowski, *Separation of hydrogen from syngas using a regenerative system*. *International Journal of Hydrogen Energy*, 2008. **33**(1): p. 332-339.

References

33. Gnanapragasam, N.V., B.V. Reddy, and M.A. Rosen, *Hydrogen production from coal gasification for effective downstream CO₂ capture*. International Journal of Hydrogen Energy, 2010. **35**(10): p. 4933-4943.
34. Semelsberger, T.A., et al., *Equilibrium products from autothermal processes for generating hydrogen-rich fuel-cell feeds*. International Journal of Hydrogen Energy, 2004. **29**(10): p. 1047-1064.
35. Solieman, A.A.A., et al., *Calcium oxide for CO₂ capture: Operational window and efficiency penalty in sorption-enhanced steam methane reforming*. International Journal of Greenhouse Gas Control, 2009. **3**(4): p. 393-400.
36. Shukla, R., et al., *A review of studies on CO₂ sequestration and caprock integrity*. Fuel, 2010. **89**(10): p. 2651-2664.
37. Schlapbach, L. and A. Züttel, *Hydrogen-storage materials for mobile applications*. Nature, 2001. **414**(6861): p. 353-358.
38. Bhatia, S.K. and A.L. Myers, *Optimum Conditions for Adsorptive Storage*. Langmuir, 2006. **22**(4): p. 1688-1700.
39. Honda. *Honda Clarity - A guide to the Hydrogen Fuel Cell Car*. 2008; Available from: <http://www.hondaclarity.org>.
40. Cabria, I., M.J. López, and J.A. Alonso, *Simulation of the hydrogen storage in nanoporous carbons with different pore shapes*. International Journal of Hydrogen Energy, 2011. **36**(17): p. 10748-10759.
41. Yang, C., *Hydrogen and electricity: Parallels, interactions, and convergence*. International Journal of Hydrogen Energy, 2008. **33**(8): p. 1977-1994.
42. Bičáková, O. and P. Straka, *Production of hydrogen from renewable resources and its effectiveness*. International Journal of Hydrogen Energy, 2012. **37**(16): p. 11563-11578.
43. McDowall, W. and M. Eames, *Towards a sustainable hydrogen economy: A multi-criteria sustainability appraisal of competing hydrogen futures*. International Journal of Hydrogen Energy, 2007. **32**(18): p. 4611-4626.
44. Lee, D.-H., *Toward the clean production of hydrogen: Competition among renewable energy sources and nuclear power*. International Journal of Hydrogen Energy, 2012. **37**(20): p. 15726-15735.
45. Andrews, J. and B. Shabani, *Re-envisioning the role of hydrogen in a sustainable energy economy*. International Journal of Hydrogen Energy, 2012. **37**(2): p. 1184-1203.
46. Yürüm, Y., A. Taralp, and T.N. Veziroglu, *Storage of hydrogen in nanostructured carbon materials*. International Journal of Hydrogen Energy, 2009. **34**(9): p. 3784-3798.
47. Fierro, V., et al., *Experimental evidence of an upper limit for hydrogen storage at 77 K on activated carbons*. Carbon, 2010. **48**(7): p. 1902-1911.
48. Stetson, N., *Hydrogen Storage Sub-Program Overview*, in *2012 annual progress report 2012*, US Department of Energy (DOE) hydrogen and fuel cell program p. IV3-IV10.

49. Yang, J., et al., *High capacity hydrogen storage materials: attributes for automotive applications and techniques for materials discovery*. Chemical Society Reviews, 2010. **39**(2): p. 656-675.
50. Halmann, M. and A. Steinfeld, *Fuel saving, carbon dioxide emission avoidance, and syngas production by tri-reforming of flue gases from coal- and gas-fired power stations, and by the carbothermic reduction of iron oxide*. Energy, 2006. **31**(15): p. 3171-3185.
51. Zhang, C., et al., *The oxidative stream reforming of methane to syngas in a thin tubular mixed-conducting membrane reactor*. Journal of Membrane Science, 2008. **320**(1-2): p. 401-406.
52. Ahmed, S., et al., *Decomposition of hydrocarbons to hydrogen and carbon*. Applied Catalysis A: General, 2009. **359**(1-2): p. 1-24.
53. Guoxin, H. and H. Hao, *Hydrogen rich fuel gas production by gasification of wet biomass using a CO₂ sorbent*. Biomass and Bioenergy, 2009. **33**(5): p. 899-906.
54. Miao, H., et al., *Effects of coal syngas major compositions on Ni/YSZ anode-supported solid oxide fuel cells*. Journal of Power Sources. **195**(8): p. 2230-2235.
55. Franco, C., et al., *The study of reactions influencing the biomass steam gasification process*. Fuel, 2003. **82**(7): p. 835-842.
56. Lin, S., et al., *Hydrogen production from coal by separating carbon dioxide during gasification*. Fuel, 2002. **81**(16): p. 2079-2085.
57. Amphlett, J.C., et al., *Hydrogen production by the catalytic steam reforming of methanol part 1: The thermodynamics*. The Canadian Journal of Chemical Engineering, 1981. **59**(6): p. 720-727.
58. Abu El-Rub, Z., E.A. Bramer, and G. Brem, *Review of Catalysts for Tar Elimination in Biomass Gasification Processes*. Industrial & Engineering Chemistry Research, 2004. **43**(22): p. 6911-6919.
59. Kluiters, S.C.A., *Status Review on Membrane Systems for Hydrogen Separation*, in *Intermediate Report for EU Project MIGREYD NNE5-2001- 6702004*.
60. Hart, A. and N. Gnanendran, *Cryogenic CO₂ capture in natural gas*. Energy Procedia, 2009. **1**(1): p. 697-706.
61. Paggiaro, R., P. Bénard, and W. Polifke, *Cryo-adsorptive hydrogen storage on activated carbon. I: Thermodynamic analysis of adsorption vessels and comparison with liquid and compressed gas hydrogen storage*. International Journal of Hydrogen Energy, 2010. **35**(2): p. 638-647.
62. Atkinson, K., et al., *Carbon nanostructures: An efficient hydrogen storage medium for fuel cells*. Fuel Cells Bulletin, 2001. **4**(38): p. 9-12.
63. Aceves, S.M., et al., *High-density automotive hydrogen storage with cryogenic capable pressure vessels*. International Journal of Hydrogen Energy, 2010. **35**(3): p. 1219-1226.
64. Züttel, A., *Materials for hydrogen storage*. Materials Today, 2003. **6**(9): p. 24-33.
65. Ahluwalia, R.K. and J.K. Peng, *Dynamics of cryogenic hydrogen storage in insulated pressure vessels for automotive applications*. International Journal of Hydrogen Energy, 2008. **33**(17): p. 4622-4633.

References

66. Atsonios, K., et al., *Cryogenic method for H₂ and CH₄ recovery from a rich CO₂ stream in pre-combustion carbon capture and storage schemes*. Energy, 2013. **53**(0): p. 106-113.
67. Ströbel, R., et al., *Hydrogen storage by carbon materials*. Journal of Power Sources, 2006. **159**(2): p. 781-801.
68. Panella, B., M. Hirscher, and S. Roth, *Hydrogen adsorption in different carbon nanostructures*. Carbon, 2005. **43**(10): p. 2209-2214.
69. Morris, R.E. and P.S. Wheatley, *Gas Storage in Nanoporous Materials*. Angewandte Chemie International Edition, 2008. **47**(27): p. 4966-4981.
70. Krishnan, G., et al., *Simulation of a Process to Capture CO₂ From IGCC Syngas Using a High Temperature PBI Membrane*. Energy Procedia, 2009. **1**(1): p. 4079-4088.
71. Bérubé, V., et al., *Size effects on the hydrogen storage properties of nanostructured metal hydrides: A review*. International Journal of Energy Research, 2007. **31**(6-7): p. 637-663.
72. Cabria, I., M.J. López, and J.A. Alonso, *The optimum average nanopore size for hydrogen storage in carbon nanoporous materials*. Carbon, 2007. **45**(13): p. 2649-2658.
73. Gogotsi, Y., et al., *Importance of pore size in high-pressure hydrogen storage by porous carbons*. International Journal of Hydrogen Energy, 2009. **34**(15): p. 6314-6319.
74. Beyaz, S., et al., *Nanoscale carbon material porosity effect on gas adsorption*. International Journal of Hydrogen Energy, 2010. **35**(1): p. 217-224.
75. Hirscher, M., et al., *Hydrogen storage in carbon nanostructures*. Journal of Alloys and Compounds, 2002. **330-332**: p. 654-658.
76. Froudakis, G.E., *Why Alkali-Metal-Doped Carbon Nanotubes Possess High Hydrogen Uptake*. Nano Letters, 2001. **1**(10): p. 531-533.
77. Kang, K.Y., B.I. Lee, and J.S. Lee, *Hydrogen adsorption on nitrogen-doped carbon xerogels*. Carbon, 2009. **47**(4): p. 1171-1180.
78. Park, M.H. and Y.S. Lee, *Hydrogen adsorption on 3D transition-metal-doped organosilica complexes*. Chemical Physics Letters, 2010. **488**(1-3): p. 7-9.
79. Na, B.-K., et al., *CO₂ recovery from flue gas by PSA process using activated carbon*. Korean Journal of Chemical Engineering, 2001. **18**(2): p. 220-227.
80. Khajuria, H. and E.N. Pistikopoulos, *Optimization and Control of Pressure Swing Adsorption Processes Under Uncertainty*. AIChE Journal, 2013. **59**(1): p. 120-131.
81. Zhao, Z., et al., *Adsorption of carbon dioxide on alkali-modified zeolite 13X adsorbents*. International Journal of Greenhouse Gas Control, 2007. **1**(3): p. 355-359.
82. Ward, J.W., *The nature of active sites on zeolites: III. The alkali and alkaline earth ion-exchanged forms*. Journal of Catalysis, 1968. **10**(1): p. 34-46.

83. Walton, K.S., M.B. Abney, and M. Douglas LeVan, *CO₂ adsorption in Y and X zeolites modified by alkali metal cation exchange*. *Microporous and Mesoporous Materials*, 2006. **91**(1–3): p. 78-84.
84. Diaz, E., et al., *Enhancement of the CO₂ Retention Capacity of Y Zeolites by Na and Cs Treatments: Effect of Adsorption Temperature and Water Treatment*. *Industrial & Engineering Chemistry Research*, 2007. **47**(2): p. 412-418.
85. Siriwardane, R.V., M.-S. Shen, and E.P. Fisher, *Adsorption of CO₂, N₂, and O₂ on Natural Zeolites*. *Energy & Fuels*, 2003. **17**(3): p. 571-576.
86. Garrone, E., B. Bonelli, and C. Otero Areán, *Enthalpy–entropy correlation for hydrogen adsorption on zeolites*. *Chemical Physics Letters*, 2008. **456**(1–3): p. 68-70.
87. Bénard, P. and R. Chahine, *Storage of hydrogen by physisorption on carbon and nanostructured materials*. *Scripta Materialia*, 2007. **56**(10): p. 803-808.
88. Paggiaro, R., et al., *Cryo-adsorptive hydrogen storage on activated carbon. II: Investigation of the thermal effects during filling at cryogenic temperatures*. *International Journal of Hydrogen Energy*, 2010. **35**(2): p. 648-659.
89. Mitchell, P.C.H., et al., *Hydrogen Spillover on Carbon-Supported Metal Catalysts Studied by Inelastic Neutron Scattering. Surface Vibrational States and Hydrogen Riding Modes*. *The Journal of Physical Chemistry B*, 2003. **107**(28): p. 6838-6845.
90. Yang, F.H., A.J. Lachawiec, and R.T. Yang, *Adsorption of Spillover Hydrogen Atoms on Single-Wall Carbon Nanotubes*. *The Journal of Physical Chemistry B*, 2006. **110**(12): p. 6236-6244.
91. Zacharia, R., et al., *Enhancement of hydrogen storage capacity of carbon nanotubes via spill-over from vanadium and palladium nanoparticles*. *Chemical Physics Letters*, 2005. **412**(4–6): p. 369-375.
92. Bowker, M., *A prospective: Surface science and catalysis at the nanoscale*. *Surface Science*, 2009. **603**(16): p. 2359-2362.
93. Cassuto, A. and D.A. King, *Rate expressions for adsorption and desorption kinetics with precursor states and lateral interactions*. *Surface Science*, 1981. **102**(2–3): p. 388-404.
94. Lachawiec, A.J. and R.T. Yang, *Reverse Spillover of Hydrogen on Carbon-Based Nanomaterials: Evidence of Recombination Using Isotopic Exchange*. *The Journal of Physical Chemistry C*, 2009. **113**(31): p. 13933-13939.
95. Rather, S.-u., et al., *Hydrogen storage of nanostructured TiO₂-impregnated carbon nanotubes*. *International Journal of Hydrogen Energy*, 2009. **34**(2): p. 961-966.
96. Zielinski, M., et al., *Hydrogen storage on nickel catalysts supported on amorphous activated carbon*. *Catalysis Communications*, 2005. **6**(12): p. 777-783.
97. Wang, L. and R.T. Yang, *New sorbents for hydrogen storage by hydrogen spillover - a review*. *Energy & Environmental Science*, 2008. **1**(2): p. 268-279.

References

98. Yang, R.T. and Y. Wang, *Catalyzed Hydrogen Spillover for Hydrogen Storage*. Journal of the American Chemical Society, 2009. **131**(12): p. 4224-4226.
99. Lachawiec, A.J., G. Qi, and R.T. Yang, *Hydrogen Storage in Nanostructured Carbons by Spillover: Bridge-Building Enhancement*. Langmuir, 2005. **21**(24): p. 11418-11424.
100. Chen, C.-H. and C.-C. Huang, *Enhancement of hydrogen spillover onto carbon nanotubes with defect feature*. Microporous and Mesoporous Materials, 2008. **109**(1–3): p. 549-559.
101. Thomas, K.M., *Hydrogen adsorption and storage on porous materials*. Catalysis Today, 2007. **120**(3-4): p. 389-398.
102. Rodríguez-Reinoso, F. and M. Molina-Sabio, *Textural and chemical characterization of microporous carbons*. Advances in Colloid and Interface Science, 1998. **76–77**(0): p. 271-294.
103. Lueking, A.D. and R.T. Yang, *Hydrogen spillover to enhance hydrogen storage—study of the effect of carbon physicochemical properties*. Applied Catalysis A: General, 2004. **265**(2): p. 259-268.
104. Yang, R.T. and J.P. Chen, *Mechanism of carbon filament growth on metal catalysts*. Journal of Catalysis, 1989. **115**(1): p. 52-64.
105. Kim, B.-J., Y.-S. Lee, and S.-J. Park, *A study on pore-opening behaviors of graphite nanofibers by a chemical activation process*. Journal of Colloid and Interface Science, 2007. **306**(2): p. 454-458.
106. Beyaz, S.K., et al., *Herringbone nanofiber CVD synthesis and high pressure hydrogen adsorption performance analysis by molecular modelling*. International Journal of Hydrogen Energy, 2009. **34**(4): p. 1965-1970.
107. Iijima, S. and T. Ichihashi, *Single-shell carbon nanotubes of 1-nm diameter*. Nature, 1993. **363**(6430): p. 603-605.
108. Dupuis, A.-C., *The catalyst in the CCVD of carbon nanotubes—a review*. Progress in Materials Science, 2005. **50**(8): p. 929-961.
109. Reilly, R.M., *Carbon Nanotubes: Potential Benefits and Risks of Nanotechnology in Nuclear Medicine*. Journal of Nuclear Medicine, 2007. **48**(7): p. 1039-1042.
110. Iijima, S., *Helical microtubules of graphitic carbon*. Nature, 1991. **354**(6348): p. 56-58.
111. Guay, P., B.L. Stansfield, and A. Rochefort, *On the control of carbon nanostructures for hydrogen storage applications*. Carbon, 2004. **42**(11): p. 2187-2193.
112. Wang, P.-J., et al., *Effect of carbon addition on hydrogen storage behaviors of Li–Mg–B–H system*. International Journal of Hydrogen Energy, 2010. **35**(7): p. 3072-3075.
113. Shang, C.X., M. Bououdina, and Z.X. Guo, *Structural stability of mechanically alloyed (Mg+10Nb) and (MgH₂+10Nb) powder mixtures*. Journal of Alloys and Compounds, 2003. **349**(1–2): p. 217-223.
114. Vajo, J.J., et al., *Altering Hydrogen Storage Properties by Hydride Destabilization through Alloy Formation: LiH and MgH₂ Destabilized with Si*. The Journal of Physical Chemistry B, 2004. **108**(37): p. 13977-13983.

115. George, L. and S.K. Saxena, *Structural stability of metal hydrides, alanates and borohydrides of alkali and alkali- earth elements: A review*. International Journal of Hydrogen Energy, 2010. **35**(11): p. 5454-5470.
116. Au, M., et al., *Hydrogen storage properties of modified lithium borohydrides*. Journal of Alloys and Compounds, 2008. **462**(1–2): p. 303-309.
117. Asakuma, Y., et al., *Numerical analysis of absorbing and desorbing mechanism for the metal hydride by homogenization method*. International Journal of Hydrogen Energy, 2003. **28**(5): p. 529-536.
118. Yun, S. and S. Ted Oyama, *Correlations in palladium membranes for hydrogen separation: A review*. Journal of Membrane Science, 2011. **375**(1–2): p. 28-45.
119. Chong, M., et al., *Reversible dehydrogenation of magnesium borohydride to magnesium triborane in the solid state under moderate conditions*. Chemical Communications, 2011. **47**(4): p. 1330-1332.
120. Yamasaki, A., *An Overview of CO₂ Mitigation Options for Global Warming - Emphasizing CO₂ Sequestration Options*. Journal of Chemical Engineering of Japan, 2003. **36**(4): p. 361-375.
121. Ali, S.H., *Kinetics of the reaction of carbon dioxide with blends of amines in aqueous media using the stopped-flow technique*. International Journal of Chemical Kinetics, 2005. **37**(7): p. 391-405.
122. Gray, M.L., et al., *Improved immobilized carbon dioxide capture sorbents*. Fuel Processing Technology, 2005. **86**(14–15): p. 1449-1455.
123. Rochelle, G.T., *Amine Scrubbing for CO₂ Capture*. Science, 2009. **325**(5948): p. 1652-1654.
124. Hicks, J.C., et al., *Designing Adsorbents for CO₂ Capture from Flue Gas-Hyperbranched Aminosilicas Capable of Capturing CO₂ Reversibly*. Journal of the American Chemical Society, 2008. **130**(10): p. 2902-2903.
125. Xiong, R., J. Ida, and Y.S. Lin, *Kinetics of carbon dioxide sorption on potassium-doped lithium zirconate*. Chemical Engineering Science, 2003. **58**(19): p. 4377-4385.
126. Symonds, R.T., et al., *CO₂ Capture from Simulated Syngas via Cyclic Carbonation/Calcination for a Naturally Occurring Limestone: Pilot-Plant Testing*. Industrial & Engineering Chemistry Research, 2009. **48**(18): p. 8431-8440.
127. Barker, R., *The reactivity of calcium oxide towards carbon dioxide and its use for energy storage*. Journal of Applied Chemistry and Biotechnology, 1974. **24**(4-5): p. 221-227.
128. Yong, Z. and A.r.E. Rodrigues, *Hydrotalcite-like compounds as adsorbents for carbon dioxide*. Energy Conversion and Management, 2002. **43**(14): p. 1865-1876.
129. Lee, K.B., et al., *Chemisorption of carbon dioxide on potassium-carbonate-promoted hydrotalcite*. Journal of Colloid and Interface Science, 2007. **308**(1): p. 30-39.

References

130. Hufton, J.R., S. Mayorga, and S. Sircar, *Sorption-enhanced reaction process for hydrogen production*. AIChE Journal, 1999. **45**(2): p. 248-256.
131. Luebke, D., C. Myers, and H. Pennline, *Hybrid Membranes for Selective Carbon Dioxide Separation from Fuel Gas*. Energy & Fuels, 2006. **20**(5): p. 1906-1913.
132. Ahmad, A.L., et al., *Synthesis and characterization of TiO₂ membrane with palladium impregnation for hydrogen separation*. Journal of Membrane Science, 2011. **366**(1–2): p. 166-175.
133. Joselevich, E., et al., *Carbon Nanotube Synthesis and Organization*, in *Carbon Nanotubes*. 2008, Springer Berlin Heidelberg. p. 101-164.
134. Mattox, D.M., *Chapter 1 - Introduction*, in *Handbook of Physical Vapor Deposition (PVD) Processing (Second Edition)*. 2010, William Andrew Publishing: Boston. p. 1-24.
135. Ohring, M., *Chapter 6 - Chemical vapor deposition*, in *Materials Science of Thin Films (Second Edition)*. 2002, Academic Press: San Diego. p. 277-355.
136. Mattox, D.M., *Chapter 5 - The Low Pressure Plasma Processing Environment*, in *Handbook of Physical Vapor Deposition (PVD) Processing (Second Edition)*. 2010, William Andrew Publishing: Boston. p. 157-193.
137. Mattox, D.M., *Chapter 6 - Vacuum Evaporation and Vacuum Deposition*, in *Handbook of Physical Vapor Deposition (PVD) Processing (Second Edition)*. 2010, William Andrew Publishing: Boston. p. 195-235.
138. Ohring, M., *Chapter 5 - Plasma and ion beam processing of thin films*, in *Materials Science of Thin Films (Second Edition)*. 2002, Academic Press: San Diego. p. 203-275.
139. Kelly, P.J. and R.D. Arnell, *Magnetron sputtering: a review of recent developments and applications*. Vacuum, 2000. **56**(3): p. 159-172.
140. Ohring, M., *Chapter 4 - Discharges, plasmas, and ion-surface interactions*, in *Materials Science of Thin Films (Second Edition)*. 2002, Academic Press: San Diego. p. 145-202.
141. Ohring, M., *Chapter 3 - Thin-film evaporation processes*, in *Materials Science of Thin Films (Second Edition)*. 2002, Academic Press: San Diego. p. 95-144.
142. Mattox, D.M., *Chapter 7 - Physical Sputtering and Sputter Deposition (Sputtering)*, in *Handbook of Physical Vapor Deposition (PVD) Processing (Second Edition)*. 2010, William Andrew Publishing: Boston. p. 237-286.
143. Cao, W. *Synthesis of Nanomaterials by High Energy Ball Milling*. 2013 [cited 2013 18th July]; Available from: <http://www.understandingnano.com/nanomaterial-synthesis-ball-milling.html>.
144. Shang, C.X. and Z.X. Guo, *Structural and desorption characterisations of milled powder mixtures for hydrogen storage*. International Journal of Hydrogen Energy, 2007. **32**(14): p. 2920-2925.

145. Jiang, J., et al., *Enhanced room temperature hydrogen storage capacity of hollow nitrogen-containing carbon spheres*. International Journal of Hydrogen Energy, 2010. **35**(1): p. 210-216.
146. Jo, C., C. Kim, and Y.H. Lee, *Electronic properties of K-doped single-wall carbon nanotube bundles*. Physical Review B, 2002. **65**(3): p. 035420.
147. Ni, M., et al., *Hydrogen storage in Li-doped charged single-walled carbon nanotubes*. International Journal of Hydrogen Energy, 2010. **35**(8): p. 3546-3549.
148. Kim, B.-J., Y.-S. Lee, and S.-J. Park, *A study on the hydrogen storage capacity of Ni-plated porous carbon nanofibers*. International Journal of Hydrogen Energy, 2008. **33**(15): p. 4112-4115.
149. Lin, K.-Y., W.-T. Tsai, and J.-K. Chang, *Decorating carbon nanotubes with Ni particles using an electroless deposition technique for hydrogen storage applications*. International Journal of Hydrogen Energy, 2010. **35**(14): p. 7555-7562.
150. Barbieri, G., et al., *Conversion–Temperature Diagram for a Palladium Membrane Reactor. Analysis of an Endothermic Reaction: Methane Steam Reforming*. Industrial & Engineering Chemistry Research, 2001. **40**(9): p. 2017-2026.
151. Dash, R., et al., *Titanium carbide derived nanoporous carbon for energy-related applications*. Carbon, 2006. **44**(12): p. 2489-2497.
152. Kuang, M.H., et al., *Catalytically active nickel {110} surfaces in growth of carbon tubular structures*. Applied Physics Letters, 2000. **76**(10): p. 1255-1257.
153. Lin, N., et al., *In situ scanning tunneling microscopic and spectroscopic investigation of magnetron-sputtered C and CN thin films*. Physical Review B, 2000. **61**(7): p. 4898-4903.
154. Scalese, S., et al., *Carbon aligned nanocolumns by RF-Magnetron sputtering: The influence of the growth parameters*. Physica E: Low-dimensional Systems and Nanostructures, 2007. **37**(1–2): p. 231-235.
155. Liu, H., et al., *Structural and morphological control of aligned nitrogen-doped carbon nanotubes*. Carbon, 2010. **48**(5): p. 1498-1507.
156. Wang, X.L., et al., *Hydrogen storage properties of nanocrystalline Mg–Ce/Ni composite*. Journal of Power Sources, 2006. **159**(1): p. 163-166.
157. Tang, L.P., et al., *Impact of synthesis temperature on hydrogen storage and emission from Ni/Ce composite oxides*. International Journal of Hydrogen Energy, 2009. **34**(17): p. 7296-7305.
158. Berlouis, L.E.A., et al., *Enhanced hydrogen storage in Ni/Ce composite oxides*. Physical Chemistry Chemical Physics, 2007. **9**(45): p. 6032-6039.
159. Pino, L., et al., *Hydrogen production by methane tri-reforming process over Ni–ceria catalysts: Effect of La-doping*. Applied Catalysis B: Environmental, 2011. **104**(1–2): p. 64-73.

References

160. Jalowiecki-Duhamel, L., et al., *Hydrogen production from ethanol in presence of water over cerium and nickel mixed oxides*. *Catalysis Today*, 2010. **157**(1–4): p. 456-461.
161. Yang, W., et al., *Cerium Oxide Promoted Ni/MgO Catalyst for the Synthesis of Multi-walled Carbon Nanotubes*. *Chinese Journal of Catalysis*, 2011. **32**(6–8): p. 1323-1328.
162. Charvin, P., et al., *Hydrogen production from mixed cerium oxides via three-step water-splitting cycles*. *Solid State Ionics*, 2009. **180**(14–16): p. 1003-1010.
163. Jalowiecki-Duhamel, L., et al., *Hydrogen production from ethanol steam reforming over cerium and nickel based oxyhydrides*. *International Journal of Hydrogen Energy*, 2010. **35**(23): p. 12741-12750.
164. Jalowiecki-Duhamel, L., A. Ponchel, and C. Lamonier, *Storage of reactive hydrogen species in CeM_xO_y ($M = Cu, Ni; 0 \leq x \leq 1$) mixed oxides*. *International Journal of Hydrogen Energy*, 1999. **24**(11): p. 1083-1092.
165. Hadano, M., et al., *The effect of O_2 preadsorption on the rate of H_2 absorption on the surface of rare earths (La, Ce, Tb, Dy) at 298 K*. *Journal of Alloys and Compounds*, 1999. **293–295**(0): p. 403-406.
166. Chen, K.Z., et al., *Catalytic properties of nanostructured hydrogen storage nickel particles with cerium shell structure*. *Nanostructured Materials*, 1997. **8**(2): p. 205-213.
167. Jalowiecki-Duhamel, L., J. Carpentier, and A. Ponchel, *Catalytic hydrogen storage in cerium nickel and zirconium (or aluminium) mixed oxides*. *International Journal of Hydrogen Energy*, 2007. **32**(13): p. 2439-2444.
168. Sohier, M.P., et al., *Hydrogenation catalysts based on nickel and rare earths oxides: I. Relation between cations nature, preparation route, hydrogen content and catalytic activity*. *Applied Catalysis A: General*, 1992. **84**(2): p. 169-186.
169. Zubizarreta, L., et al., *Ni-doped carbon xerogels for H_2 storage*. *Carbon*, 2010. **48**(10): p. 2722-2733.
170. Zhao, B., et al., *Direct electrolytic preparation of cerium/nickel hydrogen storage alloy powder in molten salt*. *Journal of Alloys and Compounds*, 2009. **468**(1–2): p. 379-385.
171. Chen, M., et al., *Synthesis of nanoparticle Ce–Mg–O mixed oxide as efficient support for methane oxidation*. *Journal of Molecular Catalysis A: Chemical*, 2005. **237**(1–2): p. 132-136.
172. Xue, W., et al., *Preparation of titania nanotubes doped with cerium and their photocatalytic activity for glyphosate*. *Chemical Engineering Journal*, 2011. **167**(1): p. 397-402.
173. Kang, J.L., et al., *In situ synthesis of ceria decorated carbon nanotubes by chemical vapor deposition*. *Materials Letters*, 2009. **63**(2): p. 182-184.
174. Yu, X. and Z. Shen, *The electromagnetic shielding of Ni films deposited on cenosphere particles by magnetron sputtering method*. *Journal of Magnetism and Magnetic Materials*, 2009. **321**(18): p. 2890-2895.

175. Yu, X. and Z. Shen, *Metal copper films coated on microparticle substrates using an ultrasonic-assisted magnetron sputtering system*. Powder Technology, 2008. **187**(3): p. 239-243.
176. Yu, X., et al., *Fabrication and structural characterization of metal films coated on cenosphere particles by magnetron sputtering deposition*. Applied Surface Science, 2007. **253**(17): p. 7082-7088.
177. Xu, Z., X. Yu, and Z. Shen, *Coating metals on micropowders by magnetron sputtering*. China Particuology, 2007. **5**(5): p. 345-350.
178. Savvides, N., et al., *Epitaxial growth of cerium oxide thin film buffer layers deposited by d.c. magnetron sputtering*. Thin Solid Films, 2001. **388**(1-2): p. 177-182.
179. Ta, M.T., et al., *Growth and structural characterization of cerium oxide thin films realized on Si(111) substrates by on-axis r.f. magnetron sputtering*. Thin Solid Films, 2008. **517**(1): p. 450-452.
180. Dixit, M., T.A. Maark, and S. Pal, *Ab initio and periodic DFT investigation of hydrogen storage on light metal-decorated MOF-5*. International Journal of Hydrogen Energy, 2011. **36**(17): p. 10816-10827.
181. Li, Y., et al., *The structural and electronic properties of Li-doped fluorinated graphene and its application to hydrogen storage*. International Journal of Hydrogen Energy, 2012. **37**(7): p. 5754-5761.
182. Yildirim, T. and S. Ciraci, *Titanium-Decorated Carbon Nanotubes as a Potential High-Capacity Hydrogen Storage Medium*. Physical Review Letters, 2005. **94**(17): p. 175501.
183. Barron, A.A. *Characterisation of graphene by Raman Spectroscopy*. [Web page] 2010 29th June 2010 [cited 2013 10th July].
184. Lui, C.H., et al., *Ultraflat graphene*. Nature, 2009. **462**(7271): p. 339-341.
185. Siokou, A., et al., *Surface refinement and electronic properties of graphene layers grown on copper substrate: An XPS, UPS and EELS study*. Applied Surface Science, 2011. **257**(23): p. 9785-9790.
186. Robertson, A.W., et al., *Atomic Structure of Interconnected Few-Layer Graphene Domains*. ACS Nano, 2011. **5**(8): p. 6610-6618.
187. Hiura, H., et al., *Liquid phase growth of graphene on silicon carbide*. Carbon, 2012. **50**(14): p. 5076-5084.
188. Grüneis, A., *Synthesis and electronic properties of chemically functionalized graphene on metal surfaces*. Journal of Physics: Condensed Matter, 2013. **25**(4): p. 043001.
189. Novoselov, K.S., et al., *Electric Field Effect in Atomically Thin Carbon Films*. Science, 2004. **306**(5696): p. 666-669.
190. Li, X., et al., *Large-Area Synthesis of High-Quality and Uniform Graphene Films on Copper Foils*. Science, 2009. **324**(5932): p. 1312-1314.
191. Howsare, C.A., et al., *Substrate considerations for graphene synthesis on thin copper films*. Nanotechnology, 2012. **23**(13): p. 135601.

References

192. Zhao, L., et al., *Influence of copper crystal surface on the CVD growth of large area monolayer graphene*. Solid State Communications, 2011. **151**(7): p. 509-513.
193. Li, X., et al., *Evolution of Graphene Growth on Ni and Cu by Carbon Isotope Labeling*. Nano Letters, 2009. **9**(12): p. 4268-4272.
194. Robertson, A.W. and J.H. Warner, *Hexagonal Single Crystal Domains of Few-Layer Graphene on Copper Foils*. Nano Letters, 2011. **11**(3): p. 1182-1189.
195. Obraztsov, A.N., et al., *Chemical vapor deposition of thin graphite films of nanometer thickness*. Carbon, 2007. **45**(10): p. 2017-2021.
196. Moghal, J., Y.A. Wu, and J.H. Warner, *Mechanical response of few-layer graphene films on copper foils*. Scripta Materialia, 2012. **67**(3): p. 273-276.
197. Wang, Z., P.M. Lee, and E. Liu, *Graphene thin film electrodes synthesized by thermally treating co-sputtered nickel-carbon mixed layers for detection of trace lead, cadmium and copper ions in acetate buffer solutions*. Thin Solid Films, (0).
198. Kim, K.S., et al., *Large-scale pattern growth of graphene films for stretchable transparent electrodes*. Nature, 2009. **457**(7230): p. 706-710.
199. Lin, M., et al., *Dynamical Observation of Bamboo-like Carbon Nanotube Growth*. Nano Letters, 2007. **7**(8): p. 2234-2238.
200. Hellgren, N., et al., *Role of nitrogen in the formation of hard and elastic CN_x thin films by reactive magnetron sputtering*. Physical Review B, 1999. **59**(7): p. 5162-5169.
201. Costa, S.D., et al., *Resonant Raman spectroscopy of graphene grown on copper substrates*. Solid State Communications, 2012. **152**(15): p. 1317-1320.
202. Ouyang, Y. and L. Chen, *Surface-enhanced Raman scattering studies of few-layer graphene on silver substrate with 514 nm excitation*. Journal of Molecular Structure, 2011. **992**(1-3): p. 48-51.
203. Chen, P., et al., *Growth of carbon nanotubes by catalytic decomposition of CH₄ or CO on a Ni MgO catalyst*. Carbon, 1997. **35**(10-11): p. 1495-1501.
204. Bekessy, L.K., N.A. Rafferty, and S. Russell, *Anomalous scattering from single crystal substrate*. Advances in X-ray analysis, 2007: p. 177-81.
205. Lutterotti, L., et al., *Combined texture and structure analysis of deformed limestone from time-of-flight neutron diffraction spectra*. Journal of Applied Physics, 1997. **81**(2): p. 594-600.
206. Lutterotti, L., et al., *Texture, residual stress and structural analysis of thin films using a combined X-ray analysis*. Thin Solid Films, 2004. **450**(1): p. 34-41.
207. Lutterotti, L., *Total pattern fitting for the combined size-strain-stress-texture determination in thin film diffraction*. Nuclear Instruments and Methods in Physics Research Section B: Beam Interactions with Materials and Atoms, 2010. **268**(3-4): p. 334-340.
208. Ferrari, A.C. and J. Robertson, *Raman spectroscopy of amorphous, nanostructured, diamond-like carbon, and nanodiamond*. Philosophical Transactions of the Royal Society of London. Series

- A: Mathematical, Physical and Engineering Sciences, 2004. **362**(1824): p. 2477-2512.
209. Srivastava, S.K., V.D. Vankar, and V. Kumar, *Growth and microstructures of carbon nanotube films prepared by microwave plasma enhanced chemical vapor deposition process*. Thin Solid Films, 2006. **515**(4): p. 1552-1560.
210. Burt, D.P., et al., *Effects of Metal Underlayer Grain Size on Carbon Nanotube Growth*. The Journal of Physical Chemistry C, 2009. **113**(34): p. 15133-15139.
211. instruments, Q., *Autosorb-1/AS1Win operational manual*. P/N 05061-2.0 RevA ed. 2008: Quantachrome instruments. 26.
212. Marsh, H. and F. Rodriguez-Reinoso, *Characterization of Activated Carbon*, in *Activated Carbon*. 2006, Elsevier Science Ltd: Oxford. p. 143-242.
213. Barnes, G.T.G., I. R., *Interfacial Science: An Introduction* 2005, Oxford: Oxford University Press.
214. Chen, C.-H. and C.-C. Huang, *Hydrogen adsorption in defective carbon nanotubes*. Separation and Purification Technology, 2009. **65**(3): p. 305-310.
215. Fierro, V., et al., *Experimental evidence of an upper limit for hydrogen storage at 77 K on activated carbons*. Carbon, 2010. **48**(7): p. 1902-1911.
216. Xu, W.C., et al., *Investigation of hydrogen storage capacity of various carbon materials*. International Journal of Hydrogen Energy, 2007. **32**(13): p. 2504-2512.
217. Nguyen, C. and D.D. Do, *The Dubinin–Radushkevich equation and the underlying microscopic adsorption description*. Carbon, 2001. **39**(9): p. 1327-1336.
218. Hutson, N.D. and R.T. Yang, *Theoretical basis for the Dubinin-Radushkevitch (D-R) adsorption isotherm equation*. Adsorption, 1997. **3**(3): p. 189-195.
219. Ismadji, S. and S.K. Bhatia, *Characterization of activated carbons using liquid phase adsorption*. Carbon, 2001. **39**(8): p. 1237-1250.
220. Rather, S.-u., et al., *Surface adsorption and micropore filling of the hydrogen in activated MWCNTs*. International Journal of Hydrogen Energy, 2008. **33**(22): p. 6710-6718.
221. Pera-Titus, M., *On an isotherm thermodynamically consistent in Henry's region for describing gas adsorption in microporous materials*. Journal of Colloid and Interface Science, 2010. **345**(2): p. 410-416.
222. Mahle, J.J., *A Henry's law limit for the DR and DA equations*. Carbon, 1997. **35**(3): p. 432-435.
223. Instruments, Q., *H. Theory and Discussion*, in *Autosorb AS-1 Gas Sorption System Operational Manual*, Q. Instruments, Editor 2008, Quantachrome Instruments: Florida. p. 114-143.
224. Bates, D.M. and D.G. Watts, *Nonlinear Regression: Iterative Estimation and Linear Approximations*, in *Nonlinear Regression Analysis and Its Applications*. 2008, John Wiley & Sons, Inc. p. 32-66.

References

225. Bates, D.M. and D.G. Watts, *Multiresponse Parameter Estimation*, in *Nonlinear Regression Analysis and Its Applications*. 2008, John Wiley & Sons, Inc. p. 134-167.
226. Isochema, H., *Buoyancy Correction*, in *IGA Systems User Manual*. 2007, Hiden Isochema Limited: 231 Europa Boulevard Warrington WA5 7TN. p. B1-B11.
227. Schoonover, R.M. and F.E. Jones, *Air buoyancy correction in high-accuracy weighing on analytical balances*. *Analytical Chemistry*, 1981. **53**(6): p. 900-902.
228. Millward, A.R. and O.M. Yaghi, *Metal–Organic Frameworks with Exceptionally High Capacity for Storage of Carbon Dioxide at Room Temperature*. *Journal of the American Chemical Society*, 2005. **127**(51): p. 17998-17999.
229. Zhang, Z., et al., *Enhancement of CO₂ adsorption on high surface area activated carbon modified by N₂, H₂ and ammonia*. *Chemical Engineering Journal*, 2010. **160**(2): p. 571-577.
230. Bimbo, N., et al., *Analysis of hydrogen storage in nanoporous materials for low carbon energy applications*. *Faraday Discussions*, 2011. **151**(0): p. 59-74.
231. Tedds, S., et al., *Characterisation of porous hydrogen storage materials: carbons, zeolites, MOFs and PIMs*. *Faraday Discussions*, 2011. **151**(0): p. 75-94.
232. Clarkson, C.R., R.M. Bustin, and J.H. Levy, *Application of the mono/multilayer and adsorption potential theories to coal methane adsorption isotherms at elevated temperature and pressure*. *Carbon*, 1997. **35**(12): p. 1689-1705.
233. Llorens, J. and M. Pera-Titus, *Influence of surface heterogeneity on hydrogen adsorption on activated carbons*. *Colloids and Surfaces A: Physicochemical and Engineering Aspects*, 2009. **350**(1–3): p. 63-72.
234. Hoang, T.K.A., et al., *Design and Synthesis of Vanadium Hydrazide Gels for Kubas-Type Hydrogen Adsorption: A New Class of Hydrogen Storage Materials*. *Journal of the American Chemical Society*, 2010. **132**(33): p. 11792-11798.
235. Shim, W.G., et al., *Adsorption characteristics of benzene on electrospun-derived porous carbon nanofibers*. *Journal of Applied Polymer Science*, 2006. **102**(3): p. 2454-2462.
236. Saha, D., Z. Wei, and S. Deng, *Equilibrium, kinetics and enthalpy of hydrogen adsorption in MOF-177*. *International Journal of Hydrogen Energy*, 2008. **33**(24): p. 7479-7488.
237. Giaque, W.F. and C.J. Egan, *Carbon Dioxide. The Heat Capacity and Vapor Pressure of the Solid. The Heat of Sublimation. Thermodynamic and Spectroscopic Values of the Entropy*. *The Journal of Chemical Physics*, 1937. **5**(1): p. 45-54.
238. Pan, H., J.A. Ritter, and P.B. Balbuena, *Examination of the Approximations Used in Determining the Isosteric Heat of Adsorption from the Clausius–Clapeyron Equation*. *Langmuir*, 1998. **14**(21): p. 6323-6327.

239. Liu, J. and M.D. LeVan, *Isosteric heats of adsorption in the Henry's law region for carbon single wall cylindrical nanopores and spherical nanocavities*. Carbon, 2009. **47**(15): p. 3415-3423.
240. Schindler, B.J. and M.D. LeVan, *The theoretical maximum isosteric heat of adsorption in the Henry's law region for slit-shaped carbon nanopores*. Carbon, 2008. **46**(4): p. 644-648.
241. Liu, J. and M.D. LeVan, *Henry's law constants and isosteric heats of adsorption at zero loading for multi-wall carbon surfaces with different geometries*. Carbon, 2010. **48**(12): p. 3454-3462.
242. Tagliabue, M., et al., *Natural gas treating by selective adsorption: Material science and chemical engineering interplay*. Chemical Engineering Journal, 2009. **155**(3): p. 553-566.
243. Mishra, P., et al., *Adsorption of CO₂, CO, CH₄ and N₂ on DABCO based metal organic frameworks*. Microporous and Mesoporous Materials, 2013. **169**(0): p. 75-80.
244. Zhou, J., et al., *Purification of Multiwalled Carbon Nanotubes and Characterization of their oxygen containing functional groups*. Acta Physico-Chimica Sinica, 2010. **26**(11): p. 3080-3086.
245. Sing, K.S.W., et al., *Reporting Physisorption Data for Gas/Solid Systems*, in *Handbook of Heterogeneous Catalysis*. 2008, Wiley-VCH Verlag GmbH & Co. KGaA.
246. Sing, K.S.W., *7 - Assessment of Surface Area by Gas Adsorption*, in *Adsorption by Powders and Porous Solids (Second Edition)*, F. Rouquerol, et al., Editors. 2014, Academic Press: Oxford. p. 237-268.
247. Calo, J.M., P.J. Hall, and M. Antxustegi, *Carbon porosity characterization via small angle neutron scattering*. Colloids and Surfaces A: Physicochemical and Engineering Aspects, 2001. **187-188**(0): p. 219-232.
248. Landers, J., G.Y. Gor, and A.V. Neimark, *Density functional theory methods for characterization of porous materials*. Colloids and Surfaces A: Physicochemical and Engineering Aspects, 2013. **437**(0): p. 3-32.
249. Elsayed, M.A., P.J. Hall, and M.J. Heslop, *Preparation and structure characterization of carbons prepared from resorcinol-formaldehyde resin by CO₂ activation*. Adsorption, 2007. **13**(3-4): p. 299-306.
250. Instruments, Q., *AS-1 Win*, in *Quantachrome Instruments*, Q. Instruments, Editor 2008: Florida.
251. Mark Winter [The University of Sheffield and WebElements Ltd, U. *WebElements: the periodic table of the Elements. Periodicity. Van der Waals radius: Periodicity* [Web Page] 2010 [cited 2011 09 May]; Available from: http://www.webelements.com/hydrogen/atom_sizes.html.
252. Shang, C.X. and Z.X. Guo, *Structural and desorption characterisations of milled (MgH₂+Y,Ce) powder mixtures for hydrogen storage*. International Journal of Hydrogen Energy, 2007. **32**(14): p. 2920-2925.
253. Bénard, P., et al., *Comparison of hydrogen adsorption on nanoporous materials*. Journal of Alloys and Compounds, 2007. **446-447**: p. 380-384.

References

254. Zhou, L., Y. Zhou, and Y. Sun, *Enhanced storage of hydrogen at the temperature of liquid nitrogen*. International Journal of Hydrogen Energy, 2004. **29**(3): p. 319-322.
255. Amankwah, K.A.G. and J.A. Schwarz, *A modified approach for estimating pseudo-vapor pressures in the application of the Dubinin-Astakhov equation*. Carbon, 1995. **33**(9): p. 1313-1319.
256. Costa, S., et al., *Comparative study on purity evaluation of singlewall carbon nanotubes*. Energy Conversion and Management, 2008. **49**(9): p. 2490-2493.
257. Gallego, N.C., T.D. Burchell, and A.M. Clark, *Carbon Materials for Hydrogen Storage*, in *Carbon 2004: An International Conference on Carbon2004*: Providence, RI.
258. Dunne, J.A., et al., *Calorimetric Heats of Adsorption and Adsorption Isotherms. 2. O₂, N₂, Ar, CO₂, CH₄, C₂H₆, and SF₆ on NaX, H-ZSM-5, and Na-ZSM-5 Zeolites*. Langmuir, 1996. **12**(24): p. 5896-5904.
259. Siriwardane, R.V., et al., *Adsorption of CO₂ on Molecular Sieves and Activated Carbon*. Energy & Fuels, 2001. **15**(2): p. 279-284.
260. Suarez-Garcia, F., et al., *Activation of polymer blend carbon nanofibres by alkaline hydroxides and their hydrogen storage performances*. International Journal of Hydrogen Energy, 2009. **34**(22): p. 9141-9150.
261. Terrado, E., et al., *Optimizing catalyst nanoparticle distribution to produce densely-packed carbon nanotube growth*. Carbon, 2009. **47**(8): p. 1989-2001.
262. Liu, H., et al., *Aligned multi-walled carbon nanotubes on different substrates by floating catalyst chemical vapor deposition: Critical effects of buffer layer*. Surface and Coatings Technology, 2008. **202**(17): p. 4114-4120.
263. El Mel, A.A., et al., *Synthesis of nickel-filled carbon nanotubes at 350 °C*. Carbon, 2011. **49**(13): p. 4595-4598.
264. Zhang, Z., et al., *Fabrication of aligned carbon nanotubes on Cu catalyst by dc plasma-enhanced catalytic decomposition*. Applied Surface Science, 2009. **255**(12): p. 6404-6407.
265. Seah, C.-M., S.-P. Chai, and A.R. Mohamed, *Synthesis of aligned carbon nanotubes*. Carbon, 2011. **49**(14): p. 4613-4635.
266. Hellgren, N., et al., *Effect of chemical sputtering on the growth and structural evolution of magnetron sputtered CN_x thin films*. Thin Solid Films, 2001. **382**(1-2): p. 146-152.
267. McKee, G.S.B., C.P. Deck, and K.S. Vecchio, *Dimensional control of multi-walled carbon nanotubes in floating-catalyst CVD synthesis*. Carbon, 2009. **47**(8): p. 2085-2094.
268. Zhang, W.D., et al., *Fabrication of vertically aligned carbon nanotubes patterns by chemical vapor deposition for field emitters*. Diamond and Related Materials, 2002. **11**(9): p. 1638-1642.
269. Zipf, E.C. and R.W. McLaughlin, *On the dissociation of nitrogen by electron impact and by E.U.V. photo-absorption*. Planetary and Space Science, 1978. **26**(5): p. 449-462.
270. Pannala, S. and R.F. Wood, *Multiscale Simulations of Carbon Nanotube Nucleation and Growth: Mesoscopic Continuum*

- Calculations*. Journal of Nanoscience and Nanotechnology, 2004. **4**(4): p. 463-470.
271. Sjöström, H., et al., *Superhard and Elastic Carbon Nitride Thin Films Having Fullerenelike Microstructure*. Physical Review Letters, 1995. **75**(7): p. 1336-1339.
272. Hellgren, N., et al., *Role of nitrogen in the formation of hard and elastic CN_x thin films by reactive magnetron sputtering*. Physical Review B, 1999. **59**(7): p. 5162-5169.
273. Zhang, G., et al., *Ultra-high-yield growth of vertical single-walled carbon nanotubes: Hidden roles of hydrogen and oxygen*. Proceedings of the National Academy of Sciences of the United States of America, 2005. **102**(45): p. 16141-16145.
274. Chun, K.-Y., H.S. Lee, and C.J. Lee, *Nitrogen doping effects on the structure behavior and the field emission performance of double-walled carbon nanotubes*. Carbon, 2009. **47**(1): p. 169-177.
275. Wang, H. and J.J. Moore, *Low temperature growth mechanisms of vertically aligned carbon nanofibers and nanotubes by radio frequency-plasma enhanced chemical vapor deposition*. Carbon, 2012. **50**(3): p. 1235-1242.
276. Lee, K.-Y., et al., *Synthesis of aligned bamboo-like carbon nanotubes using radio frequency magnetron sputtering*. Journal of Vacuum Science & Technology B: Microelectronics and Nanometer Structures, 2003. **21**(4): p. 1437-1441.
277. Scalese, S., et al., *Ex situ and in situ catalyst deposition for CNT synthesis by RF-magnetron sputtering*. Physica E: Low-dimensional Systems and Nanostructures, 2008. **40**(7): p. 2243-2246.
278. Hayashi, N., et al., *Highly aligned carbon nanotube arrays fabricated by bias sputtering*. Applied Surface Science, 2003. **212-213**(0): p. 393-396.
279. www.geolsoc.org.uk. *Testing the Accuracy of ImageJ*. [PDF] 2014 15/01/2014 [cited 2014 18/04/2014]; Available from: http://www.geolsoc.org.uk/~media/Files/GSL/shared/Sup_pubs/2014/18725_2_Testing%20the%20Accuracy%20of%20ImageJ.ashx.
280. Delzeit, L., et al., *Multilayered metal catalysts for controlling the density of single-walled carbon nanotube growth*. Chemical Physics Letters, 2001. **348**(5-6): p. 368-374.
281. Liu, H., et al., *Effects of bimetallic catalysts on synthesis of nitrogen-doped carbon nanotubes as nanoscale energetic materials*. Particuology, 2011. **9**(5): p. 465-470.
282. Liu, C., Y.C. Chen, and Y. Tzeng, *Effects of carbon content in iron catalyst coatings on the growth of vertically aligned carbon nanotubes on smooth silicon surfaces by thermal chemical vapor deposition*. Diamond and Related Materials, 2004. **13**(4-8): p. 1274-1280.
283. Lazar, G., et al., *Structural properties of nitrogenated amorphous carbon films: Influence of deposition temperature and radiofrequency discharge power*. Journal of Applied Physics, 2008. **104**(7): p. 073534.
284. Zhong, Y., et al., *Synthesis of high nitrogen doping of carbon nanotubes and modeling the stabilization of filled DAATO@CNTs*

References

- (10,10) for nanoenergetic materials. *Journal of Physics and Chemistry of Solids*, 2010. **71**(2): p. 134-139.
285. Lin, M., et al., *Direct Observation of Single-Walled Carbon Nanotube Growth at the Atomistic Scale*. *Nano Letters*, 2006. **6**(3): p. 449-452.
286. Hinz, C., *Description of sorption data with isotherm equations*. *Geoderma*, 2001. **99**(3-4): p. 225-243.
287. Gasser, J.-G. and B. Kefif, *Electrical resistivity of liquid nickel-lanthanum and nickel-cerium alloys*. *Physical Review B*, 1990. **41**(5): p. 2776-2783.
288. Franke, P. and D. Neuschütz, *Ce-Ni (Cerium - Nickel)*, in *Binary Systems. Part 5: Binary Systems Supplement 1*, P. Franke and D. Neuschütz, Editors. 2007, Springer Berlin Heidelberg. p. 1-4.
289. Terrado, E., et al., *Important parameters for the catalytic nanoparticles formation towards the growth of carbon nanotube aligned arrays*. *Diamond and Related Materials*, 2007. **16**(4-7): p. 1082-1086.
290. Mirzaeian, M. and P.J. Hall, *Preparation of controlled porosity carbon aerogels for energy storage in rechargeable lithium oxygen batteries*. *Electrochimica Acta*, 2009. **54**(28): p. 7444-7451.
291. Prevéy, P., *X-ray diffraction characterization of crystallinity and phase composition in plasma-sprayed hydroxyapatite coatings*. *Journal of Thermal Spray Technology*, 2000. **9**(3): p. 369-376.
292. Zhang, F., et al., *Cerium oxide nanoparticles: Size-selective formation and structure analysis*. *Applied Physics Letters*, 2002. **80**(1): p. 127-129.
293. Higgins, D.C., D. Meza, and Z. Chen, *Nitrogen-Doped Carbon Nanotubes as Platinum Catalyst Supports for Oxygen Reduction Reaction in Proton Exchange Membrane Fuel Cells*. *The Journal of Physical Chemistry C*, 2010. **114**(50): p. 21982-21988.
294. Nair, R.R., et al., *Fine Structure Constant Defines Visual Transparency of Graphene*. *Science*, 2008. **320**(5881): p. 1308.
295. Yao, Y., et al., *Controlled Growth of Multilayer, Few-Layer, and Single-Layer Graphene on Metal Substrates*. *The Journal of Physical Chemistry C*, 2011. **115**(13): p. 5232-5238.
296. Nolan, W.N., et al., *Templated growth of graphenic materials*. *Nanotechnology*, 2009. **20**(24): p. 245607.
297. Tao, L., et al., *Synthesis of High Quality Monolayer Graphene at Reduced Temperature on Hydrogen-Enriched Evaporated Copper (111) Films*. *ACS Nano*, 2012. **6**(3): p. 2319-2325.
298. Rao, R., et al., *Graphene as an atomically thin interface for growth of vertically aligned carbon nanotubes*. *Sci. Rep.*, 2013. **3**.
299. Jiménez, V., et al., *Hydrogen storage capacity on different carbon materials*. *Chemical Physics Letters*, 2010. **485**(1-3): p. 152-155.
300. Lupu, D., et al., *Synthesis and hydrogen adsorption properties of a new iron based porous metal-organic framework*. *International Journal of Hydrogen Energy*, 2011. **36**(5): p. 3586-3592.
301. Latroche, M., et al., *Hydrogen Storage in the Giant-Pore Metal-Organic Frameworks MIL-100 and MIL-101*. *Angewandte Chemie International Edition*, 2006. **45**(48): p. 8227-8231.

302. Saha, D., et al., *Synthesis, characterization and hydrogen adsorption properties of metal–organic framework Al-TCBPB*. International Journal of Hydrogen Energy, 2012. **37**(6): p. 5100-5107.
303. Yamamoto, Y., et al., *Temperature dependence of hydrogen adsorption properties of nickel-doped mesoporous silica*. International Journal of Hydrogen Energy, 2011. **36**(9): p. 5739-5743.
304. Li, Y. and R.T. Yang, *Gas Adsorption and Storage in Metal–Organic Framework MOF-177*. Langmuir, 2007. **23**(26): p. 12937-12944.
305. Huang, C.-C., H.-M. Chen, and C.-H. Chen, *Hydrogen adsorption on modified activated carbon*. International Journal of Hydrogen Energy, 2010. **35**(7): p. 2777-2780.
306. Zhao, W., et al., *Activated carbons doped with Pd nanoparticles for hydrogen storage*. International Journal of Hydrogen Energy, 2012. **37**(6): p. 5072-5080.
307. Figueroa-Torres, M.Z., et al., *The synthesis of Ni-activated carbon nanocomposites via electroless deposition without a surface pretreatment as potential hydrogen storage materials*. International Journal of Hydrogen Energy, 2012. **37**(14): p. 10743-10749.
308. Konduru, N., P. Lindner, and N.M. Assaf-Anid, *Curbing the greenhouse effect by carbon dioxide adsorption with Zeolite 13X*. AIChE Journal, 2007. **53**(12): p. 3137-3143.
309. Zhu, Y., et al., *The effect of grafted amine group on the adsorption of CO₂ in MCM-41: A molecular simulation*. Catalysis Today, 2012. **194**(1): p. 53-59.
310. Rad, M.D., S. Fatemi, and S.M. Mirfendereski, *Development of T type zeolite for separation of CO₂ from CH₄ in adsorption processes*. Chemical Engineering Research and Design, 2012. **90**(10): p. 1687-1695.
311. Chen, B., et al., *High H₂ Adsorption in a Microporous Metal–Organic Framework with Open Metal Sites*. Angewandte Chemie International Edition, 2005. **44**(30): p. 4745-4749.
312. Yin, G., et al., *The role of different properties of activated carbon in CO₂ adsorption*. Chemical Engineering Journal, 2013. **230**(0): p. 133-140.

APPENDIX A: TOTTH MODEL

SYNTAX SCRIPT

*** To standardise the units to K and Bar.*

COMPUTE TempK77=273.15 + Temp77.

EXECUTE.

COMPUTE PressureATM77=Pressure77 / 1000.

EXECUTE.

COMPUTE TempK298=273.15 + Temp298.

EXECUTE.

COMPUTE PressureATM298=Pressure298 / 1000.

EXECUTE.

*** Select the desired data from the experimental isotherm data at 298 K.*

COMPUTE filter_\$=(TRUST298 = 1).

VARIABLE LABEL filter_\$ 'TRUST298 = 1 (FILTER)'.

VALUE LABELS filter_\$ 0 'Not Selected' 1 'Selected'.

FORMAT filter_\$ (f1.0).

FILTER BY filter_\$.

EXECUTE.

*** Modelling for the Toth equation at 298K.*

MODEL PROGRAM W0298=0.3, b298=20, C298=1.2.

COMPUTE

PRED=W0298*((b298*PressureATM298)/((1+(b298*PressureATM298)**C298)**(1/C298))).

CNLR Conc298

/PRED PRED

/SAVE PRED

/CRITERIA=ITER(15000)

/CRITERIA STEPLIMIT 2 ISTEP 1E+20 ITER(15000)

/OUTFILE=\\ueahome5\ressci23\tzs09xru\data\Documents\Param.sav'.

MATCH FILES /FILE=*

/FILE=\\ueahome5\ressci23\tzs09xru\data\Documents\Param.sav'

/RENAME (NCASES SSE = d0 d1)

/DROP= d0 d1.

EXECUTE.

*** Select the desired data from the experimental isotherm data at 77 K.*

COMPUTE filter_\$(TRUST77 = 1).

VARIABLE LABEL filter_\$ 'TRUST77 = 1 (FILTER)'.

VALUE LABELS filter_\$ 0 'Not Selected' 1 'Selected'.

FORMAT filter_\$ (f1.0).

FILTER BY filter_\$.

EXECUTE.

*** Modelling for the Toth equation at 77K.*

MODEL PROGRAM W077=50, b77=1000, C77=0.04.

COMPUTE

PRED=W077*((b77*PressureATM77)/((1+(b77*PressureATM77)**C77)**(1/C77))).

CNLR Conc77

/PRED PRED

/SAVE PRED

/CRITERIA=ITER(15000)

/CRITERIA STEPLIMIT 2 ISTEP 1E+20 ITER(15000)

/OUTFILE="\\ueahome5\ressci23\tzs09xru\data\Documents\Param.sav'.

MATCH FILES /FILE=*

/FILE="\\ueahome5\ressci23\tzs09xru\data\Documents\Param.sav'

/RENAME (NCASES SSE = d0 d1)

/DROP= d0 d1.

EXECUTE.

FILTER OFF.

***Calculating the isosteric heat*

*** setting equivalent pressures 298K.*

SPLIT FILE SEPARATE BY Num.

MODEL PROGRAM P298=0.00001.

COMPUTE

PRED=W0298*((b298*P298)/((1+(b298*P298)**C298)**(1/C298))).

CNLR ConclSO

/PRED PRED

/SAVE PRED

/CRITERIA STEPLIMIT 2 ISTEP 1E+20 ITER(15000)

/OUTFILE='\\ueahome5\ressci23\tzs09xru\data\Documents\P298.sav'.

MATCH FILES /FILE=*

/FILE='\\ueahome5\ressci23\tzs09xru\data\Documents\P298.sav'.

/RENAME (NCASES SSE = d0 d1)

/DROP= d0 d1.

EXECUTE.

*** setting equivalent pressures 77K.*

SPLIT FILE SEPARATE BY Num.

MODEL PROGRAM P77=0.00001.

COMPUTE PRED=W077*((b77*P77)/((1+(b77*P77)**C77)**(1/C77))).

CNLR ConclSO

/PRED PRED

/SAVE PRED

/CRITERIA STEPLIMIT 2 ISTEP 1E+20 ITER(15000)

/OUTFILE='\\ueahome5\ressci23\tzs09xru\data\Documents\P77.sav'.

MATCH FILES /FILE=*

/FILE='\\ueahome5\ressci23\tzs09xru\data\Documents\P77.sav'

/RENAME (NCASES SSE = d0 d1)

/DROP= d0 d1.

EXECUTE.

SPLIT FILE OFF.

*** Isosteric heat of adsorption equation.*

COMPUTE

$H_{ads} = (\ln(P298/P77)) * ((8.314 * (\text{TempAVERAGE77} + 273.15)) * (\text{TempAVERAGE298} + 273.15) / ((\text{TempAVERAGE298} + 273.15) - (\text{TempAVERAGE77} + 273.15))))$.

Execute.

**** Calculating Henrys law.*

*** Select the desired data from the isotherm at 298K.*

COMPUTE filter_\$(TRUST298 = 1).

VARIABLE LABEL filter_\$ 'TRUST298 = 1 (FILTER)'.
VALUE LABELS filter_\$ 0 'Not Selected' 1 'Selected'.
 FORMAT filter_\$ (f1.0).
 FILTER BY filter_\$.

EXECUTE.

*** Modelling for the Toth equation at 298 K.*

MODEL PROGRAM m2982=0.3, b2982=20, C2982=1.2.

COMPUTE

PRED=(m2982*PressureATM298)/((b2982+PressureATM298**C2982)**(1/C2982)).

CNLR Conc298

/PRED PRED

/SAVE PRED

/CRITERIA=ITER(15000)

/CRITERIA STEPLIMIT 2 ISTEP 1E+20 ITER(15000)

/OUTFILE='\\ueahome5\ressci23\tzs09xru\data\Documents\Param.sav'.

MATCH FILES /FILE=*

/FILE='\\ueahome5\ressci23\tzs09xru\data\Documents\Param.sav'

/RENAME (NCASES SSE = d0 d1)

/DROP= d0 d1.

EXECUTE.

COMPUTE Kh298=m2982/(b2982**(1/C2982)).

EXECUTE.

*** Select the desired data from the isotherm at 77K.*

COMPUTE filter_\$(TRUST77 = 1).

VARIABLE LABEL filter_\$ 'TRUST77 = 1 (FILTER)'.
VALUE LABELS filter_\$ 0 'Not Selected' 1 'Selected'.
 FORMAT filter_\$ (f1.0).
 FILTER BY filter_\$.

EXECUTE.

*** Modelling for the Toth equation 77 K.*

MODEL PROGRAM m772=50, b772=10, C772=4.

COMPUTE

PRED=(m772*PressureATM77)/((b772+PressureATM77**C772)**(1/C772)).

CNLR Conc77

/PRED PRED

/SAVE PRED

/CRITERIA=ITER(15000)

/CRITERIA STEPLIMIT 2 ISTEP 1E+20 ITER(15000)

/OUTFILE="\\ueahome5\ressci23\tzs09xru\data\Documents\Param.sav'.

MATCH FILES /FILE=*

/FILE='\\ueahome5\ressci23\tzs09xru\data\Documents\Param.sav'

/RENAME (NCASES SSE = d0 d1)

/DROP= d0 d1.

EXECUTE.

COMPUTE Kh77=m772/(b772**(1/C772)).

EXECUTE.

*** calculating isosteric heat from Henry's constant.*

COMPUTE H_adsHenry=(LN(Kh298-

Kh77))/(TempAVERAGE298+273.15)-

(TempAVERAGE77+273.15)*(8.314*(TempAVERAGE77+273.15)*(TempAVERAGE298+273.15)).

EXECUTE.

APPENDIX B: LIST OF SAMPLES AND ABBREVIATIONS

4.1 The activation and chemical doping of activated carbon by mechanical ball milling and its influence on H₂ and CO₂ storage capacity

Name	Description
AC0	Unmilled activated carbon
AC15	Activated carbon ball milled for 15 minutes
AC30	Activated carbon ball milled for 15 minutes
AC60	Activated carbon ball milled for 15 minutes
AC120	Activated carbon ball milled for 15 minutes
ACNi15	Activated carbon doped with 5wt.% nickel nanopowder and ball milled for 15 minutes
ACNi120	Activated carbon doped with 5wt.% nickel nanopowder and ball milled for 120 minutes

4.2 The influence of nitrogen content and the presence of a metal substrate on the growth and H₂ storage capacity of novel carbon films deposited by magnetron sputtering

Name	Description
SiMgNiC0600	Carbon deposited for four hours at 600 °C in a 0 % N ₂ , 100 % Ar atmosphere onto a silicon substrate coated in films of magnesium and nickel which had been annealed for 30 minutes at 600 °C.
SiMgNiC25600	Carbon deposited for four hours at 600 °C in a 25 % N ₂ , 75 % Ar atmosphere onto a silicon substrate coated in films of magnesium and nickel which had been annealed for 30 minutes at 600 °C.

Appendix B

SiMgNiC50600	Carbon deposited for four hours at 600 °C in a 50 % N ₂ , 50 % Ar atmosphere onto a silicon substrate coated in films of magnesium and nickel which had been annealed for 30 minutes at 600 °C.
SiMgNiC75600	Carbon deposited for four hours at 600 °C in a 75 % N ₂ , 25 % Ar atmosphere onto a silicon substrate coated in films of magnesium and nickel which had been annealed for 30 minutes at 600 °C.
SiMgNiC100600	Carbon deposited for four hours at 600 °C in a 100 % N ₂ , 0 % Ar atmosphere onto a silicon substrate coated in films of magnesium and nickel which had been annealed for 30 minutes at 600 °C.
SiMgNiC50400	Carbon deposited for four hours at 400 °C in a 50 % N ₂ , 50 % Ar atmosphere onto a silicon substrate coated in films of magnesium and nickel which had been annealed for 30 minutes at 400 °C.
SiMgNiC50700	Carbon deposited for four hours at 700 °C in a 50 % N ₂ , 50 % Ar atmosphere onto a silicon substrate coated in films of magnesium and nickel which had been annealed for 30 minutes at 700 °C.
SiNiC0600	Carbon deposited for four hours at 600 °C in a 0 % N ₂ , 100 % Ar atmosphere onto a silicon substrate coated with a nickel film which had been annealed for 30 minutes at 600 °C.
SiNiC25600	Carbon deposited for four hours at 600 °C in a 25 % N ₂ , 75 % Ar atmosphere onto a silicon substrate coated with a nickel film which had been annealed for 30 minutes at 600 °C.
SiNiC50600	Carbon deposited for four hours at 600 °C in a 50 % N ₂ , 50 % Ar atmosphere onto a silicon substrate coated with a nickel film which had been annealed for 30 minutes at 600 °C.

SiNiC75600	Carbon deposited for four hours at 600 °C in a 75 % N ₂ , 25 % Ar atmosphere onto a silicon substrate coated with a nickel film which had been annealed for 30 minutes at 600 °C.
SiNiC100600	Carbon deposited for four hours at 600 °C in a 100 % N ₂ , 0 % Ar atmosphere onto a silicon substrate coated with a nickel film which had been annealed for 30 minutes at 600 °C.
SiC0600	Carbon deposited for four hours at 600 °C in a 0 % N ₂ , 100 % Ar atmosphere onto a silicon substrate
SiC25600	Carbon deposited for four hours at 600 °C in a 25 % N ₂ , 75 % Ar atmosphere onto a silicon substrate
SiC50600	Carbon deposited for four hours at 600 °C in a 50 % N ₂ , 50 % Ar atmosphere onto a silicon substrate.
SiC75600	Carbon deposited for four hours at 600 °C in a 75 % N ₂ , 25 % Ar atmosphere onto a silicon substrate.
SiC100600	Carbon deposited for four hours at 600 °C in a 100 % N ₂ , 0 % Ar atmosphere onto a silicon substrate.

4.3 A study of magnetron sputtering as a means to compositionally dope carbon nanotubes with cerium and nickel and its influence on H₂ storage capacity

Name	Description
RCNT	As received carbon nanotubes (CNTs)
PCNT	Purified carbon nanotubes
CNTCe0.025	CNTs sputter coated with 0.025 mol.% cerium
CNTCe0.05	CNTs sputter coated with 0.05 mol.% cerium
CNTCe0.075	CNTs sputter coated with 0.075 mol.% cerium
CNTCe0.1	CNTs sputter coated with 0.1 mol.% cerium
CNTCe0.125	CNTs sputter coated with 0.125 mol.% cerium
CNTCe0.15	CNTs sputter coated with 0.15 mol.% cerium
CNTCe0.2	CNTs sputter coated with 0.2 mol.% cerium

CNTCe0.3	CNTs sputter coated with 0.3 mol.% cerium
CNTCe0.4	CNTs sputter coated with 0.4 mol.% cerium
CNTCe0.5	CNTs sputter coated with 0.5 mol.% cerium
CNTNi0.01	CNTs sputter coated with 0.01 mol.% nickel
CNTNi0.05	CNTs sputter coated with 0.05 mol.% nickel
CNTNi0.1	CNTs sputter coated with 0.1 mol.% nickel
CNTNi0.5	CNTs sputter coated with 0.5 mol.% nickel
CNTNi1	CNTs sputter coated with 1 mol.% nickel
CNTMix1	CNTs sputter coated with 0.01 mol.% cerium and 0.07 mol.% nickel
CNTMix2	CNTs sputter coated with 0.03 mol.% cerium and 0.21 mol.% nickel
CNTMix3	CNTs sputter coated with 0.5 mol.% cerium and 0.35 mol.% nickel

4.4 Exploring the synthesis of graphene by magnetron sputtering

Name	Description
Cu	500 nm thick copper film deposited onto a silicon substrate
CuG10	Carbon film deposited for 10 s onto a CuSi substrate
CuG20	Carbon film deposited for 20 s onto a CuSi substrate
CuG30	Carbon film deposited for 30 s onto a CuSi substrate
CuG60	Carbon film deposited for 60 s onto a CuSi substrate
CuG120	Carbon film deposited for 120 s onto a CuSi substrate
CuG180	Carbon film deposited for 180 s onto a CuSi substrate
Ni	300 nm thick nickel film deposited onto a silicon substrate
NiG30	Carbon film deposited for 30 s onto a NiSi substrate
NiG60	Carbon film deposited for 60 s onto a NiSi substrate
NiG120	Carbon film deposited for 120 s onto a NiSi substrate
NiG180	Carbon film deposited for 180 s onto a NiSi substrate

Abbreviations and symbols

Abbreviation / symbol	Definition	First appearance
$\Delta G^\circ_{\text{rxn}}(T)$	Gibbs free energy change	24
ΔH_0	enthalpy of adsorption	111
$-\Delta H_{\text{ads}}$	isosteric heat of adsorption	24
$-\Delta H_{\text{ads}}^0$	isosteric heat of adsorption in the Henry's law region	112
ΔH_{vap}	isosteric heat of vaporisation	111
<i>a</i>	negatively charged ligand	48
<i>A</i>	adsorption potential	101
AC	Activated carbon	32
A_C	A Clausius-Clapeyron constant	24
A_{cs}	Cross-sectional area of an adsorbate	99
AlO_4	aluminium oxides (zeolites)	26
ANOVA	Analysis of variance	103
A_p	specific pore volume	102
<i>Ar</i>	Argon	88
<i>b</i>	adsorption affinity	108
<i>BET</i>	Brunauer, Emmett and Teller	98
BHJ	Barrett, Joyner and Halenda	101
BTU	British thermal units	5
C_B	BET constant	99
<i>C</i>	The Toth equations heterogeneity factor	109
C_2H_4	Ethylene	15
C_2H_6	Ethane	15
C_b	Buoyancy	105
CCS	Carbon capture and storage	7
<i>Ce</i>	Cerium	72
CeO_2	Ceria	73

Appendix B

C_f	carbon fraction of the EDX results	163
CH ₄	Methane	14
Cl ₂	Chlorine molecule	19
CNT	Carbon nanotube	2
CN _x	Nitrogen doped carbon structures	69
CO	Carbon monoxide	9
CO ₂	Carbon dioxide molecule	1
Cu	Copper	78
CVD	Chemical Vapour Deposition	56
DA	Dubinin-Astakhov	100
DC	direct current	59
DFT	Density functionalised theory	102
DOE	<i>US Department of Energy</i>	1
DR	Dubinin-Radushkevich	100
E _A	characteristic energy of adsorption	101
E	Energy	161
EDX	Energy Dispersive X-ray	72
<i>et al</i>	And others	10
<i>ex situ</i>	Outside/after the reaction mix	94
FLG	few layer graphene	77
FWHM	full width at half maximum	165
g	Acceleration due to gravity	104
GAI	generalised adsorption isotherm	102
GHG	Greenhouse gas	4
GNF	Graphite nanofibre	33
H ₂	Hydrogen molecule	1
H ₂ O	Water molecule	14
H ₂ S	Hydrogen sulphide	15
HCl	Hydrochloric acid	15
He	Helium	104
HNO ₃	Nitric acid	36
IGA	Intelligent Gravimetric Analyser	103

<i>in situ</i>	Within the reaction mix	9
<i>in vacuo</i>	In a vacuum	45
K	interaction constant	101
K_a	equilibrium constant	23
K_B	Boltzmann constant	24
K_H	Henry's law constant	112
K_L	rate constant	24
<i>LDH</i>	Layered double hydroxides	48
LH_2	Liquid hydrogen	11
$LiAlH_4$	Lithium alanate	40
LN_2	liquid nitrogen	28
<i>M</i>	Metal species	48
m	Mass of the adsorbate	99
M^A	alkali metals	49
m_A	Mass of the adsorbant	99
m_a	Mass of the adsorbed phase	105
<i>MEA</i>	Monoethanolamine	48
m_F	mass of the film	94
<i>Mg</i>	Magnesium	70
$Mg(B_{12}H_{12})_2$	Magnesium dodecaborane	45
$Mg(BH_4)_2$	Magnesium borohydride	45
MgH_2	Magnesium hydride	39
m_r	Mass of reference material	105
m_s	Mass of sample	104
MWCNT	multiwall carbon nanotubes	35
<i>N</i>	Avogadro's number	99
n	heterogeneity factor	101
N_2	Nitrogen molecule	17
N_C	nitrogen content of the deposited film	163
N_f	nitrogen fraction of the EDX results	163
Ni	Nickel	17
NLR	non-linear regression	103

Appendix B

O_2	Oxygen molecule	17
<i>OFN</i>	Oxygen free Nitrogen	88
<i>P</i>	Pressure (bar)	23
P_0	saturated vapour pressure	101
P_a	ambient pressure	100
<i>PACVD</i>	Plasma Assisted Chemical Vapour Deposition	58
<i>PBI</i>	polybenzimidazole	54
<i>PCNT</i>	purified CNT	120
<i>Pd</i>	Palladium	53
<i>PECVD</i>	Plasma Enhanced Chemical Vapour Deposition	58
P_D^{eq}	equilibrium partial pressure	23
PH_3	Phosphine	15
ppm	parts per million	21
<i>PSA</i>	pressure swing adsorption	26
<i>PSD</i>	pore size distribution	25
<i>PVD</i>	physical vapour deposition	59
<i>R</i>	Ideal gas constant ($8.314 \text{ J}\cdot\text{mol}^{-1}\text{K}^{-1}$)	24
<i>r</i>	average pore radius	101
<i>RCNT</i>	Raw carbon nanotube	87
R_D	rate of sputter deposition	94
<i>RF</i>	radio frequency	59
r_k	Kelvin radius of the pore	102
r_{ps}	average pore size	100
r_p	actual pore radius	102
<i>RPM</i>	Revolutions per minute	65
<i>S</i>	An empty adsorption site	49
<i>SA</i>	Surface area	99
<i>sccm</i>	standard cubic centimetres per minute	79
<i>SEM</i>	Scanning Electron Microscopy	72
<i>Si</i>	Silicon	80

"SiO ₄ "	tetrahedral silicon oxides (zeolites)	26
SMR	Steam methane reformation	14
SOR	square of residuals	110
S _s	Samples surface area	99
SSA	Specific surface area	127
S _{S-D}	London Dispersion forces	23
SWCNT	Single Walled Carbon Nanotube	35
T	Temperature (K)	101
t	thickness of the adsorbed layer	102
T _D	deposition time	94
TEM	Transmission Electron Microscopy	68
TSA	temperature swing adsorption	26
TSS	total sum of squares	110
t _{r̄}	adsorbed layer thickness at the average radius in the current pressure range	102
V _{ads}	volume of the adsorbate	100
V _{liq}	liquid volume of the adsorbate	100
V _m	molar volume of the liquid adsorbate	100
V _p	volume of the pore	102
V _s	Volume of displaced gas	106
W	The number of adsorbed molecules	24
W ₀	The number of adsorption sites	24
W _{exp}	experimental storage capacities	110
WGS	Water gas shift	9
W _M	weight of the adsorbate monolayer	99
W _{mod}	modelled storage capacities	110
W _{rec}	Recorded weight	104
w _s	Weight of sample	105
wt.%	Kg adsorbate / kg adsorbent	13
X	An unknown value	48
XRD	x-ray diffraction	72
Z	pore width	103

Appendix B

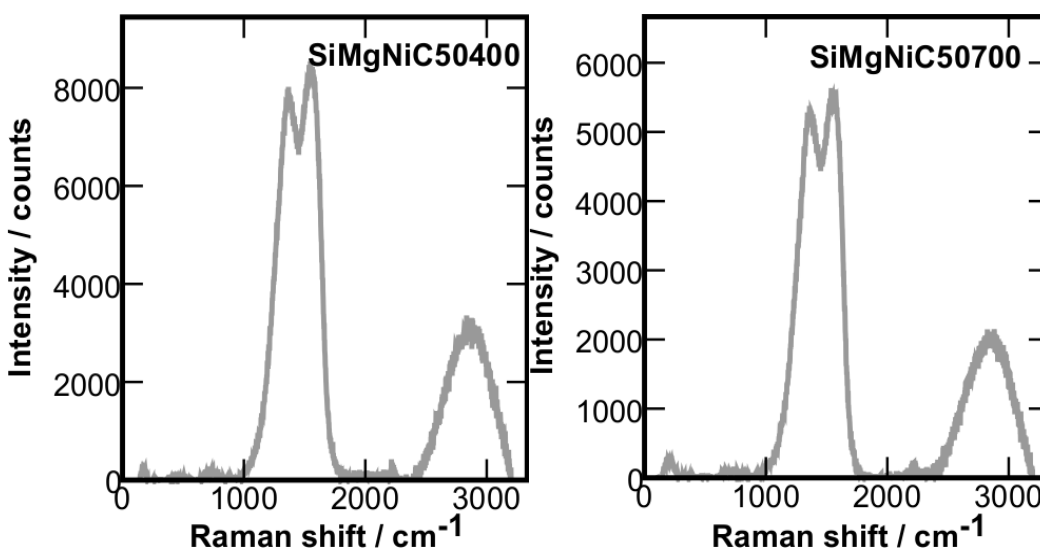
α	Polarisability	23
$\alpha_{N,M}$	separation factor	112
γ	surface tension at the adsorbates boiling point	102
ε	adsorption potential	24
θ	Fractional coverage (W/W_0)	24
θ^0	angle of incidence	161
ρ_g	Density of displaced gas	105
ρ_s	Density of sample	105
ρ_r	Density of the reference material	105
μ	chemical potential of the adsorbate	24
ϕ	difference in the weight of the sample and reference arms	106

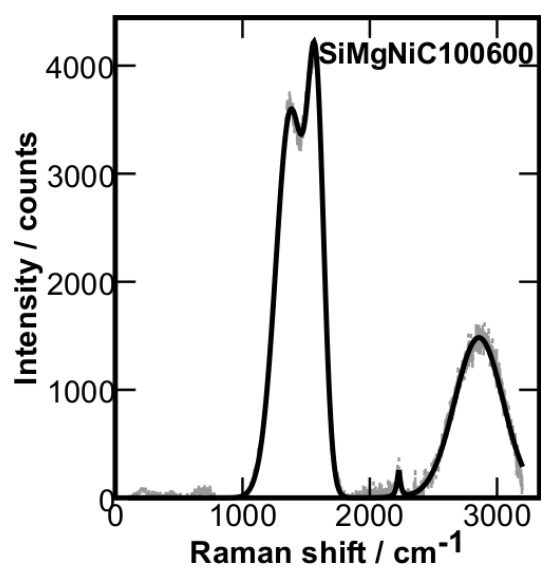
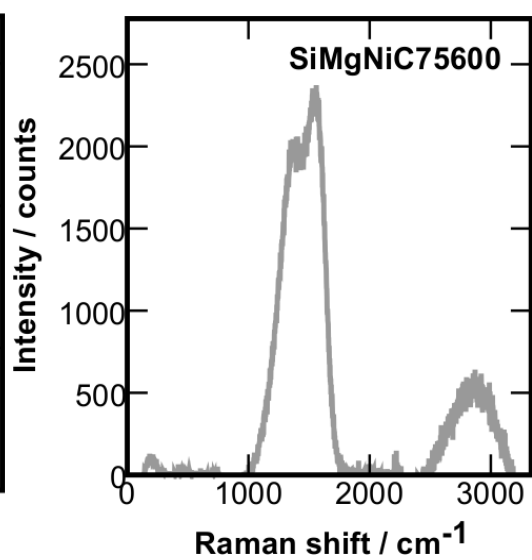
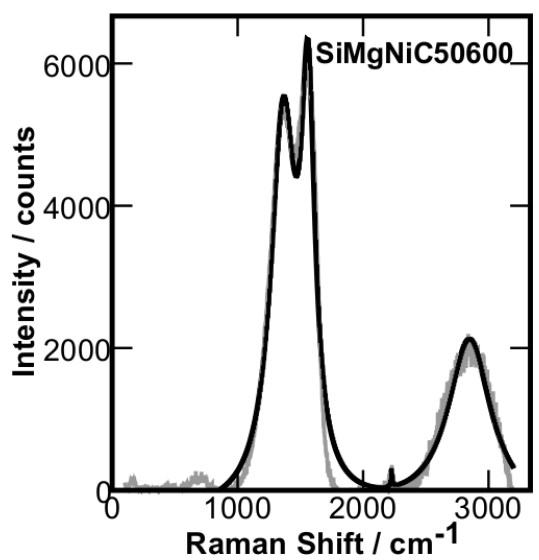
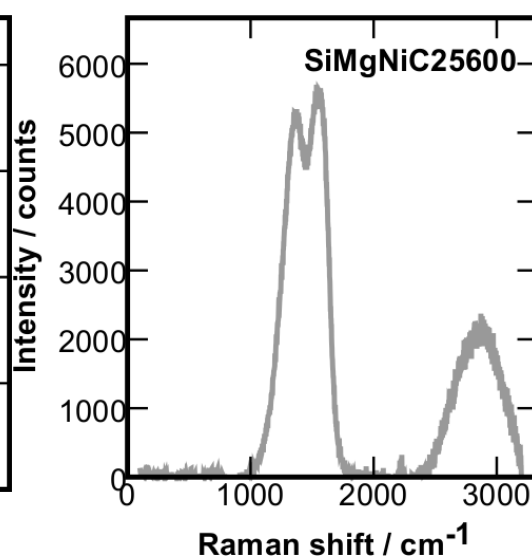
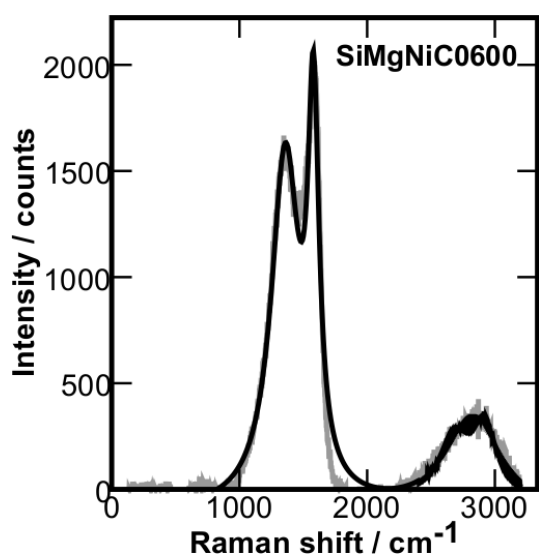
APPENDIX C: ADDITIONAL RAMAN DATA FROM SECTION 4.2

The graphs below present background corrected Raman spectra for the seventeen samples studied in experiment “*The influence of nitrogen content and the presence of a metal substrate on the growth and H₂ storage capacity of novel carbon films deposited by magnetron sputtering*”.

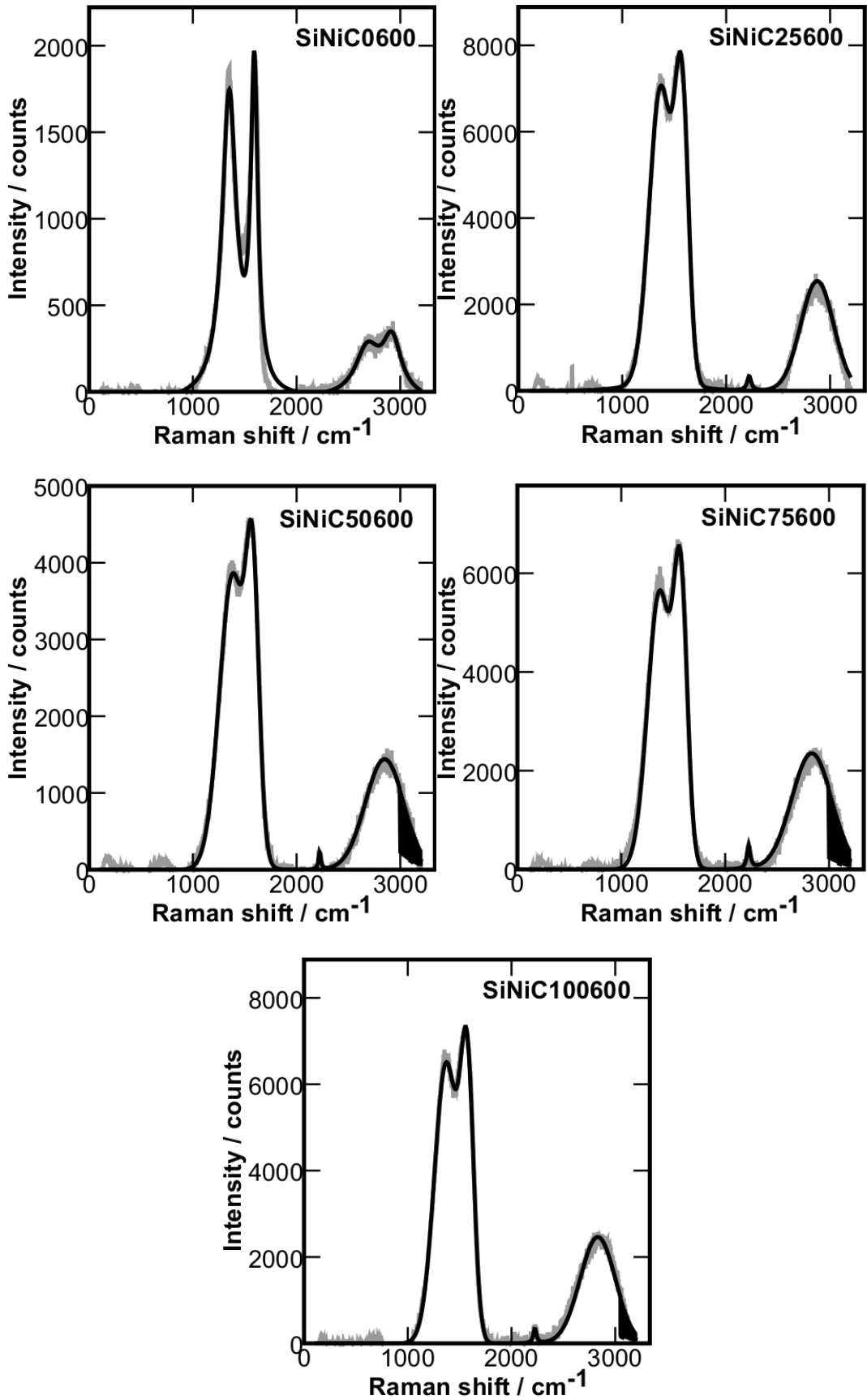
The grey lines represent the collected data. The black line represents the modelled fit used for interpretation. The collected results presented in the **Section 4.2** are averaged from the five Raman spectra collected for each sample so may not match up directly with the graphs below. Four of the graphs below do not contain the modelled fit line as the modelled curve data became corrupted and back-ups were inaccessible.

SiMgNiC50 samples deposited at different temperatures (Section 4.2.1.2.2)



SiMgNiC samples deposited at 600 °C (Section 4.2.1.1.2)

SiNiC samples deposited at 600 °C (Section 4.2.1.3.2)



SiC samples deposited at 600 °C (Section 4.2.1.2.2)